
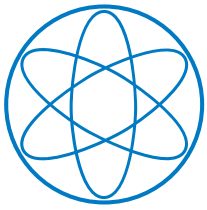


Habilitationsschrift
für das Fach Experimentalphysik
an der
Technischen Universität München

The Microscopic Picture of Plasma Edge Turbulence

vorgelegt von

Peter Manz

December 2018

Contents

Chapter 1

Introduction

1.1 Why fusion?

Energy is needed and used everywhere. It is key to economy and human development. The massive consumption of fossil fuels led to global warming, and therefore, must be strongly reduced. The surface temperature warming is related to the cumulative total of carbon dioxide emitted to the atmosphere, therefore, it may be necessary to go even beyond net-zero emission and extract actually carbon dioxide from the atmosphere. As several billion people are still pursuing a better life, whatever economy savings will be achieved, the global energy demand will increase. This is a global problem and it needs a global solution.

The technologies of renewable energy sources have significantly improved in the last years. Power supply from wind and solar sources is non-carbon emitting and legitimately part of the favored solution. However, the intermittency of power supply from wind and solar sources remains a problem. Strong additional back-up capacity will be too expensive and large-scale power storage systems seem difficult to achieve. Energy infrastructure takes a very long time to build, it is expensive to change. Traditional baseload power plants will be still indispensable in the near and far future. The other component of the non-carbon emitting energy supply is nuclear. Any reasonable scenario analysis includes a global increase of nuclear fission power in next decades [1, 2]. Nuclear fission comprised risks, stemming from involuntary and voluntary (e.g. terrorism) nuclear accidents, from long-term radioactive waste storage and from nuclear weapons proliferation. In particular, due to the current public opinion regarding nuclear fission, it may prove difficult for the public to accept nuclear plants in the landscape at the scale necessary. These risks can be strongly mitigated by nuclear fusion.

The advantages of nuclear fusion are summarized in the following: Fission energy is ten millions of times more concentrated than the energy released by combustion, and fusion even four times more. No greenhouse gases are emitted, too. The fuel for fusion is practically inexhaustible and well distributed on earth. There is no risk of uncontrolled power runaway providing safe oper-

ation. Long-term radioactive waste storage is not required, neutron activated materials can be recycled within a century.

1.2 Why plasma turbulence?

Plasma turbulence is everywhere in space and astrophysical plasmas. It stirs the galactic and stellar dynamo, it is important for magnetic reconnection, scatters particles facilitating shock acceleration of cosmic rays, drives interstellar medium scintillations and drives angular momentum transport in accretion disks [3]. With respect to magnetically confined fusion, plasma turbulence is the main obstacle from achieving ignition so far. Turbulent transport is the reason why the demonstration experiment for the feasibility of fusion power, ITER, has to be build at this large size. The region just inside the confined region, the edge of the plasma, is characterized by steep gradients, which drive instability and turbulence. The overall plasma confinement is determined by the turbulence in the plasma edge, it highly influences the overall core performance and is directly related to the fusion gain. Instability and turbulence in the plasma edge also influence the power load to the material components. With respect to magnetically confined fusion, plasma turbulence is key for understanding the plasma performance.

There is a joke about fusion, that it is the energy source of the future, and always will be. This shows that it is quite difficult to realize. Nevertheless, research on magnetically confined fusion continuously makes progress and breakthroughs can be just a bright idea away. Sometimes this takes time. Flows through pipes and hydraulic networks are generally turbulent and the friction losses encountered there are responsible for approximately 10 % of the global electric energy consumption [4]. The problem is known since the pioneering study of Osborne Reynolds in the late 19th century [5], but only recently it could be demonstrated, how turbulence in pipe flow can be annihilated [4]. Counterintuitively, by initially increasing turbulence intensities a complete collapse of turbulence can be accomplished, reducing subsequently friction losses by as much as 90 % [4]. By enhanced turbulent mixing, the mean flow profile gets more uniform and the turbulence drive is disabled, turbulent fluctuations disappear and the flow relaminarizes. The turbulence drive in a fusion plasma are the gradients, which determine the fusion performance and should not be reduced too much, but this example shows that it is not impossible to significantly reduce turbulence. A pipe is a much simpler system than a magnetically confined fusion plasma. There is no law of nature prohibiting us from adjusting turbulence and allowing for a much smaller, easier to handle and more economic fusion reactor.

Many physicists, including Heisenberg, von Weizsäcker, Onsager, and Feynman, have attempted to tackle the problem of turbulence purely analytically but with only limited success. Even though the equations require no more skills than (a lot of) undergraduate mathematics, the problem is very chal-

lenging. One reason most blamed is the nonlinearity. Due to the nonlinearity, the equations for the resolved scales contain moments of the unresolved scales. There are nonlinear problems that are completely integrable like the Korteveg-de Vries and Schrödinger equations, turbulence is not, which imposes intrinsic stochasticity and self-randomization [6]. And finally because the pressure is defined in each space point, by the velocity in the whole flow field, turbulence is essentially non-local [6]. All these lead to a loss of predictability, but stable statistical properties.

The advent of large-scale computations promised huge progress. One should be able to evaluate designs without having to do experiments or build prototypes. With direct numerical simulations (DNS) the equations of motion are integrated numerically without relying on any modeling of turbulence flows. For three-dimensional turbulence the minimum number of required grid cells is in the order of $\mathrm{Re}^{9/4}$ (with Reynolds number Re), which for flows of industrial interest (for example a commercial airliner at $\mathrm{Re} \approx 10^9$) is still often unfeasible [7]. Nevertheless, DNS provided substantial insight in the physics of turbulence. Numerical methods in general accurately predict the large scales, but the accuracy at small scales certainly remains an issue [7]. Both, the smallest and largest scales are important in many applications of fluid turbulence, including mixing, combustion, turbulent flows with chemical reactions, and some special problems in blood flow related to such phenomena as hemolysis and thrombosis [6]. It would be careless to assume plasma turbulence being an exception, and in fact it is not [8]. However, resolving all important scales (from the electron gyroradius to the reactor size) and all relevant physics from the core to the plasma edge and finally including the wall will not be feasible in the near future. All present simulation codes address only parts of the problem, their combination (called integrated modeling) cannot not be verified, because no full solution is available. Therefore, even though huge progress has been achieved in verification and validation of simulations codes, simulations will not soon reach the precision to render experiments unnecessary, which was the whole idea of simulations in the first place. In turbulence research experiments are indispensable. Even if complete simulations would be available, without some kind of understanding, we would be overwhelmed by the amount of data and its apparently random behavior.

The aim of this work is to distillate *the microscopic picture of plasma edge turbulence*. This is important for deriving meaning and/or a message from the experiment, be it physical or digital. Therefore, experiments and simulations have been carried out on different devices and simulation codes.

1.3 Structure of this thesis

This work is a German Habilitation thesis, and as such my scientific progress from the beginning of my Post Doc time will be presented in Chaps. 8 to 12 based on Refs. [9, 10, 11, 12, 13, 14, 15, 16, 17, 18, 19, 20] after the theoretical

background and methods have been explained in Chaps. 2 to 7. The basic concept of magnetic confinement, its geometry and confinement regimes are introduced in Chap. 2. Plasma turbulence is bound to the two-dimensional plane perpendicular to the magnetic field lines. Chap. 3 presents the phenomenology of two-dimensional turbulence. Different plasma instabilities are studied in Chap. 4. A more detailed mathematical treatment of the instabilities is provided in the appendix B. Plasma turbulence itself is introduced in Chap. 5. Diagnostics and analysis methods suitable for studying plasma turbulence are summarized in Chaps. 6 and 7, respectively. In the main part

- basic features of drift-wave turbulence will be studied in low-temperature laboratory experiments. The results presented in Chap. 8 are based on the publications [9, 10, 11]. To understand structure formation in drift-wave turbulence the inverse energy cascade, the transition to turbulence and the spatial nonlocality of zonal flow drive are studied in detail.

- In the low confinement regime of tokamaks the turbulence can become quite strong. Chapter 9 concerns the nonlinear drive of plasma turbulence and the possible loss of linear features. It is based on simulation results obtained with the gyrofluid code GEMR (Sec. 5.3) and is based on the publication [12].

- The transition to high confinement is one of the most important not understood phenomena in magnetically confined fusion. Various experiments found that turbulence suppression by turbulence flow generation appears strong enough to trigger a transition into the high confinement regime. Other experiments show only weak or insufficient zonal flow activity at the transition from low to high confinement. In Chap. 10 experimental results from the tokamak EAST supporting the transition by turbulence generated flows and from the tokamak ASDEX Upgrade showing no sign of turbulence generated flow activity are presented. The results are based on the publications [13],[14] and [15], respectively.

- The I-mode is another improved confinement regime, where the density and temperature are differently well confined. Turbulence in I-mode will be characterized in Chapter 11 based on experiments carried out in the tokamak ASDEX Upgrade and published in Ref. [16, 17].

- Chapter 12 deals with transport in the scrape-off layer. The scrape-off layer is the region outside the confined plasma governing the heat load on the plasma facing components, determining the power and particle balance and regulating the impurity dynamics. Therefore, the scrape-off layer is of central importance for a future fusion reactor. In particular the impact of finite ion temperatures and nonlocal transport are investigated. Results are based on the publications [18, 19, 20].

Newcomers to the field of plasma edge turbulence may find this work useful. In plasma turbulence research a lot of acronyms and concepts are used

in a self-evident way, which are never taught in lectures or textbooks. This work has also been designed to fill a gap between state of the art in work on edge plasma turbulence and available treatments in textbooks. Chapter 4 provides an introduction to the most important instabilities and provides a guide for their characterization. To guide the analysis strategy of experimental data, Chap. 7 provides an overview of different data analysis techniques useful for plasma turbulence, many of them cannot be found in textbooks. In the introductory chapters, particular attention has been paid to subjects not covered in the common introductory literature, which are important for this work. Furthermore, most phenomena important for plasma turbulence in general, which however are not very important for my personal previous work, are introduced. Someone new to the field will find concepts and phenomena at least shortly introduced and additional references are provided. The index list together with the extensive bibliography make this work a proper general reference book on plasma turbulence. Taking into account a possible diverse readership, a plasma physics curriculum is included (Appendix. A), in which all basic concepts of plasma physics necessary for understanding this work are introduced. I have tried to write this thesis as modular as possible and to reduce the mathematics to a minimum.

Chapter 2

Magnetic confinement

The processes able to sustain a star's energy balance by fusion reactions are inadequate for earth application. The main confinement mechanism by gravitational attraction is not reproducible. The power density and the corresponding temperature and cross-section would be too low to facilitate enough fusion reactions to get a net energy excess in a typical reactor-size device. Furthermore, the average power density of about 0.3 MW/m^3 is too low to be economically competitive (already existing pressurized water reactors reach about 100 MW/m^3). Therefore, much higher temperatures compared to the sun are needed to facilitate a fusion power plant on earth. Maintaining high temperature in order to achieve thermonuclear fusion requires an appropriate insulation of the plasma from the wall. A proper confinement can be achieved by closed magnetic field lines to which the charged particles are bound by the Lorentz force. Perpendicular to the magnetic field $\mathbf{B}$ the Lorentz force is balanced by the pressure gradient

$$\nabla p = \mathbf{J} \times \mathbf{B}, \tag{2.1}$$

where the current $\mathbf{J}$ to stabilize the pressure gradient is generated by the plasma itself. This route to thermonuclear fusion is called magnetic confinement. The plasma economy, e.g. how much plasma pressure can be confined at a given magnetic field, is provided by the plasma beta

$$\beta = \frac{p}{B^2/2\mu_0}. \tag{2.2}$$

It gives the ratio between the plasma pressure p to the magnetic pressure $B^2/2\mu_0$. Already in the 1940s it has been realized that a plasma can be pinched and thereby confined in a linear experiments (Sec. 2.1.4) with sufficient high currents and magnetic fields. These experiments exhibit a high plasma beta, but they have been found to be highly unstable. Two major concepts are currently intensively investigated, the tokamak (Sec. 2.1.1) and the stellarator (Sec. 2.1.3). These operate at low plasma beta.

2.1 Magnetic confinement devices

2.1.1 Tokamak

The basic setup of a tokamak is shown in Fig. 2.1. The generated plasma exhibits a toroidal shape with major radius R and minor radius a. By external coils a toroidal magnetic field $B_t = B_0 R_0/R$ is generated. Here B_0 is the magnetic field at the magnetic axis R_0. The magnetic field is superimposed by a poloidal magnetic field B_θ generated by an inductively driven plasma current I_p. The plasma current heats the plasma by resistive dissipation, this is called Ohmic heating. Additional vertical coils are needed to position the plasma within the vacuum vessel. The superposition of a toroidal and poloidal magnetic field results in a twisted total magnetic field. This twist is necessary because otherwise the entire plasma would be subject to the interchange instability (see Sec. 4.2). Due to the twist the bad curvature region is connected to the good curvature region and the unfavorable effects of the bad curvature region can be balanced. The twist is characterized by the *safety factor* $q_s = m/n$, which gives the ratio between n toroidal and m poloidal revolutions of a field line before it closes. In the case of a circular plasma cross-section the safety factor is given by $q_s = rB_0/R_0B_\theta$. A strong change of this twist with radius of the magnetic field lines is beneficial for confinement, it is given by the magnetic shear $\hat{s} = r/q_s(dq_s/dr)$ (effects of magnetic shear will be discussed in Sec. 10.3). The resulting parallel flow and current counterbalancing the charge separation by the interchange effect are called the Pfirsch-Schlüter flow or current (more details can be found in Sec. 5.2.3).

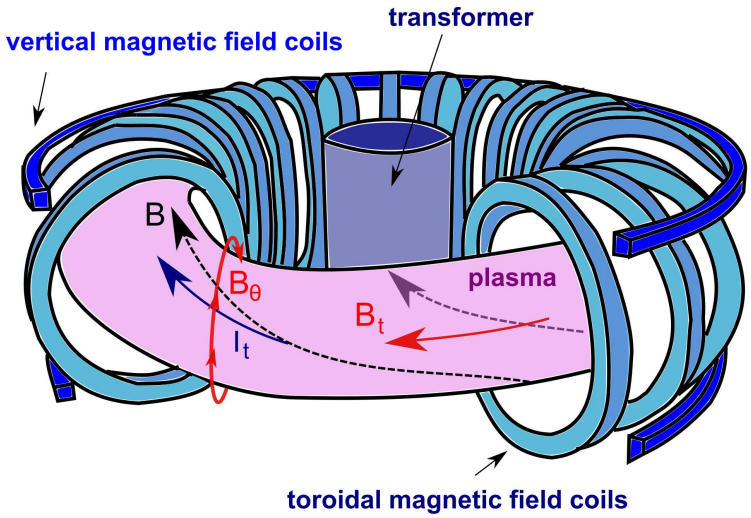

FIGURE 2.1: Schematic set up of a tokamak. The external toroidal field coils generate a toroidal magnetic field B_t. The transformer induces a toroidal plasma current I_p which generates a poloidal field B_θ. Both components lead to a twisted magnetic field necessary for magnetic confinement.

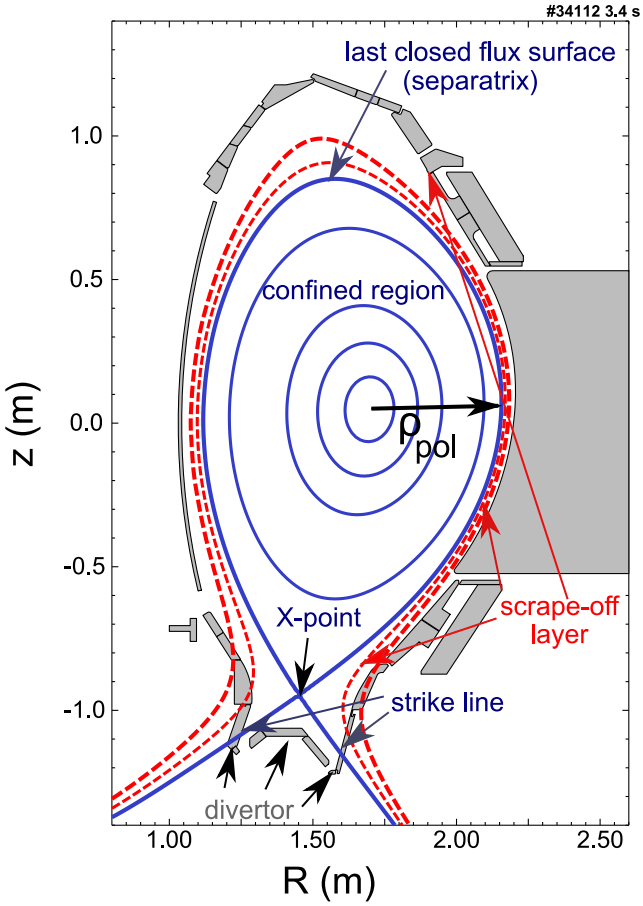

FIGURE 2.2: A poloidal cross-section of the tokamak ASDEX Upgrade. The confined region is indicated by the solid blue lines. The separatrix separates the region of closed field lines from the region of open field lines (scrape-off layer).

As the tokamak is toroidally symmetric it is for most applications sufficient to investigate the geometry in the cross-section perpendicular to the toroidal field. This is called the *poloidal cross-section*. The different regions of the tokamak are shown in the poloidal cross-section of a tokamak in Fig. 2.2. Nowadays tokamaks are rarely circular in the cross-section. For reference, different magnetic flux surfaces can be labeled with the normalized poloidal flux variable $\rho_{pol} = \sqrt{(\psi - \psi_a)/(\psi_s - \psi_a)}$ where ψ is the poloidal magnetic flux in a range between the plasma axis (label a), where $\rho_{pol} = 0$, and the last closed flux surface (LCFS) (label s) where $\rho_{pol} = 1$. In diverted configurations the last closed flux surface is called the *separatrix*. Normalized fluxes are used as radial coordinates in tokamaks. The confined region $\rho_{pol} < 1$ is shown by the closed blue lines of constant poloidal flux. The edge of the confined region is characterized by a strong radial electric field which can be approximately given by [21]

$$\frac{E_r}{B} = \frac{\nabla p_i}{enB_0} + q_s \frac{a}{R_0} u_{\parallel}. \tag{2.3}$$

Here E_r is the radial electric field, n is the plasma density, p_i is the ion plasma pressure, e the elementary charge and $u_\parallel$ is the flow parallel to the magnetic field. The typically strong ion pressure gradient gives a strong negative contribution at the plasma edge which is important for the confinement. Without heating by neutral beam injection (NBI) inducing external momentum into the system the parallel velocity is usually small and the plasma is usually not heated directly at the edge. A more advanced description of the tokamak equilibrium can be found in Sec. C.2.3.

The region of open field lines outside the separatrix ($\rho_{pol} > 1$), shown by the red dashed lines, is characterized by open field lines ending on material surfaces and called the *scrape-off layer*. Scrape-off layer transport will be studied in detail in Chap. 12.

The divertor is a setup associated with a particular magnetic configuration used in nowadays tokamaks generated by an additional magnetic field. The divertor field diverts the plasma outside the last closed flux surface to collector plates. In this way most of the heat exhausts is guided to these plates and the heat load on the vessel walls is reduced. A particular feature of diverted magnetic fields is the X-point, which is the point where the poloidal magnetic field vanishes and the field lines are nearly toroidal. Around the X-point the magnetic shear is very strong.

If the X-point is placed in the lower (upper) part of the tokamak the configuration is called *lower (upper) single null* configuration. If both regions exhibit an X-point the configuration is called double null configuration. The area where field lines connect the separatrix with the divertor is called the target area. The strike line is the toroidal circumferential line at the point where the separatrix intersects with the target. It is characterized by enhanced heat flux.

For details on tokamak physics, the interested reader is referred to the book by Wesson [22], which gives a very comprehensive overview. For scrape-off layer and divertor physics the book by Stangeby [23] is recommended.

2.1.2 Tokamak experiments

The currently largest tokamak experiment worldwide is **JET** (Joint European Torus, Oxfordshire, UK, $R_0 = 2.96$ m). JET is today the only experiment allowed to do experiments with tritium-deuterium fuel and has set the current world record for fusion output. A next generation tokamak is **ITER** (International Thermonuclear Experimental Reactor, $R_0 = 6.2$ m), currently built next to Cadarache (France). ITER shall demonstrate the principle of producing more thermal power from the fusion process than is used to heat the plasma. Furthermore, ITER will enable to develop and test technologies and processes needed for a fusion power plant as tritium breeding concepts, superconducting magnets, remote handling, suitable plasma facing components, neutron shielding and heat conversion technology.

In this work experiments performed on different tokamaks will be presented.

In the following, a short introduction to them will be given.

- **ASDEX** (AxialSymmetrisches Divertor-Experiment) **Upgrade** is a diverted tokamak experiment in Garching (Germany). The major radius is $R_0 = 1.65$ m, the minor radius $a = 0.5$ m. The magnetic field in ASDEX Upgrade (AUG) is generated by copper coils. The typical magnetic field strength is $B = 2.5$ T, discharges up to a magnetic field of $B = 3.9$ T can be conducted in principle. The duration of the discharges is in the range of several seconds. Special features of AUG are the complete first wall made of tungsten and an outstanding high heating power (in particular compared to the machine size). ASDEX Upgrade can be heated by 20 MW of neutral beam injection (NBI), 6 MW of ion-cyclotron-resonance heating (ICRH) and 4 MW of electron-cyclotron-resonance heating (ECRH). AUG is equipped with diagnostics presented in Chap. 6. It is the experiment most referred to within this work. Results presented in Secs. 9, 10.2.1 and 11 are based on measurements in ASDEX Upgrade, those presented in Secs. 9, 10.3 and 12 are based on simulations at AUG parameters.

- The **DIII-D tokamak** is operated in San Diego (USA) since the early 1980s. The name comes from the cross-sectional plasma shape, resembling the letter D. DIII-D has led to a new class of tokamaks known as advanced tokamaks. Through strong plasma shaping and active control of various plasma instabilities, advanced tokamaks operate at high plasma β (Eq. 2.2) and achieve high currents and strong pressure profiles accompanied by high performance. DIII-D is a diverted tokamak with a carbon wall. The major radius is $R_0 = 1.67$ m, the minor radius $a = 0.67$ m and the magnetic field strength is about $B = 2.2$ T. The plasma heating capabilities are strong (about 26 MW). As DIII-D is in operation since the eighties, it is very well diagnosed.

- The **Experimental Advanced Superconducting Tokamak (EAST)** is the first tokamak employing superconducting toroidal *and* poloidal magnets. It is operated in Hefei (China). It is of similar size as AUG or DIII-D with a major radius of $R_0 = 1.85$ m and a minor radius of $a = 0.45$ m. Magnetic fields of 3.5 T are achieved. One of the main objectives of EAST is long pulse operation. EAST continuously optimizes the integrated operation scenario and has been succeeded in producing steady-state H-mode discharges of over 100 s (status 2017). The results presented in Sec. 10.1 [13] have been obtained on EAST. Furthermore, the author has been regularly involved in the EAST projects [24, 25, 26, 27].

- **Alcator C-Mod** (at MIT, Cambridge, USA) was a rather small ($R_0 = 0.68$ m, $a = 0.22$ m) diverted tokamak operated at high magnetic fields up to $B = 8$ T. After more than 20 years of operation, Alcator C-Mod was

shut down in 2016. Due to its compactness the highest volume average plasma pressures could be obtained. Together with the high magnetic field, Alcator C-Mod had access to unique experimental regimes. Work on Alcator C-Mod provides a basis for the results on I-mode turbulence presented in Chap. 11.

- **Tore Supra** (in Cadarache, France) was for a long time the only tokamak of considerable size ($R_0 = 2.25$ m, $a = 0.7$ m) with superconducting toroidal magnets allowing magnetic fields up to 4.5 T. Tore supra was a limited tokamak with mainly circular plasma cross-sections, which have shown less good performance. However, as the simulation code GEMR, mostly used in this thesis, is restricted to limited plasmas with circular plasma cross-sections too, GEMR simulations offers a better comparability with Tore Supra measurements (Sec. 10.3). Beginning 2013 Tore Supra underwent an extensive refit including the installation of a tungsten divertor and was renamed to WEST. WEST is operating since 2016.

2.1.3 Stellarator experiments

In a stellarator the complete twisted magnetic field necessary for magnetic confinement is generated by the external coil system. In contrast to the tokamak no transformer is needed which allows continuous operation, one of the main advantages of the stellarator. Other advantages related to the absent current of the transformer are that several MHD instabilities are not present in a stellarator and the absence of disruptions. Also stellarators exhibit no density limit like the Greenwald limit. The twisted magnetic field is generated by twisted magnetic field coils which makes the magnetic field more complicated compared to that of a tokamak. As axisymmetry is lost, for stellarators a three-dimensional geometry has to be considered, where tokamaks exhibit a two-dimensional geometry. In general stellarators suffer from higher neoclassical transport compared to tokamaks, however, due to optimization it should be possible to reduce the neoclassical transport levels of so-called optimized stellarators to a tokamak-similar level. The stellarator Wendelstein 7-X [28] in Greifswald (Germany) is an example of such an optimized stellarator. In this thesis results based on measurements at the stellarator TJ-K are shown, which is operated with low temperatures plasmas.

- **TJ-K** [29] is a torsatron-type of stellarator which confines a low temperature plasma with dimensionless parameters similar to those in fusion edge plasmas [30]. Fundamental studies of drift waves [31, 32, 33], drift-wave turbulence [34, 35], zonal flows [36, 35, 37, 38, 39, 40] with particular attention to geometric effects [41, 38, 40] have been done. Sections 8.1, 5.1.4 and 5.1.3 are based on measurements at TJ-K.

2.1.4 Linear devices

Due to the end losses linear devices are not appropriate for magnetic confined fusion plasmas. Confinement can be improved by increasing the magnetic field strength towards the ends of the device, though. There, the magnetic mirror effect hampers particles from leaving the plasma. These are called mirror devices. In this configuration, however, in particular fast particles will still leak and the fast particles are those which matter for fusion. Nowadays mirror machines are rarely considered as design for a fusion reactor. One exceptional example is the Lockheed Martin Compact Fusion Reactor. However, due to their simple configuration linear devices are often used at universities to study basic plasma physics including plasma instabilities and turbulence. Even if the experiments would not directly be fusion relevant, general ideas can be tested and developed which can be transferred to larger devices after an appropriate revision. Linear devices are also used to study space plasma related topics as Alfvén dynamics [42, 43], magnetic field line expansion effects (i.e. double layers [44, 45, 46]), plasma thrusters for spacecraft propulsion [47]) or magnetic reconnection [48]. As fusion relevant applications plasma wall interaction [49, 50] and plasma detachment [51] are studied in linear devices.

- The Controlled Shear Decorrelation Experiment (**CSDX**) is a linear plasma device at UCSD in San Diego (USA). CSDX is 2.8 m long and a helicon antenna produces a plasma column of 4.5 cm radius. In helicon plasmas the density is proportional to the magnetic field. At a magnetic field of $B = 0.1$ T, CSDX argon plasmas exhibit usually central densities of 10^{19} m^{-3} and electron temperatures of 3 eV. The ion and neutral temperatures are small ($T_i = 0.7$ eV, $T_n = 0.5$ eV) and can be neglected. CSDX is usually operated with isolating end plates, where most other linear devices are operating with conducting end plates. As result the radial current in CSDX is stronger. The radial current is carried by the polarization current, which is responsible for structure formation (inverse energy cascade, zonal flows) enabling the study of structure formation in drift-wave turbulence [52]. Main focus for research has been the interaction between shear flows and turbulence [53, 54, 55].

2.2 Magnetic confinement regimes

2.2.1 Low confinement regime (L-mode)

A very high temperature in the confined region is required with respect to the fusion process. On the other hand a very low temperature at the plasma wall is needed to not overburden the materials. Directly at the edge of the plasma strong gradients in thermodynamic quantities such as density and temperature are inevitable. These gradients lead to plasma instabilities (Chap. 4) and turbulence (Chap. 5). Turbulence is most effective in mixing and the strong

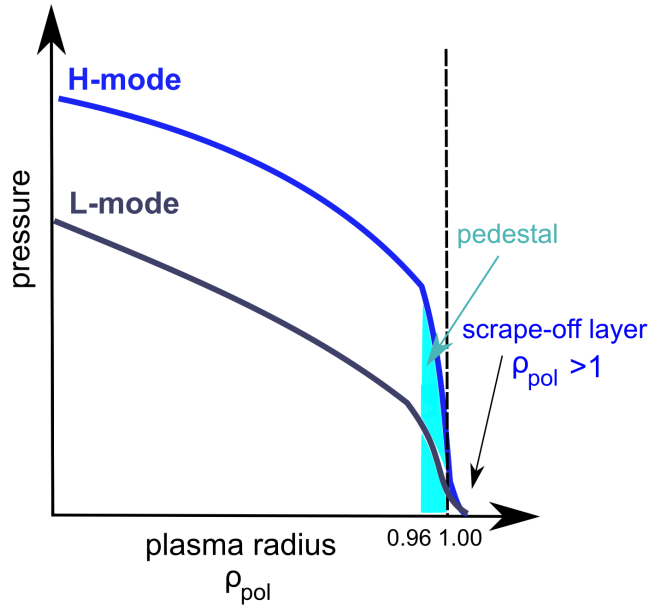

FIGURE 2.3: Schematic plasma pressure profiles in low and high confinement regimes.

associated turbulent transport prevents gradients to steepen up with increasing heating power. The operational regime dominated by turbulence is called the *low-confinement regime (L-mode)*. Fortunately, with sufficiently increased heating power the plasma transitions into a regime of higher confinement (described in the following Sec. 2.2.2). Although not interesting as a possible confinement regime for a future fusion reactor, the L-mode is the ideal regime to study plasma turbulence and most investigations of plasma turbulence are done in this regime. Chap. 9 pays particular attention to plasma turbulence in L-mode. Chap. 10 investigates the transition from L- to H-mode.

2.2.2 High confinement regime (H-mode)

The high confinement regime occurs at higher heating powers than the L-mode. It has been discovered by Wagner in ASDEX [56]. During the transition from L- to H-mode the turbulence is suppressed and the gradients steepen. The region characterized by these steep gradients just inside the separatrix is called the *pedestal* (see Fig. 2.3). Due to the stiff transport (Sec. 4.4) in the plasma core the pedestal highly influences the overall core performance and is directly related to the fusion gain. The steepening of the gradients is accompanied by a strengthening of the radial electric field and the corresponding flow shear. Flow shear has the capability to suppress plasma turbulence [57], and is therefore thought to be of central importance for the L-H transition. The physical mechanism behind this transition is not understood so far. A review on theories of the L-H transition can be found in Ref. [58].

In early studies of the radial electric field in the plasma edge of low collisionality plasmas in DIII-D a disagreement between experimental and neoclassical poloidal rotation has been found [59]. It has been widely accepted that neoclassical theory does not apply in the plasma edge. In the following years an explanation has been sought for non-neoclassical generated poloidal flows. A reasonable candidate is the turbulence generated so-called zonal flow (Sec. 3.6), which is also a strong candidate to explain the turbulence suppression from L-mode to H-mode. It should be noted, however, that state of the art simulations codes including all of the relevant zonal flow physics could not yet reproduce the L-H transition.

In the pedestal ($0.97 < \rho_{pol} < 1.00$) of ASDEX Upgrade the radial electric field in H-mode is approximately $E_r \approx (\nabla p_i)/(en)$ [60]. It should be noted that the plasma edge of ASDEX Upgrade is rather collisional. Further inwards ($0.90 < \rho_{pol} < 0.97$) both radial electric field and its ion pressure contribution differ, but the difference can be understood by the expected neoclassical poloidal rotation [61]. Therefore, in H-mode the radial electric field in the plasma edge of ASDEX Upgrade is neoclassical [60]. This has been shown to be even the case around the L-H transition [62], which rules out significant contributions from zonal flows. Collisionality hampers zonal flow self-amplification (see section 5.1.3).

The high pedestal gradients in H-mode lead to bursty quasiperiodic expulsions of energy and particles called edge localized modes (ELMs) [63]. Due to the strong particles and heat fluxes, ELMs are a serious concern for future fusion experiments like ITER and DEMO [64, 65]. ELMs are classified into three main types [66]:

- **type-I ELMs**, also defined as large ELMs, are a serious concern for large-scale fusion experiments or future reactors. The frequency of type-I ELMs increases with heating power. In nowadays' experiments their frequency is about ten to some hundred Hz. Type-I ELMs are believed to be triggered by MHD instabilities, either the ideal peeling mode (IPM) or the ideal ballooning mode (IBM), depending on which stability boundary (the current or the pressure, respectively) is reached [67, 68, 69]. The ELM is initialized by a coupled peeling-ballooning mode [70]. The ELM crash itself is a nonlinear phenomenon [71].

- **type-II ELMs**, also called grassy ELMs, show good performance for a fusion plasma. They provide helium exhaust and are accompanied by tolerable divertor heat loads at still elevated confinement. They appear at high densities (which is anyhow desirable) and strong plasma elongation. It has been suggested that type-II ELMs are pure ballooning modes [70].

- **type-III ELMs** are also much smaller in amplitude than type-I ELMs. Their frequency is higher (at several hundred Hz to kHz) and decreases with increasing heating power. Their main characteristic is the appear-

ance of a magnetic precursor mode at several tens of kHz. They appear well below the ideal ballooning limit. It is suggested that type-III ELMs are pure peeling modes [70]. Type-III ELMs are stabilized by high pedestal temperatures suggesting a resistive nature of these kind of ELMs.

Intrinsically ELM-free regimes with good confinement or small-ELM regimes would be an attractive operation regime for a fusion reactor. Such an ELM-free operation regime is the I-mode, described in the next section. Reviews on small-ELM regimes can be found in Refs. [72, 73]. A review on naturally ELM-free regimes can be found in Ref. [74].

2.2.3 Improved L-mode regime (I-mode)

The I-mode typically appears in the unfavorable configuration where the ion ∇B drift is directed away from the X-point. This configuration is called unfavorable, because the power necessary to reach H-mode conditions is higher than in a configuration, where the ion ∇B drift is directed towards the X-point (favorable configuration). The I-mode has been discovered in AUG [75], but the recent extensive studies in Alcator C-Mod [76, 77, 78, 79, 80, 81] have attracted attention on the I-mode regime as a possible operation scenario for ITER. In the unfavorable configuration the H-mode power threshold is about 2 times higher compared to the favorable configuration. The I-mode is an improved energy confinement regime exhibiting an edge energy transport barrier but without an accompanying particle transport barrier (see Fig. 2.4). This has several benefits [76]:

i) H-mode like energy confinement

ii) weak degradation of energy confinement with increasing heating power

iii) less accumulation of helium ash due to the lack of the particle transport barrier

iv) absence of ELMs due to the smaller edge pressure gradient compared to H-mode.

An harmless disadvantage is the high L-I power threshold compared to the L-H threshold in favorable ion ∇B-drift direction [82]. Furthermore, the I-mode often evolves slowly in an uncontrolled manner, until a transition to H-mode with large ELMs occurs [82]. This would negate all advantages of the I-mode. It has been observed in both AUG and Alcator C-Mod that the power threshold from L- to I-mode scales at most weakly with the magnetic field ($P_{\text{L-I}} \sim B^{0.39}$ in AUG [83] and $P_{\text{L-I}} \sim B^{0.25}$ in C-Mod [81]) whereas the L- to H-mode power threshold scales nearly linear with B ($P_{\text{L-H}} \sim B^{0.8}$ [84]). This would enhance the operation window of the I-mode at higher magnetic fields compared to the small operation window faced in the majority of present

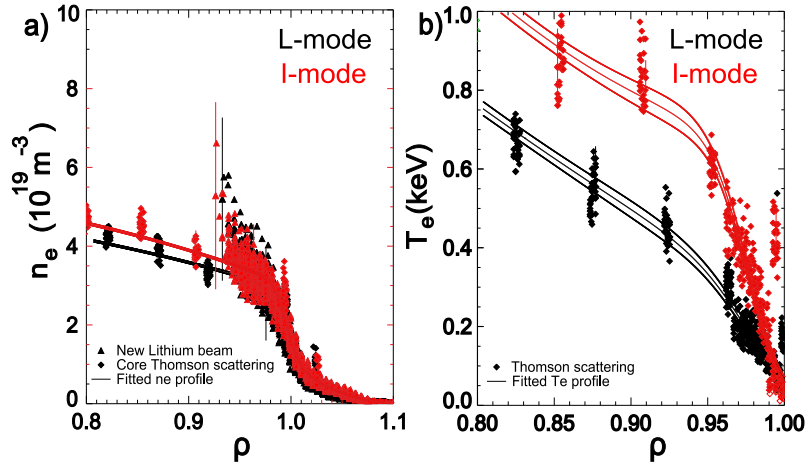

FIGURE 2.4: a) Electron density and b) electron temperature profiles at the plasma edge for the L-mode (black at 2.5 s) and I-mode (red at 4.0 s) case. The development of a temperature pedestal is clearly observable, whereas the density is only subject to marginal changes. Figure taken from [16].

day tokamak experiments. At a magnetic field of 8 T no transitions to H-mode have been observed in Alcator C-Mod [81]. This indicates that at high magnetic fields the I-mode may be a promising operation regime for a fusion reactor. To qualify the I-mode as an operating scenario for ITER, threshold and accessibility studies [82] also on a multi-machine basis [80] are needed.

Furthermore, studies of turbulence in I-mode may offer a better understanding of the physics of the interaction of energy and particle transport barriers in general. The mechanism which selectively reduces only one of the transport channels is not understood. Turbulence in the I-mode regime will studied in detail in Chap. 11.

Chapter 3

Two-dimensional turbulence

In this chapter the phenomenology of turbulence is shortly introduced with special focus on two-dimensional turbulence which is most relevant to magnetically confined plasmas. Particular attention is paid to subjects not covered in the common introductory literature, but important for this work such as vortex physics (Sec. 3.3), three-wave interactions (Sec. 3.4), zonal flows (Sec. 3.6) and turbulence spreading (Sec. 3.8).

3.1 Fluid equations and Reynolds number

The conservation of mass yields the *continuity equation*

$$\frac{\partial}{\partial t}\rho_m + \nabla \cdot (\rho_m \mathbf{u}) = \left(\frac{\partial}{\partial t} + \mathbf{u} \cdot \nabla\right) \rho_m + \rho_m \nabla \cdot \mathbf{u} = 0. \tag{3.1}$$

Note that the first term on the left-hand side gives the fixed frame and the bracket in the second equation indicates the co-moving frame. The equation is valid independent of the viscosity. The right-hand side of the equation is zero, because the mass is expected to be source free. The density can only change if a net flow into or out of the fluid element exists. Often we will consider an *incompressible* fluid

$$\nabla \cdot \mathbf{u} = 0 \tag{3.2}$$

and the *incompressible continuity equation* reads

$$\left(\frac{\partial}{\partial t} + \mathbf{u} \cdot \nabla\right) \rho_m = 0. \tag{3.3}$$

Momentum conservation implies the equation of motion. In a neutral fluid this is the *Navier-Stokes-equation*

$$\rho_m \left(\frac{\partial}{\partial t} + \mathbf{u} \cdot \nabla\right) \mathbf{u} = -\nabla p + \eta \Delta \mathbf{u}. \tag{3.4}$$

The bracket on the left hand side gives the inertia. It can be written as a total derivative $\frac{\mathrm{d}}{\mathrm{d}t} = \left(\frac{\partial}{\partial t} + \mathbf{u} \cdot \nabla\right)$. The first term on the right-hand side of (3.4) is

the pressure force. This can be seen to be representative of all other possible external forces. For example if gravitational forces have to be considered, the gravitational force density $\rho_m \mathbf{g}$ (with $g = 9.81$ m/s^2 on earth for example) adds to the right-hand side of Eq.(3.4). The last term is the viscous force $\eta \Delta \mathbf{u}$ with viscosity η. Most important for the turbulence will be the nonlinearity $(\mathbf{u} \cdot \nabla)\mathbf{u}$ and the viscosity.

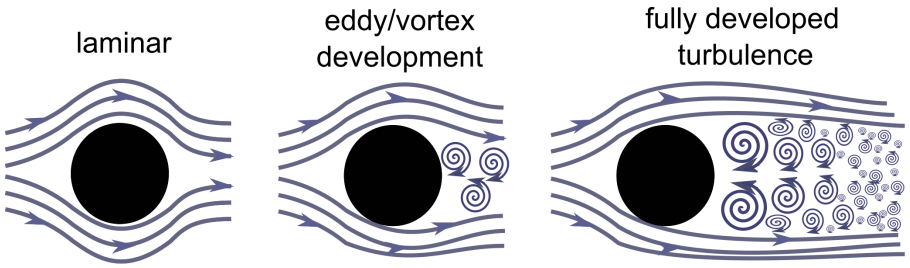

FIGURE 3.1: A neutral fluid flows at the velocity U_0 across an obstacle of size L. Shown is the qualitative streaming pattern as a function of the Reynolds number. At first, the pattern is laminar, then shows vortex streets and ends in a turbulent state.

To estimate the impact of these two terms characteristic quantities are considered: the characteristic size of the system is L and the characteristic velocity is U_0. Both provide a characteristic time $T = L/U_0$. By normalization

$$t' = t/T, \tag{3.5}$$

$$\mathbf{u}' = \mathbf{u}T/L, \tag{3.6}$$

$$p' = p(T/L)^2/\rho_m \tag{3.7}$$

the Navier-Stokes equation can be recast into

$$\frac{d}{dt'}\mathbf{u}' = -\nabla' p' + \frac{1}{\mathrm{Re}}\Delta' \mathbf{u}'. \tag{3.8}$$

For simplicity, the prime is omitted in the following representations. The only (dimensionless) control parameter is the *Reynolds number*

$$\mathrm{Re} = \frac{\rho_m L^2}{\eta T} = \frac{\rho_m}{\eta} U_0 L = \frac{U_0 L}{\mu} \tag{3.9}$$

with the *kinematic viscosity* $\mu = \eta/\rho_m$ (η is called the *dynamic viscosity*).

Figure 3.1 shows how the flow changes with the Reynolds number. At low Reynolds numbers the flow is called laminar. With increasing Reynolds number eddies (or vortices) develop. The vortices are advected by the flow, the so-called *Kármán vortex street* can be observed. The vortex street consists of pairs of vortices with different sense of rotation direction. At higher Reynolds

numbers these eddies interact with each other and turbulence occurs. The Reynolds number can be seen as the ratio between non-linearity and viscosity

$$\mathrm{Re} = \frac{u\nabla u}{\mu\Delta u} = \frac{U_0^2/L}{\mu U_0/L^2} = \frac{U_0 L}{\mu}. \tag{3.10}$$

Therefore, turbulence occurs at relatively high velocities or low viscosity.

3.2 Energy transfer and cascades

By just observing turbulent motion, the most striking feature is its chaotic behavior involving a large spectrum of different scales. Turbulence is composed of eddies of different sizes. In the following a closer look at the interaction between different scales of motion is given.

Figure 3.2 shows the kinetic energy as a function of the wavenumber k, which is inverse proportional to the scales of motion. The scales of motions can be separated in three regimes. The energy is inserted by whatever mechanism (externally or by linear instabilities), in the large-scale so-called injection range. At the small (thermal) scales the energy is dissipated. In between the energy has to be nonlinearly transferred. In this *inertial range* the energy is neither injected nor dissipated. By considering the balance between the nonlinear term $\sim U^2/L$ and the dissipation $\sim \mu U/L^2$, the dissipation $\sim \mu U/L^2 = (1/\mathrm{Re}) \cdot (U^2)/L$ is proportional to the nonlinear term, but inversely proportional to the Reynolds number. It follows that at the typical scale L, where the energy is injected, only a small fraction $(1/\mathrm{Re})$ of the energy injected into the system can be dissipated. In order to balance the injected energy smaller scales have to be generated. The energy transfer is illustrated by a cascading process which goes back to Richardson [85]: The larger eddies are unstable and break up into smaller ones, thereby pass their energy from large scales of motion to smaller scales until the length scale is small enough that the viscosity can dissipate the kinetic energy.

The energy spectrum in wavenumber space (Fig. 3.2) can be estimated by simple dimensional arguments. A typical scale L with a typical velocity U corresponds to a time scale $T \sim L/U$. Energy transfer is given by energy per time $\epsilon \sim U^2/T \sim U^3/L$, which means the energy itself scales with

$$E \sim U^2 \sim \epsilon^{2/3} L^{2/3}. \tag{3.11}$$

This is known as *Kolmogorov's two-third law*. In wavenumber space $L \sim 1/k$ and $E = \int \mathrm{d}k E(k) \sim \beta\epsilon^{2/3}k^{-2/3}$ and the energy spectrum must scale with

$$E(k) \sim \epsilon^{2/3} k^{-5/3}, \tag{3.12}$$

which has been predicted by Kolmogorov in 1941 [86] and shown in Fig. 3.2a. This is called the turbulent cascade.

Naively one could think it is possible to control dissipation by viscosity as it should be responsible for dissipation. In a turbulent system this is not possible

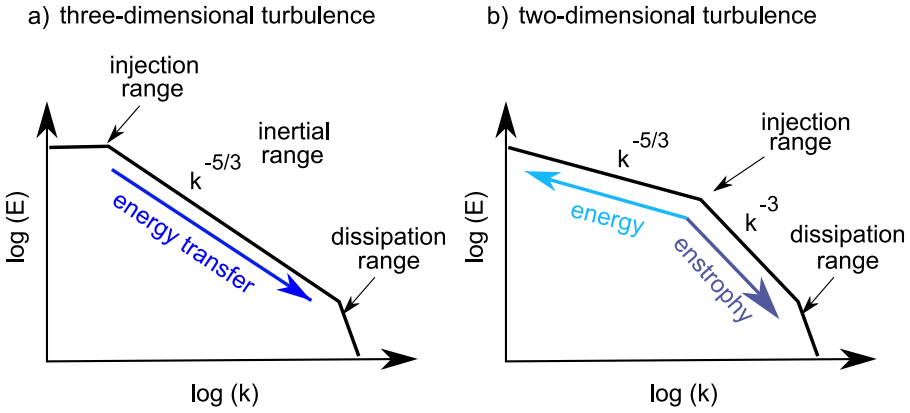

FIGURE 3.2: Kinetic energy spectrum of three- (a) and two-dimensional (b) fluid turbulence as proposed by Kolmogorov and Kraichnan, respectively.

as we will see in the following. The length scale at the dissipative range L_μ can be estimated from a balance of the nonlinear transfer of energy $\epsilon \sim U_\mu^3/L_\mu$ and the energy dissipation rate $\epsilon_\mu \sim \mu U_\mu^2/L_\mu^2$ (with the energy leaving the system at the dissipative scale is given by U_μ^2). Setting both equal gives $L_\mu \sim \mu/U_\mu$. From the transfer of energy $\epsilon \sim U_\mu^3/L_\mu$ follows $U_\mu = (\epsilon L_\mu)^{1/3}$. This expression is now inserted into $L_\mu \sim \mu/U_\mu$, which yields

$$L_\mu = \left(\frac{\mu^3}{\epsilon}\right)^{1/4}, \tag{3.13}$$

which gives the so-called Kolmogorov scale. This length is typically quite small. For example in atmospheric motions where the typical measured length scales are in kilometers, the Kolmogorov scale is in the order of millimeters. This illustrates one of the major challenges in turbulence research: to capture all relevant scales of motion in atmospheric turbulence, it has to be resolved with millimeter accuracy. Another important feature of the turbulence is that the energy transfer to the dissipative scales is equal to the energy transfer out of the injection scales $\epsilon \sim U_0^3/L_0$ and, therefore, the energy dissipation rate is set by the large scales and not by the small scales or by the viscosity. The energy enters the injection range, flows through the inertial range to the dissipation range, where it left the systems (Fig. 3.2a). By increasing (decreasing) the viscosity the inertial range is reduced (enlarged) by increasing (decreasing) the Kolomogrov scale. The dissipation rate does not change significantly. Therefore, it is not possible to increase the dissipation rate by increasing the viscosity. Even if the viscosity goes to zero ($\mu \to 0$) the turbulence itself generates more vorticity ($L_\mu \to 0$) to balance the energy. In this way the turbulence ensures finite dissipation in the limit of vanishing viscosity! This is called the *dissipation anomaly*.

Due to the strong background magnetic field, the dynamics of turbulence in fusion experiments is nearly bound to the plane perpendicular to the mag-

netic field and therefore is approximately two-dimensional. Therefore, the two-dimensional case deserves special attention. Two dimensional turbulence is not just a dimensionally reduced version of three-dimensional turbulence, because new conservation laws arise, giving two-dimensional turbulence its own phenomenology. A review of recent developments in two-dimensional turbulence can be found in Ref. [87]. In two-dimensional turbulence the energy transfer is reversed. This is called the *inverse energy cascade*. Due to this inverse energy transfer large-scale structures are generated. One example is the hurricane, a large-scale vortex in the atmosphere. Another kind of large-scale structures generated by turbulence are zonal flows or jet streams. Jet streams lead to varying times for transatlantic flights. Zonal flows are responsible for the stripes of Jupiter. The reason for this inverse energy transfer is the conservation of vorticity $\Omega = \nabla \times \mathbf{u}$ in two-dimensional flows. Similar to the three-dimensional case described above, a dimensional scaling can be carried out. The enstrophy is given by $W \sim \Omega^2 \sim U^2/L^2$. For 2D turbulence the enstrophy flux is constant. It is given by $\epsilon_\Omega \sim W/T$. As $T \sim L/U$ it follows that $\epsilon_\Omega \sim (U^2/L^2)(U/L) \sim U^3/L^3$ which can be also written as $U \sim \epsilon_\Omega^{1/3} L$. As in the three-dimensional case, the energy is given by $E \sim U^2$, therefore $\int \mathrm{d}k E(k) = E \sim U^2 \sim \epsilon_\Omega^{2/3} L^2$, thus $E(k) = (\mathrm{d}/\mathrm{d}k)\epsilon_\Omega^{2/3} k^{-2} = \epsilon_\Omega^{2/3} k^{-3}$. This is the famous scaling law for two-dimensional turbulence. Both together, the inverse energy cascade and the direct enstrophy cascade, are called the *dual cascade* [88, 89, 90, 91, 92] . It is shown in Fig. 3.2b.

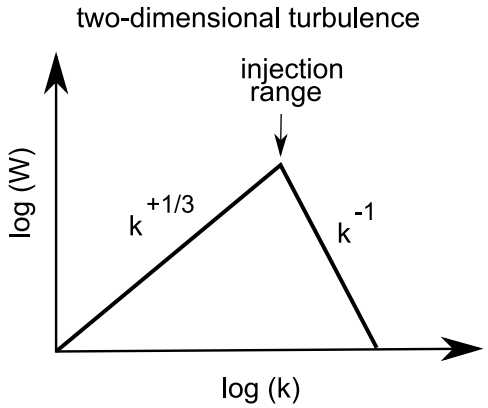

FIGURE 3.3: Enstrophy spectrum of two-dimensional turbulence.

The enstrophy spectrum $W(k) = k^2 E(k)$ scales with $k^{1/3}$ in the inverse energy cascade region and with k^{-1} in the direct cascade region, therefore most of the vorticity can be found around the injection scale. In three-dimensional turbulence the enstrophy spectrum also scales with $k^{1/3}$. Therefore, in three-dimensional turbulence most of the vorticity can be found around the dissipation scale as seen in Fig. 3.3.

Kinetic energy cannot be dissipated by viscosity in two dimensions; it is rather transferred to larger scales in motion by the inverse energy cascade.

Commonly the physical mechanism behind the inverse energy cascade is understood as a sequence of merging eddies of similar size producing larger and larger vortices (Sec. 3.3.1). It constitutes a local inverse transfer for kinetic energy in wavenumber k-space. Experimentally it has been found that the cascade could rather be driven by a clustering mechanism involving same sign vortices [93]. Another mechanism called vortex thinning (Sec. 3.3.2) has been suggested by Chen et al. [94]. Here the interaction of structures of different scales is responsible for the inverse energy transfer and the energy is transferred between non-continuous spectral ranges (which means also nonlocal in k-space) [94]. How to estimate the energy transfer in wavenumber space and determine the amount of locality is shown in Sec. 3.4.

The direction of the energy transfer towards lower wavenumbers can be understood as follows [95, 3]: Let us assume the turbulence is initially located around the injection scale. The averaged wavenumber

$$\langle k \rangle = \frac{1}{E} \int \mathrm{d}k k E(k) \tag{3.14}$$

will be close to the injection scale, too. Here, $E = \int \mathrm{d}k E(k)$. The nonlinearity leads to a broadening in wavenumber space

$$\Delta k^2 = \frac{1}{E} \int \mathrm{d}k (k - \langle k \rangle)^2 E(k), \tag{3.15}$$

as a variance this can be written as

$$\Delta k^2 = \frac{1}{E} (W - \langle k \rangle^2 E) \tag{3.16}$$

or

$$\Delta k^2 = \frac{W}{E} - \langle k \rangle^2. \tag{3.17}$$

Due to nonlinear interactions between the different scales of motion the turbulence will broaden ($\partial_t \Delta k^2 > 0$) as the turbulence evolves in time. As energy E and enstrophy W are conserved, also W/E is constant. This directly means that the mean wavenumber has to decrease in time $\partial_t \langle k \rangle < 0$. Hence, the spectrum shifts to lower wavenumbers which reflects the inverse energy cascade. A direct cascade ($\partial_t \langle k \rangle > 0$) is only possible if the enstrophy is not conserved and in fact increasing. This is possible in three dimensions due to the vortex stretching effect generating enough enstrophy W to allow also for an increase of $\langle k \rangle^2$.

3.3 Vortex interaction

3.3.1 Vortex merger

Figure 3.4 illustrates the merging process of two vortices. The vortex merging process consists of three phases [96, 97]. In the first phase the vortex cores grow

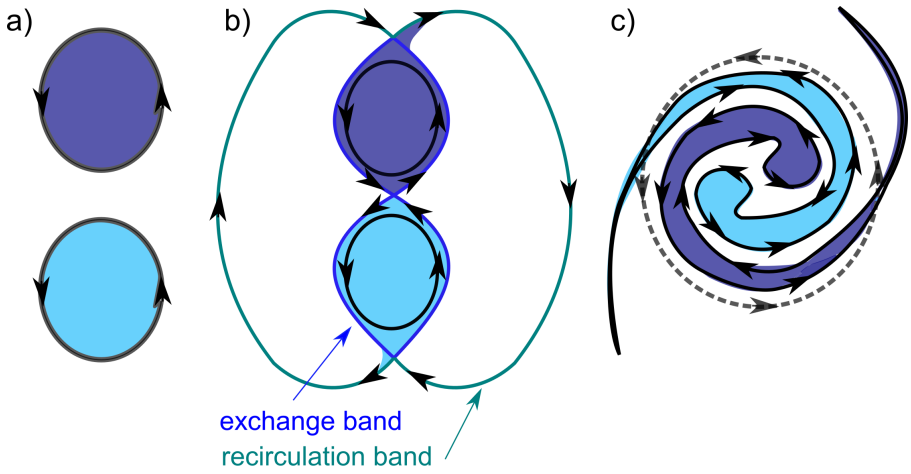

FIGURE 3.4: Schematic view of the vortex merger process of two co-rotating vortices of equal size (a). As the vortices approach each other, both vortices are connected by an exchange band and a recirculation band by which vorticity is transferred between the two vortices. In the final stage both vortices appear as one vortex of nearly twice the size of the original vortices. Figure adapted from [9].

by viscous diffusion where the distance between the vortices stays constant. If the vortex cores reach a critical size the distance decreases by convection and vortex filaments (very thin stripes of vorticity) are formed. This is the heart of the vortex merging process. The streamline configuration [96, 97] is shown in Fig. 3.4b. The vortex filaments are responsible for particle and momentum exchange between both vortices. The flow consists of two inner core regions (these are the two eddies), the exchange band and two outer recirculation regions. Vorticity which enters the recirculation bands leads to the formation of vorticity filaments. Vorticity from one eddy can enter the exchange band. The exchange band constitutes a filamentary structure as well. The vorticity within the exchange-band can then be absorbed by the other eddy. In such a way vorticity can be transferred from one vortex to the other. In the last phase the vorticity maxima are reduced by diffusion (Fig. 3.4c). Both vortices are deformed in such a way, that they appear similar to the Tai Chi symbol for yin and yang. Viewed from the outside the configuration of the two vortices appear as one larger vortex (as indicated by the dashed line). Within this virtual larger vortex, both vortices can theoretically be separated. At the boundary between both vortices the flow direction is in opposite direction, which lets the virtual vortex appear to be more smooth.

3.3.2 Vortex thinning

The vortex merger process is restricted to an interaction of vortices of similar size. In general, however, also vortices of different sizes will interact with each other. This case is addressed in this section.

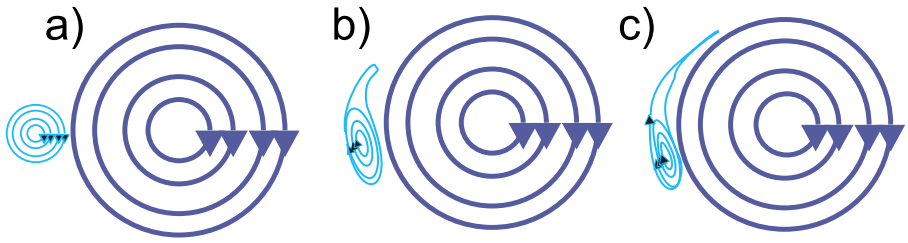

FIGURE 3.5: Schematics of the vortex thinning process. A smaller eddy in the shear of a larger one (a) is elongated and tilted (b). Finally, the smaller eddy is subject to a straining-out process. [9]

Figure 3.5 shows a schematic view of the vortex thinning process. Real measurements of the interaction of vortices with different scales in a rotating tank experiment can be found in Ref. [98]. Due to the shear induced by the larger eddy, the smaller one will be tilted and elongated [99] (3.5b). Since the circulation of an eddy is conserved, the velocity around the eddy is lowered and its energy is reduced [100, 94]. At the same time, the velocity of the eddy is mainly directed such, that it reinforces the large-scale strain [100, 94]. Thus, energy is transferred from the smaller structure into the larger one by an elongation and tilting (and thinning) of the smaller structure. This process is effective, if the scales of the interacting structures are clearly different resulting in the pronounced nonlocality of this process in wavenumber space. This behavior is reminiscent of the Howard-Krishnamurti mechanism [101] by which series of two-dimensional convective rolls tilt, stretch, and then merge to form a larger scale eddy.

3.3.3 Straining out

After elongation and thinning by the vortex thinning effect described above, the smaller vortex can be seen as a vortex filament. This vortex filament can be threaded and finally incorporated by the larger vortex [98, 102]. The tilting of the smaller vortex by the larger vortex already leads to a conservative energy transfer between both of them. This leads to a reduction of amplitude of the smaller vortex and an increase of energy of the larger one. However, this effect has additional consequences for the vortex at smaller scale. As this vortex gets very thin in the perpendicular direction, the second derivative of the velocity is increased. This leads to much higher viscous dissipation of the structures. Therefore, the small-scale vortex will be dissipated much faster. As the strain field is responsible for the elongation this effect is called *straining out*.

3.3.4 Vortex stripping

The vortex thinning and straining out mechanism describes the interaction of likewise rotating vortices, or a vortex subject to a shear whose corresponding

vorticity exhibits the same sign. In this case the vortices or the vortex and the shear are called prograde. In the opposite case the vortices or the vortex and the shear are called adverse. In Ref. [103] illustrative simulations can be found, which show, that the sign of vorticity matters for their interaction. A vortex subject to external adverse shear can survive if its vorticity exceeds the external shearing rate. However, the outer parts of the vortex may not have a strong vorticity and the external shear field is capable of penetrating the outer parts of the vortex. Subsequently, vorticity filaments are expelled from the vortex. The shear removes the outer part of the vortex (it is stripped) and leaves the inner part intact [104]. The inner core is not interacting with the background shear. This leads to higher vorticity gradients on the edge of the vortex [104]. This is an important process for the formation of strong, localized vortices as for example the red spot on Jupiter [105] and the polar vortex on earth [106]. The generation of strong vorticity gradients leads to deviations to the scaling of the enstrophy cascade described above. Due to vortex stripping, infrequent, giant events can be generated. Therefore, vortex stripping is a possible mechanism for the generation of intermittency in two-dimensional turbulence (see Sec. 3.5.3).

3.3.5 Elliptical instability

Since in two-dimensional turbulence vorticity is conserved, structures can be generated as pairs of counter rotating vortices. The flow configuration of two parallel counter rotating vortices is subject to instability. As an example, such a flow configuration is generated by an aircraft and is particularly dangerous during take-off and landing, imposing limits on the time between aircraft departures and, therefore, airport capabilities [107]. Two kinds of instabilities are excited in such a flow configuration, the Crow and the cooperative elliptical instability. The *Crow instability* exhibits a long wave-length (of about eight vortex spacings) and the deformation is symmetric with respect to the center plane of the pair. The vortices are periodically moving away and closer to each other. If the vortices touch each other, the vortices may reconnect and build a vortex ring.

Once the vortices are close to each other, the vortex cores can be elliptically deformed by each other. This leads to the so-called *cooperative elliptical instability* [107, 108]. Elliptic flows can be decomposed into a solid body rotation and strain. Plane wave disturbances, which are advected by the rotating flow, can be resonantly amplified if the wave and the straining frequencies match [107]. This is a secondary nonlinear instability driven by three-wave interaction (see appendix D). The matching condition is only fulfilled for one phase difference, which results in the cooperative motion of the vortex cores [107]. The cooperative elliptical instability is a three-dimensional instability of a two-dimensional flow, which means it generates finite parallel wavenumbers [107, 108]. The relevance of the cooperative elliptical instability for linear plasma devices will be discussed in Sec. 12.2.

3.4 Energy transfer between different scales in 2D turbulence

We have seen before that the turbulence cascade is a result of an energy redistribution between the different scales of motion, which can be assigned to different wavenumbers. The result of the spectral index (-5/3 for the inverse cascade and -3 for the direct cascade) are results of energy and enstrophy conservation. However, this does not tell us if structures really break up in structures of similar sizes as proposed in the Richardson cascade, neither if merging of vortices of similar size resulting in vortices of twice the size, is the main mechanism to generate the inverse cascade. In the following it is described how the energy transfer between the different scales can be calculated. The idea of describing the nonlinear interaction by an energy transfer in wavenumber space goes back to Kraichnan [109]. The formalism is based on the work by Domaradzki [110]; for drift-wave turbulence it has been introduced by Camargo [111]. The derivation can also be found in Ref. [112].

In three dimensions, the vorticity $\mathbf{\Omega} = \nabla \times \mathbf{u}$ equation is given by

$$\left(\frac{\partial}{\partial t} + \mathbf{u} \cdot \nabla\right) \mathbf{\Omega} = (\mathbf{\Omega} \cdot \nabla)\mathbf{u} + \mu \Delta \mathbf{\Omega}. \tag{3.18}$$

The first term on the right-hand side is the *vorticity stretching*. Vorticity stretching is important for three-dimensional turbulence as it can generate vorticity and enstrophy. This is relevant for the direct energy cascade (Sec. 3.2) and intermittency (Sec. 3.5). In two-dimensional turbulence, where fluctuations are restricted to a plane, which we can choose to be the x-y plane. Therefore, the velocity fluctuations are $u_x(x, y)$ and $u_y(x, y)$, but $u_z(x, y) = 0$ and the vorticity is given by

$$\mathbf{\Omega} = \nabla \times \mathbf{u} = (\partial_x u_y - \partial_y u_x)\hat{\mathbf{z}} = \Omega \hat{\mathbf{z}}. \tag{3.19}$$

The vorticity has only non-zero contributions perpendicular to the turbulent flow field. It can be described by a scalar. The vorticity stretching vanishes because the velocity cannot change in direction of the vorticity. In two dimensions the vorticity evolution is given by

$$\left(\frac{\partial}{\partial t} + \mathbf{u} \cdot \nabla\right) \mathbf{\Omega} = +\mu \Delta \mathbf{\Omega} \tag{3.20}$$

and conserved in the co-moving frame of reference. In the inviscid case this is called the *two-dimensional Euler equation*

$$\frac{\partial \Omega}{\partial t} + \mathbf{u} \cdot \nabla \Omega = 0. \tag{3.21}$$

To account for the reduced dimensionality it is possible to describe the flow by a *stream function* ψ. The flow is always tangential to a curve of constant ψ

$$\mathbf{u} = \nabla \times (\psi \hat{\mathbf{z}}) = \frac{\partial \psi}{\partial y}\hat{\mathbf{x}} - \frac{\partial \psi}{\partial x}\hat{\mathbf{y}} \tag{3.22}$$

therefore

$$u_x = \frac{\partial \psi}{\partial y}, \quad u_y = -\frac{\partial \psi}{\partial x}. \tag{3.23}$$

This can also be written as

$$\mathbf{u} = -\hat{\mathbf{z}} \times \nabla \psi \tag{3.24}$$

Note that in magnetized plasmas the potential of the $E \times B$ velocity fulfills the conditions of a stream function. The vorticity is given by

$$\mathbf{\Omega} = \nabla \times \mathbf{u} = -\Delta \psi \hat{\mathbf{z}}. \tag{3.25}$$

By means of Fourier decomposition of Eq. (3.21) the concept of *three-wave interaction* will be introduced. The feature of energy and vorticity conservation is used to estimate the energy and enstrophy transfer between different modes or waves which represent different scales in the turbulence. The Fourier decomposition is $\mathbf{u} = \sum_{\mathbf{k}} \mathbf{u}_{\mathbf{k}} e^{i\mathbf{kr}}$, and the 2D Euler Eq. (3.21) reads

$$\sum_{\mathbf{k}'} \frac{\partial \Omega_{\mathbf{k}'}}{\partial t} e^{i\mathbf{k}'\mathbf{r}} + \sum_{\mathbf{k}''} \mathbf{u}_{\mathbf{k}''} e^{i\mathbf{k}''\mathbf{r}} \cdot \sum_{\mathbf{k}'} i\mathbf{k}' \Omega_{\mathbf{k}'} e^{i\mathbf{k}'\mathbf{r}} = 0.$$

By making use of the stream function (3.24) in the second term

$$\sum_{\mathbf{k}'} \frac{\partial \Omega_{\mathbf{k}'}}{\partial t} e^{i\mathbf{k}'\mathbf{r}} + \sum_{\mathbf{k}''} (-\hat{\mathbf{z}} \times i\mathbf{k}'') \psi_{\mathbf{k}''} e^{i\mathbf{k}''\mathbf{r}} \cdot \sum_{\mathbf{k}'} i\mathbf{k}' \Omega_{\mathbf{k}'} e^{i\mathbf{k}'\mathbf{r}} = 0$$

is obtained. This expression is subsequently multiplied by $\exp(-i\mathbf{kr})$

$$\sum_{\mathbf{k}'} \frac{\partial \Omega_{\mathbf{k}'}}{\partial t} e^{i\mathbf{k}'\mathbf{r}} e^{-i\mathbf{kr}} + \sum_{\mathbf{k}',\mathbf{k}''} (\hat{\mathbf{z}} \times \mathbf{k}'') \cdot \mathbf{k}' k'^2 \psi_{\mathbf{k}'} \psi_{\mathbf{k}''} e^{i(-\mathbf{k}+\mathbf{k}'+\mathbf{k}'')\mathbf{r}} = 0.$$

Next, the orthogonality of the Fourier transform of $e^{i\mathbf{k}'\mathbf{r}}$ and $e^{i\mathbf{kr}}$ for $\mathbf{k} \neq \mathbf{k}'$

$$\int \exp\left(i(-\mathbf{k} + \mathbf{k}' + \mathbf{k}'')\mathbf{r}\right) d\mathbf{r} = \delta(-\mathbf{k} + \mathbf{k}' + \mathbf{k}'') \tag{3.26}$$

is used to obtain

$$\frac{\partial \Omega_{\mathbf{k}}}{\partial t} + \sum_{\mathbf{k}=\mathbf{k}'+\mathbf{k}''} (\hat{\mathbf{z}} \times \mathbf{k}'') \cdot \mathbf{k}' k'^2 \psi_{\mathbf{k}'} \psi_{\mathbf{k}''} = 0,$$

with $(\hat{\mathbf{z}} \times \mathbf{k}'') \cdot \mathbf{k}' = \mathbf{k}' \cdot (\hat{\mathbf{z}} \times \mathbf{k}'') = \hat{\mathbf{z}} \cdot (\mathbf{k}'' \times \mathbf{k}')$. This is equivalent to

$$\frac{\partial \Omega_{\mathbf{k}}}{\partial t} = -\sum_{\mathbf{k}=\mathbf{k}'+\mathbf{k}''} \hat{\mathbf{z}} \cdot (\mathbf{k}' \times \mathbf{k}'') k'^2 \psi_{\mathbf{k}'} \psi_{\mathbf{k}''}.$$

With $\mathbf{k} = \mathbf{k}' + \mathbf{k}'' = 0 \rightarrow \mathbf{k}'' = \mathbf{k} - \mathbf{k}'$ and $\hat{\mathbf{z}} \cdot (\mathbf{k}' \times \mathbf{k}'') = \hat{\mathbf{z}} \cdot (\mathbf{k} \times \mathbf{k}')$

$$\frac{\partial \Omega_{\mathbf{k}}}{\partial t} = -\sum_{\mathbf{k}=\mathbf{k}'+\mathbf{k}''} \hat{\mathbf{z}} \cdot (\mathbf{k} \times \mathbf{k}') k'^2 \psi_{\mathbf{k}'} \psi_{\mathbf{k}''}.$$

By introducing coupling coefficients $C_{k,k'} = \hat{\mathbf{z}} \cdot (\mathbf{k} \times \mathbf{k}') = (k_x k'_y - k_y k'_x)$ this can be rewritten as

$$\frac{\partial \Omega_{\mathbf{k}}}{\partial t} = \sum_{\mathbf{k}=\mathbf{k}'+\mathbf{k}''} -C_{k,k'} \Omega_{\mathbf{k}'} \psi_{\mathbf{k}''}$$

and the enstrophy transfer is given by

$$\frac{\partial}{\partial t} W = \frac{1}{2} \frac{\partial \left|\Omega_{\mathbf{k}}^2\right|}{\partial t} = \frac{1}{2} \left(\Omega_{\mathbf{k}}^* \frac{\partial \Omega_{\mathbf{k}}}{\partial t} + \Omega_{\mathbf{k}} \frac{\partial \Omega_{\mathbf{k}}^*}{\partial t} \right) = \frac{1}{2} 2 \operatorname{Re}(\Omega_{\mathbf{k}} \frac{\partial \Omega_{\mathbf{k}}^*}{\partial t}).$$

Here $\operatorname{Re}(\cdot)$ denotes the real part operator and not the Reynolds number. Hence,

$$\frac{\partial}{\partial t} W(\mathbf{k}) = - \sum_{\mathbf{k}=\mathbf{k}'+\mathbf{k}''} C_{k,k'} \operatorname{Re}(\Omega_{\mathbf{k}'} \psi_{\mathbf{k}''} \Omega_{\mathbf{k}}^*),$$

or purely in terms of the stream function

$$\frac{\partial}{\partial t} W(\mathbf{k}) = - \sum_{\mathbf{k}=\mathbf{k}'+\mathbf{k}''} \hat{\mathbf{z}} \cdot (\mathbf{k} \times \mathbf{k}') k'^2 k^2 \operatorname{Re}(\psi_{\mathbf{k}'} \psi_{\mathbf{k}''} \psi_{\mathbf{k}}^*). \tag{3.27}$$

The direction of enstrophy transfer depends on the sign of the triple correlation which is called the *bispectrum* $\langle \psi_{\mathbf{k}'} \psi_{\mathbf{k}''} \psi_{\mathbf{k}}^* \rangle$. The energy is given by $U = \frac{1}{2} \int dx dx u^2 = \frac{1}{2} \int dx dx |\nabla_\perp \psi|^2$. Hence $U(\mathbf{k}) = |\mathbf{k} \psi_{\mathbf{k}}|^2 = -\psi_{\mathbf{k}} \Omega_{-\mathbf{k}}$ with $\Omega_{\mathbf{k}} = -k^2 \psi_{\mathbf{k}}$. The energy transfer can be written as

$$\begin{aligned} \tfrac{\partial}{\partial t} U(\mathbf{k}) &= \frac{1}{2} \frac{\partial}{\partial t} \mathbf{k}^2 \psi_{\mathbf{k}} \psi_{\mathbf{k}}^* = \frac{1}{2} (\psi_{\mathbf{k}} \frac{\partial}{\partial t} \mathbf{k}^2 \psi_{-\mathbf{k}} + \psi_{-\mathbf{k}} \frac{\partial}{\partial t} (i\mathbf{k})^2 \psi_{\mathbf{k}}) \\ &= -\frac{1}{2} \left(\psi_{\mathbf{k}} \frac{\partial}{\partial t} \Omega_{\mathbf{k}}^* + \psi_{\mathbf{k}}^* \frac{\partial}{\partial t} \Omega_{\mathbf{k}} \right) = - \operatorname{Re}(\psi_{\mathbf{k}}^* \frac{\partial}{\partial t} \Omega_{\mathbf{k}}), \end{aligned}$$

hence

$$\frac{\partial}{\partial t} U(\mathbf{k}) = \sum_{\mathbf{k}=\mathbf{k}'+\mathbf{k}''} \hat{\mathbf{z}} \cdot (\mathbf{k} \times \mathbf{k}') k'^2 \operatorname{Re}(\psi_{\mathbf{k}'} \psi_{\mathbf{k}''} \psi_{\mathbf{k}}^*). \tag{3.28}$$

The sign of the bispectrum $\langle \psi_{\mathbf{k}'} \psi_{\mathbf{k}''} \psi_{\mathbf{k}}^* \rangle$ again determines the direction of the energy transfer. Energy and enstrophy transfer exhibit a different sign, thus their spectral transfer is in different directions. Furthermore, the enstrophy is weighted more strongly towards smaller scales (or higher wavenumbers) due to the additional factor k^2. This also shows that energy and enstrophy transfer are not independent, but directly linked.

3.5 Intermittency

Intermittency is a feature of nonlinear dynamic systems, showing most of the time regular dynamics, but including short phases of chaotic behavior characterized by very strong random (non-periodically appearing) events. This way it induces a deviation from Gaussian statistics. In fluid turbulence the term

intermittency can describe two distinct aspects of turbulent flows [6], which are not independent. The first one, the so-called *external intermittency*, is associated with partly-turbulent flows, with the strongly irregular and convoluted structure and random appearance of turbulent and non-turbulent fluid [6]. A demonstrative, recent review [113] on intermittency during the transition from laminar to turbulent flows in pipe flows is in particular recommended to the interested reader. External intermittency is characterized by an on-off variation. This on-off variation induces the strong deviation from Gaussian statistics [6]. Such kind of intermittency is a key problem for renewable energy as solar generators only produce energy when the sun is shining or wind mills only produce energy as the wind is blowing. Also intermittency in the context of critical phenomena as in stock market dynamics or earth quakes is related to this kind of intermittency and not to a particular scale as the on-off variation affects all scales. The second aspect is the so-called *internal or small-scale intermittency*, which is usually associated with the tendency to spatial and temporal localization of the fine- or small-scale structure of flows [6]. It is a feature of turbulent flows. This kind of intermittency is related to dissipation at the smallest scales and possibly to a deviation from self-similarity in the large wavenumber region.

Here, we focus on small-scale structure of flows always in the turbulent state. Intermittency also occurs in plasma turbulence. The most studied case are plasma blobs as studied in Chap. 12. We will also study intermittent event in the I-mode confinement regime (see Secs. 11.4–11.5).

3.5.1 Deviation from Gaussian statistics

In plasma physics, intermittency is usually described by the deviation from Gaussian statistics. Here, the higher moments of the distribution function are calculated. The first moment is the mean $\langle X \rangle$, the second is the standard deviation $\sigma = \sqrt{\langle (X - \langle X \rangle)^2 \rangle}$. The third and fourth moments are the skewness

$$S = \frac{\langle (X - \langle X \rangle)^3 \rangle}{\sigma^3} \tag{3.29}$$

and the kurtosis

$$K = \frac{\langle (X - \langle X \rangle)^4 \rangle}{\sigma^4} - 3, \tag{3.30}$$

respectively. For Gaussian statistics the skewness and kurtosis are zero. The skewness describes the skew of the distribution function, a positive skewness indicates a stronger tail towards positive events. The kurtosis indicates how peaked the distribution is. A positive kurtosis exhibits more events directly at the mean value, but also more events in the tails, therefore it indicates the presence of more rare events. For negative kurtosis more events are found within the standard deviation compared to a Gaussian distributed signal. Rare events with high amplitudes lead to high absolute values of skewness and kurtosis. Usually a threshold in the standard deviation σ is defined above

which the fluctuations are associated with intermittent events. This is usually around σ =2–3.

3.5.2 Deviation from self-similarity

Intermittency in three dimensional turbulence is characterized by the structure function $S_p(l) = \langle(\Delta u)^p(l)\rangle$ with

$$\langle(\Delta u)^p(l)\rangle = (\mathbf{u}(\mathbf{x} + l\hat{\mathbf{x}}) - \mathbf{u}(\mathbf{x}))^p, \tag{3.31}$$

where $\mathbf{u}$ is the velocity in the direction of $\mathbf{x}$ and l is a distance, which represents the scale. The structure function provides information about the self-similarity of the scales. Kolmogorov's two-third law (Eq. 3.11) states that the kinetic energy is proportional to $U^2 = \beta\epsilon^{2/3}L^{2/3}$. This can be generalized to any power of the velocity

$$\langle(\Delta u)^p\rangle = \beta_p(\epsilon l)^{p/3} \tag{3.32}$$

and is called *Kolmogorov's similarity hypothesis*. For $p = 2$ $\beta_2 \approx 2$ this is Kolmogorov's two-third law and the energy spectrum $E(k) \sim \epsilon^{2/3}k^{-5/3}$ (Eq. 3.12) is recovered. For $p = 3$, $\beta_3 = -4/5$ and $\langle(\Delta u)^3\rangle = -4/5\epsilon l$. This relation is called *Kolmogorov's four-fifth law*. The precise factor $\beta_3 = -4/5$ can be derived from the Karman-Howarth equation [114]. The two-third law as well as four-fifth law are found experimentally to be very robust, which supports the universality of three-dimensional turbulence. If the scales would be self-similar then $S_p(l) \sim l^n$, where $n = p/3$. However, above $p > 3$ this is not the case in general. As p reaches 12 the exponent n is about 2.8 instead of 4. Since the discrepancy occurs at small-scales it is thought to be related to small-scale coherent turbulent structures. In the context of three-dimensional turbulence the discrepancy from self-similarity is called *(internal or small-scale) intermittency*.

The question arises, how this is related to non-Gaussian statistics? The skewness as defined by

$$S = \frac{\langle(\Delta u)^3\rangle}{\langle(\Delta u)^2\rangle^{3/2}} = \frac{S_3(l)}{S_2^{3/2}(l)} = \beta_3\beta_2^{-3/2} \tag{3.33}$$

is scale invariant. Furthermore, it is finite and negative $-\frac{4}{5}2^{-3/2} \approx -0.3$. Therefore, in the sense of deviation from self-similarity, the skewness is a bad qualifier for intermittency. It can be shown that the skewness is directly connected to vortex stretching [114]

$$\langle\boldsymbol{\Omega}\cdot(\boldsymbol{\Omega}\cdot\nabla)\mathbf{u}\rangle = -\frac{7}{6\sqrt{15}}S\langle\Omega^2\rangle^{3/2}, \tag{3.34}$$

where $\langle\boldsymbol{\Omega}\cdot(\boldsymbol{\Omega}\cdot\nabla)\mathbf{u}\rangle$ is responsible for enstrophy generation. Therefore, a negative skewness is necessary to ensure that $\langle\boldsymbol{\Omega}\cdot(\boldsymbol{\Omega}\cdot\nabla)\mathbf{u}\rangle$ is positive and vorticity can be generated. Otherwise the viscous term $-\nu\langle(\nabla\times\Omega)^2\rangle$ would

drive the system into viscous dissipation. Non-Gaussian statistic is an essential part of the dynamics. Neglecting the viscosity for now

$$\frac{1}{2}\frac{\partial}{\partial t}\langle\Omega^2\rangle = -\frac{7}{6\sqrt{15}}S\langle\Omega^2\rangle^{3/2} \tag{3.35}$$

can be integrated with the solution

$$\langle\Omega^2\rangle \sim \frac{1}{(t_0 - t)^2} \tag{3.36}$$

which gives an explosive growth of enstrophy around t_0. This can lead to a very fast increase in enstrophy within a short time, which is one of the main features of intermittency.

3.5.3 Coherent structures in two-dimensional turbulence

As vorticity stretching is absent in two-dimensional turbulence, the argumentation above cannot be responsible for intermittency in two-dimensional turbulence. Indeed, experiments show that the turbulent flows in two dimensions are non-intermittent with respect to the velocity field [93]. However, intermittency in the vorticity field is observed [115, 116, 117]. An explanation has been given by Okubo [118] and Weiss [119]. The time evolution of the vorticity gradient is given by [3]

$$\frac{\partial\nabla\Omega}{\partial t} = \sqrt{S^2 - \Omega^2} \tag{3.37}$$

where $S = \partial^2\varphi/\partial x\partial y$ is the local flow shear and φ is the stream function. Within the Okubo-Weiss framework it is also possible to define coherent structures, these will be discussed in detail in chapter 8.1. The above equation states that if the local shear exceeds the magnitude of the local vorticity, the vorticity gradient will steepen. Of course this leads to generation of finer structures in the vorticity, therefore this is equivalent to a transfer of vorticity to smaller scales. This is what happens in the enstrophy cascade. On the other hand, if the vorticity exceeds the local shear a coherent vortex will just rotate without distortion and the vorticity gradient will not steepen. This means that structures with sufficiently high vorticity will not be subject to decay, but rather be long living. Simulations in two-dimensional decaying turbulence show that the criterion (3.37) successfully predicts the position of long-living vortices [3]. Also the spatial position of the appearance of intermittent structures in two-dimensional turbulence is correlated with the flow topology as prediced by the the Okubo-Weiss criterion [120]. The tails of the distribution of longitudinal velocity differences are dominated by saddle points of the stream function [120] corresponding to strain dominated region of the flow.

3.6 Zonal flows

Zonal flows [121] are azimuthal-symmetric band-like shear flows. Those flows are omnipresent in two-dimensional turbulence. The most famous represen-

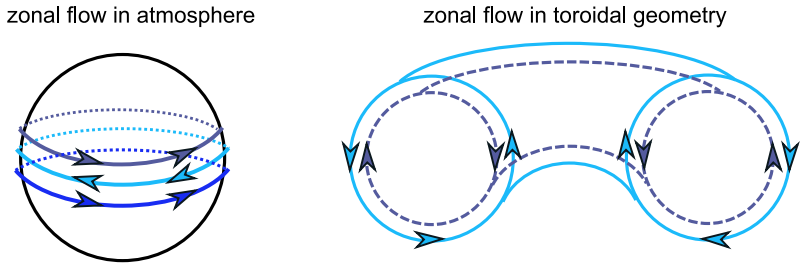

FIGURE 3.6: Zonal flows as they appear in the atmosphere and in tokamak geometry.

tation of zonal flows appear as the rings in the atmosphere of Jupiter [122, 123, 124], but also in the atmosphere of the earth zonal flows are present. The topology of a zonal in atmosphere is shown on the l.h.s. in Fig. 3.6. Due to the shear suppression mechanism zonal flows can act as transport barriers and reduce transport. The underlying instability in the atmosphere are Rossby waves. Due to their strong similarity to drift waves it has been postulated already at the end of the 70s that zonal flows should be present in magnetically confined plasmas [125] and they are now recognized as the most important saturation mechanism for plasma turbulence. In a tokamak the zonal flow appear with the topology as indicated on the r.h.s. in Fig. 3.6. Experimental evidence for zonal flows have been provided by Fujisawa in the CHS stellarator [126] and by Hillesheim in the JET tokamak [127]. They are exclusively driven through turbulence by the so-called Reynolds stress [128], which is explained in detail in the following Sec. 3.6.1. The drive of the zonal flow can also be understood as a parametric modulation instability (see Sec. D.3) [129, 130, 131, 132]. This corresponds to nonlocal energy transfer in wavenumber space [36]. How zonal flows appear in a toroidal geometry with twisted magnetic field lines like a tokamak will be discussed in detail in Sec. 5.2.3. Their role in the evolution of transport barrier formation and the high confinement regime is still an open issue, which will be discussed in Chap. 10.

3.6.1 Reynolds stress

We study the impact of fluctuations on the stationary solution of the equation of motion – the Navier Stokes equation. The velocity field is decomposed in a background and a fluctuating part

$$\mathbf{u}(\mathbf{x},t) = \bar{\mathbf{u}}(\mathbf{x}) + \tilde{\mathbf{u}}(\mathbf{x},t). \tag{3.38}$$

This is the so-called *Reynolds decomposition* regularly used in hydrodynamic stability analysis. It should be noted that the kind of average taken (time, space, filter techniques) is not important in particular, but has to be chosen self consistent and be considered very carefully regarding the interpretation. The background value refers to the average chosen. If time averaging is used,

the fluctuations are changing in time and the background value is stationary. If zonal averaging is chosen then the fluctuations are changing in the zonal direction and the background value is zonally averaged. One can also use a low pass filter and motions faster (higher frequency) than the low pass frequency are considered as fluctuations and those at lower frequency as background values. For the velocity field holds

$$\langle \mathbf{u} \rangle = \bar{\mathbf{u}} \qquad \langle \tilde{\mathbf{u}} \rangle = 0. \tag{3.39}$$

Incompressibility and continuity apply to both components of the Reynolds decomposition

$$\nabla \cdot \tilde{\mathbf{u}} = 0 \qquad \nabla \cdot \bar{\mathbf{u}} = 0.$$

For simplicity the dissipation terms such as viscosity or friction are neglected and the equation of motion is obtained

$$\frac{\partial}{\partial t} \left(\bar{\mathbf{u}} + \tilde{\mathbf{u}} \right) + \left(\left(\bar{\mathbf{u}} + \tilde{\mathbf{u}} \right) \cdot \nabla \right) \left(\bar{\mathbf{u}} + \tilde{\mathbf{u}} \right) = 0.$$

For each spatial component i holds

$$\partial_t \left(\bar{u}_i + \tilde{u}_i \right) + \left(\sum_j \left(\bar{u}_j + \tilde{u}_j \right) \partial_j \right) \left(\bar{u}_i + \tilde{u}_i \right) = 0. \tag{3.40}$$

The notation $\partial_j = \partial / \partial x_j$ has been used. From the above equation the ensemble average is taken. This yields

$$\langle \tilde{u_i} \bar{u}_j \rangle = \langle \tilde{u_i} \rangle \bar{u}_j = 0$$

and also holds for derivatives of $\tilde{u_i}$ and $\bar{u}_j$ not taking part in the averaging operator. It follows

$$\left\langle \left(\sum_j \left(\bar{u}_j + \tilde{u_j} \right) \partial_j \right) \left(\bar{u}_i + \tilde{u_i} \right) \right\rangle = \sum_j \left(\bar{u}_j \partial_j \bar{u}_i + \langle \tilde{u}_j \partial_j \tilde{u}_i \rangle \right). \tag{3.41}$$

Next we will have a closer look at the convective part containing the fluctuations only. In general the product rule gives

$$\sum_j (\tilde{u}_j \partial_j) \tilde{u}_i = \sum_j \partial_j (\tilde{u}_i \tilde{u}_j) - \tilde{u}_i \sum_j \partial_j \tilde{u}_j. \tag{3.42}$$

Here due to $\nabla \cdot \tilde{\mathbf{u}} = 0$ (3.39) the second term on the right-hand side vanishes. The resulting relation (3.42) is inserted into Eq. (3.41) and the average of (3.40) is equal to

$$\frac{\partial}{\partial t} \bar{u}_i + \sum_j \langle \partial_j (\tilde{u}_j \tilde{u}_i) \rangle + \sum_j \bar{u}_j \partial_j \bar{u}_i = 0$$

which in vector notation corresponds to

$$\frac{\partial}{\partial t}\bar{\mathbf{u}} + (\bar{\mathbf{u}} \cdot \nabla)\bar{\mathbf{u}} = -\nabla\langle\tilde{u}_j\tilde{u}_i\rangle. \tag{3.43}$$

The quantity $\tilde{u}_j\tilde{u}_i$ is a tensor. It has been introduced by Reynolds in 1883 [5, 133] and is called the *Reynolds stress*. It contains the impact of turbulence on the main background flow. Mathematically it is very similar to a viscosity. However, in 2D turbulence it has exactly the opposite effect and, therefore, it is also called *negative viscosity*.

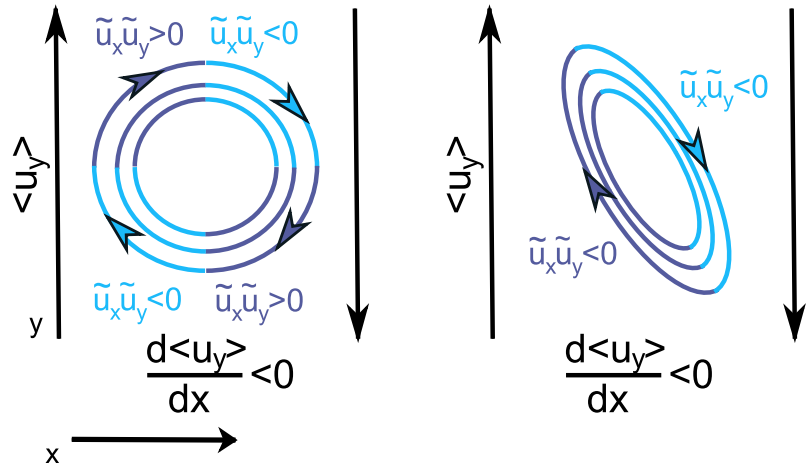

FIGURE 3.7: The left figure shows an isotropic vortex in a shear flow. The vortex can be divided into four regions where the contributions to the Reynolds stress cancel each other. Isotropic flow fields exhibit no Reynolds stress. The same holds for an elongated vortex in one direction, which is an anisotropic structure. A vortex tilted in direction of the shear flow is shown in the figure on the right. Here the Reynolds stress is finite and the shear flow and the Reynolds stress have the same sign.

The Reynolds stress can be imagined as the tilt of turbulent structures. This is illustrated in Fig. 3.7. Isotropic structures exhibit no Reynolds stress. Only if the structures are tilted a finite Reynolds stress is observed. Suppose an eddy is inserted into a shear flow, the tilt of the eddy by the shear flow would result in a Reynolds stress of the same sign as this flow shear. This is called prograde. In this case shown in Fig. 3.7 the Reynolds stress is negative. In the case of a positive Reynolds stress the eddies are preferentially tilted into the opposite (adverse) direction as the flow shear. In a plasma the Reynolds stress as part of $\mathbf{u} \cdot \nabla\mathbf{u}$ is equivalent to a polarization current (as seen by Eq. (A.15)).

3.6.2 K-ϵ model

The most basic interactions between a mean shear flow and the turbulence can decribed by a K-ϵ. A K-ϵ models describe the dynamics of turbulence by the

total kinetic energy K and a dissipation rate ϵ [134]. The following discussion can be found in Ref. [11]. We begin with the momentum balance which in its simplest form for two-dimensional divergence free flows is given by

$$\partial_t u_y + u_x \partial_x u_y = \mu \partial_x^2 u_y. \tag{3.44}$$

Here the x-direction is in the radial direction and the y-direction is in the poloidal, azimuthal or binormal direction. However, it also could be in principle in the toroidal or parallel direction. Azimuthal, i.e. poloidal or binormal, derivatives are omitted for simplicity. A discussion on this assumption can be found in Ref. [11]. The velocity field can be decomposed into a mean field and a fluctuating field $\mathbf{u} = \langle \mathbf{u} \rangle + \tilde{\mathbf{u}}$ in the usual Reynolds decomposition. Averaging Eq. (3.44) provides the governing equation for the mean flow

$$\partial_t \langle u_y \rangle = -\partial_x \langle \tilde{u}_x \tilde{u}_y \rangle + \mu \partial_x^2 \langle u_y \rangle. \tag{3.45}$$

Mean always refers to the average; if the equation is averaged over time the equation describes the mean flow in time, if the flux-surface (zonal) average is implemented it is the zonal flow. In either case, the flow is driven by the Reynolds stress $\langle \tilde{u}_x \tilde{u}_y \rangle$, which is determined by the asymmetry of the velocity fluctuations, and thus can also be interpreted as an averaged tilt of the turbulent structures. Here the damping is provided by the viscosity.

The evolution of the mean (zonal) energy can be obtained by multiplying Eq. (3.45) by $\langle u_y \rangle$

$$\partial_t \frac{1}{2} \langle u_y \rangle^2 = -\langle u_y \rangle \partial_x \langle \tilde{u}_x \tilde{u}_y \rangle + \mu \langle u_y \rangle \partial_x^2 \langle u_y \rangle. \tag{3.46}$$

Substituting the Reynolds decomposition into Eq. (3.44), recasting as an energy equation and averaging gives the evolution equation for the total kinetic energy

$$\begin{aligned} \partial_t \frac{1}{2} (\langle u_y \rangle^2 + \langle \tilde{u}_y^2 \rangle) = &-\langle u_y \rangle \partial_x \langle \tilde{u}_x \tilde{u}_y \rangle - \partial_x \langle \tilde{u}_x \tilde{u}_y \tilde{u}_y \rangle \\ &-\langle \tilde{u}_x \tilde{u}_y \rangle \partial_x \langle u_y \rangle + \mu \langle u_y \rangle \partial_x^2 \langle u_y \rangle + \mu \langle \tilde{u}_y \partial_x^2 \tilde{u}_y \rangle. \end{aligned} \tag{3.47}$$

Subtracting Eq. (3.46) from Eq. (3.47) results in the evolution of the fluctuating energy

$$\partial_t \tilde{K} = -\partial_x \tilde{T} - \mathcal{P} + \tilde{\epsilon}, \tag{3.48}$$

where

$$\begin{aligned} \tilde{K} = \frac{1}{2} \langle \tilde{u}_y^2 \rangle, \tilde{\epsilon} = \mu \langle \tilde{u}_y \partial_x^2 \tilde{u}_y \rangle, \\ \mathcal{P} = \langle \tilde{u}_x \tilde{u}_y \rangle \frac{\partial \langle u_y \rangle}{\partial x}, \tilde{T} = \langle \tilde{u}_x \tilde{u}_y^2 \rangle. \end{aligned} \tag{3.49}$$

Using the partial derivative

$$\partial_x (\langle u_y \rangle \langle \tilde{u}_x \tilde{u}_y \rangle) = \langle \tilde{u}_x \tilde{u}_y \rangle \partial_x \langle u_y \rangle + \langle u_y \rangle \partial_x \langle \tilde{u}_x \tilde{u}_y \rangle \tag{3.50}$$

the mean (zonal) energy (3.46) satisfies

$$\partial_t \bar{K} = -\partial_r \bar{T} + \mathcal{P} + \bar{\epsilon}, \tag{3.51}$$

where

$$\bar{K} = \frac{1}{2}\langle u_y \rangle^2, \bar{\epsilon} = \mu \langle u_y \rangle \partial_x^2 \langle u_y \rangle, \tag{3.52}$$
$$\bar{T} = \left(\langle u_y \rangle \langle \tilde{u}_x \tilde{u}_y \rangle \right).$$

In the framework of a standard K-ϵ model, one equation for the mean (zonal) energy (3.51) and one for the fluctuating energy (3.48) are obtained. The physical mechanisms behind the different terms in Eqs. (3.48) and (3.51) are discussed in detail in the following two sections. The energy transfer between mean and fluctuating kinetic energy is investigated in the Sec. 3.6.3. This is relevant for turbulence suppression. In Sec. 3.8 the spatial transport of kinetic energy, called turbulence spreading, is studied. It is relevant for subcritical excitation of turbulence [135]. A recent review of nonlocal turbulent transport in magnetized plasmas can be found in Ref. [136].

3.6.3 Energy transfer and limit-cycle oscillations

Turbulence production $\mathcal{P}$ is the product of shear and Reynolds stress. It appears in both equations, the one of the turbulent and the one of the mean kinetic energy. If both factors are positively correlated the mean flow can amplify itself, if they are negatively correlated the mean flow is damped. In three-dimensional turbulence this term is responsible for the drive of the turbulence and it is negatively correlated. Therefore, it is called *production*. In the case of two-dimensional turbulence the production term acts like an energy source of the shear flow. This mechanism produces flow *only* if the Reynolds stress is in the same direction as the shear $\langle \tilde{u}_x \tilde{u}_y \rangle \propto \partial_x \langle u_y \rangle$. The vortex has to be prograde with respect to the flow shear. However, a vortex tilted by the shear flow will be naturally in this direction (see Fig. 3.7). In the other case $\langle \tilde{u}_x \tilde{u}_y \rangle \propto -\partial_x \langle u_y \rangle$ the flow drives the turbulence and in turn the flow is reduced. Therefore, the resulting momentum drive by the radial gradient in the Reynolds stress $\partial_t \langle u_y \rangle \propto -\partial_x \langle \tilde{u}_x \tilde{u}_y \rangle \propto -\partial_x^2 \langle u_y \rangle$ acts like a negative viscosity, which is also called turbulent viscosity. $\mathcal{P}$ is a transfer channel between the turbulent energy and the energy of the background flow and appears with different signs in the equations of the energies of the mean flow (3.51) and the turbulence (3.48). Therefore the generation process of zonal flows directly includes a suppression mechanism of the turbulence. As this part of the mean flow is exclusively generated by the turbulence this is the zonal flow by definition.

Turbulence suppression and zonal flow generation are directly linked to each other, which leads to a very interesting phenomenon; the so-called *limit-cycle oscillation* known from population dynamics in biology. These are described

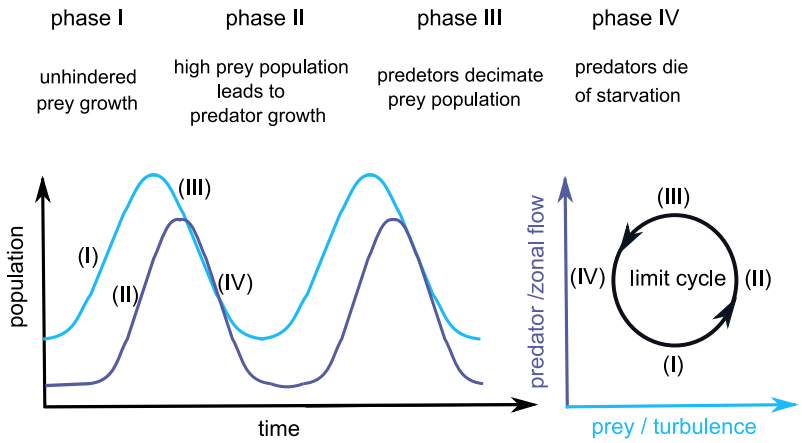

FIGURE 3.8: Principle of limit cycle oscillations by a predator-prey relationship.

by the *Lotka-Volterra equations* [137] for a prey x

$$\frac{\mathrm{d}x}{\mathrm{d}t} = x(a - by) \tag{3.53}$$

and predator y

$$\frac{\mathrm{d}y}{\mathrm{d}t} = y(cx - d). \tag{3.54}$$

The prey population grows by birthrate a, the predator population is damped by mortality d. A high prey population leads to an increase of the predator population by the rate cxy but also to damping of the prey population by the rate $-bxy$. Such systems can oscillate as shown in Fig. 3.8. In the case of zonal flows and drift-wave turbulence, the turbulence takes the role of the prey and the zonal flow the role of the predator. In the absence of shear flow the turbulence can grow. With increasing turbulence amplitude the zonal flow grows at the expense of the turbulence level. This leads to saturation and finally a suppression of the turbulence level. With decreasing turbulence level also the zonal flow amplitude decreases due to the reduction of the zonal flow drive. The turbulence can recover and the cycle starts over. The frequency at which the zonal flow is measured is this frequency [37].

3.7 Shear Suppression

The interaction of vortices at different spatial scales is important for magnetically confined fusion plasmas, as large-scale shear flows are thought to be responsible for turbulence suppression due to their interaction with the small-scale micro-turbulence. In the common heuristic explanation, the so-called *shear decorrelation mechanism* illustrated in Fig. 3.9, the large-scale shear tears small-scale turbulent structures apart. Thereby, the vortices are getting smaller in size. Due to their smaller size, the typical step size in a

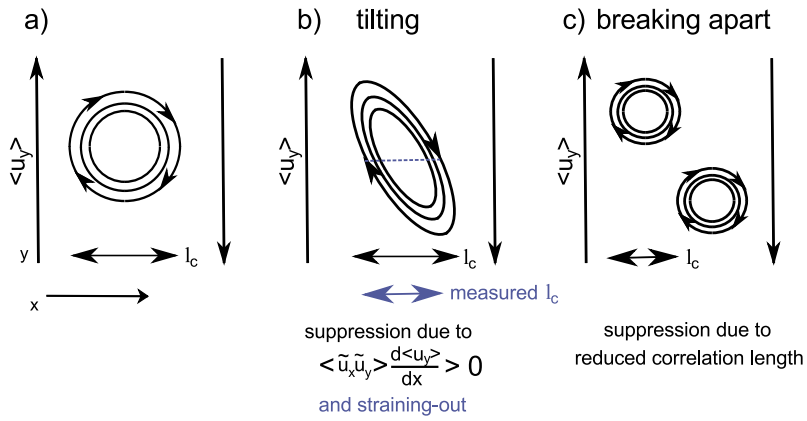

FIGURE 3.9: An isotropic vortex in a shear flow (a). In the common shear decorrelation mechanism the eddies are tilted (b) and finally teared apart by the shear (c). Thereby the correlation length l_c is reduced, which reduces the turbulent transport. Actually, tearing apart the structures is not necessary, the turbulence will be suppressed already by tilting (due to energy transfer by the Reynolds stress) and thinning, which leads to enhanced dissipation by the straining-out process (b).

diffusion based model is reduced. Thus, the turbulent diffusion coefficient and the turbulent transport are reduced. Direct experimental evidence for vortices breaking apart in a strong flow shear is rare. So far, this phenomenon has been only reported from the TEXTOR tokamak [138].

Even though turbulence suppression by the shear decorrelation mechanism is widely accepted in the fusion community, there are some drawbacks. Under high flow shear turbulent structures get tilted (Fig. 3.9b). If the radial correlation length is measured by a radially aligned diagnostic, as usually done, the measured radial correlation length will appear to be reduced compared to the turbulent structure not being tilted (Fig. 3.9a), even though the actual radial correlation length (the radial distance which is connected by the structure) is not reduced at all (Fig. 3.9b).

Good confinement is correlated with a low turbulence level. As in the plasma edge the radial electric field is proportional to the ion pressure gradient $E_r \approx (\nabla p_i)/(en)$ and improved confinement is intrinsically correlated to a deep radial electric field. As the radial electric field exhibits a finite radial extent, the deep radial electric field is also correlated to high flow shear. Therefore, confinement and flow shear are collinear and just the correlation of improved confinement and a high flow shear does not provide any insight into the reason behind improved confinement. To investigate the principle of shear suppression of plasma turbulence, the collinearity between radial electric field and ion pressure gradient has to be avoided, which can be done in low-temperature plasmas. In such experiments, where strong $E \times B$ shear is externally excited by plasma biasing, the turbulence can be indeed suppressed [139, 140, 141]. However, no reduction of the radial correlation length has

been observed in a linear device [140], no relation between the flow shear and the turbulence level have been found in a simple magnetized torus [141] or the large-scale coherent structures even become dominant at not reduced but instead increased correlation lengths as observed in a stellarator [139]. The simplified picture of the heuristic shear decorrelation mechanism seems to be untenable.

Furthermore, as we will see in Chap. 9, in the plasma edge the small-scale vorticity suppresses linear wave-like features, in particular the growth rate becomes irrelevant. That means the often used quenching rule, that the flow shear has to exceed the linear growth rate of the dominant instability $S > \gamma$ does not apply. If the background shear exceeds the local vorticity, the turbulence will be not suppressed, instead the local vorticity gradient will steepen up (Sec. 3.5.3), which leads to a transfer of vorticity to smaller scales and intermittent behavior. As enstrophy and energy transfer are directly coupled (Sec. 3.4) and in opposite direction, this also leads to a transfer of kinetic energy from small to large scales.

There are two mechanisms, which allow turbulence suppression by flow shear and the reason for shear suppression is likely a combination of both. One is due to the direct energy transfer from the turbulence to the shear flow by the turbulence production term $\mathcal{P}$. This energy transfer leads to a reduction of the turbulence amplitude. The other is due to the enhanced dissipation. Small-scale structures are elongated and thinned by the larger scale flows. The structures at larger scales absorb the smaller ones by coiling them up [142] or they are finally destroyed by a straining-out process (Sec. 3.3.3) though enhanced dissipation due to their thinness. The enhanced dissipation can lead to a significantly reduced lifetime of the turbulent structures.

There are some experimental results supporting this mechanism. The shear decorrelation process corresponds to the reverse of the vortex merging process. It is local in wavenumber space. The vortex-tilting-straining-out mechanism appears nonlocal in wavenumber space. Experimental measurements of drift-wave turbulence at the TJ-K stellarator [35, 142, 143, 21] have shown that due to the strongly pronounced nonlocality in the energy transfer in wavenumber space between the turbulence and the zonal flow [142], but also within the turbulence itself [35]. The vortex thinning process has been directly observed in configuration space (not in wavenumber space) with fast imaging in CSDX [144]. In Ref. [142] scales at $k\rho_s \sim 1$–2 are found to be preferentially suppressed by the shear flow. A preferential reduction of these intermediate scales $k\rho_s \sim 1$–2 has been found in H-mode plasmas in the TJ-II stellarator [145]. Recently it has been shown that vortex thinning is strongly enhanced by finite Larmor radius effects in a gyrofluid [146]. The effects are stronger in the ideal 2D case. In 3D gyrofluid simulations with finite ion temperatures, vorticity sheets are less pronounced due to geodesic curvature (Sec. 5.2.3) and magnetic shear [146]. Based on the vortex-tilting mechanism an alternative shear suppression criterion to the standard one has been suggested, which will be discussed in detail in Sec. 10.1.

3.8 Turbulence spreading

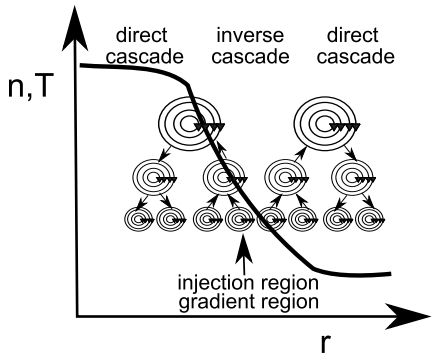

FIGURE 3.10: Illustration of turbulence spreading by nonlinear interaction.

The term $\partial_x \tilde{T}$ in Eq. (3.48) does not lead to a change of energy in the total domain. It fulfills energy conservation. It contains a quantity related to a velocity to the power of three and describes the three-wave coupling introduced before (Sec. 3.4). Therefore, the inverse energy cascade is accomplished by this term. Because it redistributes the energy between the different scales and all scales are included in $\tilde{K}$, this effect is not obvious in the K-ϵ model. Besides a redistribution in wavenumber space, this term can spatially lead to a radial redistribution of kinetic energy. Indeed, if the energy is locally injected in a certain spatial region, larger structures are formed which will penetrate also into the stable region. Keep in mind that the cascade is a statistical process. Just as larger structures emerge from smaller ones, some decay into smaller ones, too. Therefore, once larger structures penetrate the stable region, those structures will decay into smaller structures (Fig. 3.10), thus, the turbulence is able to spread into the stable region.

Turbulence spreading can be modeled by the *Fisher-Kolmogorov-Petrovsky-Piscounov* equation [147]

$$\frac{\partial I}{\partial t} = \nabla \cdot (D_{turb} \nabla I) + \gamma_L I - \gamma_{NL} I^2 \tag{3.55}$$

describing a diffusion of turbulence intensity I with a diffusion coefficient D_{turb}. Here, γ_L describes the linear growth of the fluctuations and γ_{NL} provides nonlinear saturation of the turbulence level. Such an equation is fundamentally local. However, the one-to-one correspondence between turbulence intensity and global parameters (density, temperature and their gradients) does not hold. This can lead to propagation of turbulence intensity fronts. The Fisher-Kolomogorov-Petrovski-Piskounov equation is usually applied in a heuristic way and used to model non-local heat transport and the propagation of cold pulses [148, 149, 150], which is the most frequently studied case related to non-local transport in magnetically confined fusion plasmas. However, in principle this equation can also be derived from gyro-kinetic theory [151].

From the K-ϵ model described above in Sec. 3.6.2 it is possible to estimate the coefficients of the Fisher-Kolmogorov-Petrovsky-Piscounov equation in the case of turbulence spreading of turbulent kinetic energy. By comparing Eq. (3.55) to (3.48) we identify $I = \tilde{K}$, $\gamma_L = \mathcal{P}/\tilde{K}$, $\gamma_{NL} = -\tilde{\epsilon}/\tilde{K}^2$ and $D_{turb} = -\tilde{T}/(\partial_x \tilde{K})$. Therefore, $\tilde{T}$ is the responsible term for turbulence spreading also in the framework of the Fisher-Kolmogorov-Petrovsky-Piscounov equation. Note, these coefficients have to be estimated from the stationary solution and not from the time-varying quantities. Turbulence spreading of turbulent kinetic energy is examined in detail in Sec. 8.3. However, such a deviation based on a K-ϵ model is also possible for other fluctuating quantities like density or temperature fluctuations. In Sec. 12.2.3 such a turbulence spreading model has been applied to the scape-off layer, derived from density fluctuations.

Further reading on turbulence in general

For further reading, the introductions on fluid, flows and fluid instabilities by Oertel [152] can be recommended. A very detailed introduction on vortex physics – also in three dimensions – is given by Wu, Ma and Zhou [153]. The general introductions to turbulence by Pope [134], Frisch [154] and Davidson [114] are recommended, too. A recent short introduction with particular attention to modern topics can be found in Ref. [7]. Once familiar with the basic concepts, it is worthwhile to have a look in the book by Tsinober [6]. This book offers a very critical discussion on the basic concepts found in most literature.

Chapter 4

Plasma micro-instabilities

Turbulence in the edge of magnetized confined plasmas offers a wide number of different modes resulting from various linear instabilities and diverse nonlinear self-organized phenomena. Before the nonlinear phenomena are investigated in detail in Chap. 5, in the present chapter the linear instabilities are presented. In tokamaks the most prominent micro-instabilities are the ion-temperature-gradient (ITG) mode (Sec. 4.4) and the trapped electron mode (TEM) (Sec. 4.5), which are distinguished by their drive. Most relevant for plasma turbulence in the very edge of the confined region are the drift wave (Sec. 4.3), the ITG mode and maybe TEM mode. Turbulence in the scrape-off layer (SOL) is interchange (Sec. 4.2) (also called resistive ballooning mode (RBM)) dominated. In the near SOL the conducting wall instability may be important (Sec. 4.6). As electromagnetic effects become important (Sec. B.2.4) the turbulence changes its nature and micro-tearing modes (MTMs) (Sec. 4.7) and kinetic ballooning modes (KBMs) (Sec. 4.8) can become important. Both, the interchange (Sec. 4.2) and the drift-wave mechanism (Sec. 4.3), underlie the other instabilities. They are always present and in competition (Sec. 5.2.1).

4.1 Instability characterization

To interpret the measured data, a characterization of the different instabilities is carried out (see Tab. 4.1) as published in Ref. [161]. Instabilities can be distinguished by their characteristic size scale, frequency, propagation direction, parity, cross-phases and drive. Most micro-instabilities such as the electrostatic drift-wave, or ITG, TEM, MTM, KBM occur close to the ion scale. Usually the size is compared to the hybrid Larmor radius $\rho_s = \sqrt{T_e m_i}/eB$. Drift waves, TEM and ITG are a bit smaller, $k_y\rho_s \sim 0.1$–1, than RBM, MTM and KBM which occur at $k_y\rho_s \sim 0.01$–0.1. The electron temperature gradient mode (ETG) is the electron counterpart of the ITG and appears on the electron scale. Long wavelength macro-MHD instabilities as ideal peeling ballooning modes (IPM) and ideal ballooning modes (IBM) appear at much smaller wave numbers. The size of global instabilities is not given in $k\rho_s$, but rather in terms of poloidal and toroidal mode numbers. They occur also at much lower

Instability	**drive**	**prop.**	**scale**	$\alpha_{\phi,\tilde{\mathbf{p}}}$	$\omega(\mathbf{L}_\perp/\mathbf{c_s})$	**parity**	**Ref.**
IPM	$J_\parallel$	n.p.	$k_\theta\rho_s \ll 0.1$			global	
(I-R)BM	∇p	n.p.	$k_\theta\rho_s < 0.1$	$\pi/2$		ball.	
KBM	$\nabla T_{e,i}$	i dia.	$k_\theta\rho_s \sim 0.1$	$\pi/2$		ball.	[155]
MTM	∇T_e	e dia.	$k_\theta\rho_s \sim 0.1$	0	0.1-1	tear.	[156, 157, 158]
DW	∇n	e dia.	$0.1 < k_\theta\rho_s \leq 1$	0	0.1-1	ball.	
ITG	∇T_i	i dia.	$0.1 < k_\theta\rho_s \leq 1$	> 0	0.1-1	ball.	[159, 158]
TEM	∇T_e,∇n	e dia.	$0.1 < k_\theta\rho_s$	0		ball.	[160]
ETG	∇T_e	e dia.	$k_\theta\rho_s > 1$	$\pi/2$	0.5-100	ball.	[160, 158]

TABLE 4.1: Properties of linear instabilities: ideal peeling mode (IPM), ideal and resistive ballooning mode ((I-R)BM), kinetic ballooning mode (KBM), micro tearing mode (MTM), electrostatic drift wave (DW), ion temperature gradient mode (ITG), trapped electron mode (TEM) and electron temperature gradient mode (ETG). The structures propagate either in electron (e dia.) or ion diamagnetic direction (i dia.) or do not have any preferential direction (n.p.). They have ballooning (ball.) or tearing (tear.) parity. Times are normalized to $L_\perp/c_s$, perpendicular spatial scales to ρ_s, where $L_\perp$ is the mean profile scale length, c_s is the sound speed, $\rho_s = \sqrt{T_e m_i}/eB$ with electron temperature T_e, ion mass m_i, elementary charge e and magnetic field strength B. Adapted from Ref. [161].

frequencies compared to micro-instabilities. In Chapter 9 we will see that for broadband turbulence with high fluctuation levels a characterization by linear features may not work out. How to characterize different turbulence regimes will be discussed in Chap. 5.2.

4.2 Interchange instability

The interchange instability in principle is the MHD analogon of the Rayleigh-Taylor instability. It is sketched in Fig. 4.1. Most important for the interchange instability to occur is the magnetic curvature. On the right hand side the curvature is in the opposite direction to the density gradient. This is the situation on the low field side of the tokamak. Due to the curvature drift, ions tend to move upwards out of the high density region and electrons tend to move downwards. This leads to a charge separation. As a result an electric field is generated. The $E \times B$ drift due to the electric field will accelerate the density perturbation which propagates outwards. A negative perturbation is moving inwards. The configuration is unstable. On the high field side the perturbations are stable against this mechanism. That is why the region on the low-field side is called the *bad curvature region* and the region on the high-field side the *good curvature region*.

The same result is obtained using the diamagnetic current instead of the curvature drift [162]. Consider the isobar of the pressure perturbations. Due to the pressure gradient dependence, the diamagnetic current flows along the

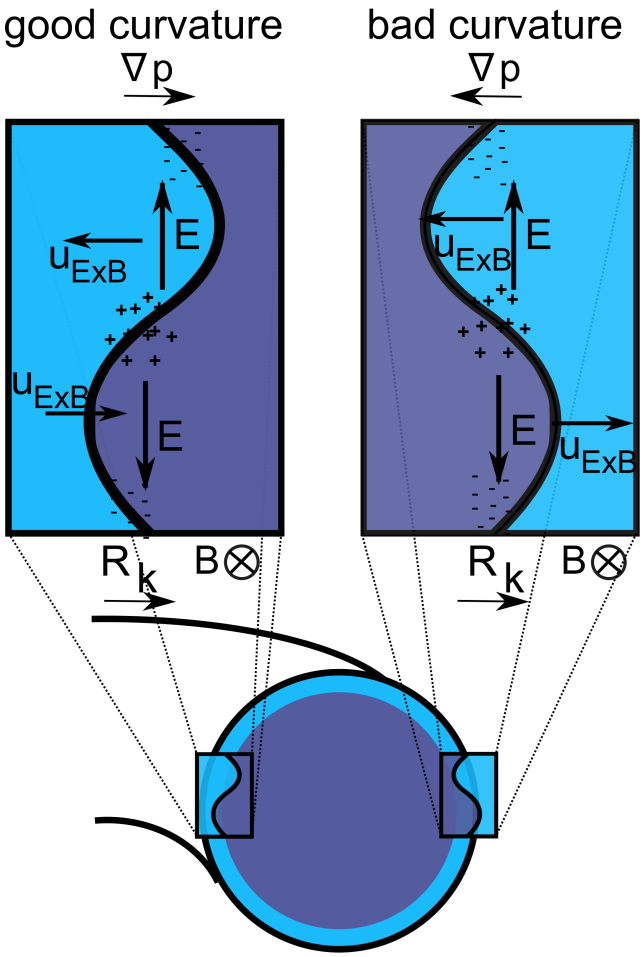

FIGURE 4.1: Interchange instability. Explanation in the main text. Figure adapted from Ref. [162].

curved isobars, but mainly downwards in the good curvature region and upwards in the bad curvature region. More inside the plasma the diamagnetic current is weaker due to the magnetic field dependence of the diamagnetic current. The continuity equation gives $\mathrm{d}\rho/\mathrm{d}t = -\nabla \cdot \mathbf{J}$. An increase in the current leads to negative charge accumulation, a decrease in positive charge accumulation. The resulting electric fields lead to $E \times B$ velocities in a similar way as described above. The interchange instability is unstable in the bad curvature region and stable in the good curvature region. A mathematical description of the interchange instability is given in the appendix B.1.

Overall stability is gained if the turbulent structures stay longer in the good curvature region than in the bad curvature region. This is also the reason why D-shaped plasmas are favorable. The magnetic field lines favor the high-field side, where the curvature is stabilizing and, therefore, the unstable region on the low-field can be avoided for a large fraction of the trajectories.

4.3 Drift wave

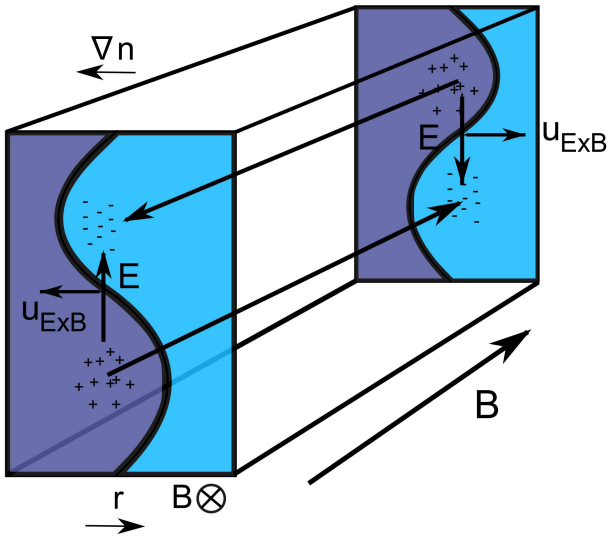

FIGURE 4.2: Mechanism of the drift wave. Explanation is given in the main text. Figure adapted from Ref. [162].

Here the simplest case of the drift wave without any curvature effects will be introduced. This is illustrated in Fig. 4.2. The main requirement for the drift wave to occur is a perturbation along the magnetic field line $k_\parallel \neq 0$. Similar to the interchange case described above, we consider a density perturbation perpendicular to the radial and the magnetic field direction (called binormal in the following) which is embedded in a background density gradient in negative radial direction. As the density perturbation is also along the field line, it is accompanied by a parallel pressure gradient. Due to their small inertia, electrons will react with their thermal velocity to the parallel pressure gradient and try to compensate it. This induces the indicated charge densities in Fig. 4.2. The resulting electric fields and $E \times B$ drifts lead to a shift of the perturbation in the binormal direction, which can be interpreted as a propagation. This is the reason why it is called drift wave. The propagation will be studied in more detail in the appendix B.2.2. In the case illustrated in Fig. 4.2 the perturbation is neither growing nor damped, it is stable. The particle transport is given by $\Gamma = \langle \tilde{u}_x \tilde{n} \rangle_y = \langle \mathrm{Re}(ik_y \tilde{\phi} \tilde{n}) \rangle_y$ with $\mathrm{Re}(\cdot)$ being the real part and harmonic perturbations assumed $\tilde{n}, \tilde{\phi} \sim e^{i\varphi}$. As $\tilde{\phi}$ and $\tilde{n}$ are in phase, $ik_y \tilde{\phi} \tilde{n}$ is purely imaginary and therefore no transport is associated with a stable drift wave. However, if the parallel motion of the electrons is hampered a small phase difference between density and potential is initialized. This leads to transport and to a finite growth rate of the drift wave. Drift-wave instability will be investigated in detail in the appendix B.2.3. Drift-wave turbulence will be discussed in detail in the appendix 5.1.

4.4 Ion temperature gradient mode (ITG)

The ion temperature gradient mode is an instability driven by the ion temperature gradient ∇T_i. By replacing the density gradient by the ion temperature gradient in the explanation of the interchange instability using the diamagnetic current (see Chap. 4.2) one can realize that a high ion temperature gradient is subject to the interchange instability (compare Figs. 4.3 and 4.1). In this sense the ITG is an interchange instability.

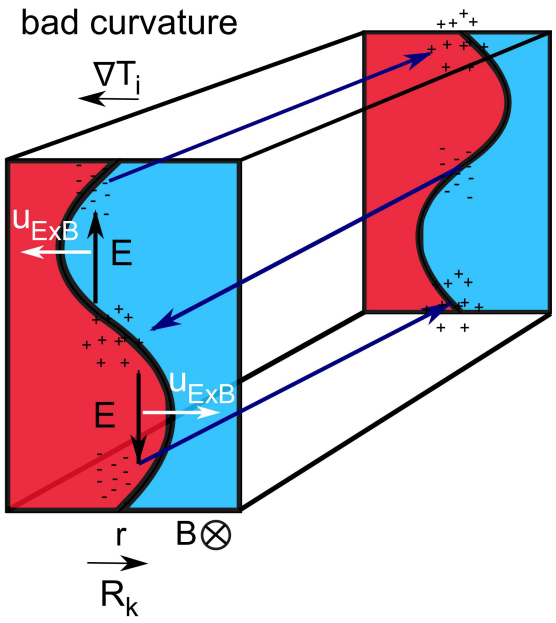

FIGURE 4.3: ITG instability. The ITG is driven by the ion temperature gradient due to the curvature. The color indicates the ion temperature, warm is red, cold is blue. With respect to the ion temperature the potential shows interchange characteristics. Due to the Boltzmann response $\tilde{\phi} \sim \tilde{n}$, the density follows the induced potential perturbations and with respect to the density the potential is drift-wave-like.

In general a density gradient has stabilizing influence on the ITG mode. A finite density gradient reduces the growth rate of the ITG mode. As a result the ion temperature gradient has to overcome a certain threshold in the density gradient to induce instability. The ratio of the ion temperature to density gradient scale length is given by $\eta_i = (T_i/n)(\nabla n/\nabla T_i) = \nabla(\ln n)/\nabla \ln(T_i)$. Therefore, the ITG mode is also called the η_i mode. Critical gradients are connected to an interesting phenomenon called *stiff transport*. Transport is considered to be non-stiff if it is proportional to the gradient length scale as assumed for an usual diffusion process. Stiff transport is low below a critical gradient and than explodes once the critical gradient is exceeded. Relevant for the ITG is the heat flux $q_i = -n\chi_i \nabla T_i$ with density n and ion thermal conductivity χ_i. In the case of a critical gradient, the ion thermal conductivity

is given by

$$\chi_i = \frac{\rho_i}{a}\frac{T_i}{eB}\left(\frac{R}{L_{Ti}} - \frac{R}{L_{Ti,crit}}\right) \propto \left(\frac{R}{L_{Ti}} - \frac{R}{L_{Ti,crit}}\right), \tag{4.1}$$

where the critical gradient scale length depends on the density gradient for the ITG. We assumed gyro-Bohm diffusivity $\chi_i \sim \frac{\rho_i}{a}\frac{T_i}{eB}$. As $dT_i/dr \sim T_i R/L_{Ti}$ and $\rho_i = \sqrt{T_i m_i}/eB$ the heat flux is proportional to $q_i \sim T_i^{5/2}\frac{R}{L_{Ti}}\left(\frac{R}{L_{Ti}} - \frac{R}{L_{Ti,crit}}\right)$. This means once the critical gradient is exceeded the heat flux increases dramatically. This increase is particularly strong at high temperatures due to the $T_i^{5/2}$ dependence. Therefore, this phenomenon is highly relevant for the plasma core. Due to the high heat flux, the gradient flattens and as a result the ion temperature gradient is more or less pinned to the critical gradient level. The critical gradient is not the same for linear and nonlinear calculations. The corresponding nonlinear threshold in R/L_{Ti} is larger than in linear calculation, which is called the *Dimits shift* [163].

The ITG can also appear in a homogenous plasma without curvature as a pure drift wave [164, 165]. Interestingly, this also needs a critical gradient in the ion temperature to be overcome ($\eta_i \gtrsim 2/3$). In a real tokamak the ITG instability is subject to a competition between the drift-wave and the interchange mechanism. The curvature induced potential perturbations by the ion temperature fluctuations can be partially compensated by the parallel electron motion, which gives rise to the drift wave (compare Figs. 4.3 and 4.2). The ion temperature is the only state variable which does not participate in the adiabatic response. Therefore, ion temperature fluctuations always exhibit interchange dynamics to some degree. The charge separation by the interchange mechanism cannot be fully compensated by the parallel electron dynamics. This does not mean that the density fluctuations exhibit interchange dynamics, too. The density perturbations appear very similar to the drift wave and measurements based only on density fluctuations will hardly be able to clearly identify ITGs. In DALF3 simulations [166] the electron part of the system follows drift-wave dynamics even though the dynamics of the ion temperature fluctuations is fundamentally different. These modes are called ITG drift waves.

The ITG is in competition with the TEM instability discussed in the next section. Both instabilities exhibit very similar characteristic sizes. Whether the turbulence is ITG or TEM dominated can have severe consequences for the entire discharge concerning confinement, density peaking and impurity accumulation. These are discussed after introducing the TEM in the next section. Which instability is dominant depends highly on the gradient scale lengths ratio. This is illustrated in Fig. 4.4. However, there are some regions in the phase diagram where both instabilities can coexist. In competition with electron temperature gradient modes (ETGs), turbulence at ion scales eliminates electron-scale streamers and dominates heat transport, not only of ions but also of electrons [167]. Ion temperature gradient mode turbulence is

stabilized by electromagnetic effects [168, 169]. Furthermore, ITG turbulence is stabilized by fast ions [170, 171].

4.5 Trapped electron mode (TEM)

The basic mechanism of trapped particle driven instabilities can be described as follows. Due to the magnetic mirror effect, particles can be trapped in the magnetic field. Trapped particles are localized on the low-field side of the torus. As trapped particles cannot move freely along the magnetic field lines they respond differently to a perturbed potential compared to passing (i.e. non-trapped) particles. The vertical $\nabla B \times B_\varphi$ drift (with toroidal magnetic field B_φ) is responsible for the characteristic banana orbits in the poloidal plane [162]. The $\nabla B \times B_\theta$ leads to a toroidal precession [162]. As electrons and ions drift in opposite directions, this leads to a toroidal current called the Bootstrap current. Perturbations of the trapped particle density of electrons and ions drift in opposite directions. Because trapped particles are localized in the bad curvature region, the resulting charge separation have the same consequences as the interchange instability. At low frequencies $\omega \ll k_\parallel v_{thi}$ where the passing electrons and ions follow approximately the Boltzmann response (see Sec. A.3), both species contribute to the charge separation. The passing electrons cannot compensate the charge separation. This is called the trapped ion mode (TIM). It can be seen as an interchange mode. At higher frequencies $\omega > k_\parallel v_{thi}$ the response of the ions will deviate from a Boltzmann response and the passing electrons move along the field lines and can compensate the charge separation of the trapped particles. The interchange-like drive of the trapped particles induces the drift-wave-like parallel response. The mode is a drift wave and as additionally the fraction of trapped particles retards the electron response, this is called the (dissipative) trapped electron mode (TEM). As the particles are trapped on the low field side the TEM is ballooned.

Like the ITG also the TEM is a critical gradient mode, this means the electron temperature gradient needs to exceed the density gradient by a certain fraction. Like in the ITG case, this leads to stiff transport. The critical gradient can be experimentally investigated by heat modulation in power balance studies as done in Refs. [172, 173].

The transition from TEM to ITG dominated turbulence seems to play a role in the transition from the linear Ohmic confinement (LOC) regime to the saturated Ohmic confinement (SOC) regime. The two regimes are characterized by the energy confinement time, which increases linearly with the density in the LOC regime and saturates in the SOC regime. In the Alcator C-mod tokamak the LOC-SOC transition is accompanied by a reversal of toroidal rotation and the disappearance of modes propagating in the electron diamagnetic direction [174]. These modes are thought to be TEMs [174].

One important difference between TEM and ITG is the higher eigenfrequency of the TEM. This is important as in a tokamak a perturbed distri-

bution function can have excess of particles at a given energy range as the gyro-center drift depends on energy. This is called *thermo-diffusion* [175]. If the resonance is at low energies, a net inward flux is produced, at high energies an outward flux can be produced. Therefore, for electrons a low resonance appears, if the eigenfrequency is low, as in the case of ITG. This results in thermo-diffusive inward flux. If the frequency becomes large, as in the case of TEMs, the thermo-diffusive flux is outwards. For impurity ions the direction of thermo-diffusion changes sign [175]. Therefore, ITG turbulence leads to impurity ejection and TEM turbulence to impurity accumulation. In a tungsten experiment as ASDEX Upgrade impurity control is very important as tungsten is a high Z material leading to high radiation losses in the plasma. If the plasma turbulence in the core is ITG dominated, which is the case in medium to high density L-modes (SOC regime) and H-modes, by applying central ECRH, the main plasma particles move inwards leading to central density peaking and the impurity particles moves outwards avoiding impurity accumulation. In the case of TEM dominated turbulence at low densities (LOC regime) the electrons are transported outwards leading to the so-called density pump out. If the edge turbulence would be TEM dominated, impurities from the SOL would be transported into the core. At lower collisionality also the plasma core will most likely be TEM dominated. In such a case the impurities will be further transported into the center, leading to impurity accumulation and radiation death.

Trapped particle modes are frequently discussed also in the context of plasma edge turbulence. However, due to the high collisionality in the plasma edge trapped electrons as a destabilizing mechanism are basically unavailable. The ratio of the collisional detrapping rate to the bounce time $\nu_* = \epsilon^{-3/2}\nu_e qR/V_e$ is about 40 for typical L-mode plasma edge parameters [166]. In H-mode the plasma beta is higher and electromagentic modes like MTMs and KBMs (see Secs. 4.7 and 4.8) get more important. Therefore, for the present investigations in the plasma edge, trapped particle modes are most likely negligible.

4.6 Conducting wall instability (CWI)

The radial electric field in the SOL is needed to maintain quasi-neutrality, where the potential limits electron end losses to the wall. The resulting poloidal velocity gives rise to the CWI [178].

The basic mechanism of the CWI is shown in Fig. 4.5. The CWI is driven by electron temperature gradient. Fluctuations of the parallel current are induced by electron temperature fluctuations via the Bohm criterion [179]. Then the fluctuations in the parallel current couple electron temperature and plasma potential fluctuations. Similar to the common drift-wave instability, the thermodynamic fluctuations (for the CWI it is the electron temperature, for the drift wave it is the density) are in phase with the potential fluctuations. In this

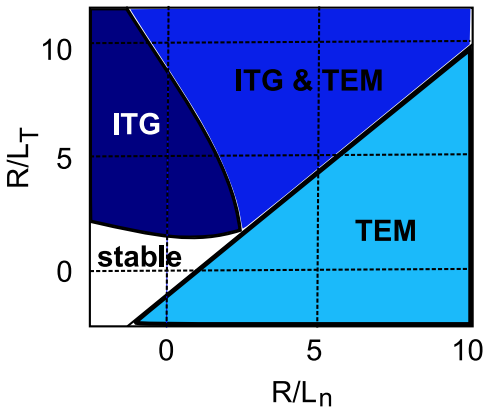

FIGURE 4.4: Regions of ITG and TEM instability with respect to the gradient scale lengths. Figure adapted from Ref. [176]. A similar figure for R/L_{T_e} and R/L_{T_i} can be found in Ref. [177].

case the CWI is stable. But as for the drift wave any restriction on the parallel electron dynamics like collisions will drive the CWI unstable. In contrast to the drift-wave instability, the CWI exhibits no finite parallel wavenumber like the interchange instability does. In general the linear growth rate of the CWI is of the same order as that of the interchange instability [179]. As seen in a previous study [180], electron temperature fluctuations are strong enough to dominate floating potential fluctuations close to the separatrix. At ASDEX Upgrade these fluctuations are in general non-negligible and the dominance of the CWI for ASDEX Upgrade parameters is consistent with a combined experimental-numerical study [180].

In general it seems that the transition from a drift-wave dominated turbulence region inside the confined plasma to an interchange dominated turbulence region in the SOL happens at the main generation location of blobs [181, 182]. These results have been obtained in low temperature experiments. With respect to transport characteristics, the CWI is a drift-wave-like instability. Both, drift wave and CWI, exhibit similarly low cross-phases and transport. The presence of a CWI in the near-SOL can possibly extent the region of drift-wave-like transport a few millimeters into the SOL in high temperature experiments.

4.7 Micro-tearing mode (MTM)

Magnetic flux surfaces with rational values of the safety factor $q_s = m/n$ are very sensitive to perturbations in the current parallel to the magnetic field. At this positions a closed magnetic flux tube which is bounded by a separatrix and isolated from the rest of space can appear. These closed magnetic flux tubes are called magnetic islands. Low mode numbers correspond to large instabilities which are all dangerous for the plasma confinement. Stellarators

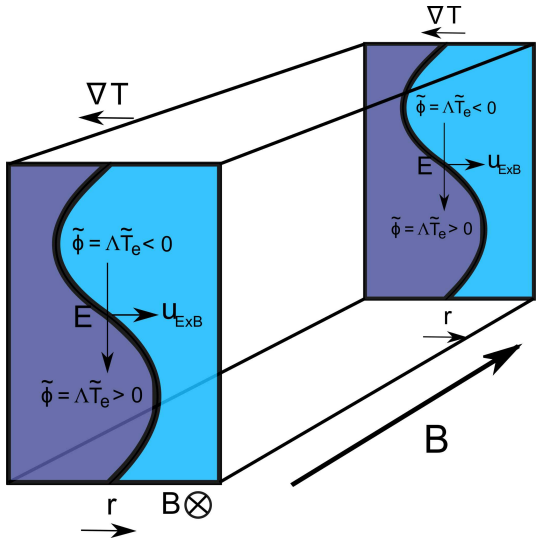

FIGURE 4.5: Dark regions indicate higher electron temperature. Electron temperature fluctuations induce in-phase potential fluctuations via the floating potential ΛT_e. The resulting $E \times B$ drift leads to a propagation in the electron diamagnetic direction.

may have a vacuum magnetic field structure that already contains natural islands. With finite resistivity the flux surfaces can reconnect and *magnetic islands* can form. Current induced magnetic islands are called *tearing modes*. Neoclassical tearing modes (NTMs) are a concern for magnetically confined fusion devices as they significantly degrade the performance and may lead to disruptions. NTMs are driven by a loss of the bootstrap current which can be triggered by various MHD instabilities (e.g. sawtheeth, fishbones, edge localized modes). As the bootstrap current is a neoclassical effect, they are called NTMs. The magnetic field lines on the inner part of the islands are connected over the X-point of the island and temperature and density can be transported directly over the island size. Therefore, the island can be seen as a flattening of the temperature profile. By means of external heating, the current inside the island leading to the instability can be compensated and such NTM can be externally controlled. Such localized heating is challenging, but possible. The interaction of micro-turbulence and NTMs is an active field of research [183, 184, 185, 186, 187, 188, 189].

The micro-tearing modes (MTMs) are the small-scale brother of the neoclassical tearing modes. With respect to the plasma edge they are in particular relevant for the high confinement regime because of the high plasma beta. In the plasma edge they are in competition with kinetic ballooning modes ((KBMs) see following Sec. 4.8). GEMR simulations of the ELM blowout found that in the electrostatic regime, $\beta \leq 10^{-4}$, the ELM blowout is dominated by the ion temperature gradient mode (ITG). For values of large $\beta \geq 8 \cdot 10^{-4}$ a micro-tearing mode grows and saturates by transferring its energy into more

violent ITG MHD turbulence [190]. Gyrokinetic simulations of inter-ELM turbulence in spherical tokamaks found MTMs close to the pedestal top where KBMs are found at the pedestal foot [191, 192]. Gyrokinetic simulations of ASDEX Upgrade and JET inter-ELM plasmas are unstable against MTMs in the pedestal [193, 194]. In the ASDEX Upgrade case the plasma is just a bit below the KBM threshold [193].

The dispersion relation can be solved given a real frequency of [195]

$$\frac{\omega}{v_{th,e}/a} = k_y \rho_e \left(\frac{a}{L_{ne}} + \frac{5}{4} \frac{a}{L_{Te}} \right), \tag{4.2}$$

with thermal electron velocity $v_{th,e}$, minor radius a, binormal wavenumber k_y, electron Larmor radius ρ_e, density fall-off length L_{ne} and electron temperature fall-off length L_{Te}. The dispersion relation is closely related to the electron diamagnetic frequency which reflects the drift-wave nature of the mode. In a conventional tokamak MTMs are of similar size as KBMs [158] but larger than ITG modes. In a spherical tokamak the MTM is closer to the ITG scale [196, 157]. The growth rate can be found in Ref. [195, 197]. The MTM is driven by the electron temperature gradient and stabilized by magnetic field line bending. Also MTMs are like ITGs and TEMs critical gradient modes.

The radial extent of the perturbation in the vector potential $\tilde{A}_\parallel$ is much wider as in the electrostatic potential $\tilde{\phi}$ [198]. The collisionality is critical for MTM as the corresponding resistivity is indispensable to the reconnection process. On the other hand, a high collisionality leads to resistive damping of the mode. The dependence of the growth rate on the collisionality is moderate and the maximum growth rate can be found at collision frequencies around $\nu_{ei}/\omega = 1$–10 [198]. MTMs are suppressed by ETG turbulence. Fine-scale $E \times B$ flows driven by the ETG turbulence strongly distort the radially localized current-sheet structures of MTMs [199].

4.8 Kinetic ballooning mode (KBM)

MHD ballooning modes get unstable when a critical value in plasma beta β_{crit}^{MHD} is exceeded. Similarly also KBMs become unstable after reaching a critical β threshold. These thresholds do not need to coincide. The critical threshold is found analytically [200] to be reduced compared to the MHD prediction:

$$\beta_{crit}^{KBM} = \frac{\beta_{crit}^{MHD}}{1 + \frac{a}{R}}. \tag{4.3}$$

Further literature on the KBM threshold can be found in Refs. [201, 202, 203, 204]. This threshold makes KBMs important within the ELM cycle. The ELM is induced by the MHD ballooning threshold. Before this happens the KBM threshold will be reached and KBM turbulence can clamp the gradient below the critical MHD threshold preventing the ELM from occurring. This

is one of the main central elements of the famous EPED model predicting the H-mode pedestal height and width of the ELM cycle [205, 206].

The KBM occurs at high plasma beta and has been called drift-Alfvénic mode in ballooning approximation in the early times where most of the analytic work has been done. The main elements of this instability are:

i) the ion temperature gradient as a source of free energy providing a relative strong ballooning envelope as fluctuations in the ion temperature cannot be compensated well by the electron dynamics (c.f. Sec. 4.4) and

ii) Alfvénic coupling of the drift mode (c.f. Sec. B.2.4).

The nomenclature *kinetic ballooning mode* is misleading and fluid [207] or gyrofluid simulations can be used to study KBM turbulence [208]. The reason why kinetic effects are very important in particular for the KBM is the closeness of the KBM and MHD ballooning threshold. As both are very close, the threshold prediction of the KBM has to be very precise which makes a kinetic treatment necessary. The dispersion relation can be found in Ref. [209], recent analytical work on the KBM can be found in Ref. [210].

The instability can be understood as follows. Let us assume the ion temperature gradient to be the strongest gradient and responsible for the energetic drive of the instability. For this reason the KBM propagates in the ion diamagnetic direction. Due to the curvature potential fluctuations are induced by the interchange effect. However, flute modes like the interchange instability are only allowed for rational surfaces. In the presence of a finite parallel wavelength the drift-wave mechanism as explained above will be present. The KBM is a drift-wave mode. The curvature is still active and will result in stronger turbulence on the low-field side of the torus. Therefore it is called a ballooning mode. As seen in Sec. B.2.4, the drift waves have two limits in the case of magnetic fluctuations. For small or large β the electrostatic ITG drift wave and the electromagnetic Alfvénic wave can be well separated. In the case of the KBM finite beta effects have to be considered, however the plasma beta is still not strong enough to neglect the electrostatic branch. For intermediate values in beta, both the electrostatic and the magnetic potential take equivalently part in the polarization at a given frequency, the roots are strongly interacting and the dispersion cannot be idealized [209]. Furthermore, the dispersion of the branch propagating in ion-diamagnetic direction is also very sensitive to the plasma β [209] making it impossible to characterize the KBM by dispersion. Therefore the KBM is identified by its main features: the propagation in the ion diamagnetic direction and the β threshold beyond which strong growth takes place.

Chapter 5

Plasma turbulence models

In the following we turn to plasma edge turbulence models. The complexity of the description will increase from two-dimensional electrostatic drift-wave turbulence in plane (so-called slab) geometry (Sec. 5.1), over three-dimensional electromagnetic fluid turbulence in a curvilinear toroidal geometry with sheared magnetic field lines (Sec. 5.2) to three-dimensional electromagnetic gyrofluid turbulence with self-consistent equilibrium (Sec. 5.3). Reviews on theory and experiment of drift-wave turbulence can be found in Refs. [211, 212], respectively.

5.1 Hasegawa-Wakatani

The most basic model for plasma turbulence is the so-called *Hasegawa-Wakatani* model [125, 213] for drift-wave turbulence in a homogenous magnetic field at finite collisionality. It describes the stationary model for potential (hence velocity) and density fluctuations. To simplify the system as much as possible, also the electron temperature is assumed to be constant and much higher than the ion temperature, which is assumed to be small. Even though the Hasegawa-Wakatani system is very simplified, it can describe the nonlinear dynamics quite well.

The *Hasegawa-Wakatani equations in 3D* are two coupled equations, one for the evolution of density perturbations

$$\partial_t \tilde{n} + \{\tilde{\phi}, \tilde{n}\} + \kappa_n \partial_y \tilde{\phi} = \frac{1}{\nu} \nabla_\parallel^2 (\tilde{n} - \tilde{\phi}) \tag{5.1}$$

and one equation for the vorticity fluctuations $\tilde{\Omega} = \nabla_\perp \tilde{\phi}$

$$\partial_t \tilde{\Omega} + \{\tilde{\phi}, \tilde{\Omega}\} = \frac{1}{\nu} \nabla_\parallel^2 (\tilde{n} - \tilde{\phi}). \tag{5.2}$$

Their derivation can be found in the appendix C.1. Density and potential fluctuations are coupled via the collisionality with each other. The nonlinearity is represented by the Poisson brackets $\{A, B\} = \partial_x A \partial_y B - \partial_x B \partial_y A$. $\{\tilde{n}, \tilde{\phi}\}$ is the nonlinearity due to the $\mathbf{E} \times \mathbf{B}$ *-drift* in the continuity equation, $\{\tilde{\Omega}, \tilde{\phi}\}$

is the nonlinearity equivalent to $\tilde{\mathbf{u}} \cdot \nabla \tilde{\mathbf{u}}$ in the Navier-Stokes equation. As seen by Eq. (A.15) this nonlinearity corresponds to a polarization drift and current and, therefore, is called *polarization nonlinearity*. One important aspect of magnetized plasmas is that the dominant nonlinearities and turbulence are restricted to the plane perpendicular to the magnetic field. This is similar to two-dimensional fluid turbulence. In contrast to fluid turbulence, two nonlinearities are coupled in a magnetized plasma.

The finite conductivity related to ν results in a delayed electron response in parallel direction. This leads to a deviation from the Boltzmann response (normalized $\tilde{n} \sim \tilde{\phi}$). Without such a deviation, the fluctuations do not have any access to the free energy reservoir provided by the background gradient which are converted by the $\mathbf{E} \times \mathbf{B}$-velocity field in density fluctuations. These fluctuations lead to transport and flatten the density gradient. At high collisionality the coupling between potential and density fluctuations is weak and the equations can develop more or less independent of each other. The system behaves as a nearly neutral fluid in two dimensions. This is called the *hydrodynamic limit*. In the case of a small collisonality, the coupling between density and potential fluctuations is strong. The amplitude and phase of density and potential perturbations are nearly the same which is called the *adiabatic limit*.

The parallel dynamics can be incorporated with a characteristic scaling quantity defined as

$$C = 1/(L_\parallel^2 \nu) \tag{5.3}$$

with a typical parallel wavelength $\nabla_\parallel^2 \approx -(1/L_\parallel)^2$. It follows

$$\partial_t \tilde{n} + \{\tilde{\phi}, \tilde{n}\} + \kappa_n \partial_y \tilde{\phi} = C(\tilde{\phi} - \tilde{n}) \tag{5.4}$$

$$\partial_t \tilde{\Omega} + \{\tilde{\phi}, \tilde{\Omega}\} = C(\tilde{\phi} - \tilde{n}). \tag{5.5}$$

These are the *Hasegawa-Wakatani equations in 2D*.

5.1.1 Hasegawa-Mima turbulence

The Hasegawa-Mima model is a simplification of the Hasegawa-Wakatani model. The Hasegawa-Mima equation [214] offers the possibility to study the impact of the nonlinearity without any linear growth. This can be realized with the assumption of an ideal Boltzmann response $\tilde{n} \sim \tilde{\phi}$ for adiabatic electrons $C \to \infty$. Subtracting (5.5) from (5.4) yields

$$\partial_t(\tilde{\phi} - \tilde{\Omega}) + \kappa_n \partial_y \tilde{\phi} = \{\tilde{\phi}, \tilde{\Omega}\}. \tag{5.6}$$

This model is identical to the Charney model [215] describing Rossby waves in geophysical fluids (in the atmosphere). For this reason, the equation is called *Charney-Hasegawa-Mima equation*. Hence drift waves and Rossby waves exhibit a very similar dispersion relation [125].

5.1.2 Cascades in drift-wave turbulence – self-sustainment

The direction of the energy and enstrophy transfer of the Hasegawa-Wakatani turbulence has been shown analytically by Gang et al. [216] to be in the same direction as in two-dimensional fluid turbulence. Therefore, as in quasi two-dimensional turbulence kinetic energy is transferred to larger scales. With

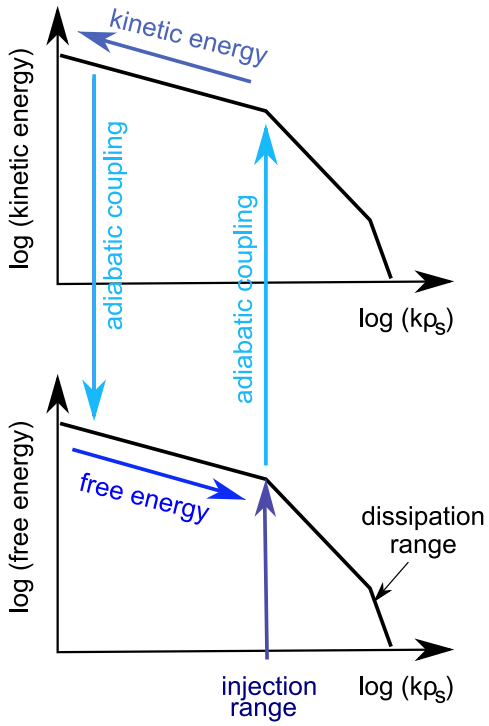

FIGURE 5.1: Energy injected into the system by the density background gradient induces fluctuations in the density. Via adiabatic coupling potential fluctuations are driven. Due to the inverse energy cascade larger scales are excited. Once potential fluctuations are excited at larger scales, at these scales transport is driven and fluctuations can tap energy from the background gradient even if they would have a negative growth rate. At larger scales the energy can be recycled and only a small amount has to be transferred to small scales, where it is dissipated.

regard to the inverse energy transfer in 2D turbulence, the question arises what happens to the energy at the large scales, where it cannot be dissipated by viscosity. At large scales friction and dissipation are fairly irrelevant and the energy could indefinitely accumulate. This is called the *infrared catastrophe*. For the Hasegawa-Wakatani turbulence this is solved by the interplay of the two nonlinearities. The one due to the polarization nonlinearity acts like an inverse energy cascade and transfers kinetic energy to larger scales. The nonlinearity due to the $E \times B$-drift acts in the different direction: it transfers free energy from large to small scales. This prevents the infrared catastrophe. For drift-wave turbulence both cascades are present. These are shown in Fig. 5.1.

One main consequence of the nonlinear energy transfer with a direct and an inverse energy cascade in drift-wave turbulence is the mechanism of self-sustainment of organized states of turbulence [217, 218, 10]. For simplicity we will consider only three scales: mid-scale fluctuations in the spectral region of maximum energy fed by the gradients, large-scale (low wavenumber) fluctuations and small-scale fluctuations. The mid-scale fluctuations are unstable, they tap energy from the background gradient. The large-scale and small-scale fluctuations may have a negative growth rate. Due to adiabatic coupling potential fluctuations at the mid-scale are induced. The inverse energy cascade generates fluctuations in the potential at large scale. Due to adiabatic coupling also density fluctuations at large scales are excited. These will induce transport, which leads to energy transfer from the background gradient to fluctuations at the larger scales. The energy transfer by adiabatic coupling together with this additional energy transfer from the gradient can compensate the negative growth rate. Furthermore, by this mechanism the energy can be recycled at mid to large scales without significant losses at small scales.

5.1.3 Zonal flow self-amplification in drift-wave turbulence

From the discussion on the Reynolds stress in Sec. 3.6.1 it can be implied that an initial tilt of turbulent structures or an initial shear flow will indefinitely self-amplify. This is not the case as the zonal flow does not tilt the vortices directly. Including a background shear in Eq. (5.5) yields

$$\partial_t \tilde{\Omega} + \{\tilde{\phi}, \tilde{\Omega}\} + \{\langle\phi\rangle, \tilde{\Omega}\} + \{\tilde{\phi}, \langle\Omega\rangle\} = C(\tilde{\phi} - \tilde{n}). \tag{5.7}$$

The third term $\{\langle\phi\rangle, \tilde{\Omega}\} = \partial_x\langle\phi\rangle\partial_y\tilde{\Omega} = \langle u_y\rangle\partial_y\tilde{\Omega}$ as $\partial_y\langle\phi\rangle = 0$ vanishes since zonal components do not vary in y-direction. Similar, the fourth term is $-\partial_y\tilde{\phi}\partial_x\langle\Omega\rangle$. This term can be also written as

$$-\partial_y\tilde{\phi}\partial_x\langle\Omega\rangle = -\partial_x(\langle\Omega\rangle\partial_y\tilde{\phi}) + (\partial_x\langle u_y\rangle)\partial_{xy}\tilde{\phi}.$$

As $(\partial_x\langle u_y\rangle)\partial_{xy}\tilde{\phi} = \partial_x(\langle u_y\rangle\partial_{xy}\tilde{\phi}) - \langle u_y\rangle\partial_y\partial_x^2\tilde{\phi}$ and together with $\Omega = \partial_x^2\phi$

$$-\partial_y\tilde{\phi}\partial_x\langle\Omega\rangle = \partial_x(\langle u_y\rangle\partial_{xy}\tilde{\phi} - \langle\Omega\rangle\partial_y\tilde{\phi}) - \langle u_y\rangle\partial_y\tilde{\Omega}.$$

The last term balances the third term of (5.7). The remaining term is under the ∂_x operator which is equivalent to a divergence. This means that the vorticity is globally neither generated nor dissipated as expected for two-dimensional turbulence. Therefore, in the hydrodynamic limit the zonal flow cannot result in indefinite self-amplification. The vorticity is radially redistributed, which will be discussed in detail in Sec. 8.3. However, for high adiabaticity the coupling to the density fluctuation can lead to self-amplification of the zonal flow. We include the zonal flow in the density equation (5.4)

$$\partial_t\tilde{n} + \{\tilde{\phi}, \tilde{n}\} + \langle u_y\rangle\partial_y\tilde{n} + \kappa_n\partial_y\tilde{\phi} = C(\tilde{\phi} - \tilde{n}). \tag{5.8}$$

By the third term, the zonal flow can tilt turbulent structures in the density. This tilt can be transmitted to the vorticity field by adiabatic coupling $C(\tilde{\phi}-\tilde{n})$ (terms on the r.h.s. of Eqs. (5.7) and (5.8)). Therefore, in the adiabatic limit strong self-amplification can be expected.

The collisional dependence of the energy transfer from drift-wave turbulence into the zonal flow has been investigated in the stellarator TJ-K. It has been found [39] that the coupling of the tilt of density and potential structures measured by the pseudo Reynolds stress $-\langle\partial_x\tilde{n}\partial_y\tilde{n}\rangle$ and Reynolds stress $-\langle\partial_x\tilde{\phi}\partial_y\tilde{\phi}\rangle$ decreases with collisonality. As a consequence, the nonlinear energy transfer into the zonal flow decreases. Therefore, zonal flows favor the adiabatic regime and a high collisionality hampers self-amplification.

5.1.4 Intermittency in drift-wave turbulence

Drift-wave turbulence is close to quasi-two-dimensional turbulence which is discussed in Sec. 3.5.3. Two-dimensional turbulence is non-intermittent with respect to the flow, but shows intermittency in the vorticity. This has been shown by simulations of Hasegawa-Wakatani turbulence [219, 220] and experiments in the stellarator TJ-K [220]. Potential fluctuations are in general self-similar. In contrast to fluid turbulence, in drift-wave turbulence, additionally to the potential and/or vorticity also the density is an active quantity. By increasing the collisionality the density shows no intermittency in the adiabatic regime, whereas in the hydrodynamic regime, where density and potential decouple and the density behaves like a passive scalar, the intermittency level of the density is similar to that of the vorticity [219, 220].

5.2 Drift-Alfvén (DALF) model

The DALF model [221, 222, 223] describes drift-Alfvén turbulence in toroidal geometry and, therefore, also includes interchange and MHD instabilities. Most basic mechanisms of plasma turbulence in toroidal geometry relevant for the plasma edge can be understood by the DALF model. The DALF model will be used later to study analytically the sideband balance during the L-H transition (see Sec. 10.2.2) and different regimes of plasma filament propagation (Sec. 12.1).

It consists of evolution equations for the the vorticity $\tilde{\Omega}$

$$\left(\frac{\partial}{\partial t}+\tilde{u}_E\cdot\nabla\right)\tilde{\Omega}=B\nabla_\parallel\frac{\tilde{J}_\parallel}{B}-(1+\tau_i)\mathcal{K}(\tilde{p_e}), \tag{5.9}$$

the electron pressure $\tilde{p}_e$

$$\left(\frac{\partial}{\partial t}+\tilde{u}_E\cdot\nabla\right)\tilde{p}_e+\tilde{u}_E\nabla p_e=B\nabla_\parallel\frac{\tilde{J}_\parallel-\tilde{u}_\parallel}{B}+\mathcal{K}(\tilde{\phi}-\tilde{p_e}), \tag{5.10}$$

the parallel current $\tilde{J}_\parallel$

$$\hat{\beta}\left(\frac{\partial}{\partial t}+\tilde{u}_E\cdot\nabla\right)\tilde{A}_\parallel+\mu\left(\frac{\partial}{\partial t}+\tilde{u}_E\cdot\nabla\right)\tilde{J}_\parallel=\nabla_\parallel(p_e+\tilde{p}_e-\tilde{\phi})-C\tilde{J}_\parallel. \quad (5.11)$$

and the ion velocity

$$\hat{\epsilon}\left(\frac{\partial}{\partial t}+\tilde{u}_E\cdot\nabla\right)\tilde{u}_\parallel=-(1+\tau_i)\nabla_\parallel(p_e+\tilde{p}_e)+\mu_\parallel\nabla_\parallel^2\tilde{u}_\parallel. \quad (5.12)$$

The equations are completed by Ampere's law

$$-\nabla_\perp^2\tilde{A}_\parallel=\tilde{J}_\parallel \quad (5.13)$$

and polarization

$$\frac{1}{B^2}\nabla_\perp^2\tilde{W}=\tilde{\Omega}. \quad (5.14)$$

Times are normalized to $L_\perp/c_s$, perpendicular spatial scales to ρ_s and parallel scales to q_sR with safety factor q_s and major radius R. Here $L_\perp$ is the relevant gradient scale length, which is in most cases $L_\perp=-T_e/\partial_xT_e$. The normalization is done by the ion sound speed and ρ_s. The the ion sound speed is given by $c_s=\sqrt{T_e/m_i}$ and it should be noted that the ion sound speed used for normalization does not include the contribution of the ions (their contribution is accounted for by τ_i as explained later). The ratio between ion and electron temperature is given by $\tau_i=T_i/T_e$. The hybrid Larmor radius is given by $\rho_s=\sqrt{T_em_i}/eB$ with electron temperature T_e, ion mass m_i, magnetic field strength B and elementary charge e. $\mathrm{d}/\mathrm{d}t=\partial/\partial t+u_E\cdot\nabla$ is the advective derivative with $E\times B$ velocity u_E. The main fluctuating quantities are the electrostatic potential $\tilde{\phi}=e\phi/T_{e0}$ normalized to the background mean electron temperature T_{e0} and the electron pressure fluctuations normalized to a characteristic mean background pressure value p_{e0}. The fluctuations are additionally normalized and given in units of $\rho_s/L_\perp$ which is the smallness parameter (see Sec. B.2.1). This is also the reason why times are normalized by $L_\perp/c_s$ and not by ρ_s/c_s. Due to finite ion temperatures, the stream function is not the plasma potential as in the Hasegawa-Wakatani model (see Sec. 5.1) and the *total ion flow stream function* given by $\tilde{W}=\tilde{\phi}+\tau_i\tilde{p}_e$ determines the vorticity $\tilde{\Omega}=(1/B^2)\nabla_\perp^2\tilde{W}$. The difference between parallel ion flow $\tilde{u}_\parallel$ and current $\tilde{J}_\parallel$ defines the parallel electron flow $\tilde{v}_\parallel=\tilde{u}_\parallel-\tilde{J}_\parallel$. For the pressure we consider the background together with the disturbance and drop the tilde symbol. In some cases we will investigate the total pressure $p=p_e+p_i$.

The DALF model includes the Hasegawa-Wakatani model (Eqs. (5.1) and (5.2)) as a subset. The nonlinearities $\{\tilde{\Omega},\tilde{\phi}\}$ and $\{\tilde{n},\tilde{\phi}\}$ are included in the operator $\mathrm{d}/\mathrm{d}t$ of Eqs. (5.9) and (5.10). As p denotes the total pressure in DALF also $\kappa_n\partial_y\tilde{\phi}$ is included in the $\mathrm{d}/\mathrm{d}t$ operator in Eq. (5.9). The adiabatic coupling of pressure (5.10) and potential (5.9) is done by a coupling of both of these equations to Eq. (5.11). These parts of the DALF model describe drift-wave turbulence with all features described in Sec. 5.1. Also MHD is

included as a subset of the DALF equations. For this reason also interchange and Alfvén wave dynamics are included in the DALF framework.

The coordinates used here are (x, y, s), where s is in direction of the unperturbed magnetic field line and x and y are radial and binormal, respectively, locally perpendicular to the unperturbed magnetic field line. A shifted metric coordinate system is used with a different y coordinate at each location in s. It is important to note that in a tokamak, the direction parallel to the magnetic field is not toroidal and perpendicular is not poloidal. In a flux tube coordinate system as in DALF and later in GEM (see Sec. 5.3) the parallel coordinate s is represented by the poloidal angle θ defined in $[-\pi, \pi]$ with its origin at the outer midplane. This is called a *ballooning angle*. The parallel wavenumber is given by $k_\parallel = \frac{m - n q_s}{q_s R}$ with poloidal mode number m and toroidal mode number n. The local perpendicular or binormal wavenumber in drift direction is given by the toroidal wavenumber $k_y = \frac{n q_s}{r}$ with the radius of the flux tube r. The local shift, which is different at each radial position, allows to take the effect of magnetic shear into account. The curvature operator is given by

$$\mathcal{K} = \omega_B(\sin s\partial_x + \cos s\partial_y) \tag{5.15}$$

with $\omega_B = 2L_\perp/R$ and the curvature radius R, which is set to the major radius. The first contribution to the curvature is the geodesic curvature, the second the normal curvature. The flux surface (zonal) average is given by $\langle f \rangle = \oint \oint dsdyf$. The normalized magnetic field strength is $B = 1$ with the component parallel to the field line $b_s = 1$. The parallel derivative includes magnetic fluctuations of the flux-surface

$$\nabla_\parallel = b_s \frac{\partial}{\partial s} + \tilde{b}_x \frac{\partial}{\partial x} + \tilde{b}_y \frac{\partial}{\partial y}. \tag{5.16}$$

They are calculated as $\tilde{b}_x = \hat{\beta} \frac{\partial \tilde{A}_\parallel}{\partial y}$ and $\tilde{b}_y = -\hat{\beta} \frac{\partial \tilde{A}_\parallel}{\partial x}$. These magnetic fluctuations can lead to additional electromagnetic transport. Terms including these magnetic fluctuations are called *magnetic flutter* terms.

Different regimes are set by the square of the parallel/perpendicular scale ratio $\hat{\epsilon} = (q_s R/L_\perp)^2$, the normalized plasma beta given by $\hat{\beta} = (4\pi n T_e/B^2)\hat{\epsilon}$ and the normalized mass ratio $\hat{\mu} = (m_e/m_i)\hat{\epsilon}$, which determine the relative transit Alfvén and electron thermal frequencies, respectively. The parallel current is dissipated by collisions represented by $C = \hat{\mu}(0.51\nu_e/c_s L_\perp)$ with collision frequency (given in SI units)

$$\nu_e = \frac{Z_{eff} e^4 n_e \ln \Lambda}{6\sqrt{2}\pi^{3/2}\epsilon_0^2 \sqrt{m_e}(k_B T_e)^{3/2}},$$

with Coulomb logarithm $\ln \Lambda$. Details on the collision frequencies can be found in Ref. [224]. Flow damping is controlled by an artificial neoclassical viscosity parameter $\mu_\parallel$.

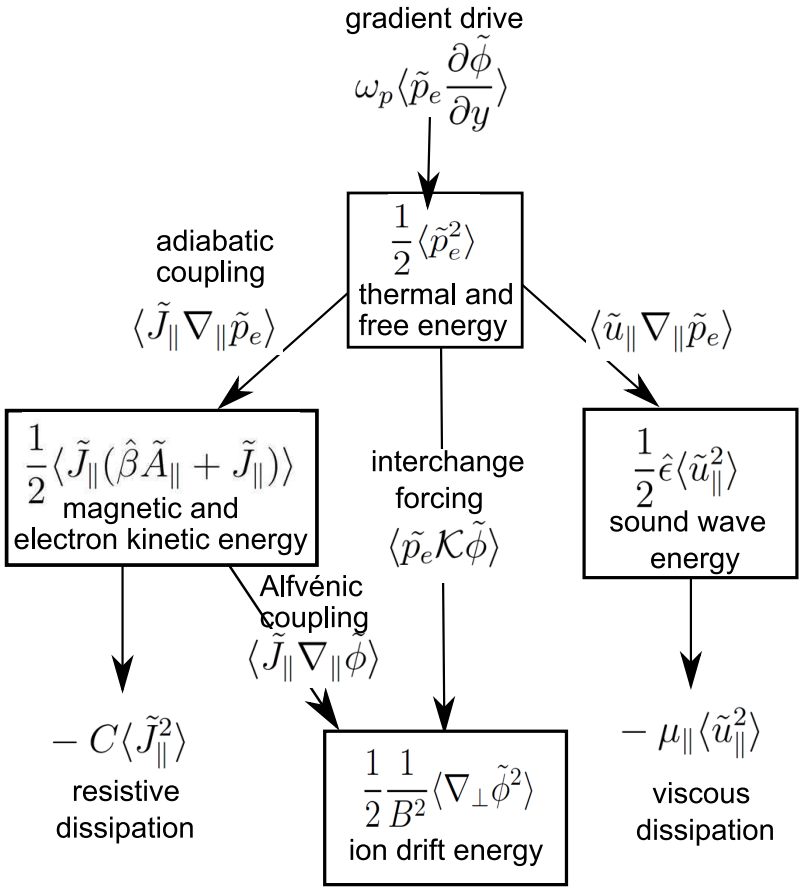

FIGURE 5.2: Flow of energy flow between the different fields in the DALF model.

5.2.1 Energetics in DALF

A main difference between fluid and plasma turbulence is the appearance of different fields for a magnetized plasma, where fluid turbulence can be understood by only the velocity field. All fields exhibit a nonlinearity by the advective term $d/dt = \partial/\partial t + u\cdot\nabla$ but the fields can also interact with each other. We have already seen for the case of Hasegawa-Wakatani turbulence that the coupling between density and vorticity field provides an additional physical mechanism. Here this is discussed for the more complete electromagnetic DALF model.

The evolution of the different energies is given in Ref. [223]. The ion drift energy (or $E\times B$ turbulent energy) is determined by

$$\frac{\partial}{\partial t}\frac{1}{2}\frac{1}{B^2}\langle\nabla_\perp\tilde{\phi}^2\rangle = \langle\tilde{J}_\parallel\nabla_\parallel\tilde{\phi}\rangle - (1+\tau_i)\langle\tilde{p}_e\mathcal{K}\tilde{\phi}\rangle, \tag{5.17}$$

the thermal and free energy by

$$\frac{\partial}{\partial t}\frac{1}{2}\langle\tilde{p}_e^2\rangle = -\langle\tilde{J}_\parallel\nabla_\parallel\tilde{p}_e\rangle + \langle\tilde{u}_\parallel\nabla_\parallel\tilde{p}_e\rangle + \langle\tilde{p}_e\mathcal{K}\tilde{\phi}\rangle + \omega_p\langle\tilde{p}_e\frac{\partial\tilde{\phi}}{\partial y}\rangle \tag{5.18}$$

with $\omega_p = L_\perp/L_p$ the magnetic and electron kinetic energy follows

$$\frac{\partial}{\partial t}\frac{1}{2}\langle \tilde{J}_\parallel(\hat{\beta}\tilde{A}_\parallel + \tilde{J}_\parallel)\rangle = +\langle \tilde{J}_\parallel \nabla_\parallel \tilde{p}_e\rangle - \langle \tilde{J}_\parallel \nabla_\parallel \tilde{\phi}\rangle - C\langle \tilde{J}_\parallel^2\rangle. \tag{5.19}$$

The sound wave energy (or parallel ion kinetic energy) reads

$$\frac{\partial}{\partial t}\frac{1}{2}\hat{\epsilon}\langle \tilde{u}_\parallel^2\rangle = -(1+\tau_i)\langle \tilde{u}_\parallel \nabla_\parallel \tilde{p}_e\rangle + \omega_p\hat{\beta}\langle \tilde{u}_\parallel \frac{\partial \tilde{A}}{\partial y}\rangle - \mu_\parallel \langle \tilde{u}_\parallel^2\rangle. \tag{5.20}$$

The energy flow across the different fields is illustrated in Fig. 5.2 The energy is injected by the pressure gradient into the system by the last term of (5.18). There are two pathways how the energy can be passed to the $E \times B$ turbulence. There is a direct transfer of energy by $\langle \tilde{p_e}\mathcal{K}\tilde{\phi}\rangle$. This term appears in both equations (5.17) and (5.18) but with a different sign. This effect can be attributed to the curvature. To make a significant contribution the cross-phase between potential and pressure fluctuations has to be close to $\pi/4$. The term is called *interchange forcing*. The other possibility to couple the free energy of the background gradient into the ion drift energy is by coupling through the parallel dynamics $\tilde{p}_e \longleftrightarrow \tilde{J}_\parallel \longleftrightarrow \tilde{\phi}$. The relevant transfer terms are $\langle \tilde{J}_\parallel \nabla_\parallel \tilde{p}_e\rangle$ and $\langle \tilde{J}_\parallel \nabla_\parallel \tilde{\phi}\rangle$. This coupling resembles the drift-wave mechanism. The coupling between pressure and parallel current perturbations $\langle \tilde{J}_\parallel \nabla_\parallel \tilde{p}_e\rangle$ is called *adiabatic coupling*. The coupling between potential and parallel current perturbations $\langle \tilde{J}_\parallel \nabla_\parallel \tilde{\phi}\rangle$ is called *Alfvénic coupling*.

5.2.2 Regimes of edge turbulence

Edge turbulence can be classified following Scott [166, 207]. Turbulence is ITG dominated, if the ion temperature fluctuations are the strongest state variable which is also the most strongly ballooned one, hence $\tilde{p}_i > \tilde{p}_e$. ITG turbulence exhibits a higher ion than electron heat flux. Turbulence is drift-wave-like if all state variables are similar $\tilde{\phi} \sim \tilde{p}_e \sim \tilde{p}_i$ with similar spectrum and similar degree of ballooning. In the case of ballooning-like turbulence, potential fluctuations $\tilde{\phi}$ are the largest ones and also the most strongly ballooned. The change around the poloidal direction is also part of the parallel derivative, hence strong ballooning needs strong parallel gradients. This becomes a MHD regime with $\nabla_\parallel \tilde{\phi} \gg \nabla_\parallel \tilde{p}_e$, $\nabla_\perp \tilde{\phi} \gg \nabla_\perp \tilde{p}_e$. In MHD often $E_\parallel = \nabla_\parallel \phi - \partial_t A_\parallel = 0$ is assumed, where $\nabla_\parallel \phi$ balances $\partial_t A_\parallel$. Hence, $\nabla_\parallel \phi \gg 1$ is not in contradiction to $E_\parallel = 0$. The transition from drift-wave turbulence to resistive ballooning takes place at $C\omega_B \approx 1$. Note that including finite ion temperature effects, this threshold reduces to $C\omega_B \approx 1/(1+\tau_i)$ [159]. There is another parameter determining the transition from resistive ballooning turbulence to drift-wave turbulence given by the ratio of the typical scales of drift waves and the resistive ballooning mode called α_d [225, 226, 227], which can be related to the L-H transition [226, 228] and the density limit [226, 229]. The transition to ideal ballooning happens at $\alpha_{MHD} = \hat{\beta}\omega_B\omega_p \sim 1$. Here $\omega_p = L_{pe}/L_\perp$ is the normalized electron

pressure gradient, where $L_\perp = \min(L_n, L_{Te}, L_{T_i})$. Where the transition to ideal ballooning is rather sharp, the transition to resistive ballooning is rather gradual.

Electromagnetic turbulence changes with plasma beta. At low plasma beta the plasma edge turbulence is electrostatic and ITG dominated. At high plasma beta ITG turbulence is suppressed and the plasma edge turbulence is KBM dominated [207]. In between a region of suppressed ion heat transport and enhanced electromagnetic (induced by magnetic flutter) electron heat transport can be observed which can be related to MTM dominated edge turbulence [207]. The region where the particle transport, the ion heat transport and electrostatic electron heat transport strongly decrease with plasma beta and the electromagnetic heat transport strongly increases can be attributed to MTM turbulence [207].

5.2.3 Dynamics of zonal flows, geodesic acoustic modes and Pfirsch-Schlüter currents

Zonal flows have been introduced in Sec. 3.6. Now we will take a closer look at zonal flows in a toroidal geometry with twisted magnetic field lines like in a tokamak. How different modes are connected in toroidal geometry is illustrated in Fig. 5.3. The zonal flow is a potential perturbation which is homogenous on a flux surface exhibiting a poloidal mode number $m = 0$ and toroidal mode number $n = 0$. It is generated by the Reynolds stress (see Sec. 3.6.1 for details). The $E \times B$ flow excited by such a perturbation is not homogenous on a flux surface as $u_{E\times B} \sim 1/B$ and therefore the flow is faster on the low-field side radially outwards and slower on the high-field side closer to the center of the tokamak. Such a flow results in a compression or expansion of a passively advected quantity as the density, temperature or pressure, on the top and vise versa on the bottom of the tokamak. An up-down asymmetric pressure perturbation is the result. This up-down asymmetric pressure perturbation would like to relax, which leads to a characteristic oscillation between the zonal potential perturbation and the up-down asymmetric pressure perturbation which is called the geodesic acoustic mode (GAM).

As the bottom and the top are connected by the twisted magnetic field lines, the plasma can flow along the parallel direction to compensate the establishing parallel gradients. As the electrons react faster on these parallel gradients, they precede the parallel ion flow, which leads to a current. This current is called the Pfirsch-Schlüter current and it also appears in equilibrium without any zonal flow to compensate the electric field generated by interchange forcing. The Pfirsch-Schlüter current is in-out asymmetric. As a current, the Pfirsch-Schlüter current induces magnetic field perturbations.

A detailed analysis of the energy transfer system between turbulence, zonal modes and further sidebands in an axisymmetrical configuration is presented in Ref. [223] and will be summarized in the following. The description is based on the DALF model explained above. s is the ballooning angle [223]. As s is

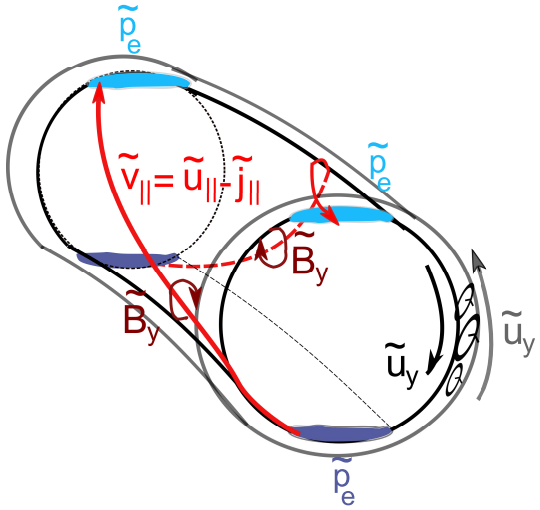

FIGURE 5.3: Artist view of the Pfirsch-Schlüter current sideband balance.

defined to be zero at the outer midplane $\langle \sin s \rangle$ gives the *up-down asymmetric* components to the flux surface average and $\langle \cos s \rangle$ the *in-out asymmetric* component. Sidebands are modes with finite parallel wavevector $k_\parallel \neq 0$ but vanishing binormal wavevector $k_y = 0$ (corresponding to $n = 0$, $m \neq 0$). The sidebands are obtained by multiplying the evolution equations for current, flow, pressure and vorticity by the asymmetry function $\sin s$ or $\cos s$ first and by taking the zonal average $\langle \cdot \rangle$, subsequently. In this way the resulting modes exhibit a parallel wavenumber of $k_\parallel = \pm \frac{1}{qR}$ with poloidal and toroidal mode numbers of one and zero, respectively.

The zonal pressure evolution is

$$\frac{\partial}{\partial t}\langle p_e \rangle = -\frac{\partial}{\partial x}\langle \tilde{v}_{Ex} p_e + \tilde{b}_x \tilde{v}_\parallel \rangle - \omega_B \langle (p - \tilde{W}) \sin s \rangle. \tag{5.21}$$

Through the gradient drive, energy is transferred from the background pressure p_0 to the turbulence $\tilde{p}$. This is done by the coupling between the second term on the left hand side of Eq. (5.10) with the first term on the right hand side of Eq. (5.21). Due to adiabatic coupling (first terms on the right hand side of Eqs. (5.9) and (5.10)) fluctuating energy is transferred to vorticity fluctuations $\tilde{\Omega}$. The zonal vorticity is obtained by taking the zonal average of Eq. (5.9)

$$\frac{\partial}{\partial t}\langle \Omega \rangle = -\frac{\partial^2}{\partial x^2}\langle \tilde{v}_{Ex} \tilde{u}_y \rangle + \frac{1}{\hat{\beta}} \frac{\partial^2}{\partial x^2}\langle \tilde{b}_x \tilde{b}_y \rangle - \omega_B \frac{\partial}{\partial x}\langle p \sin s \rangle \tag{5.22}$$

giving the zonal flow $\langle \tilde{u}_y \rangle = \langle \frac{\partial \tilde{W}}{\partial x} \rangle$

$$\frac{\partial}{\partial t}\langle \tilde{u}_y \rangle = -\frac{\partial}{\partial x}\langle \tilde{v}_{Ex} \tilde{u}_y \rangle + \frac{1}{\hat{\beta}} \frac{\partial}{\partial x}\langle \tilde{b}_x \tilde{b}_y \rangle - \omega_B \langle p \sin s \rangle. \tag{5.23}$$

Note that, the zonal flow includes the ion diamagnetic contribution and $\langle \frac{\partial \tilde{u}_y}{\partial x} \rangle = \langle \tilde{\Omega} \rangle$. The turbulent $\tilde{\Omega}$ drives the zonal vorticity $\langle \Omega \rangle = \langle \tilde{\Omega} \rangle$ via the Reynolds

stress $\frac{\partial}{\partial x}\langle\tilde{v}_{Ex}\tilde{u}_y\rangle$ (Eq. (5.23)). The zonal vorticity determines the zonal flow. The second term is the *Maxwell stress*. The zonal flow is saturated by driving an up-down asymmetric pressure sideband $\langle\tilde{p}\sin s\rangle$. This results from the geodesic curvature $\omega_B \sin s$ and is called the *geodesic transfer effect* [223, 230, 231]. The evolution of this pressure sideband is

$$\begin{aligned}\frac{\partial}{\partial t}\langle p_e \sin s\rangle = & -\frac{\partial}{\partial x}\langle(\tilde{v}_{Ex}p_e + \tilde{b}_x\tilde{v}_\parallel)\sin s\rangle + \langle v_\parallel \cos s\rangle \\ & -\frac{\omega_B}{2}\left\langle\left(\frac{\partial p}{\partial x} - \tilde{u}_y\right)(1-\cos 2s)\right\rangle. \end{aligned} \tag{5.24}$$

The coupling to the zonal flow is accomplished by the last term. The oscillation between the zonal flow $\langle\tilde{u}_y\rangle$ and this pressure sideband $\langle p_e \sin s\rangle$ is the *geodesic acoustic mode*. Neglecting all other contributions except $\frac{\partial}{\partial t}\langle p_e \sin s\rangle = \frac{1}{2}\omega_B\langle\tilde{u}_y\rangle$ and also just considering the coupling to this pressure sideband for the zonal flow equation (5.23) $\frac{\partial}{\partial t}\langle\tilde{u}_y\rangle = -(1+\tau_i)\omega_B\langle p_e \sin s\rangle$ a natural frequency of $\omega_B\sqrt{(1+\tau_i)/2}$ or in physical units $f_{GAM} = \sqrt{2}c_{si}/2\pi R$ with $c_{si}^2 = (1+\tau_i)T_e/m_i$ can be derived which is the GAM frequency. This pressure sideband can also be driven by an up-down asymmetric transport as seen in the first term on the right hand side of Eq. (5.24). Most damping occurs due to $\langle\tilde{v}_\parallel \cos s\rangle$ which is connected to the flow and current by $\langle\tilde{v}_\parallel \cos s\rangle = \langle\tilde{u}_\parallel \cos s\rangle - \langle\tilde{J}_\parallel \cos s\rangle$. Via adiabatic coupling the energy is transferred from the pressure sideband to perturbations in the *Pfirsch-Schlüter current* $\langle\tilde{J}_\parallel \cos s\rangle$ where the energy is dissipated by the collisionality

$$\begin{aligned}\frac{\partial}{\partial t}\langle(\hat{\beta}\tilde{A}_\parallel + \hat{\mu}\tilde{J}_\parallel)\cos s\rangle = & -\frac{\partial}{\partial x}\langle\tilde{v}_{Ex}\hat{\mu}\tilde{J}_\parallel \cos s\rangle \\ & +\langle\tilde{b}_x(\frac{\partial p}{\partial x} - \frac{\partial\tilde{\phi}}{\partial x})\cos s\rangle \\ & +\langle(p-\tilde{W})\sin s\rangle \\ & -C\langle\tilde{J}_\parallel \cos s\rangle. \end{aligned} \tag{5.25}$$

As shown in a previous numerical investigation [223] the most important sidebands related to zonal flow physics are the up-down asymmetric pressure sideband $\langle p \sin s\rangle$ taking part in the geodesic acoustic oscillation (GAM), the vorticity sideband $\langle\tilde{\Omega}\sin s\rangle$ (directly linked to the sidebands of the ion stream function $\langle\tilde{W}\sin s\rangle$ and flow $\langle\tilde{u}_y \sin s\rangle$) as well as the Pfirsch-Schlüter current $\langle\tilde{J}_\parallel \cos s\rangle$. The Pfirsch-Schlüter sound sideband $\langle\tilde{u}_\parallel \cos s\rangle$ plays a minor role.

5.3 Gyrofluid Electro Magnetic (GEM) model

The results presented in the Chap. 9 and Sec. 12.2.3 are based on simulations carried out with the code GEMR. The GEMR code is based on the GEM model described in this section. As the scales of the perpendicular dynamics of tokamak edge turbulence are of the order of the ion gyroradius, the turbulence model should take the effects of a finite ion Larmor radius (FLR) into

account. The gyrofluid electromagnetic model (GEM) is a six field model including the density n_z, the parallel velocity $u_{z\parallel}$, the parallel and perpendicular temperatures $T_{z\parallel}$ and $T_{z\perp}$ and the parallel and perpendicular heat fluxes $q_{z\parallel}$ and $q_{z\perp}$, where $z \in \{i, e\}$ denotes the species. It is derived by taking the moments over the gyrokinetic equations. This kind of model is called gyrofluid model. Electrostatic gyrofluid equations have been derived by Dorland [232] and extended to toroidal geometry by Beer [233]. Nonadiabatic electrons and electromagnetic effects have been added by Scott [234] and Snyder [208]. Energy conserving toroidal electrostatic gyrofluid equations have been derived from Lagrangian theory by Strintzi [235, 236], Scott included electromagnetic effects [237].

Basics of gyroaveraging and finite Larmor radius effects can be found in the appendix C.2.1, the moments are defined in Sec. C.2.2. The model equations of the six-field GEM model used in the code GEMR are discussed next.

Even though the normalization of GEM is similar to DALF, it is different in detail. The radial spatial scale is normalized by the minor radius $\mathbf{x} \leftarrow \mathbf{x}/a$, time scales are normalized by $t \leftarrow t/(a/c_{s0})$ with sound speed $c_{s0} = \sqrt{T_{e0}/m_i}$. The general normalization is done by $n_z \leftarrow n_z/n_{z0}$, $T_z \leftarrow T_z/T_{z0}$, $u_z \leftarrow u_{z\parallel}/c_{s0}$, $q_{z\parallel} \leftarrow q_{z\parallel}/(n_{z0}T_{z0}c_{s0})$, $\phi \leftarrow e\phi/T_{e0}$ and $A_\parallel \leftarrow A_\parallel/\rho_{s0}\beta_{e0}B_0$. Here $\beta_{e0} = 4\pi n_{e0}T_{e0}/B_0^2$. Note that the GEM model uses CGS units.

GEM uses Padé approximated (a particular kind of approximation for the Bessel function) gyroaveraging and gyroscreening operators

$$\Gamma_0 = \frac{1}{1-b_z} \tag{5.26}$$

$$\Gamma_1 = \Gamma_0^{1/2} = \frac{1}{(1-b_z)^{1/2}} \tag{5.27}$$

$$\Gamma_2 = b_z\frac{\partial\Gamma_1}{\partial b_z} = \frac{b_z}{(1-b_z)^{3/2}} \tag{5.28}$$

with

$$b_z = k_\perp^2\rho_{z0}^2 \tag{5.29}$$

and

$$\rho_{z0} = c\frac{\sqrt{M_zT_{z0}}}{ZeB_0}. \tag{5.30}$$

The finite Larmor radius (FLR) corrected potentials are $\phi_G = \Gamma_1(\phi)$, $\Omega_G = \Gamma_2(\phi)$, $A_G = \Gamma_1(A_\parallel)$ and $\chi_G = \Gamma_2(A_\parallel)$. FLR correction terms result from the gyroaveraging operator (see Sec. C.2.1). The $E\times B$ velocity is $\mathbf{u}_E = \delta_0\mathbf{b}\times\nabla\phi_G$ and its FLR corrected part is $\mathbf{w}_E = \delta_0\mathbf{b}\times\nabla\Omega_G$. The $E\times B$ velocity is part of the advective derivative

$$\frac{d}{dt} = \frac{\partial}{\partial t} + \mathbf{u}_E\cdot\nabla = \frac{\partial}{\partial t} + \{\phi_G, \cdot\}\,. \tag{5.31}$$

Here $\{\cdot,\cdot\}$ denotes the Poisson bracket. The magnetic fluctuations are mainly part of the parallel derivative

$$\nabla_\parallel = \frac{1}{B}\mathbf{B}\cdot\nabla + \mathbf{b}_\perp\cdot\nabla = \mathbf{b}\cdot\nabla - \beta_e\{A_G,\cdot\}. \tag{5.32}$$

The potential ϕ is the most important quantity for the turbulence. In the gyrofluid model it is determined by the polarization equation resulting from quasi-neutrality

$$\sum_z a_z\left(\Gamma_1 n_z + \Gamma_2 T_{z\perp} + \frac{\Gamma_0 - 1}{\tau_z}\phi\right) = 0. \tag{5.33}$$

The equation determines the potential which determines the vorticity and therefore this equation takes the role of the vorticity equation ((Eq. (5.2) in the Hasegawa-Wakatani model and Eq. (5.9) in DALF). As GEM is an electromagnetic model the induction equation is of central importance

$$\sum_z a_z u_{z\parallel} = -\nabla_\perp^2 A_\parallel = J_\parallel. \tag{5.34}$$

Electromagnetic effects are important for the Alfvén dynamics and all electromagentic modes like MTMs or KBMs. We have defined some constants $\tau_z = T_{z0}/ZT_{e0}$ and $a_z = Zn_{z0}/n_{ze}$.

The curvature operator is given by

$$\mathcal{K} = -\delta_0\nabla\cdot\frac{1}{B^2}\mathbf{B}\times B. \tag{5.35}$$

The normal curvature allows for the interchange forcing effect (described in detail in Sec. 5.2.1), whereas the geodesic curvature is important for zonal flow saturation by the the geodesic transfer effect (described in detail in Sec. 5.2.3).

The governing equations for each species will be given in the following. The first moment gives the density evolution

$$\frac{\partial}{\partial t}n_z = -\mathbf{u}_E\cdot\nabla n_z - \mathbf{w}_E\cdot\nabla T_{z\perp} - \nabla_\parallel u_{z\parallel} - \mathcal{K}\left(\phi_G + \frac{\Omega_G}{2} + \tau_z\frac{p_{z\parallel}+p_{z\perp}}{2}\right). \tag{5.36}$$

The first term on the r.h.s is the usual advection, corresponding to $\{n,\phi\}$ in the Hasegawa-Wakatani model (5.1) or in (5.10) in the DALF model. The second term is the FLR correction of the advection. The third term couples the density to the parallel velocity, which is part of the induction equation (5.34). Therefore, the two density equations (5.36) are coupled by the induction equation (5.34). This is part of the adiabatic coupling. This is important for effects like the sound wave, parallel currents and the drift-wave dynamics. It corresponds to a part of the first term on the r.h.s. of (5.10) in the DALF model. The fourth term describes compressional effects induced by the curvature and part of the interchange forcing. The corresponding part in DALF is

the last term on the r.h.s. in (5.10). The three parts are the usual potential, the FLR correction and finite temperature effects. Potential fluctuations leading to advection u_E are provided through the difference of ions and electrons by the polarization Eq. (5.33).

Magnetic fluctuations and parallel velocities are determined by

$$\begin{aligned}\frac{\partial}{\partial t}(\beta_{e0}A_\parallel + \mu_z u_{z\parallel}) = \; & -\mu_z \mathbf{u}_E \cdot \nabla u_{z\parallel} - \mu_z \mathbf{w}_E \cdot q_{z\perp} - \nabla_\parallel(\phi_G + \tau_z p_{z\parallel}) \\ & +\mu_z \tau_z \mathcal{K}\left(\frac{4u_{z\parallel} + 2q_{z\parallel} + q_{z\perp}}{2}\right) \\ & -\nu_{e0}|\mu_e|\left(\eta J_\parallel + \frac{\alpha_e}{\kappa_e}\left(q_{e\parallel} + q_{e\perp} + \alpha_e J_\parallel\right)\right). \end{aligned} \quad (5.37)$$

Again, the first term on the r.h.s is the usual advection, the second term the FLR correction of it. The third term is important for the sound wave and Alfvénic dynamics. Its analogon within the Hasegawa-Wakatani framework can be found in the generalized Ohm's law (C.5). Currents as well as perturbations in the vector potential result from the difference of ions and electrons of this equation and the induction Eq. (5.34). Magnetic field fluctuations are induced by the parallel derivative (5.32) from vector potential fluctuations. These so-called magnetic flutter terms are important for electromagnetic instabilities as the MTM (see Sec. 4.8) or the KBM (see Sec. 4.8). The last term does not result form the gyroaveraging and, therefore, it is not part of the basic gyrofluid equations. It describes the collisional dissipation. It appears for both species, since the resistivity adds to $\partial A_G/\partial t$. $\mu_e = -m_e/m_i$ is the mass ratio ($\mu_i = 1$), thermoelectric coupling $\alpha_e = 0.71$, thermal conduction $\kappa_e = 3.2$ and resistivity $\eta = 0.51$ are constants delivered by the Braginskii model [238].

The temperature evolutions follow

$$\begin{aligned}\tfrac{1}{2}\tfrac{\partial}{\partial t}T_{z\parallel} = \; & -\frac{1}{2}\mathbf{u}_E \cdot \nabla T_{z\parallel} - \nabla_\parallel(u_{z\parallel} + q_{z\parallel}) - \mathcal{K}\left(\frac{\phi_G}{2} + \tau_z \frac{p_{z\parallel} + 2T_{z\parallel}}{2}\right) \\ & -\frac{\nu_{z0}}{3\pi_z}(|\tau_z|(T_{z\parallel} - T_{z\perp}) - \Omega_G) + 3a_z\nu_{e0}|\mu_e|(T_{e\parallel} - \tau_i T_{i\parallel}). \end{aligned} \quad (5.38)$$

The perpendicular advection by the $E \times B$ velocity is provided by the first term on the r.h.s. If a strong ion temperature gradient exists, this term allows for the drive of the ITG instability (see Sec. 4.4). The second term describes the parallel advection. Similar to the density compressional effects due to the curvature are given by the third term. The last terms describe collisional dissipation important for temperature equipartition. Anisotropy dissipation of perpendicular and parallel temperatures is provided by the fourth term, the one of ion and electron temperatures by the last term. More on temperature equipartition, relevant to the scrape-off layer and separatrix region, can be

found in Ref. [23].

$$\begin{aligned}\frac{\partial}{\partial t}T_{z\perp} = & -\mathbf{u}_E\cdot\nabla T_{z\parallel} - \mathbf{w}_E\cdot\nabla(n_z+2T_z) - \nabla_\parallel q_{z\perp} \\ & -\mathcal{K}\left(\frac{\phi_G}{2}+2\Omega_G+\tau_z\frac{p_{z\perp}+3T_{z\perp}}{2}\right) \\ & -\frac{\nu_{z0}}{3\pi_z}(|\tau_z|(T_{z\parallel}-T_{z\perp})-\Omega_G)+3a_z\nu_{e0}|\mu_e|(T_{e\perp}-\tau_i T_{i\perp}) \quad (5.39)\end{aligned}$$

The terms are similar as for the parallel temperature. The parallel heat fluxes follow

$$\begin{aligned}\mu_z\frac{\partial}{\partial t}q_{z\parallel} = & -\mu_z\mathbf{u}_E\cdot\nabla q_{z\parallel} - \frac{3}{2}\nabla_\parallel(T_{z\parallel}) - \mu_z\tau_z\mathcal{K}\left(\frac{3u_{z\parallel}+8q_{z\parallel}}{2}\right) - \mu_z a_L(q_\parallel) \\ & -\frac{5}{2}\frac{\mu_z\tau_z\nu_{z0}}{\kappa_z}\left(1.28\left(q_{z\parallel}-\frac{3}{2}q_{z\perp}\right)+q_{z\parallel}+\frac{3}{5}\alpha_z J_\parallel\right). \quad (5.40)\end{aligned}$$

The first and second term provide perpendicular and parallel advection, respectively, the third term the compression by the magnetic curvature. The forth term describes the collisionless Landau damping. $a_L = \frac{\nu_z}{qR_0}(1-0.125q^2R_0^2\nabla_\parallel^2)$ is a Landau damping operator. The last terms are collisional dissipation. Similarly the perpendicular parallel heat fluxes are given by

$$\begin{aligned}\mu_z\frac{\partial}{\partial t}q_{z\perp} = & -\mu_z\mathbf{u}_E\cdot\nabla q_{z\perp} - \mathbf{w}_E\cdot\nabla(u_{z\parallel}+2q_{z\perp}) - \frac{3}{2}\nabla_\parallel(\Omega_G+\tau_z T_{z\perp}) \\ & -\mu_z\tau_z\mathcal{K}\left(\frac{u_{z\parallel}+6q_{z\perp}}{2}\right) - \mu_z a_L(q_\parallel) \\ & -\frac{5}{2}\frac{\mu_z\tau_z\nu_{z0}}{\kappa_z}\left(1.28\left(q_{z\parallel}-\frac{3}{2}q_{z\perp}\right)-q_{z\parallel}+\frac{2}{5}\alpha_z J_\parallel\right). \quad (5.41)\end{aligned}$$

Details on the time dependent equilibrium as well as a discussion on limitations of GEMR can be found in the appendix C.2.3 and C.2.4.

Chapter 6

Measurement techniques to study plasma edge turbulence

Measurements in such a harsh environment as fusion plasmas call for special methods for investigating its properties as for example temperature, density or current. Passive and active diagnostics are distinguished. Passive diagnostics do not perturb the plasma and are favorable. The plasma emits electromagnetic waves in a wide range of frequencies, which can be detected. One example is electron cyclotron emission (ECE) [239, 240, 241]. Also the magnetic field outside of the plasma can be measured without perturbing the plasma. Active methods disturb the plasma. However, in most cases the disturbance is marginal as for reflectometry (using microwaves) or laser diagnostics as Thomson scattering. Particle beams can also be used for diagnostics. Here, one also has to take care that the beam does not significantly disturb the plasma or beams, which are already present for other purpose as a heating beam from the neutral beam injection, are used. This technique is called beam emission spectroscopy (BES) (Sec. 6.3).

In this chapter, a short overview of the different diagnostics suitable to study plasma turbulence is given. Selected diagnostics will be introduced in more detail in the following sections. Most of the diagnostics measure density fluctuations; these are Langmuir probes (Sec. 6.1), Li- (Sec. 6.3) and He-BES [242] and all different kinds of reflectometry (Secs. 6.2.1 and 6.2.2). Electron temperature fluctuations can be obtained by Langmuir probes (Sec. 6.1), ECE, He-BES and correlation-ECE [243]. Ion temperature measurements can be done by charge exchange recombination spectroscopy [244, 245, 246], retarding field analyzers [247], and laser induced fluorescence [248, 249]. Those are usually too slow to measure fluctuations directly, but important for the background values and with conditional sampling (Sec. 7.1.2) these diagnostics can provide valuable information on the fluctuation as well. Velocity measurements can be done by Doppler reflectometry (Sec. 6.2.2) directly or by measurements of multiple spatial points of thermodynamic quantities such as density, temperature or a combination of both like gas-puff-imaging (Sec. 6.4) or bolometry and using a time delay estimation (TDE) or velocimetry tech-

niques (Sec. 7.1.1). The difference between the direct approach and the one by TDE-based methods is discussed in detail in Chap. 9. Parallel flows can be measured by Mach probes. Electrostatic potential fluctuations can be obtained only by Langmuir probes (Sec. 6.1) and heavy ion beam probes. Magnetic field and current fluctuations can be measured with magnetic probes (Sec. 6.5).

6.1 Langmuir probes

Technically the easiest diagnostics to build to study plasmas are Langmuir probes. A Langmuir probe is an electrically conducting, usually rod-shaped solid inserted into the plasma. From the current-voltage characteristics information on the surrounding plasma can be deduced. The region effected by the probe is called the sheath. First let us consider the probe not being biased. As electrons are usually much faster than ions, the probe is negatively charged. This electric field repels the electrons and attract the ions. The resulting electric potential at which no current is flowing through the Langmuir probe is the floating potential (Eq. (A.41)). The floating potential is regularly used to determine plasma potential fluctuations, which is valid if temperature fluctuations can be neglected. This is the case in low temperature plasma experiments like TJ-K [250] or CSDX. The results presented in Chap. 8 are based on floating potential measurements in low-temperature plasmas. For high temperature plasmas like in ASDEX Upgrade this assumption is not reasonable as the electron temperature fluctuations are dominantly contributing to the floating potential [251, 180, 252]. Also the Reynolds stress suffers from this contribution [253]. The results presented in Sec. 10.1 are based on floating potential measurements in the edge of the tokamak EAST which confines high temperature plasmas. Therefore, absolute values given in Chap. 10.1 have to be regarded with caution.

The probe can be biased negatively against the plasma potential. At sufficient high biasing ideally all ions would arrive at the probe and the current saturates at the ion-saturation current (Eq. (A.40)) which depends on the effective probe area and the plasma temperatures and the plasma density. The ion-saturation current is regularly used to estimate the density of the background and fluctuations as well. As the temperature dependence of the ion-saturation current is weaker compared to that of the floating potential, its interpretation can be regarded to be more robust.

Two modifications of the Langmuir probe technique can provide direct measurements of plasma potential fluctuations in the presence of high electron temperature fluctuation levels. These are emissive probes or ball-pen probes. Emissive probes can be realized by heating the probe tip externally or by the heat flux from the plasma onto the probe. At a critical temperature due to the heat flux from the plasma onto the probe, the probe tips can start emitting electrons [180]. Once emissive the influence of the electron temperature is reduced by a factor of five to six [180] allowing direct measurements of the

plasma potential. The ball-pen probe [254, 251, 255] is a simple modification of a Langmuir probe, where the conducting collector is within a hole providing a magnetic shadow. This leads to a strong suppression of the electron current reducing the influence of the electron temperature on the potential measurements accordingly. If the ball-pen probe provides a direct measurement of the plasma potential as claimed it also allows to measure the electron temperature in combination with a standard Langmuir probe measuring floating potential [254, 251, 255].

6.2 Reflectometry

6.2.1 Normal incidence reflectometry

A microwave beam is launched perpendicularly to the magnetic field into the plasma as indicated in Fig. 6.1. The microwave propagates until it reaches its cut-off position and is reflected. In O-mode the cut-off position corresponds to the plasma frequency $\omega_p = \sqrt{e^2 n_e/\epsilon_0 m_e}$ and therefore depends only on the density. The reflected beam can be measured either by the same antenna or by another one at a different position. From the phase difference between the transmitted and reflected waves the distance of the cut-off layer can be calculated. By changing the probing frequency the distance of different densities can be measured, from which the density profile can be reconstructed.

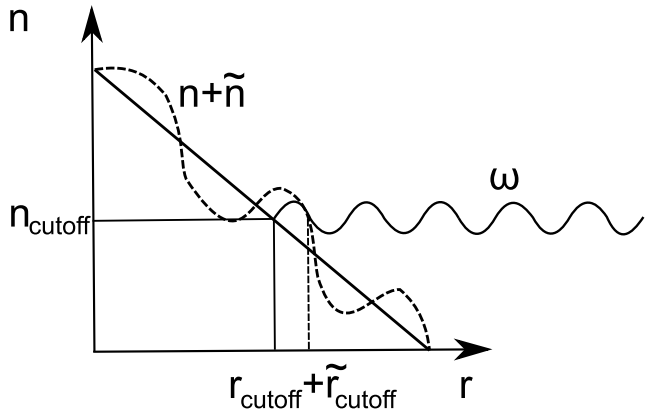

FIGURE 6.1: Principle of reflectometry.

By simultaneously measuring different probing frequencies at the same time, it is possible to measure density fluctuations at different radial locations. By correlation the radial correlation length can be estimated. By simultaneously measuring with poloidally and toroidally separated receiving antennas probing the same reflection layer, density fluctuations at different poloidal and toroidal positions can be measured. Such a configuration is called *Poloidal correlation reflectometry* (PCR). From correlation analysis, poloidal and toroidal

correlation lengths and velocities can be calculated and quantities like parallel and perpendicular velocity, inclination angle and life time of turbulent structures can be estimated. More details can be found in Ref. [256].

6.2.2 Doppler reflectometry (DR)

The principle of Doppler reflectometry is shown in Fig. 6.2. Similar to the conventional reflectometry a transmitted microwave beam is reflected at the cut-off. For Doppler reflectometry the beam is launched with a given incident wavevector k_i and a specific angle α with respect to the flux surface. At the cut-off layer the beam is scattered by density fluctuations modulating the cut-off layer. Density fluctuations at a given wave vector $k_\perp$ act like a diffraction grating and the reflected radiation exhibits diffraction maxima. The scattered wave vector is given by the Bragg condition $k_s = k_i + k_\perp$. At the position of the first order the measured intensity is directly proportional to the density fluctuation level with $k_\perp = 2k_i \sin\alpha$. By changing this angle different wave vectors can be probed and a wavenumber spectrum of the density fluctuations can be obtained. However, the interpretation of these spectra is not straight forward. For quantitative comparisons with simulations synthetic diagnostics with the help of full-wave simulations are often necessary. Depending on the polarization (O- or X-mode) strongly different wavenumber spectra can be found even at the same location [257]. In particular Doppler reflectometry in X-mode polarization suffers more likely from nonlinearities [257].

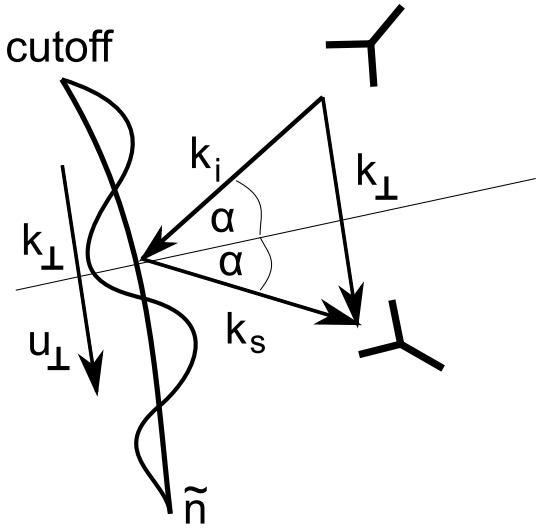

FIGURE 6.2: Principle of Doppler reflectometry.

As density fluctuations are advected by the flow, the frequency of the backscattered signal is Doppler shifted by $2\pi f_D = v_\perp k_\perp$ which provides a measurement of the perpendicular velocity.

6.3 Beam emission spectroscopy (BES)

A beam of particles is injected into the plasma. One can use the beam of the neutral beam injection (NBI) or a particular impurity beam. This beam interacts with the plasma and emits light which is investigated at different spectral lines to determine the plasma quantities. A beam emission spectroscopy (BES) system can be used to estimate profiles and for fluctuation studies [258], too. At ASDEX Upgrade a lithium beam emission spectroscopy (Li-BES) system [259] is the standard diagnostic providing density profiles in the plasma edge. Details on the current Li-BES system at ASDEX Upgrade can be found in Ref. [260]. By collisions of the neutral lithium atoms with mainly the electrons of the plasma bulk, the lithium atoms get excited and ionized. De-excitation by collisions are also possible. The excited state decays by emitting photons at a characteristic frequency which is detected by an optical observation system. A collisional radiative model [261] can be used to deduce the density from the measured, background corrected line radiation. At ASDEX Upgrade a probabilistic data analysis approach [262] based on Bayesian probability theory is used to determine the density profile. Fluctuation measurements are also possible, but, due to the large contribution of photon noise at high frequencies [260], effectively restricted to frequencies less than 20 kHz [263].

6.4 Gas-puff imaging (GPI)

Gas-puff imaging (GPI) is now a well established technique in many fusion experiments to study edge turbulence [264, 265, 266, 138, 267, 268, 79, 269, 270, 271, 272]. A review can be found in Ref. [273]. The main advantage of the GPI is the good spatial temporal resolution of the fluctuations. The main disadvantage is that the light analyzed is usually a result from both, density and temperature fluctuations, making it difficult to assign the measured fluctuations to one individual physical quantity like density or temperature. To locally increase the neutral background pressure a gas puff of typically deuterium or helium is used. Due to collisions of the neutrals of the gas cloud with mainly bulk plasma electrons, the gas cloud emits radiation and is observed by a high speed camera. The GPI set up for ASDEX Upgrade can be found in Ref. [274]. For the time being GPI measurements in ASDEX have been restricted to the far-SOL [274]. Fast imaging has been also used to study plasma turbulence in linear devices [144, 275].

6.5 Magnetic field diagnostics

In a coil with several windings a magnetic field induces a voltage according to Faraday's law. By time integration of this voltage one can deduce the magnetic field. An introduction to different coil setups to measure different quantities can be found in Refs. [277] and [276]. As an example some coil setups are

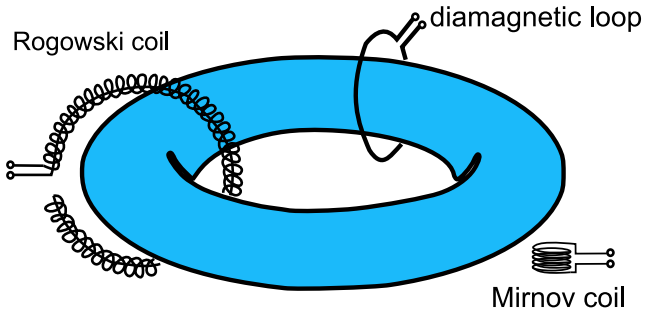

FIGURE 6.3: Schematic figure of a toroidal plasma, showing the basic types of magnetic probes: Rogowski coil, diamagnetic loop, Mirnov coil. Figure has been adapted from Ref. [276].

shown in Fig. 6.3. The plasma current can be measured with a so-called Rogowski coil, which is a solenoidal coil of toroidal shape. The windings have a uniform cross section. To compensate for the change in the toroidal flux at the end of the coil the conductor is returning through the center of the coil to the other end. The energy content of the plasma W_{MHD} can be measured by diamagnetic loops. The most interesting diagnostics for fluctuation measurements are Mirnov coils. Mirnov coils are used for measurements of one component of magnetic field (radial, poloidal or toroidal) near the plasma edge. As the toroidal magnetic field component strongly exceeds the poloidal and radial one, theses coils have to be very precisely adjusted. They are also used for equilibrium reconstruction and plasma control. With respect to turbulence measurements Mirnov coils have the advantage of a high temporal resolution and being available for all discharge conditions. The main disadvantage is that the radial localization of the cause of the detected fluctuations is not straightforward.

ASDEX Upgrade is equipped with an extensive sets of inductive sensors. The positions of the Mirnov coils are shown in Fig. 6.4. In this work mainly a poloidal array of Mirnov coils (C09-XX) measuring the time variation in the poloidal magnetic field components has been used to investigate the magnetic signature of the I-phase and I-mode as discussed in detail in Secs. 11.3 and 10.2.1, respectively.

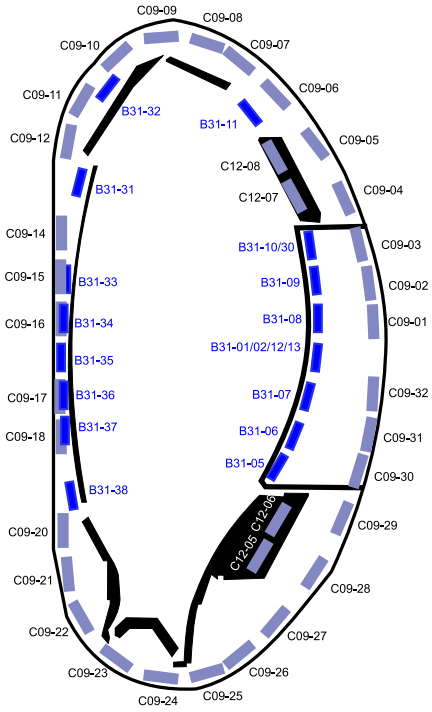

FIGURE 6.4: Positions of the Mirnov coils in ASDEX Upgrade.

Chapter 7

Turbulence data analysis

7.1 Correlation analysis

To quantify a monotone relationship of two random quantities X and Y, the *covariance* of these two random variables defined by

$$\mathrm{cov}(X,Y) \equiv \langle (X - \langle X \rangle)(Y - \langle Y \rangle) \rangle \tag{7.1}$$

can be calculated. The expectation value is given by $\langle \cdot \rangle$. For a positive covariance, both random variables exhibit an accordant linear relationship. A negative covariance corresponds to a reciprocal linear relationship. Although the direction of the relationship is provided by the covariance, no statement on the strength of this relation can be made. In general the random variables can be time dependent. In such case the covariance is called *correlation function*

$$C_{XY}(t_1, t_2) = \mathrm{cov}(X(t_1), Y(t_2)). \tag{7.2}$$

Under stationary conditions using $t_1 = t$ and $t_2 = t+\tau$, Eq. (7.2) depends only on the time delay τ. The correlation function recognizes a linear relationship also in the case, where the effect follows the cause with a time delay and both variables are shifted with respect to each other. In the special case of $Y = X$ and $\langle X(t) \rangle = \langle X(t+\tau) \rangle = 0$ the *auto-correlation function*

$$C_{XX}(\tau) = \mathrm{cov}(X(t), X(t+\tau)) = \langle X(t) X(t+\tau) \rangle \tag{7.3}$$

is obtained. The auto-correlation function describes the capacity of remembering of the fluctuations. It also provides information on the relevant time scale of the auto-correlation of $X(t)$. In general the normalized auto-correlation function reads

$$c_{XX}(\tau) = \frac{C_{XX}(\tau)}{C_{XX}(0)}. \tag{7.4}$$

The *cross-correlation function*

$$C_{XY}(\tau) = \mathrm{cov}(X(t), Y(t+\tau)) = \langle X(t) Y(t+\tau) \rangle \tag{7.5}$$

describes the time scale of correlation of two different variables $X(t)$ and $Y(t)$. The normalization is done accordingly

$$c_{XY}(\tau) = \frac{C_{XY}(\tau)}{\sqrt{C_{XX}(0)C_{YY}(0)}}. \tag{7.6}$$

A value of one means that the random variables exhibit an accordant linear relationship and both variables follow each other one-to-one. One says both variables are completely correlated. On the other hand a value of zero means no relationship of both variables can be found and those are completely uncorrelated. Therefore, the correlation function provides signed strength of the relationship.

In most cases it is useful to normalize the measured or simulated time series of fluctuating quantities X with respect to a standard normal distribution with zero mean and a standard deviation of unity according to $\frac{X-\langle X\rangle}{\sigma_X}$.

7.1.1 Time delay estimation (TDE) and velocimetry

Time-delay estimation

Time-delay estimation (TDE) techniques as well as velocimetry estimate the flow via the displacement of small structures. The estimated flow field describes the movement of those structures and is called optical flow. For the interpretation it is necessary to relate the optical flow to the plasma flow.

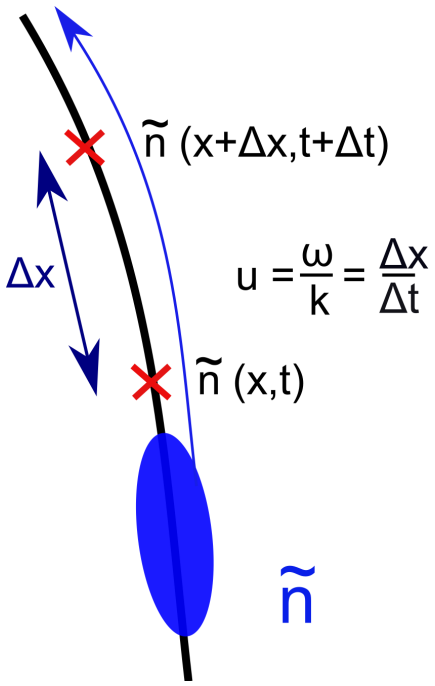

FIGURE 7.1: Principle of time delay estimation.

The TDE principle is illustrated in Fig. 7.1. Structures pass two points of measurement, which are spatially separated by Δx. Two signals are measured, for example $X = \tilde{n}(x,t)$ and $Y = \tilde{n}(x+\Delta x,t)$. Next, the time delay between the signals is estimated from the correlation $\Delta t = \mathrm{argmax}_t(c_{XY}(\tau))$. A velocity can be composed by $u = \Delta x/\Delta t$. This velocity is superposition of the background velocity and the phase velocity of the turbulent structure (see Sec. 4.1). Due to poor time resolution, high structure speeds may lead to $\Delta t = 0$ detections resulting in undefined velocities. The TDE method also faces problems if the points of measurement are separated too much and the correlation is lost. In such a case the result is more or less random. This can be checked by the amount of correlation (7.6). There are additional problems like propagation into the distance orthogonal to the probed measurement positions or eddy tilting (Sec. 3.6.1) which can be diminished by taking into account multiple spatial points [24, 278, 279]. By taking more points into account there is a smooth transition from TDE to velocimetry, which is studied below.

Eddy-lifetime measurements

With the standard TDE method described above, it is possible to measure a velocity by the time delay between spatially two separated probing areas. With varying distance between the probed areas, the correlation is not only shifted, but also decreases with distance. From the reduction of amplitude a dissipation time (or lifetime) can be estimated [280, 256, 281]. The lifetime is the *decorrelation time* in the plasma frame and does not have to be equal to the auto-correlation time. Heuristic descriptions of turbulence suppression strongly rely on the decorrelation time. The time step in a diffusion-like description of turbulent transport is given by the decorrelation time. Also the regime of turbulence depends on the decorrelation time. The ratio of the decorrelation time to the eddy-turn-over time (inverse proportional to the rms vorticity level $\tilde{\Omega}_{rms}$), the so-called Kubo number $\mathcal{K}$ [3], determines, if the turbulence is in the weak ($\mathcal{K} \ll 1$) or strong turbulence regime ($\mathcal{K} \gg 1$). In the case of weak turbulence, linear instabilities and wave physics are important and turbulence can be described by quasi-linear theory. In such a case the plasma transport behaves diffusively and the quasi-linear diffusion coefficient $D_{QL} \sim \mathcal{K}^2$ [282]. In the case of Hasegawa-Mima turbulence $\mathcal{K} \sim 1$ [3]. In such a case the decorrelation time can be approximated by the eddy-turn-over time, as often done in plasma turbulence. In Sec. 9.3 effects of the eddy-turn-over time on growth rates and dispersion are discussed in more detail.

Velocimetry

Velocimetry is distinguished mainly in two types; particle imaging velocimetry (PIV) and particle tracking velocimetry (PTV). In PIV tracer particles much larger than the particles of the fluid are seeded and tracked, in PTV individual particle resident in the fluid are tracked. Therefore, PIV is a Eulerian approach and PTV is a Lagrangian approach. As individual particles cannot be tracked in a plasma, velocimetry in plasmas [283] refers to PIV. In contrast to a neutral fluid no tracer particles are seeded, but intrinsic structures in the turbulence

are traced. In PIV two consecutive images are compared for similar structures. Subsets of the larger first image are compared to the second image. The region where the second image most closely resembles the first images subset indicates the structures destination. Therefore, by comparing the structure of these two consecutive images the displacement of these structures is estimated. There are very sophisticated ways to implement PIV. The displacement of the structures gives the velocity field. Velocimetry has been widely used for the interpretation of gas-puff-imaging data [283, 266, 79, 284, 25]. The technique avoids misinterpretation due to tilted structures as possible in the standard TDE approach [24].

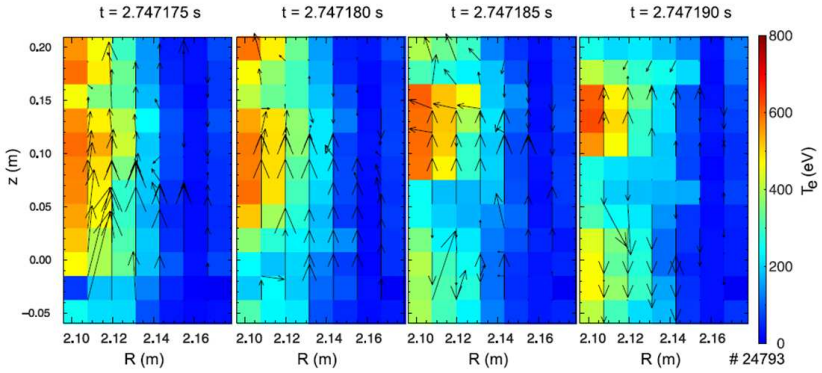

FIGURE 7.2: Four panels in the consecutive frames (with 5 μs temporal resolution) showing the T_e evolution just prior the ELM crash at 2.7472 s. A mode is propagating in electron diamagnetic direction. Arrows show the velocimetry results, which are showing a mostly poloidal propagation. Figure taken from Ref. [161].

As an example for PIV the T_e evolution just prior to the ELM crash at 2.7472 s is shown in Fig. 7.2 by four panels in consecutive frames (with 5 μs temporal resolution). The propagation velocity of turbulent structures has been estimated with a rather simple particle image velocimetry (PIV) algorithm optimized for noisy data [285], including a pattern matching technique, subpixel interpolation and denoising by removing displacement vectors which seem quite different from any of their neighboring displacements. Arrows represent the velocimetry results, which show a mostly poloidal propagation in electron diamagnetic direction in the lab frame. This mode is a type-I ELM precursor which has been identified as an MTM [161] (see Sec. 4.7 for MTM).

7.1.2 Conditional average and sampling

Conditional average

Conditional averaging is used to study the effects of prominent features. Two examples where this method is regularly used in plasma turbulence studies are the dynamics of blobs in the scrape-off layer, and the dynamics around

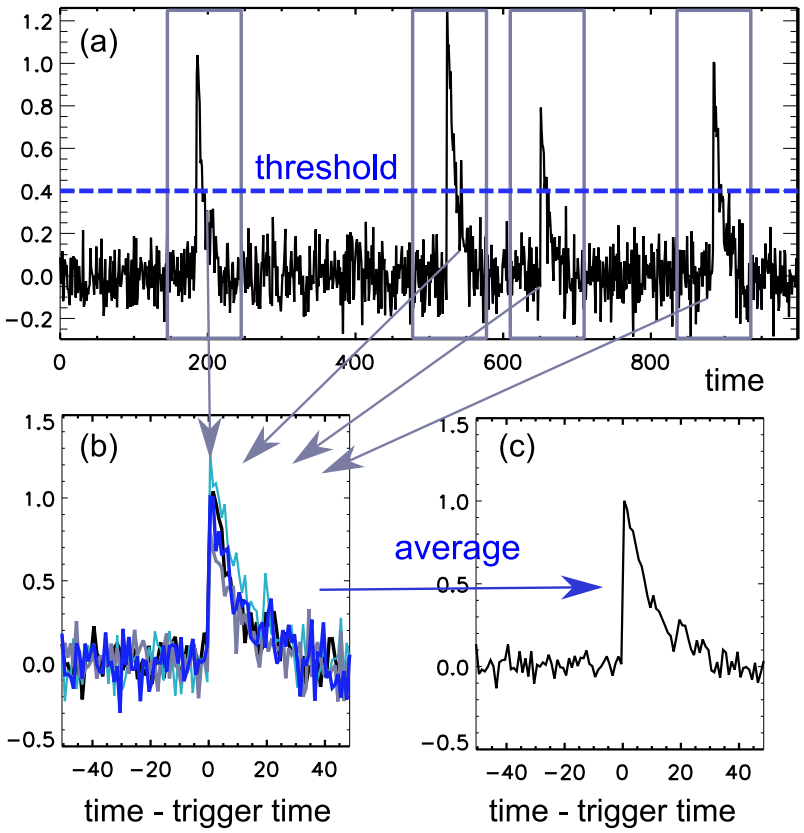

FIGURE 7.3: Principle of conditional average. A condition is defined, usually this is a threshold to overcome. Where this condition is fulfilled the time series around this point is cut out and it is averaged over all of these cutouts.

ELMs (Sec. 2.2.2) [286, 287, 288]. The analysis procedure can be described as emphasized in Fig. 7.3:

i) A trigger condition is defined, usually this is a threshold in a reference signal.

ii) If the condition is fulfilled at time t, sub-windows in the same but also in related signals are extracted around the trigger condition at t. Related signals can be those of different variables than the reference or at other positions. E.g., one can extract sub-windows at different positions to investigate the conditional averaged dynamics in two or three dimensions.

iii) The extracted sub-windows are averaged with respect to the condition.

One advantage of conditional average is that small events correlated or coherently coupled to the trigger events (such as precursors for example) might be detected, which otherwise might be unnoticed in the ambient fluctuation level. The conditional dynamics can provide great indications on the physical mechanisms at play. The pictures shown in Fig. 12.7 or the results reported in

Ref. [275] are examples of conditionally averaged pictures. However, one must not forget that the averaged dynamics cannot be translated to the dynamics of individual events. For example, if you throw a dice several times, on average you obtain 3.5, but this result is never obtained at an individual throw. One should not expect that the conditionally averaged dynamics can be observed most often in the dynamics of the individual events. This does not mean the conditional averaged picture is irrelevant in general; it is even highly important for the physics with the specific condition as it carves out the statistical relevant parts of the physics.

Conditional sampling

A similar technique is conditional sampling. If the diagnostic is sampling actually fast enough to record the fluctuations or events which are desired to be analyzed, but the calculation of the desired quantity needs post processing, this is the technique to use. For example one would be interested in the electron temperature of plasma blobs in the scape-off layer. The temperature can be estimated from the current-voltage characteristics of a Langmuir probe (Sec. 6.1). The Langmuir probes are sampling fast enough to detect the blobs. But as the probe sweeps not fast enough to record the full current-voltage characteristics during the event, it is not possible to calculate a time series of the temperature capturing these events. However, because one is sampling fast enough one can conditional sample the current voltage characteristics to estimate the average electron temperature of these events. An example for conditional sampling can be found in Refs. [289, 290].

7.2 Spectral data analysis

By Fourier-transformation a periodic signal $X(t)$ can be decomposed in its spectral (in this case frequency) contributions $\hat{X}(\omega)$. By spectral analysis these spectral components are investigated in more detail. The *power spectrum* of a fluctuating quantity $\hat{X}(\omega)$ is defined by

$$P_X(\omega) = \langle |\hat{X}(\omega)|^2 \rangle = \langle \hat{X}(\omega)\hat{X}^*(\omega) \rangle. \tag{7.7}$$

Here $\langle \cdot \rangle$ denotes ensemble averaging. The power spectrum identifies the contributions of different frequencies to the signal. Within the spectral analysis Fourier transformed time series build a statistical ensemble. To gain statistical significance a longer time series can be split up in smaller time series which are Fourier transformed. These are called sub-windows. It can be recommended to build sub-windows up to the lowest frequency of interest. Similar to the individual time series also the Fourier transform exhibits a stochastic character. Features like stationarity and ergodicity are not passed to the ensemble of Fourier transforms. Therefore, to account for the stochastic character of the fluctuating quantity a large number of realizations in the ensemble is necessary [291]. This is in particular problematic for high-temperature plasmas (see Sec. 2.1.1) which only allow for short time series and, hence, short number of

realizations under the same experimental conditions, but also for simulations exhibiting usually short time series. On the other hand this shows the merit of low-temperature plasmas (see Secs. 2.1.3 and 2.1.4) which allow for a high number of realizations through long time series.

$P_X(\omega)\,d\omega$ can be interpreted as the mean power contribution of the harmonic component of $X(t)$ at frequencies within $[\omega, \omega + d\omega]$ to the total power of the fluctuations in time. The power spectrum is a real valued quantity and does not contain information on the phase. Due to hermiticity of the Fourier transformation of real functions ($\hat{X}(-\omega) = \hat{X}^*(\omega)$) the power spectrum fulfills $P_X(-\omega) = P_X(\omega)$. The Wiener-Khintchine theorem states a relation between the power spectrum (7.7) and the auto-correlation function (7.3) given by [292]

$$P_X(\omega) = \int_{-\infty}^{+\infty} C_{XX}(\tau)\, e^{i\omega\tau}\, d\tau.$$

The power spectrum is the Fourier transform of the auto-correlation function.

The generalization of the power spectrum of two signals $\hat{X}(x,\omega)$ and $\hat{Y}(x+\Delta x,\omega)$ at a spatial positions x and $x+\Delta x$ is the *cross-power spectrum*, defined by [293]

$$P_{XY}(\Delta x, \omega) = \langle \hat{X}^*(x,\omega)\hat{Y}(x+\Delta x,\omega)\rangle. \tag{7.8}$$

By analogy to the cross-correlation function (7.5) the cross-power spectrum is a measure of the correlation of two quantities $\hat{X}$ und $\hat{Y}$, appearing at different spatial positions x and $x+\Delta x$, in frequency space. As the cross-power spectrum is a complex valued quantity it can be decomposed into an amplitude and a phase

$$P_{XY}(\Delta x, \omega) = p_{XY}(\Delta x, \omega)\, e^{i\theta(\Delta x,\omega)}. \tag{7.9}$$

$p_{XY}(\Delta x,\omega)$ is called *cross-amplitude spectrum* and $\theta(\Delta x,\omega)$ is called the *phase spectrum*. If the phase $\theta(\Delta x,\omega)$ of $\hat{X}(x,\omega)$ and $\hat{Y}(x+\Delta x,\omega)$ is equally distributed within the interval $(-\pi,\pi]$, the phase spectrum as well as the cross-amplitude spectrum vanishes. There is no coherent phase relationship between the signals at both observation positions. The signals are phase incoherent. Finite contributions to $P_{XY}(\Delta x,\omega)$ can only be obtained by a mean coherent phase relationship. The normalized cross-amplitude spectrum [291] or *coherency* is

$$\gamma^2(\Delta x,\omega) = \frac{p_{XY}(\Delta x,\omega)^2}{\langle P_X(x,\omega)\rangle\langle P_Y(x+\Delta x,\omega)\rangle} \tag{7.10}$$

The values of γ^2 are limited to the interval $[0,1]$, where $\gamma^2 = 0$ means phase incoherence, $\gamma^2 \in (0,1)$ partially phase coherence and $\gamma^2 = 1$ complete phase coherence. As cross-phases are very important for plasma instabilities, estimation of the cross-phases by the cross-phase spectrum $\theta(\omega)$ is an important technique for plasma turbulence studies.

In analogy to the power spectrum, the mean cross-power spectrum is the Fourier transform of the mean cross-correlation function.

7.2.1 Envelope modulation technique

The following method provides a possibility to measure velocity fluctuations from a time series measured at a single point in space. The basic idea of this technique is that large scale turbulent flows like zonal flows or geodesic acoustic modes lead to a modulation of the small-scale turbulence due to the parametric modulation instability (Secs. D.3, 3.6, 5.2.3). The envelope of the small-scale turbulence can be used to estimate the time-evolution of these large-scale flows [294]. As small-scale structures correspond to high-frequency structures, the signal has to be high-pass filtered. The envelope of the high-pass filtered density fluctuations $\tilde{n}_{hp}(t)$ is given by $\mathrm{Env}(t) = \sqrt{\mathrm{Re}(\tilde{n}_{hp}(t))^2 + \mathrm{Im}(\tilde{n}_{hp}(t))^2}$. The real part is measured directly. The unknown imaginary part can be reconstructed. It can be deduced in frequency space from the Fourier transform $\tilde{n}_{hp}(\omega)$ and is given by $-i \cdot \mathrm{sgn}(\omega)\tilde{n}_{hp}(\omega)$. The inverse Fourier transform of this relation is the convolution $n_{hp}(t) * 1/(\pi t) = \mathcal{H}(n_{hp}(t))$ which is the Hilbert transform $\mathcal{H}$ by definition. Therefore the envelope is given by $\mathrm{Env}(t) = \sqrt{(\tilde{n}_{hp}(t))^2 + (\mathcal{H}(\tilde{n}_{hp}(t)))^2}$. Low frequency modulation frequencies can be inferred by the auto power spectrum of the envelope (below the high pass filter frequency). The envelope modulation technique has been used in Sec. 11.2.

7.2.2 Pseudo wavenumber spectra

In a tokamak the temporal resolution of a diagnostic is usually pretty good, but the spatial resolution is very limited. The dispersion relation or eigenfrequency characterizes the underlying instability, but how can information in wavenumber space be gathered at poor spatial resolution? The method by Beall [295] allows to study dispersion relations with a minimum effort (at least two points of measurements). Any harmonic perturbation ϕ at a particular position x can be written in polar form

$$X(x,\omega) = \hat{X}(x,\omega)\exp(i\theta(x,\omega)) \tag{7.11}$$

with amplitude $\hat{X}(x,\omega)$ and phase $\theta(x,\omega)$. A (local) wavenumber can be defined by the spatial derivative of the eikonal

$$k(x,\omega) = \frac{\partial}{\partial x}\theta(x,\omega) \tag{7.12}$$

which in discrete form is given by

$$k(x,\omega) = \frac{\theta(x+\Delta x,\omega) - \theta(x,\omega)}{\Delta x}. \tag{7.13}$$

Measurements at at least two spatially displaced positions allow to estimate a local wavenumber. The time series is divided into small sub-windows. Each frequency ω in this sub-window is attributed to a local wavenumber k and the spectral power at this frequency $P(\omega)$ is assigned to this wavenumber $P(\omega) \rightarrow$

$P(\omega, k)$. By averaging over a lot of sub-windows a pseudo wavenumber-frequency spectrum $P(\omega, k)$ can be obtained. Mode numbers of magnetic signals are usually estimated by the phase difference between spatially separated magnetic coils [287, 288].

7.2.3 Wavelet analysis

If the phenomenon to study is very dynamic and/or inherently non-stationary, as for example the L-H transition (see Chap. 10) or the ELM cycle, the Fourier transform will face problems. In such situations the wavelet transformation offers advantages. Using a Fourier transform all temporal information is lost due to the integral over the time series. One can calculate a *spectrogram*, which is a sequence of sub-windows which are Fourier transformed. In a spectrogram the lowest resolved frequency determines the time resolution. The sampling of low frequencies with a Fourier transform prohibits a high time resolution investigation at high frequencies. In general the time and frequency resolution Δt and $\Delta\omega$, respectively, are subject to the uncertainty principle $\Delta t \Delta\omega \geq 1$. This holds for every frequency itself. In a wavelet transform higher frequencies can have a higher time resolution than the low frequencies, where of course every frequency is still subject to the uncertainty principle. Furthermore, the appearance of the pulses does not have to be periodic in the wavelet analysis, which is interesting regarding intermittency studies. The wavelet transformation provides the frequency information for every point of the time series. Also less basis functions may be sufficient to describe the data. This makes wavelets a powerful tool for data denoising or data compression (as JPEG 2000 for example). The wavelet transform is given by

$$X(t) \rightarrow X(t, \tau) = \frac{1}{\sqrt{\tau}} \int dt' \psi(\frac{t - t'}{\tau}) X(t') \tag{7.14}$$

where τ is a characteristic time and $\psi(t)$ is a defined basis function called the *mother wavelet*. As the characteristic time τ can be related to a characteristic frequency ω the corresponding signal $X(t, \omega)$ provides information on the time evolution of X at a given frequency. Choosing suitable basis functions is the art in wavelet analysis. The choice of basis function always constitutes a compromise between time and frequency resolution, which has to be adapted to the concrete problem. The pulse form should be similar to the typical pulse form observed in the data, as otherwise higher harmonics are generated. In the present work only the Morlet wavelet

$$\psi(t) = C(e^{i2\pi t} - e^{-2\pi^2}) e^{-t^2/2} \tag{7.15}$$

is used as it is proved in plasma turbulence [296]. In principle all data analysis techniques presented here can be carried out either with a Fourier transform or with a wavelet transform.

7.3 Higher order spectral analysis

7.3.1 Bispectrum

The power spectrum does not distinguish between independently excited and nonlinearly coupled waves. As shown in Sec. 3.4 the three-wave coupling is a feature of quadratic nonlinearities in Fourier space, in wavenumber space $\mathbf{k} = \mathbf{k}' + \mathbf{k}''$ as well in frequency space $\omega = \omega' + \omega''$. A measure of the quadratic (nonlinear) coupling of two frequencies ω_1, ω_2 with a third one ω_3 is the *bispectrum*. It is defined by [297]

$$B(\omega_1, \omega_2) = \langle \hat{X}(x, \omega_1)\hat{X}(x, \omega_2)\hat{X}^*(x, \omega_1 + \omega_2)\rangle. \tag{7.16}$$

If spectral components at frequencies ω_1, ω_2 and $\omega_3 = \omega_1 + \omega_2$ are present and spontaneously excited and independent from each other, they are characterized by a statistical random phase relationship. The *bi-phase*

$$\beta(\omega_1, \omega_2) = \theta(\omega_1) + \theta(\omega_2) - \theta(\omega_1 + \omega_2) \tag{7.17}$$

with corresponding phase angle $\theta(\omega_i)$ of the Fourier transform is randomly distributed within the interval $(-\pi, \pi]$. By taking the expectation value the bispectrum vanishes. In contrast a coherent coupling leads to fixed phase relationship between the spectral components among each other. In such a case the bispectrum takes a finite value.

Different regions of the bispectrum in the (ω_1, ω_2)-plane are shown in Fig. 7.4. Since of the Fourier transform of a real valued quantity is a Hermitian function, some symmetry features can be obtained [298]

$$\begin{aligned} B(\omega_1, \omega_2) &= B(\omega_2, \omega_1) = B^*(-\omega_1, -\omega_2) && (7.18)\\ &= B^*(-\omega_1, \omega_1 + \omega_2) = B^*(-\omega_2, \omega_1 + \omega_2). && (7.19) \end{aligned}$$

Due to discretization the definition region is limited by the Nyquist-frequency

$$-\omega_{Ny} \leq \omega_1, \omega_2 \leq \omega_{Ny} \quad \text{and} \quad -\omega_{Ny} \leq \omega_1 + \omega_2 \leq \omega_{Ny}. \tag{7.20}$$

The symmetry (7.18) leads to mirror symmetry at the axis $\omega_1 - \omega_2 = 0$ and $\omega_1 + \omega_2 = 0$ and reduces the hexagon to the regions

$$\begin{aligned} \text{I:} \quad & 0 \leq \omega_2 \leq \omega_{Ny}/2 \quad \text{and} \quad \omega_2 \leq \omega_1 \leq \omega_{Ny} - \omega_2 && (7.21)\\ \text{II:} \quad & -\omega_{Ny} \leq \omega_2 \leq 0 \quad \text{and} \quad \omega_2 \leq \omega_1 \leq \omega_{Ny}. && (7.22) \end{aligned}$$

Region I contains the sum-interactions. Region II contains the differential interactions [298]. Additionally the symmetry (7.19) maps region II onto region I. Therefore the region I contains all information of the discrete bispectrum. This region is non-redundant.

A measure of the statistical relation of experimental in general complex quantities $\hat{X}(\omega_3)$ and $\hat{X}(\omega_1)\hat{X}(\omega_2)$ is the quadratic correlation coefficient [291]

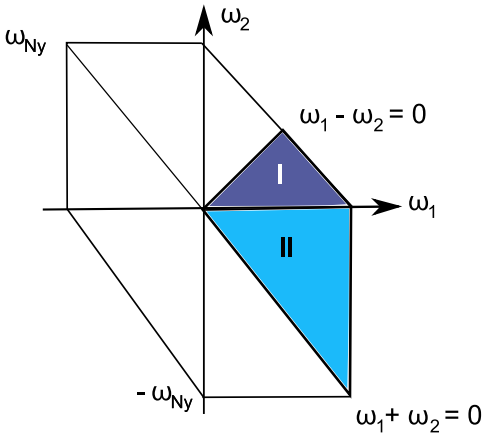

FIGURE 7.4: Domain of the bispectrum of a directed time series. The domain is restricted to the hexagon, given by the condition $|\omega_1|, |\omega_2|, |\omega_1 + \omega_2| \leq \omega_{Ny}$. The symmetry (7.18) leads to a reflection about the axes $\omega_1 - \omega_2 = 0$ and $\omega_1 + \omega_2 = 0$. Due to the additional symmetry (7.19) region II can be mapped onto the region I and vice versa (adapted from Ref. [299]).

$|B(\omega_1, \omega_2)|^2/(|\hat{X}(\omega_1)\hat{X}(\omega_2)|^2|\hat{X}(\omega_1 + \omega_2)|^2)$, which motivates the definition of the *quadratic bicoherence*

$$b^2(\omega_1, \omega_2) = \frac{|\langle \hat{X}(\omega_1)\hat{X}(\omega_2)\hat{X}^*(\omega_1 + \omega_2)\rangle|^2}{\langle|\hat{X}(\omega_1)\hat{X}(\omega_2)|^2\rangle\langle|\hat{X}(\omega_1 + \omega_2)|^2\rangle}. \tag{7.23}$$

With the help of the Schwarz-inequality it can be shown that the *bicoherency spectrum* $b(\omega_1, \omega_2)$ is limited to the interval $[0, 1]$. Values close to one indicate that a wave at $\omega_3 = \omega_1 + \omega_2$ is excited by coupling to waves at ω_1 and ω_2. A value close to zero indicates that the wave is independently excited [298].

It should be noted that a phase coupling not necessarily means the existence of nonlinear wave interaction [300]. Instrumentally nonlinear effects can also lead to fixed phase relationships. On the other hand a low bicoherence implies low nonlinear activity or noise. The symmetry (7.18) also holds for the discrete bicoherence spectrum, the symmetry (7.19) does not [299]. Therefore, in practice the non-redundant bispectrum should be examined in regions I and II.

Using bispectral analysis it is possible to distinguish the parameteric decay instability (Sec. D.2) and the parametric modulational instability (Sec. D.3). As indicated in Fig. 7.5 the parametric decay instability occurs as one localized region of enhanced coupling in region I, whereas the parametric modulational instability occurs as stripes. A non-local coupling characteristic for parametric modulational instabilities between turbulence and zonal flows including GAMs has been demonstrated using bispectral analysis methods in Refs. [301, 302, 303, 304, 305].

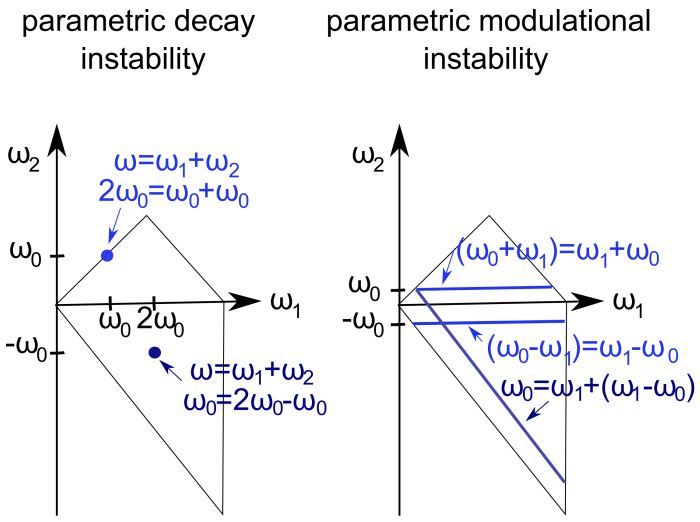

FIGURE 7.5: How parametric instabilities appear in the bispectrum. The decay instability is usually restricted to a local coupling process of the driving frequency, the modulational instability appears as lines at low frequencies compared to the driving frequencies.

7.3.2 Spectral power and energy transfer

The bicoherence can only identify possible nonlinear interactions, but does not provide information on the direction and strength of the spectral power transfer (which mode is actually driving which other mode). In particular, this information is necessary to determine the direction of the turbulent cascades (see Secs. 3.2 and 5.1.2) and and also important for studying the impact of secondary instabilities as zonal flows or geodesic acoustic modes (see Secs. 3.6 and 5.2.3). Once possible nonlinear interactions have been identified it would be desirable to estimate the spectral power transfer from one mode to the other.

Let us consider a nonlinear system described by a nonlinear wave coupling equation

$$\frac{\partial X(\mathbf{k},t)}{\partial t} = \Lambda_L(\mathbf{k})X(\mathbf{k},t) + \frac{1}{2}\sum_{\mathbf{k}=\mathbf{k_1}+\mathbf{k_2}} \Lambda^Q_{\mathbf{k}}(\mathbf{k_1},\mathbf{k_2})X(\mathbf{k_1},t)X(\mathbf{k_2},t). \quad (7.24)$$

Examples of equations fulfilling this relation are the Navier-Stokes-equation (3.4) as well as the most important nonlinearity $\{\Omega,\phi\}$ appearing in the Hasegawa-Wakatani model (5.2). Here $X(\mathbf{k},t)$ is the spatial Fourier spectrum of a fluctuating quantity. Λ_L is the linear transfer function and contains the growth rate $\gamma_\mathbf{k}$ and the dispersion $\omega_\mathbf{k}$

$$\Lambda_L(\mathbf{k}) = \gamma_\mathbf{k} + i\omega_\mathbf{k}. \quad (7.25)$$

The coupling coefficients $\Lambda^Q_{\mathbf{k}}(\mathbf{k_1},\mathbf{k_2})$ determine the strength of the coupling between the three waves $(\mathbf{k},\omega)$, $(\mathbf{k_1},\omega_1)$ and $(\mathbf{k_2},\omega_2)$. Therefore, coupling

coefficients, growth rate and dispersions characterize the turbulence. For drift-waves the growth rate is given by Eq. (B.28) the dispersion by Eq. (B.23).

The simplest proposed method to determine the direction of energy transfer is called *amplitude correlation technique* [306, 307]. Here the direction of the energy transfer is deduced by the causality from the temporal relation between the modes, based on the assumption that an energy gaining mode should increase later in time than the driving mode. Therefore, first the coupling partners are identified by bicoherence and afterward the time lag between them is estimated by cross-correlation. However, this assumption does not hold in general, since the energy must be transferred at the same time. Else the energy conservation is violated. Energy transfer processes appear as a negative correlation at zero time lag [37]. With linear analysis methods such as cross-correlation it is intrinsically impossible to get detailed information about the nonlinear terms in general. Only if the system is completely dominated by the interaction of the modes determines by bicoherence analysis before, it can be excluded that the energy increase found later is due to this interaction and not due to another mechanism.

The coupling coefficients can be calculated from the governing equation as done in Refs. [110, 111, 112]. If the coupling coefficients are known the spectral power transfer can be calculated by estimating the bispectrum and multiplication with these coupling coefficients. The Camargo method [111] (see Sec. 3.4) provides such a method. It is the most precise and comparatively fast. As the coupling coefficients depend on the wavenumbers this method can only be used for spatially resolved measurements since the wavenumber spectrum is needed. As the wavenumber spectrum cannot be directly measured in a high temperature plasma for the time being, this method is restricted to low-temperature plasmas, where it has been used to study the turbulent cascade [35] and the interaction of zonal flows and turbulence [142].

If the nonlinearity to be studied is known, e.g. $(\mathbf{u}\cdot\nabla)\mathbf{u}$ or $(\mathbf{u}\cdot\nabla)n$, one may be successful in measuring it directly in configuration space in a particular spatial region. This can be achieved with the help of a multi-tip configuration of a Langmuir probe array or with GPI for example. However, these methods allow to deduce the nonlinearity of interest in frequency space at a single point in space, but not in terms of spectral wavenumber decomposition as needed for the Camargo method described above. But as $\partial_t\mathbf{u} \sim (\mathbf{u}\cdot\nabla)\mathbf{u}$ the nonlinearity $(\mathbf{u}\cdot\nabla)\mathbf{u}$ corresponds to the bispectrum $\mathbf{u}(f)(\nabla\mathbf{u})(f)\mathbf{u}(-f)$ from which the energy transfer in frequency space can be calculated directly. This has been proposed by Xu [54, 55]. It has recently been used to study energy transfer before the L-H transition in HL-2A tokamak [308], during I-mode and L-H and L-I transitions in Alcator C-Mod [79, 270, 271, 272]. This method is the most reasonable one for high-temperature plasmas from a practical point of view.

If only data from a single point is available, if the precise analytical form of the nonlinearity is unknown, or if quantities to calculate the nonlinearity are missing, approaches based on statistical properties [309, 310, 311, 312, 313] are recommended. Here the unknown coupling coefficients are determined by

higher order moments. The solution of an equation can equally be described by an unlimited number (hierarchy) of moments of this equation. Higher moments need a higher realization number to converge on averaging. The method proposed by Ritz [309, 310] allows to estimate growth rate, dispersion relation and coupling coefficients from the experimental data. From the coupling coefficients and the bispectrum the spectral power transfer can be calculated. As turbulence is close to be Gaussian distributed [314, 315] the Ritz method assumes a Gaussian distribution [309, 310]. For Gaussian distributed variables the fourth order moment can be replaced by second order moments [316] which are much faster and easier to calculate. For strong turbulence this should hold [309]. If the turbulence is weak one should take the fourth order moment into account. This is done by the Kim method [311]. The Ritz as well as the Kim method can be used in wavenumber or frequency space [10]. The Kim method has been used to provide evidence of the dual cascade in drift-wave turbulence [34], to study the evolution of energy transfer during the transition to plasma turbulence [10] and most recently to study the impact of collisionality on self amplification of the Reynolds stress drive of zonal flows [39]. An improvement of the Kim method by taking into account central differences instead of a forward differences has been provided by Baver [312, 313], where also the interaction of different fluctuating quantities (like density and potential for example) has been taken into account. Energy transfer studies of the turbulence-zonal flow interaction and the turbulent cascades have been carried out for example in Ref. [306, 317, 318, 319, 54]. Usually only the real part of the spectral energy transfer is considered. However, also the imaginary part may be important as it can lead to nonlinear modifications of the cross-phase as shown in Hasegawa-Wakatani simulations [320]. This nonlinear cross-phase modification may be in particular important for intermittency [321].

Chapter 8

Drift-wave turbulence

8.1 Structure formation in the inverse energy cascade

In three-dimensional turbulence in the case of a direct cascade, large *coherent* structures are getting smaller and smaller due to vortex interaction. Finally, they pass their energy to the random field and the energy is dissipated. The information necessary for time reversal is not lost, instead it is transferred to the smallest scales in the system where it is invisible for practical purposes. In two-dimensional turbulence the energy is transferred to large scales and a dissipation process like in three dimensions is not possible. Instead the inverse energy cascade results in a reduction of the degrees of freedom and therefore in negative entropy generation. However, also for two-dimensional turbulence the energy must be dissipated and transferred finally to the small-scale random (*noncoherent*) field. It appears reasonable to suggest that there is an interaction between the coherent and the random part of two-dimensional turbulence.

In this chapter the generation mechanisms of large-scale turbulent structures as well as the dissipation mechanisms in a close to two-dimensional system will be investigated in detail considering the energy transfer between different scales of *coherent* and *noncoherent* motion. This provides the possibility to distinguish the different mechanisms of large-scale turbulent structure formation. This chapter is adapted from Ref. [9].

The energy transfer between turbulent vortices of different scales has been investigated experimentally [34, 35] in a toroidally confined low-temperature plasma in the stellerator experiment TJ-K [30] (Sec. 2.1.3). By means of a two-dimensional probe array [34] potential fluctuations have been measured, from which the turbulent $E \times B$ flow can be derived. Energy and the enstrophy are transferred in opposite directions in k-space as expected for two-dimensional fluid turbulence [35, 34]. Nonlocal transfer plays an important role in the inverse cascade supporting the vortex thinning picture (see Sec. 3.3.2).

The Reynolds decomposition (see Eq. (3.38)), where the measure of interest

is decomposed in a mean and a fluctuating part, is the most often applied statistical method to investigate turbulent flows. To study coherent structures the Reynolds decomposition can be extended to the triple decomposition [153]

$$\varphi = \langle\varphi\rangle + \varphi_c + \varphi_n, \tag{8.1}$$

where any quantities as the stream function φ is decomposed in its mean $\langle\varphi\rangle$, the coherent φ_c and noncoherent (random) φ_n contributions. Several definitions of coherent structures exist in literature. The identification used in the following goes back to Okubo and Weiss [118, 119]. The *Weiss number* is defined by $\mathrm{tr}((\nabla \otimes \mathbf{u})^2) - (\mathrm{tr}(\nabla \otimes \mathbf{u}))^2$ which can also be written as

$$\mathcal{Q} = \frac{1}{2}(\sigma^2 - \Omega^2) \tag{8.2}$$

where

$$\sigma^2 = (\partial_x \tilde{u}_x - \partial_y \tilde{u}_y)^2 + (\partial_y \tilde{u}_x + \partial_x \tilde{u}_y)^2 \tag{8.3}$$

is the rate of deformation. The rate of deformation is the symmetric part of the stress tensor $\nabla \otimes \mathbf{u}$. The first term on the r.h.s. in Eq. (8.3) is called stretching strain including both elongation and compression. The second term on the r.h.s. in Eq. (8.3) is due to shear effects and called shear deformation. The asymmetric part of the stress tensor $\nabla \otimes \mathbf{u}$ is $\Omega = \nabla^2\varphi$ which is the vorticity. Here $\tilde{u}_x = \partial_y\varphi$ and $\tilde{u}_y = -\partial_x\varphi$ are the velocity components in the radial x and poloidal y directions in slab geometry, respectively. φ is the stream function (Eq. 3.24), which is directly proportional to the plasma potential ϕ assuming the $E \times B$ velocity as the dominant velocity and the magnetic field B constant. Most important, the Weiss number locally characterizes the motion. A positive Weiss number indicates a hyperbolic motion and for negative $\mathcal{Q}$ the motion is elliptical [119]. Hyperbolic motion corresponds to strain or deformation dominated regions, where elliptical regions are vorticity or rotation dominated. As proven by Weiss [119], $\mathcal{Q}$ measures whether two particles will separate ($\mathcal{Q} > 0$) or not ($\mathcal{Q} < 0$) when following the frozen streamlines. In this way, a flow can be separated into structures which stay together (coherent) and structures which will separate. We identify non-separating trajectories ($\mathcal{Q} < 0$) as belonging to coherent structures [322].

Using the stream function the Weiss number $\mathcal{Q}$ reduces to

$$\mathcal{Q} = (\partial_x\partial_y\varphi)^2 - (\partial_x^2\varphi)(\partial_y^2\varphi). \tag{8.4}$$

The first term is always positive and it is exactly one half of the stretching strain (compare to the first term in Eq. (8.3)). Stretching or compression increases the Weiss number which can even result in a transition from a coherent structure ($\mathcal{Q} < 0$) to an open-streamline vorticity concentration ($\mathcal{Q} > 0$). Thus, these effects always try to decorrelate the turbulence. This is called straining-out. It appears as the second term of Eq. (8.4) and means that the circular motion is stabilizing the turbulent structure. The second term does

not only result from the vorticity, but comes from the shear deformation (second term in Eq. (8.3)) and the vorticity to the same extend. For a negative Weiss number $\mathcal{Q} < 0$ the vorticity must compensate the stretching deformation by the term $(\partial_x^2\varphi)(\partial_y^2\varphi)$, which also results in a stabilizing contribution in the same amount from the shearing deformations. This means, as long as the turbulent structure remains as a structure ($\mathcal{Q} < 0$), the shear is stabilizing.

The energy transfer (Sec. 7.3.2) is estimated by the Camargo method (Sec. 3.4) [111]. In a Fourier decomposition in terms of wavenumbers k, waves (or modes) can interact satisfying the constraint $k = k_1 + k_2$. The time evolution of the kinetic energy E^{Vq} of the coherent ($q = c$) or noncoherent ($q = n$) potential fluctuation field can be separated in linear and nonlinear terms, whereas the nonlinear terms have our main attention:

$$\frac{\partial E^{Vq}(\mathbf{k})}{\partial t} = \text{linear terms} + \sum_{\mathbf{k_1}} T^{Vqrs}(\mathbf{k} \leftarrow \mathbf{k_1}). \tag{8.5}$$

Here $\sum_{\mathbf{k}_1} T^{Vqrs}(\mathbf{k} \leftarrow \mathbf{k_1})$ is the nonlinear transfer function which describes the nonlinear energy transfer to or from the mode $\mathbf{k}$ by the interaction with the modes $\mathbf{k}_1$ and $\mathbf{k}_2 = \mathbf{k} - \mathbf{k}_1$. The spectral transfer of the fluid kinetic energy from mode $\mathbf{k}_1$ to mode $\mathbf{k}$ is given by [323, 111]

$$T^{Vqrs}(\mathbf{k} \leftarrow \mathbf{k_1}) = -2(k_x k_{1y} - k_{1x} k_y) k_2^2 \mathrm{Re}\left\langle \phi^*_{\mathbf{kq}} \phi_{\mathbf{k_1 r}} \phi_{\mathbf{k_2 s}} \right\rangle, \tag{8.6}$$

where $q, r, s \in \{c, n\}$ denote the coherent and noncoherent potential field, respectively. The bispectrum $\left\langle \phi^*_{\mathbf{kq}} \phi_{\mathbf{k_1 r}} \phi_{\mathbf{k_2 s}} \right\rangle$ only exhibits a finite value if all three waves k, k_1 and k_2 are phase-locked and therefore coherently coupled to some degree. The distinction between coherent and noncoherent fluctuating fields distinguishes between elliptical (closed) and hyperbolical (open) streamline configurations. It does not give any information about the coherency of the coupling process between these modes. There is a difference between coherent structures and coherent nonlinear coupling. The asterisk denotes the complex conjugate and Re is the real part of a complex number. The factor $k_x k_{1y} - k_{1x} k_y = \mathbf{b}(\mathbf{k} \times \mathbf{k_1})$ is intrinsically two dimensional and follows from the nonlinearity. Here $\mathbf{b}$ is the unit vector in direction of the magnetic field. The method has been tested successfully on Hasegawa-Wakatani simulations [35] (see Chapter 5.1) and it was used for investigations of the dual cascade [35] and turbulence zonal flow interactions [142] on TJ-K. In difference to the previous investigations [35, 142] the method is applied to the potential field, decomposed in coherent and noncoherent structures to investigate the nonlinear interaction of both fields.

The data analysis procedure is as follows. First the Weiss number $\mathcal{Q}(\phi(x, y))$ is calculated using Eq. (8.3) at every point in time. Then the potential field is decomposed in coherent and noncoherent structures, where

$$\phi_c(x, y) = \left\{ \begin{array}{cc} \phi(x, y) & \mathcal{Q} < 0 \\ 0, & \mathcal{Q} \geq 0 \end{array} \right\} \tag{8.7}$$

$$\phi_n(x,y) = \left\{ \begin{array}{cc} 0 & \mathcal{Q} < 0 \\ \phi(x,y), & \mathcal{Q} \geq 0 \end{array} \right\}. \tag{8.8}$$

Afterward both potential fields are Fourier transformed into the two-dimensional wave number space and the energy transfer functions are estimated according to Eq. (8.6).

Here, fluctuation data from a Langmuir probe array measuring floating potential fluctuations obtained in the stellarator experiment TJ-K are analysed. The results are summarized in Fig. 8.1. Large-scale coherent structures ($k < 2.5$) are driven by coherent structures ($\sum_{\mathbf{k_1}} T^{Vccn} > 0$ and $\sum_{\mathbf{k_1}} T^{Vccc} > 0$). Note $\sum_{\mathbf{k_1}} T^{Vccn}$ and $\sum_{\mathbf{k_1}} T^{Vcnc}$ result from the same coupling (two coherent structures and one noncoherent structure). Both show the energy transfer into the coherent field, but $\sum_{\mathbf{k_1}} T^{Vccn}$ gives the energy coming from the coherent field and $\sum_{\mathbf{k_1}} T^{Vcnc}$ gives the energy from the noncoherent (random) field. The energy in the large scale coherent fluctuations ($\sum_{\mathbf{k_1}} T^{Vcnc} < 0$ for $k < 2.5$) is transferred directly to the random fluctuations ($\sum_{\mathbf{k_1}} T^{Vncc} > 0$ for $k > 2.5$). The nonlinear coupling of coherent fluctuations with coherent fluctuations T^{Vncc} appears as the main drive of random fluctuations at small scales and consequently represents dissipation. A large-scale strain field is generated ($\sum_{\mathbf{k_1}} T^{Vncn} > 0$ with $k < 2.5$) which is in turn balanced by a direct energy cascade of noncoherent fluctuations $\sum_{\mathbf{k_1}} T^{Vnnc}$ as in three-dimensions.

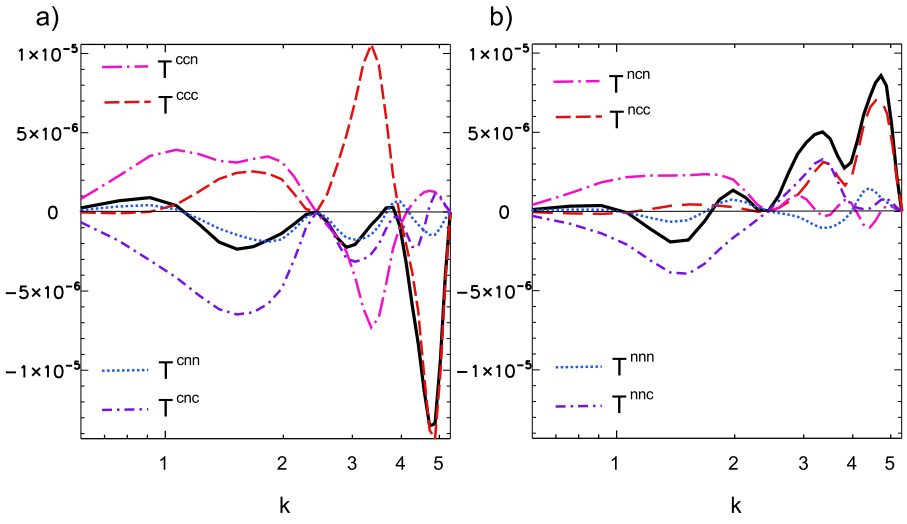

FIGURE 8.1: Energy transfer into coherent T^{Vcrs} (a) and noncoherent T^{Vnrs} (b) potential fluctuations. The solid black lines depict the total energy transfer $\sum_{r,s} T^{Vcrs}$ and $\sum_{r,s} T^{Vnrs}$. Figures taken from Ref. [9].

In the following the energy transfer will be investigated and discussed in more detail. $T(\mathbf{k} \leftarrow \mathbf{k_1})$ forms a four-dimensional quantity depending on $(k_x, k_y, k_{1x}, k_{1y})$, with the constraint $\mathbf{k} = \mathbf{k_1} + \mathbf{k_2}$. Hence, for a graphical

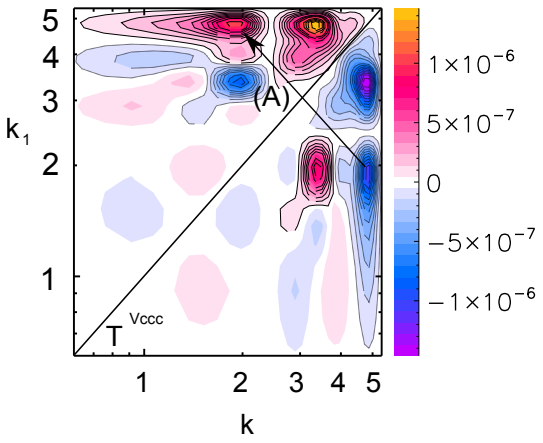

FIGURE 8.2: Kinetic energy transfer between coherent structures. Figures taken from Ref. [9].

representation, sums of all contributions at given $|k|$ and $|k_1|$ have been taken and divided by the number of contributions.

The kinetic energy transfer into or from the coherent field in the k-k_1 plane is shown in Fig. 8.2. As the interactions are among coherent structures it depicts the energy transfer between different scales of eddies. Nonlinear interactions in general conservatively transfer energy in wavenumber space k, $T^{Vqrs}(\mathbf{k} \leftarrow \mathbf{k_1}) = -T^{Vrqs}(\mathbf{k_1} \leftarrow \mathbf{k})$. As in this case no cross-field transfer is involved and the energy transfer is restricted to interaction within a subfield as (T^{Vccc} or T^{Vnnn}) the energy is conserved. The energy conservation is reflected in the antisymmetric behavior around the line given by $k = k_1$, the energy transfer is as expected conservative. Compared to the energy transfer including noncoherent fluctuations (Figs.8.3 and 8.4) the energy transfer between eddies is strongest in amplitude and therefore eddies dominate the total energy transfer. As seen in a previous investigation [35] the energy is dominated by energy transfer from the smallest scales ($k > 4$) into larger scales ($k < 4$) by nonlocal interactions (arrow (A) in Fig.8.2). Nonlocal energy transfer can be attributed to vortex thinning (see Sec. 3.3.2). As the nonlocal inverse kinetic energy transfer takes place as the dominant mechanism (Fig. 8.1) for interaction among eddies. It does not include noncoherent fluctuations.

Interactions between random fluctuations are about an order of magnitude lower and furthermore do not show a preferred direction. The interaction among noncoherent fluctuations is therefore random and does not lead to coherence in the nonlinear coupling and subsequently to no significant intermodal energy transfer. This supports the work by Bruneau [324] where it is shown that in neutral 2D fluids eddies are indeed responsible for the inverse energy transfer. However, the conclusion that noncoherent structures do not significantly participate in the nonlinear coupling process is misleading as we will see in the following.

In order to investigate the interaction of the coherent and noncoherent

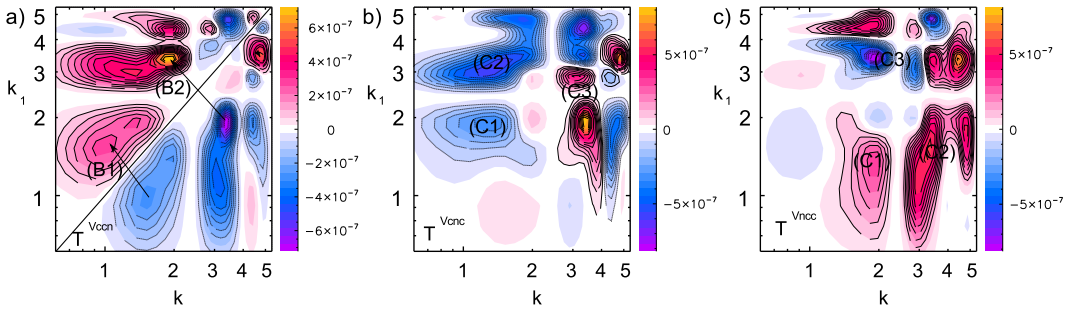

FIGURE 8.3: Kinetic energy transfer between two coherent and one noncoherent structure. Within this process the energy is transferred between the two coherent structures (a), from the noncoherent into the coherent (b) and from the coherent into the noncoherent fluctuations (c). Figures taken from Ref. [9].

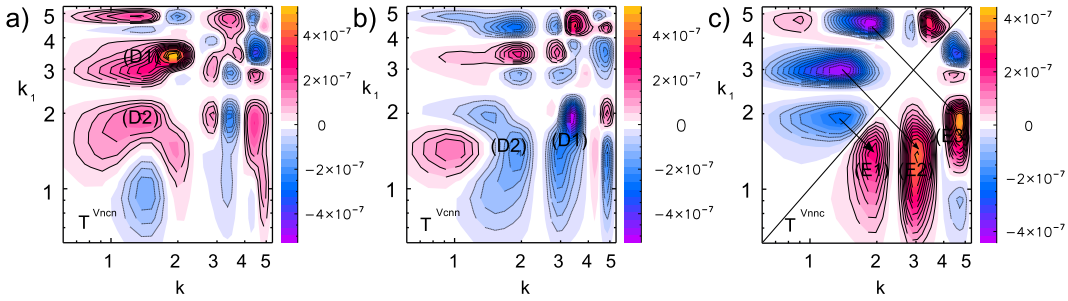

FIGURE 8.4: Kinetic energy transfer between one coherent and two noncoherent structures. Within this process the energy is transferred from the coherent into the noncoherent (b) and from the noncoherent into the coherent fluctuations (c) and between the two noncoherent structures (c). Figure taken from Ref. [9].

field two cases can be distinguished. In the first two coherent modes couple with a noncoherent mode. In the second two noncoherent modes couple with one coherent mode. The first case is shown in Fig. 8.3. The energy transfer between different coherent scales $T^{Vccn}(\mathbf{k} \leftarrow \mathbf{k_1})$ in the presence of noncoherent scales is inverse and local as shown by the arrows (B1) and (B2) in Fig. 8.3a. The energy is conservative as seen by the asymmetry around the $k = k_1$ line due to $T^{Vccn}(\mathbf{k} \leftarrow \mathbf{k_1}) = -T^{Vccn}(\mathbf{k_1} \leftarrow \mathbf{k})$. The common vortex merger is representative of a local event by merging two (corotating) eddies of the same size to an eddy of nearly twice the size. However, one would assume this process is taking place within interaction among only coherent structures (Fig. 8.2). To understand why this process is observed here as a cross-field transfer a closer look on the anatomy of the flow field of vortex mergers is necessary (see Chapter 3.3.1). In fact the interaction between two merging vortices is mediated by noncoherent filamentary structures, either the so-called exchange band or the recirculation band.

Let us consider the transfer from or into the coherent field $T^{Vcnc}(\mathbf{k} \leftarrow \mathbf{k_1})$

first. As seen in Fig. 8.3b energy in the coherent field at large scales is lost to noncoherent structures at small scales ((C1) and (C2)), which could be the filamentary structure in the exchange band or the filaments in the outer recirculation region. Furthermore, coherent structures gain energy from noncoherent structures at small but similar scales (the red region (C3) in T^{Vcnc}). This process displays the alignment of random vortices giving them a preferred direction which in turn increases the coherent vortices at larger scales. However, this mechanism is not as important as the vortex merger. The energy transfer in Fig. 8.3b is not anti-symmetric around the line $k = k_1$, however, the process is still conservative. Because it is a cross-field transfer, the contribution T^{Vcnc} has to be studied together with the contribution T^{Vncc}. Considering $T^{Vncc}(\mathbf{k} \leftarrow \mathbf{k_1})$ in Fig. 8.3c the balance comes out likewise. Due to the interaction of two coherent and one noncoherent structure the noncoherent field is strongly driven by coherent fluctuations at large scales. Since all these observations are related to the same three-wave coupling process the local inverse energy cascade of coherent structures is directly bound to a transfer of large-scale coherent energy to small-scale noncoherent energy. As a result coherent energy is transferred to larger coherent scales and to small noncoherent structures. Although large coherent structures are formed the overall process just transfers energy from small-scale coherent into small-scale noncoherent structures using the coherent field as an interim energy reservoir or catalyst. The transfer of energy into the noncoherent field can be seen as a mechanism of dissipation and an increase in entropy. Vortex merging does not only decrease, but it also partially increases the entropy.

Just by the superposition of the vorticity field cluster of same-sign vortices constitutes a large-scale strain field, which can interact with other structures. A cluster does not exhibit closed streamlines and is therefore a large-scale noncoherent structure consisting of small-scale coherent structures (eddies). The self-organization into a cluster should transfer energy from the small-scale coherent into the large-scale noncoherent field. The coupling between two noncoherent and one coherent mode is shown in Fig. 8.4. As seen in Fig. 8.4a coherent fluctuations at smaller scales transfer energy into the large-scale noncoherent field (D1). This large-scale noncoherent structure is not an eddy but it constitutes a strain field, which can be seen as a cluster. As energy is transferred from small-scale coherent to large-scale noncoherent fluctuations (Fig. 8.4a) there must be a loss of coherent energy at small scales to noncoherent fluctuations as seen in Fig. 8.4b. Also here a cascade within the noncoherent energy is involved (Fig. 8.4c). Kinetic energy is transferred from large to small scales as in three-dimensional turbulence. Left to themselves without energy supply from the coherent field the vortex clusters cannot sustain themselves. This is a result of the rather weak self-rotation, since the vorticity is smaller than the strain as $\mathcal{Q} > 0$, and therefore the eddies within the vortex cluster will diffuse out of the cluster and the cluster is splitting up in smaller and smaller ones. Even though large noncoherent structures are formed the overall process transfers energy from small-scale coherent into small-scale

noncoherent structures as in the case of the vortex merger. Therefore vortex clustering increases the entropy.

In summary, the linear drive in two-dimensional turbulence provides a constant source of coherent kinetic energy into the system. Since the kinetic energy in two-dimensional turbulence cannot be dissipated as in three dimensions, the turbulence has to find a way to transfer the coherent energy into the noncoherent field. The kinetic energy transfer between the different scales of coherent and noncoherent motion in two-dimensional drift-wave turbulence in a confined magnetized plasma has been studied experimentally. Large-scale turbulent structures are generated by vortex merging, thinning and clustering. The process of vortex merging constitutes an inverse cascade process of coherent energy, which is accompanied by a transfer from large-scale coherent to small-scale noncoherent energy (negative coherence production at large scales). Large-scale strain fields can be generated by an alignment of coherent structures, where energy is transferred from small-scale coherent to large-scale noncoherent fluctuations. This negative coherence production at small scales is coupled to a direct cascade of noncoherent energy resulting in dissipation. It is therefore convenient for two-dimensional turbulent systems or it is even required that large-scale turbulent structures are generated due to vortex merging and clustering to transfer energy from the coherent into the noncoherent field as a way to dissipate coherent energy. Nonlocal energy transfer by vortex thinning appears to be the strongest process in structure formation in drift-wave turbulence.

8.2 Subcritical transition to plasma turbulence

The process of a laminar flow becoming turbulent, the transition to turbulence, is an extraordinary complicated not yet fully understood process. It remains one of the main intriguing problems of turbulence research. The process is in general not instantaneous, but proceeds through a series of stages. There are two major kinds of transitions to turbulence. In the first kind a linear instability grows which due to nonlinear saturation will lead to turbulence. If the growth rate depends on the Reynolds number a critical Reynolds number can be estimated and often this critical Reynolds number agrees quite well with the observed onset of turbulence. This is called *supercritical* turbulence. There are some flows which do not care much on this critical Reynolds number or a linear instability. In particular the pipe flow experiment, Reynolds started to study turbulence phenomena in, is one of them. Here the onset of turbulence is far below the estimated critical Reynolds number. If the onset is below the critical Reynolds number, theses flows are called *subcritial*. In such systems externally excited perturbations can lead to turbulence even if the instability threshold is not exceeded. A linear instability is not necessary.

Despite the important progress in theory [211] and experiment [212] on understanding drift-wave turbulence, studies on the transition to turbulence

[325, 326, 327, 328] in magnetized plasmas are still uncommon. In large confinement experiments, fully developed turbulence is usually observed. Once a flow becomes turbulent, it can be difficult to determine its origin due to the chaotic nature and the irreversibility of turbulent flows. In contrast, laboratory-scale plasma experiments are well suited to study the transition to a turbulent state. In this chapter experimental results from a laboratory-scale plasma experiment CSDX (Sec. 2.1.4) will be presented. Previous studies, for example the phase-locked regime observed in [325] and the appearance of a quasi coherent mode [326] will be related with each other and connected to theory [217]. This chapter is based on the results published in Ref. [10]. It will be shown that drift-wave turbulence is subcritical. This is an important observation, since in the plasma physics community turbulence is commonly treated as supercritical and the calculation of growth rates is one of the most important working horses. Subcritical turbulence will be also studied in detail in Sec. 9.3.

Commonly the development of broadband turbulence from an initial instability is explained in terms of wave-wave interactions (Sec. 3.4) due to the nonlinearities. For an increasing control parameter (similar to the Reynolds number for fluid turbulence (Eq. (3.9))) the drift-wave modes undergo a series of mode coupling phenomena until reaching a turbulent state [325, 326]. Klinger et al. [325] found that the bifurcation sequence of these different mode coupling phenomena follows the *Ruelle-Takens scenario*. Beginning with one mode, in the so called *periodic regime*, this mode is subject to nonresonant three-wave interaction in the *quasi periodic regime*. By a transition from nonresonant to resonant three-wave interactions the system reaches the *phase locked regime*, which is characterized by a dominant mode and its harmonics. Small phase dislocations lead to a broadening of the dominant peaks (*chaotic regime*) and with further increasing control parameter the *weakly turbulent regime* can be achieved.

During a similar transition, the evolution of mode coupling using a bicoherence analysis (Sec. 7.3.1) was investigated by Burin et al. [326]. The results are shortly summarized next. In the quasi linear regime many discrete and intensive regions of three-wave coupling appear. In what will be identified as the phased locked regime later, the bicoherence is dominated by the interactions of a quasi coherent mode and its second harmonic with all other frequencies. Above a certain threshold in the control parameter the maximum bicoherence significantly reduces and with increasing control parameter no significant discrete area of coupling in the bicoherence appears. Since the total bicoherence is not reduced, the coupling must then occur across a much larger range of time scales. This is the weak turbulence regime. The present study mainly closes a gap between these previous investigations [325, 326] by estimating the evolution of the nonlinear power transfer (Sec. 7.3.2) of the nonlinearities, which are the major players in turbulence.

Drift-wave turbulence exhibits mainly two nonlinearities, where one acts on the vorticity (Eq. (5.5)) and the other on the density fluctuations (Eq. (5.4)). The vorticity fluctuations are perturbations of the perpendicular polarisation

current [213]. The polarisation drift itself can be commonly neglected in the hydrodynamic derivative, therefore it is determined by the $E \times B$-drift $d_t = \partial_t + v_{E\times B}\nabla$. However, since the nonlinearity fundamentally results from polarisation current fluctuations it will be here referred to as the polarisation drift nonlinearity. Due to quasi neutrality the divergence of the perpendicular current is balanced by that of the parallel current, which also occurs in the continuity equation for the electrons. The hydrodynamic derivative in the electron continuity equation gives rise to the nonlinearity of the density fluctuations, here called $E \times B$-drift nonlinearity. The spectral power transfer functions are calculated with the Kim method [311] (Sec. 7.3.2). Details can be found in the original reference [10].

Experiments were carried out on the linear cylindrical laboratory plasma device CSDX heated by a helicon antenna. A higher magnetic field results in a tightening of the Larmor radius and also in a reduction of the ion viscosity. Therefore the ratio of convection (nonlinearity) to viscosity (dissipation) is enhanced. This can be seen as an enhancement of the Reynolds number (3.9), which also gives the ratio of convection to dissipation. Furthermore, in a helicon plasma as CSDX the central plasma density is also proportional to the magnetic field, therefore the density gradient as a drive for turbulence enhances, too. The magnetic field strength was varied from 54 mT to 98 mT and used as the control parameter as used also in Refs. [326, 329]. Measurements were done with Langmuir probe arrays (Sec. 6.1), which were used for detailed studies of the interactions of the turbulence and zonal flows [53, 54, 55]. More details on the experimental setup can be found in Ref. [10].

Below 58 mT turbulence has not developed yet, the spectra are dominated by one mode. The potential fluctuations are much stronger than the density fluctuations $(\tilde{n}/n_0)^2 < (e\tilde{\phi}/T_e)^2$, which is a clear feature of shear instabilities like Kelvin-Helmholtz or centrifugal modes, but not of drift waves [330]. At 58 mT the low frequencies begin to fill up. In contrast to the earlier potential-dominated fluctuations the Boltzmann criterion is roughly satisfied $(\tilde{n}/n_0)^2 \sim (e\tilde{\phi}/T_e)^2$, which is characteristic for drift waves. On the other hand the cross-coherence of potential and density fluctuations is decreasing and their cross-phase is still close to $\pi/2$ [326]. As discussed in Sec. 4.3 drift waves exhibit a cross-phase between potential and density perturbations close to zero, where essentially all activity is below about $\pi/4$ [112]. A cross-phase close to $\pi/2$ points to interchange-like instabilities as the centrifugal instability in the case of a linear device like CSDX.

Coupling of the dominant mode to sidebands is observed. This is a signature of the parametric instability consistent with earlier observations [325, 327]. Through this coupling with incommensurate frequencies the energy can be transferred to larger and smaller scales. The sidebands also gain energy, which is a clear signature of the quasi-periodic regime [325, 327]. The broadband free energy is transferred to the smaller scales by a coupling through the $E \times B$ nonlinearity to large scale potential fluctuations. Due to this mechanism more modes are incorporated into the system, which means that the excited degrees

of freedom increase with the control parameter. This is the most important feature during a transition to a turbulent state. By increasing the control parameter up to 66 mT this feature is getting more and more pronounced.

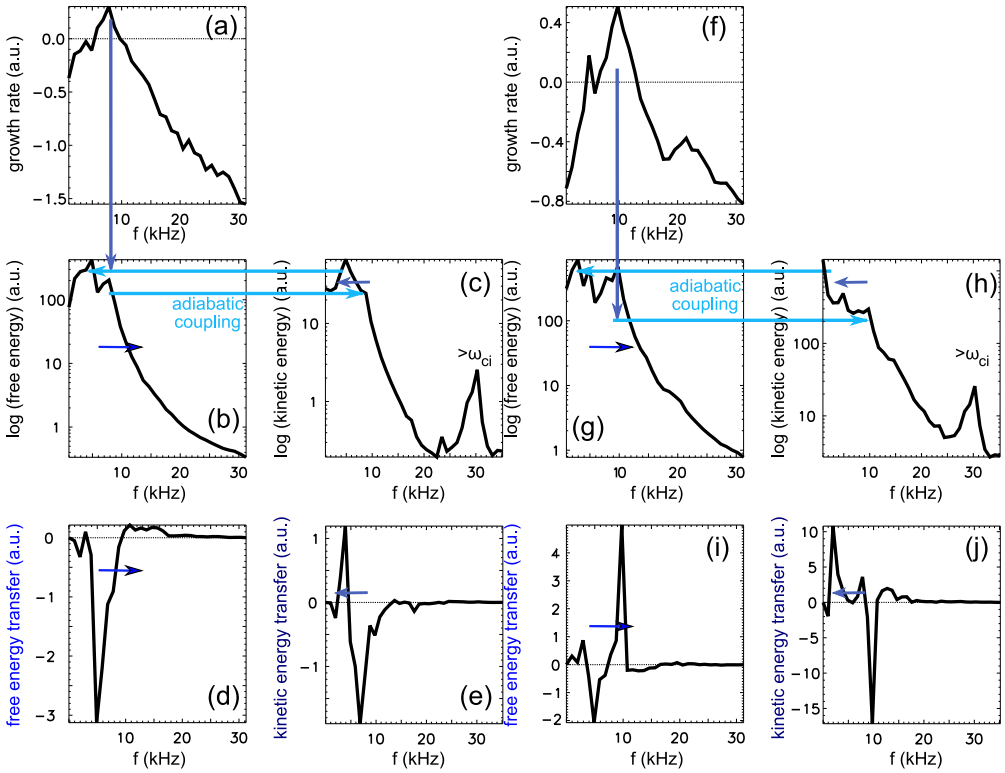

FIGURE 8.5: Growth rate of density fluctuations (a,f), power spectra of density (free energy) (b,g) and potential (kinetic energy) (c,h) fluctuations as well as the spectral energy transfer functions of the free (d,i) and kinetic (e,j) energies in the phase-locked regime at 70 mT (a-e) and the weak turbulent regime at 94 mT (f-j). Measurements done at CSDX. Figure adapted from Ref. [10].

For $B = 70 - 78$ mT, both density and potential spectra are dominated by one mode at 5 kHz corresponding to the quasi coherent mode [326]. In the framework of the Ruelle-Takens scenario this corresponds to the phase locked regime [325, 327]. In this regime the cross-phase is significantly smaller and also the cross-coherence is much higher [326], suggesting that these fluctuations can be related to drift-wave turbulence. This point is very important and has not been emphasized in the original publication [10]. *Even though the fluctuations are centrifugal-instability-driven in the linear regime, in the nonlinear regime the fluctuations are drift-wave dominated.*

The density spectra do not exhibit a strong amplitude increase at the larger scales, but instead show a strong broadening of the turbulence. Since the larger scale potential fluctuations transfer energy to the small scale density perturbations, the power in the larger scale potential fluctuations does not increase as the magnetic field is increased, even though the inverse energy cascade is strongly present between 60 and 74 mT. The large scale potential

fluctuations thus act like a catalyst in this regime, nonlinearly scattering or transferring density fluctuations to smaller spatial scales.

In this regime the small-scales (high frequency) density fluctuations do not become linearly unstable (Fig. 8.5a). Instead, through a coupling to the large scale potential perturbations, which result from the turbulent inverse cascade (Fig. 8.5e), the small scale density fluctuations have access to the free energy of the background density gradient (Fig. 8.5d). Thus, these small scale modes are nonlinearly driven. This mechanism is in principle similar to that one described in Refs. [217] (see Sec. 5.1.2). Due to adiabatic coupling initial density fluctuations appear also as potential fluctuations at the same scale. While the kinetic energy is always transferred to larger scales, the free energy is always transferred to smaller scales. The free energy transfer analysis (Fig. 8.5d) clearly shows that large scale potential fluctuations generated by inverse kinetic energy transfer (Fig. 8.5e) effectively modulate density fluctuations at all scales and not just at the linear driving scale. Therefore density fluctuations at a given scale can be destabilized even if the energy input at the same scale from the density gradient is much smaller than expected from the linear growth rate. Thus drift-wave turbulence is always subcritical. As new born density perturbations at smaller scales are generated in this manner the density perturbations become phase locked with the potential perturbation at large scale. The density perturbations are not long lived, but generated in phase to the larger-scale potential fluctuations. As these structures are phase locked *all of them appear* as the long-living quasi coherent mode observed in the previous investigation [326] at intermediate magnetic field strengths up to 75 mT. As the density fluctuations are nonlinearly generated the energy will be transferred due to adiabatic coupling to the potential fluctuations at the same frequency, which results in a broadening of the linear growth rate in the potential as observed [10].

Above 75 mT this quasi coherent mode breaks down. The reason can be related to two effects. First, the power of the low frequency potential fluctuations decreases. As the large scale flows get weaker they cannot modulate the new born density perturbations any more. As a result the nonlinear free energy transfer to high frequencies weakens. Second, the drive of drift-wave turbulence is given by the background pressure gradient scale length, which also increases with the magnetic field at the position, where the measurements were done [326]. Therefore, the linear growth rate of the density fluctuations increases. These new born density fluctuations are dominantly linearly driven and no longer phase locked to the large scale potential perturbations, and thus they altogether do not appear as a quasi coherent mode anymore. As the spectral power gets more and more concentrated in the dominant modes and these modes are no longer phase locked to the large scale potential fluctuations, they start to undergo parametric instability themselves and couple to a wide number of different modes. This weakens the large scale potential structures additionally. Since the observed break up is accompanied by a onset of disturbances of the quasi coherent mode, its break up could be referred to a

chaotic regime in the framework of Ref. [325].

Above 80 mT the low frequency range in the potential increases dramatically, where that of the density fluctuations only increases slightly. This feature is consistent with expectations for two-dimensional turbulence, while the kinetic energy is transferred to larger scales [89]. The range above 80 mT is denoted here as the *weakly turbulent regime*. The kinetic energy is mainly transferred from the unstable region around 10 kHz to the larger scales. This is the common inverse energy cascade, also observed in [34, 35, 54, 55, 317, 331, 332]. One can observe local interactions at low frequencies, which can be related to vortex merging. Also a second nonlocal mechanism can be found. The 10 kHz mode loses energy to all larger scales consistent with the vortex-thinning mechanism explained in Refs. [21, 35, 94, 143], in which small-scale structures are elongated and thinned by large scaled flows. The structures at larger scales absorb the smaller ones progressively by coiling them up. The inverse kinetic energy transfer could raise large scale fluctuations, as for example zonal flows, which have been studied intensively in CSDX, see e.g. [53, 54, 55, 333, 334]. Above 94 mT the free energy is transferred to the smaller scales following a direct cascade (Fig. 8.5i) as observed in Ref [331]. Indeed, the forward transfer of the free energy is necessary to avoid the infrared catastrophe, which would result from the inverse energy cascade of the kinetic energy [335] and provides a saturation mechanism by the large scale flows that are created by the inverse energy transfer (Fig. 8.5j). This mechanism develops after the kinetic energy gets condensated in the large scale region. Furthermore, it acts as an additional source of free energy for the mode at 10 kHz as a mechanism of *self-sustainment* of drift-wave turbulence [217].

8.3 Spatial nonlocality of zonal flow excitation

Zonal flow generation being a nonlocal phenomenon in wavenumber space is quite well established (see Chapter 3.6). In the present chapter, which has been published in Ref. [11], it will be shown that zonal flow generation is also a nonlocal phenomenon in the original position space domain in the sense that a finite amplitude mean flow structure also requires a spatial separation of excitation and dissipation regions [336, 337]. It follows that the spatial structure and wave propagation are of central importance for the flow generation. Also previous experimental results in magnetized plasmas indicated that the zonal flow formation is linked to an emission, propagation and absorption process of drift-wave packets [144], indicating that an additional investigation of the energy redistribution in configuration space as it was proposed earlier [338, 339] together with the information obtained from previous Fourier analyses [10, 34, 35, 37, 54, 55, 302, 340, 303, 304, 142, 319, 317, 318, 341, 342] appears necessary to gain a more complete picture of the self-organization of the turbulence - zonal flow system.

The energy equations for the turbulence-shear flow systems have been de-

rived in Sec. 3.6.2. For easier readability the main equations are recapitulated here. The turbulence energy $\tilde{K}$ evolution is given by (3.48)

$$\partial_t \tilde{K} = -\partial_x \tilde{T} - \mathcal{P} + \tilde{\epsilon},$$

the mean (zonal) energy $\bar{K}$ satisfies (3.51)

$$\partial_t \bar{K} = -\partial_r \bar{T} + \mathcal{P} + \bar{\epsilon}.$$

The global energy exchange between turbulence and shear flow is completely determined by the turbulence production $\mathcal{P}$. But this does not determine their local values. The growth or damping of the local mean flow is not determined by the production itself. In addition to the turbulent production a further term $\frac{\partial}{\partial r}\bar{T}$ contributes to the mean flow energy as described by Eq. (3.51) [134]; this is denoted as the turbulent kinetic energy transport here. This term results as well from the Reynolds stress, but it does not appear in the energy equation of the turbulence and thus does not act like a direct suppression mechanism of the turbulence. This term is a divergence of a flux and thus it does not generate mean kinetic energy, but instead corresponds to the radial transport of mean kinetic energy by the turbulence. At the position of strong shear, where the zonal flow is expected to be generated, we have $\langle \tilde{u}_r \tilde{u}_\theta \rangle \partial_r \langle u_\theta \rangle \gg \langle u_\theta \rangle \partial_r \langle \tilde{u}_r \tilde{u}_\theta \rangle$ and thus at such a location we can write

$$-\frac{\partial}{\partial r}\bar{T} \approx -\langle \tilde{u}_r \tilde{u}_\theta \rangle \partial_r \langle u_\theta \rangle = -\mathcal{P}. \tag{8.9}$$

Therefore, most of the mean kinetic energy produced by the turbulence will be transported away from this position. At the position of weak shear we can write $-\frac{\partial}{\partial r}\bar{T} \approx -\langle u_\theta \rangle \partial_r \langle \tilde{u}_r \tilde{v}_\theta \rangle$. Substituting the Reynolds stress drive by the stationary case of Eq. (3.45) gives

$$-\frac{\partial}{\partial r}\bar{T} \approx -\langle u_\theta \rangle \mu \partial_r^2 \langle u_\theta \rangle = -\bar{\epsilon}. \tag{8.10}$$

The mean kinetic energy is therefore transported to the extremal positions of the velocity profile, where the energy is nearly completely dissipated. Already from this consideration it is clear that a spatial separation of the production or generation region and the dissipation region is necessary to obtain a finite mean flow structure.

The fluctuating energy balance (Eq. (3.48)) exhibits a similar quantity $\frac{\partial}{\partial r}\tilde{T}$ which is mainly responsible for the redistribution of the turbulent kinetic energy in configuration space via the radial flux of kinetic energy in the fluctuating field; this has been denoted as turbulence spreading elsewhere [343, 344].

Measurements of flows and the Reynolds stress were done in the linear device CSDX with two 3×3 Langmuir probe arrays, which were also used before for detailed studies of the interactions of the turbulence and zonal flows [53, 54, 55, 10, 144]. A shear layer at about $r_{sh} = 3.7$ cm is observed. As

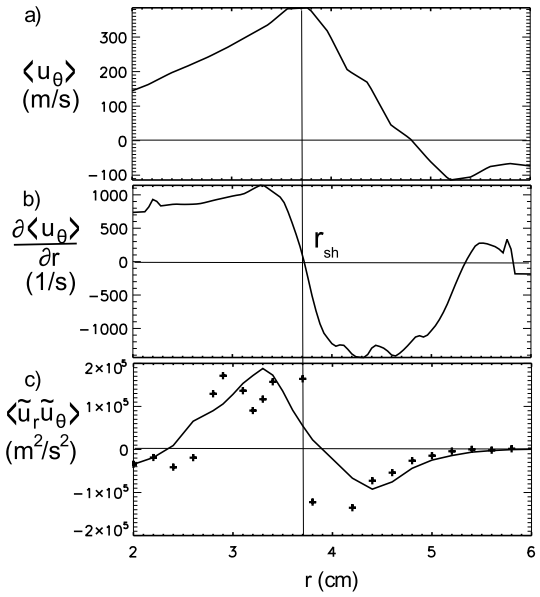

FIGURE 8.6: Radial profile of the (a) velocity, (b) shear and (c) Reynolds stress in the linear device CSDX. Figure adapted from Ref. [11].

shown in Fig. 8.6b the shear is nearly constant and positive ($r \leq 3.5$ cm) and strongly negative from 4 to 5 cm.

The Reynolds stress is shown in Fig. 8.6c by the + symbols. For further analysis the Reynolds stress has to be smoothed (shown by the solid line). The Reynolds stress is positive in the region 2.8 cm $\leq r \leq$ 3.7 cm, which means it transports positive momentum outwards or negative momentum inwards. Toward the plasma center ($r \approx 2$ cm) the Reynolds stress is negative indicating inwards transport. Therefore, the turbulent momentum must be generated around $r = 2.5$ cm and is then transported inward and outward from this position. The position corresponds to the maximum density gradient region, where most of the turbulent structures are born. At the outer region of the plasma (4 cm $\leq r \leq$ 5 cm) the Reynolds stress is also negative, consistent with inward transport of positive momentum. Together with the outwards flux of positive momentum from $r \leq 3.5$ cm, these fluxes act to accumulate positive momentum and thus amplify the shear layer at $r_{sh} = 3.7$ cm. The divergence of the flux of turbulent kinetic energy (Fig. 8.7a) supports this consideration. Turbulent kinetic energy is transported out of the region between $2.5 \leq r \leq 3$ cm, which can be interpreted as spreading. Also from $r \geq 3.5$ cm the turbulent kinetic energy is transported inwards resulting in its concentration in the region from 3 to 3.5 cm.

The turbulent production of shear flow $\mathcal{P}$ is shown in Fig. 8.7b. At the position of the shear layer at 3.7 cm the shear vanishes. Therefore the energy transfer from the turbulence into the mean flow vanishes at this location and the mean flow cannot be generated by the turbulence and thus $\mathcal{P} = 0$ here.

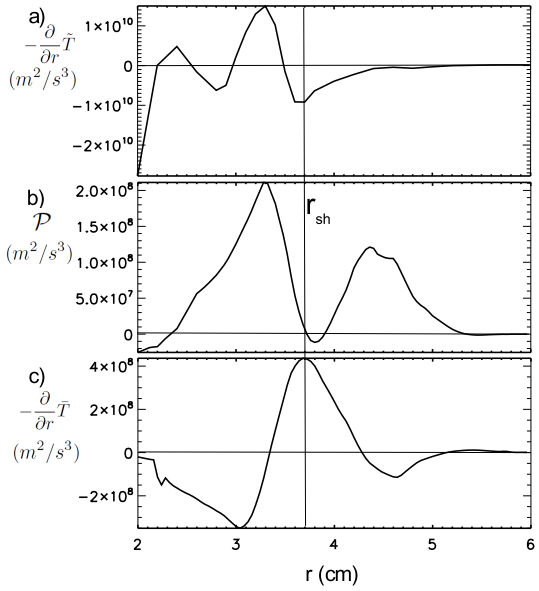

FIGURE 8.7: Radial profile of the (a) transport of turbulent energy, (b) the energy production and (c) the transport of mean kinetic energy in the linear device CSDX. Figure adapted from Ref. [11].

However, at $r \approx 3.3$ cm and $r \approx 4.4$ cm on either side of the shear layer the Reynolds stress and the background flow are in the same direction and therefore the production is high. Therefore the turbulent kinetic energy which has been transported from $r \approx 2.5$ cm to $r \approx 3.2$ cm (Fig. 8.7a) is then absorbed in part by the shear flow at this location.

To understand the profile of the local mean flow the transport of mean kinetic energy $-\partial_r \bar{T}$ has to be considered as shown in Figure 8.7c. Nearly all the energy transferred from the turbulence to the mean flow (denoted by $\mathcal{P}$ Fig. 8.7b) is radially transported ($-\partial_r \bar{T} > 0$ in Fig. 8.7c) to the shear layer at $r_{sh} \approx 3.7$ cm, consistent with our considerations (see Eq. (8.9)). At the same position an outgoing wave energy flux is observed ($-\partial_r \tilde{T} < 0$ in Fig. 8.7a).

The following picture arises as summarized in Fig. 8.8: In the region of the maximum (density or pressure) gradient turbulent structures are generated. Since they are just generated they have no preferential tilt and no associated Reynolds stress. The structures are transported outward, where those exhibiting positive vorticity will become positively tilted by the background shear (see Chapter 3.6.1). This yields a Reynolds stress, which is correlated with the mean shear flow and thus leads to a subsequent amplification of the mean flow shear by turbulent production $\mathcal{P} > 0$. The energy is transferred from the eddies to the zonal flow by an elongation and tilting (and thinning) of the eddy [142, 144]. Beside this energy transfer of kinetic energy from the turbulence to the mean or zonal flow, the Reynolds stress transports mean kinetic energy across the radius, resulting in a flux of mean kinetic energy from either side of the shear layer into the shear layer. Since the turbulence exhibits

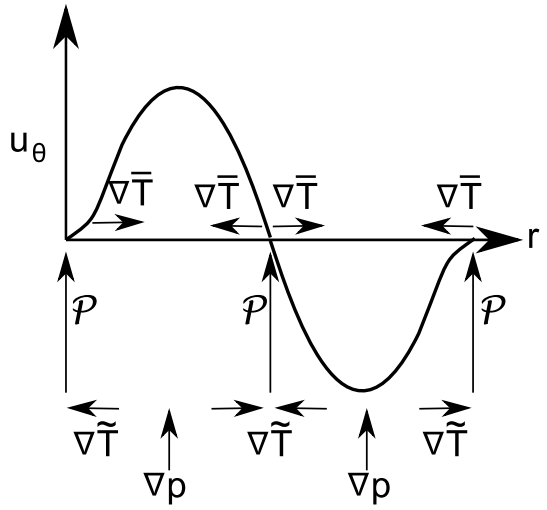

FIGURE 8.8: Principle mechanism of the spatial redistribution of turbulent and mean kinetic energy.

backward-wave character the transport of mean kinetic energy is coupled to the spreading of the turbulence [336, 337]. Finally the mean energy gets dissipated at the shear layer. The transport of mean kinetic energy appears to be the dominant mechanism for transfer of energy into the mean flow; however the direct turbulence flow interaction (the production term $\mathcal{P}$) is also of central importance and cannot be neglected, since it reflects the generation mechanism of the mean kinetic energy.

Finally, the results shown here explicitly show that the spatial structure and (wave) propagation are of central importance for the flow formation. Therefore, these dynamics are inherently nonlocal and cannot be captured by inherently localized flux-tube type computational approaches. The presented considerations also show that a local balance of driving and damping of zonal flows will not provide much insight into the zonal flow generation and damping process. In regions the zonal flow is excited and the turbulence is suppressed the zonal flow itself maybe quite weak, whereas in regions the zonal flow is strong and dissipated the suppression of the turbulence and its drive maybe very weak.

8.4 Concluding remarks on basic drift-wave turbulence studies in low-temperature plasmas

Low-temperature plasma experiments offer possibilities to study basic effects and mechanisms of plasma turbulence not feasible in high-temperature experiments. In particular sets of Langmuir probes enable fluctuation measurements with high spatial and temporal resolution. This enables for example the in-

vestigation of wavenumber spectra, the energy transfer among different spatial scales (Sec. 8.1) and global investigations (Sec. 8.3). Studies of the transition to turbulence have been only possible in linear devices so far (Sec. 8.2). Langmuir probes would not withstand the high heat fluxes under high temperature more fusion relevant conditions. Of course in principle other diagnostics can be used instead, however, a high spatial coverage of the domain is simply too expensive.

The studies presented in this chapter revealed:

i) The kinetic energy transfer in drift-wave turbulence follows the dual cascade (Sec. 8.1). Generation of large-scale structures has been found to be mainly due to the vortex-thinning mechanism. Vortex-thinning occurs at rather small scales (enstrophy cascade range $k\rho_s \geq 1$), where the enstrophy is large and most of the vorticity is concentrated. Indeed, the large-scale region (energy cascade range $k\rho_s \leq 1$) is dominated by the vortex merger process and is local in wavenumber space. Therefore, if the experiments reported in Sec. 8.1 would exhibit a more pronounced inertial range, the cascade might be more local in wavenumber space. This identifies a weak point of turbulence studies in low-temperature plasmas. On the other hand, plasma turbulence simulations usually resolve vortices at $k\rho_s \sim 1$ with just a few points at best and vortex interactions as depicted in Sec. 3.3 are most likely artificially suppressed. Therefore, the experimental findings also identify a weak point of simulations. Vortex merging is accompanied by strong energy transfer to small-scale noncoherent fluctuations (dissipation) balancing the negative entropy generation due to the self-organization process.

ii) The transition to (interchange-)drift-wave turbulence follows the Ruelle-Takens scenario (Sec. 8.2). Once the system is dominated by nonlinear processes, the turbulence shows drift-wave character. The underlying mechanism of the phase-locked regime have been traced back to the phase locking of large-scale potential fluctuations with subcritically excited density fluctuations. Those together appear as a quasi-coherent mode. The experiments could also provide evidence for the self-sustainment mechanism of drift-wave turbulence.

iii) The excitation and dissipation region of zonal flows are radially disjunct (Sec. 8.3). Therefore, it is not possible to balance zonal flow drive and dissipation based on local measurements. Also radial propagation of fluctuation energy is an intrinsic feature of a (even stationary) zonal flow profile.

Although experimental results from low-temperature experiments cannot be transferred one-to-one to high temperature experiments, as essential additional physics is missing in the low temperature experiments, the identified mechanisms will be present. Such essential additional physics are due to finite ion temperatures, conduction (due to the higher electron temperature),

off-diagonal transport like thermodiffusion (due to the higher temperature gradient), a much more pronounced inertial range (due to the smallness of ρ_s/a) and of course, considering experiments in linear devices, magnetic field curvature. The importance of these mechanisms with respect to high-temperature plasmas can only be studied by experiments in high-temperature plasmas or simulations.

Chapter 9

Turbulence in the L-mode

In this chapter we will have a look at the strength of turbulence. What does weak and strong turbulence mean? Under which circumstances turbulence is considered to be weak or strong? Does the physics of turbulence change with its fluctuation amplitude? The here presented chapter is based on the publication [12].

It is assumed that turbulence in the edge of the confined region of the plasma in the low confinement regime is drift-wave dominated [166]. Drift waves exhibit a well defined phase velocity in the electron diamagnetic direction. Doppler reflectometry measurements in ASDEX Upgrade show no significant phase velocity in the plasma edge. The measured velocity is approximately the $E \times B$ background velocity [345] with no signs of dispersion [256]. This has also been observed in W7-AS [346] and seems to be in contradiction to drift waves being the dominant instability in the plasma edge from a linear perspective. On the other hand finite phase velocities have been reported from the plasma core in ASDEX Upgrade [347, 348] and rather in the core ($r/a = 0.8$) in Tore Supra [349].

For the purpose of illustration an example of measurements at different wavenumbers is shown in Fig. 9.1. The data is shown in normalized dimensionless units (left and bottom axis) and in dimension-assigned units (right and top axis). The Doppler reflectometer (DR) (see Sec. 6.2.2) with a movable mirror allows to probe varying wavenumbers ($6 < k_\perp < 12$ cm^{-1}) during the discharge, the poloidal correlation reflectometer (PCR) [256] (see Sec. 6.2.1) is sensitive at low wavenumbers ($k_\perp < 3$ cm^{-1}). The measured Doppler frequency shows a linear relationship to the probed wavenumber. The measured frequencies by the PCR align well with the one by the DR. The $E \times B$ background velocity has been estimated by $u_{E\times B} \approx (1/en)\nabla p_i \approx (1/en)\nabla p_e$ to be around 4 km/s ($u_{E\times B}k_\perp$ is indicated by the blue shaded area in Fig. 9.1), the measured dispersion in the phase velocity is small (< 0.35 km/s) and within the error bars of the measurements. A possible phase velocity is significantly lower than the electron diamagnetic velocity which is of the order of $u_{E\times B}$ as indicated by the grey shaded line in Fig. 9.1.

Fully developed fluid turbulence is usually not classified by driving insta-

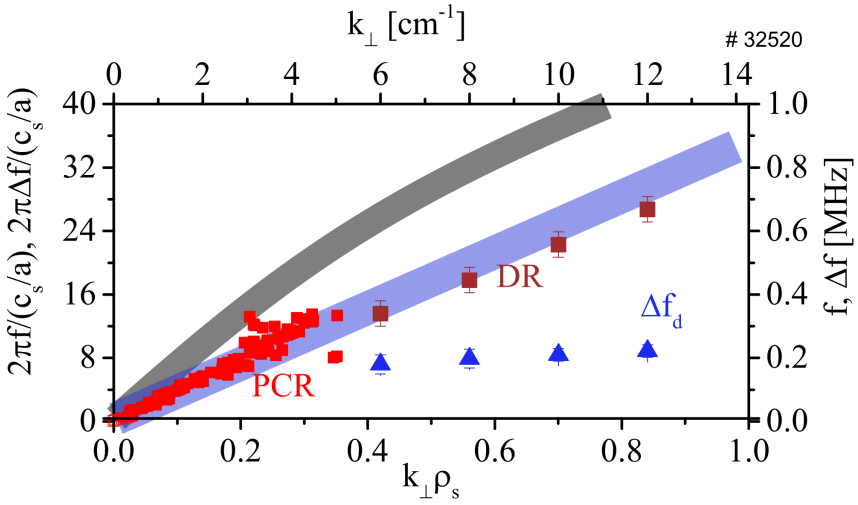

FIGURE 9.1: Frequency versus wavenumber measured at the plasma edge ($\rho_{pol} = 0.985$) of a typical ASDEX Upgrade L-mode plasma at a temperature of $T_e = 124$ eV. Measurements are done with Doppler (DR) and poloidal correlation reflectometry (PCR). The frequency is normalized to the cold ion sound speed c_s, the wavenumber to $\rho_s = 0.7$ mm calculated with the magnetic field on axis $B = 2.6$ T. The frequency broadening Δf (blue) is about 1/3 of the measured frequency. The corresponding perpendicular velocity $\partial f/\partial k$ is not varying with the wavenumber within the error bars. The estimate for the $E \times B$ velocity is indicated by the blue shaded area, an estimate of the drift-wave dispersion relation is indicated by the gray shaded area. Figure taken from Ref. [12].

bilities as it is common in plasma physics [198, 350, 193]. The reason is the strength of the nonlinearity. Is it possible that plasma turbulence loses linear features as growth rates and dispersion at high fluctuation levels? This question will be studied in detail in Sec. 9.3. Before, turbulence will be classified in weak and strong turbulence regimes (Sec. 9.1). We will find that it is indeed possible that dispersion is suppressed by strong fluctuations. Subsequently we will spend some attention (Sec. 9.4) to the question, how measurements of the phase velocity are affected by strong fluctuation levels. In the following a short discussion on how phase velocities are measured in a plasma is given.

To infer spatial characteristics from temporal signals, experimentally one has to map time to space. This is done by Taylor's hypothesis of frozen turbulence [351]. It is assumed that at a single point in space the change of turbulent velocity fluctuations in time can be directly related to their spatial change via the mean convection velocity. Already in the fifties it was shown that the hypothesis is restricted to a limited range of wavenumbers (or frequencies) for shear flows [352]. The applicability of Taylor's hypothesis also depends on the fluctuation level: for validity, turbulent velocity fluctuations must be significantly smaller than the mean velocity [352]. The averaged phase velocity is not unique. One can integrate in wavenumber direction keeping frequency constant

or integrate in frequency direction and keep wavenumber constant. Depending on the shape and the broadening of the wavenumber-frequency distribution $P(k,\omega)$, this results in different answers as we will see in the following.

For example by choosing the wavenumber to be constant, k_0, we take a cut in the frequency direction. The average frequency is defined by

$$\langle\omega\rangle(k_0) = \frac{\int P(k_0,\omega)\omega d\omega}{\int P(k_0,\omega)d\omega}. \tag{9.1}$$

Doppler reflectometry measures a power spectrum $P(k_0,\omega)$ at a given wavenumber k_0, from which a wavenumber dependent phase velocity $u(k_0) = \frac{\langle\omega\rangle(k_0)}{k_0}$ can be estimated in principle. Since the low frequency range is often corrupted by the directly reflected microwave beam this approach is often misleading and the Doppler shift should be determined by fitting a Gaussian to the power spectrum.

By choosing a constant frequency ω_0 to examine wave velocities, cuts along the wavenumber direction in $P(k,\omega_0)$ give an average wavenumber defined by

$$\langle k\rangle(\omega_0) = \frac{\int P(k,\omega_0)kdk}{\int P(k,\omega_0)dk}. \tag{9.2}$$

A wave velocity can be estimated by $u(\omega_0) = \frac{\omega_0}{\langle k\rangle}$. An estimate of a wavenumber is provided through the phase difference of spatially separated points. If fluctuations can be represented by an eikonal $\sim \exp(i\theta)$ with $\theta = kx - \omega t$ the effective or pseudo wavenumber [295] (Sec. 7.2.2) is given by $\langle k\rangle(\omega) = \frac{\partial\theta}{\partial x}$. Time delay estimation (TDE) (Sec. 7.1.1) works in a similar manner. Also here the phase is measured at two spatially displaced positions $\theta(x,t)$ and $\theta(x+\Delta x,t)$. Now the time lag Δt is estimated, where both signals are in phase. Hence, $\theta(x,t) = \theta(x+\Delta x, t+\Delta t)$ or $k\Delta x = \omega\Delta t$. From this a frequency dependent phase velocity can be directly inferred $u_{ph}(\omega) = \frac{\omega}{k} = \frac{\Delta x}{\Delta t}$. The spatial displacement Δx, a time delay Δt and the frequency at which the time delay is measured are determined. What is actually estimated here is an effective phase velocity $\langle u\rangle_{TDE}(\omega) = \frac{\omega}{\langle k\rangle_{TDE}}$ which corresponds to effective wavenumber $\langle k\rangle_{TDE}(\omega) = \frac{\omega}{\Delta x}\Delta t$. Of note, the operator $\langle\cdot\rangle_{TDE}$ is not equal to simply averaging over wavenumber space as in Eq. (9.2). Nearly all measurements of velocities done with Langmuir probe arrays, gas-puff or electron-cyclotron emission imaging, beam emission spectroscopy, correlation reflectometry or phase contrast imaging measure an effective wavenumber $\langle k\rangle(\omega)$.

In the following the two methods for estimating phase velocities are investigated for weak and strong plasma edge turbulence cases.

9.1 Turbulence regimes

The distinction between weak and strong turbulence goes back to Kadomtsev [353]; The latest review can be found in Ref. [354]. The regimes of turbulence are distinguished by the strength of fluctuations represented by spectral

broadening. The frequency broadening is defined by $\sqrt{\langle\omega^2\rangle - \langle\omega\rangle^2}$

$$\Delta\omega(k) = \sqrt{\frac{\int P(k,\omega)\omega^2 d\omega}{\int P(k,\omega)d\omega} - \langle\omega\rangle^2}. \tag{9.3}$$

The wavenumber broadening is defined by $\sqrt{\langle k^2\rangle - \langle k\rangle^2}$

$$\Delta k(\omega) = \sqrt{\frac{\int P(k,\omega)k^2 dk}{\int P(k,\omega)dk} - \langle k\rangle^2}. \tag{9.4}$$

In the picture of weak turbulence a wave-like instability grows and its nonlinear saturation is responsible for the turbulence. To retain its wave-like features the frequency is similar to the linear eigenfrequency $\langle\omega\rangle \sim \omega_l$ and the growth rate is smaller than the linear eigenfrequency $\gamma_l \ll \omega_l$. The weak turbulence regime is also called *wave turbulence*. An introduction to wave turbulence in general can be found in Ref. [355]. The growth rate of the instability is balanced by nonlinear saturation $\gamma_l \sim \Delta\omega$. Weak turbulence is characterized by small frequency broadening $\Delta\omega \ll \omega_l$.

In the strong turbulence regime the nonlinearities dominate and the turbulence is independent of the excitation process. Strong turbulence is characterized by strong frequency broadening $\Delta\omega$ exceeding the analytically expected eigenfrequency, $\Delta\omega \gg \omega_l$. As a result strong turbulence does not feature a linear wave frequency due to the short decorrelation time $\tau \approx 1/\Delta\omega$ resulting in $\gamma_l \ll \Delta\omega$, $\omega_l \ll \Delta\omega$. Equivalent considerations apply for the wavenumber.

The nonlinearity not being dominant in the weak turbulence case does not imply that redistribution of spectral energy (cascades) is not present. It just means that the turbulent spectral power $P(k,\omega)$ is tightly bound to the linear dispersion relation in the wavenumber-frequency plane as indicated by the grey region in Fig. 9.2a. Along the dispersion relation the spectral power can be redistributed and a cascade can be observed as indicated by the blue upper spectrum in Fig. 9.2a. However, vertical and horizontal cuts through the wavenumber-frequency plane, corresponding to frequency (wavenumber) spectra at a given wavenumber (frequency), show no cascades but just the dispersion. In the case of strong turbulence (Fig. 9.2b) the dispersion relation can be neglected and the spectral power mainly follows the Doppler shift of the background flow. Due to the strong nonlinearity the spectral power spreads in all directions with the tendency to lower frequencies and wavenumbers in the two-dimensional case. These can be also observed in the frequency (wavenumber) spectra at a given wavenumber (frequency). Weak and strong turbulence are ideal cases. Real plasma edge turbulence will be somehow in between.

9.2 Weak turbulence regime $\Delta\omega < \omega_l$

For the purpose of introduction we start to study a weak turbulence case. Weak turbulence can be obtained for small gradients appearing for example in

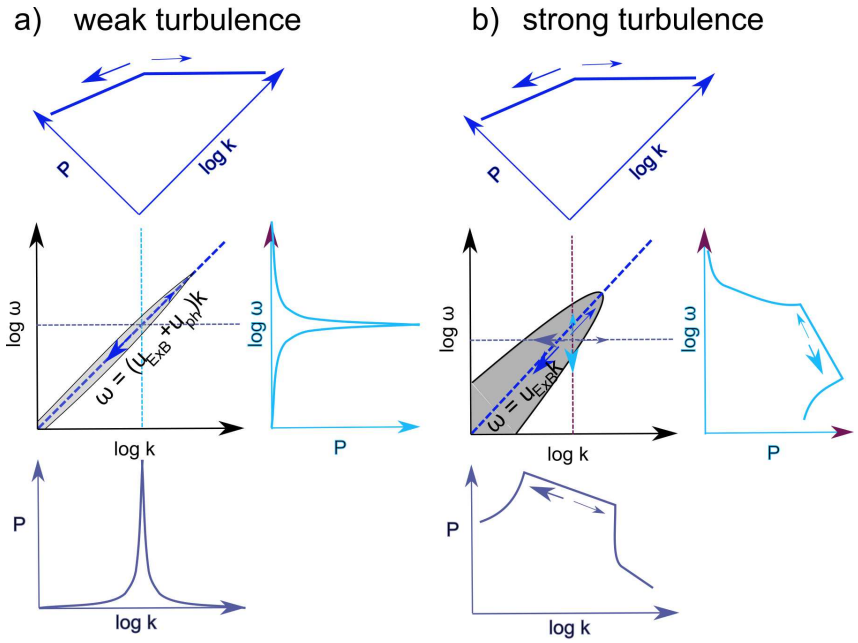

FIGURE 9.2: Schematic view of spectral features of weak and strong turbulence. Figure taken from Ref. [12].

the core. Simulations have been carried out at ASDEX Upgrade parameters ($R = 1.65$ m, $a = 0.5$ m, $B = 2.4$ T, $q_s = 4.6$). The reference surface has been chosen to be at $\rho = 0.5$. The simulations cover the region $0.3 < \rho < 0.7$ with a gradient scale lengths of $L_{Ti} = L_{Te} = 0.3L_n = 20$ cm, which is rather flat compared to the edge cases studied. Only the drift plane at the outboard midplane is analyzed here.

The wavenumber-frequency power spectrum $P(k, \omega)$ of density fluctuations in the plasma frame of reference at $\rho = 0.5$ are shown in Fig. 9.3a in the late growth phase of the simulation. The directions are defined positive for the ion diamagnetic direction and negative in the electron diamagnetic direction. As ω/k is positive a clear phase velocity in the ion diamagnetic direction can be observed, which is a signature of ITG turbulence. From Eq. (9.1) the linear phase velocity can be calculated, which is shown by the black line in Fig. 9.3c. Most of the turbulence activity is restricted to this very narrow line. This situation corresponds to the weak turbulence case. The turbulence saturates at a fluctuation level of about $\tilde{n}/n \approx 1$ %. In the saturated phase the turbulence gets more broadband as shown by Fig. 9.3b. The averaged frequency $\langle\omega\rangle$ as shown by the red dotted line in Fig. 9.3c is reduced compared to the growth phase, but a phase velocity in ion diamagnetic direction is clearly observable. The averaged frequency $\langle\omega\rangle$ is above the frequency broadening $\langle\omega\rangle > \Delta\omega$ (shown by the blue line in Fig. 9.3c). Therefore, this case is in the weak turbulence regime even though not ideal as the frequency does not clearly exceed the broadening. The underlying instability (ITG) can imprint

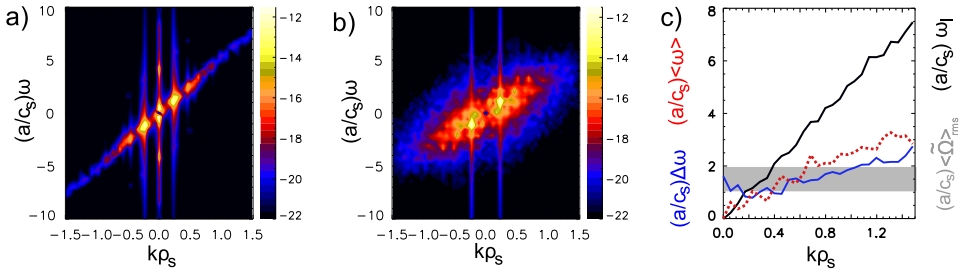

FIGURE 9.3: Weak turbulence case: Wavenumber-frequency power spectrum $P(k,\omega)$ of density fluctuations at $\rho = 0.5$ in the plasma frame in the late growth phase (a) and in the saturated phase (b). Frequency broadening shown by the blue solid line compared to the average frequency in the plasma frame shown by black solid (red dotted line) in the growth (saturated) phase, respectively (c). The rms vorticity level is indicated by the gray area. The linear eigenfrequency (black line) exceeds both the frequency broadening and rms vorticity level. Figures taken from Ref. [12].

its linear phase velocity to the turbulence. The linear frequency significantly exceeds the frequency broadening $\omega_l \sim \langle\omega\rangle \gg \Delta\omega$ and rms vorticity, indicated by the gray region in Fig. 9.3c, which will be important later.

9.3 Marginal strong case $\Delta\omega \gtrsim \omega_l$

Next, simulations have been carried out, corresponding to typical experimental parameters at the last closed flux surface (LCFS) as those shown in Fig. 9.1. Why this is called the marginal strong case will be clear by the end of this section. The simulations cover the region $0.96 < \rho < 1.04$.

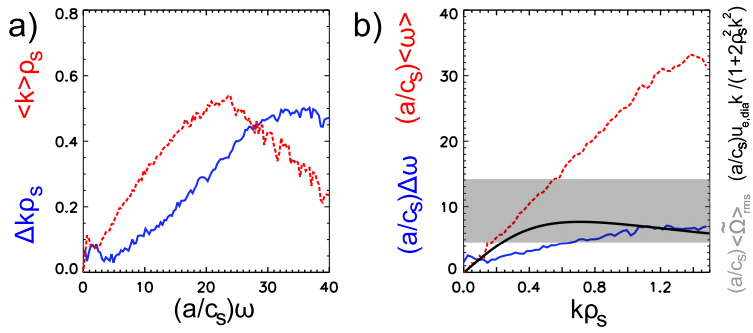

FIGURE 9.4: Marginal strong case: Wavenumber (a) and frequency (b) broadening shown by blue solid lines compared to the average wavenumber and frequency shown by red dashed lines. The drift-wave eigenfrequency is included as a black line and the rms vorticity level is indicated by the grey area. Data is shown in the laboratory frame of reference taken at $\rho = 0.980$. Figures taken from Ref. [12].

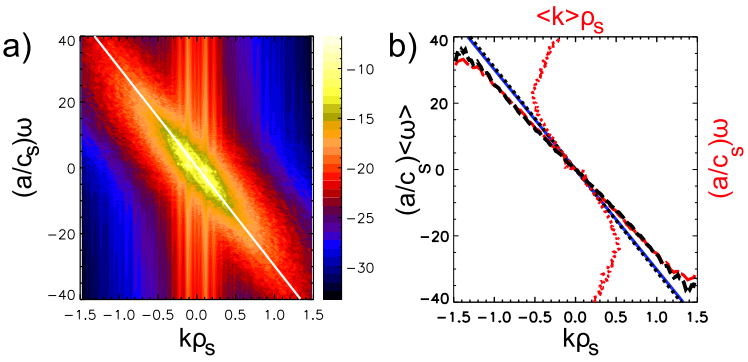

FIGURE 9.5: Marginal strong case: Wavenumber-frequency power spectrum $P(k,\omega)$ of density fluctuations at $\rho = 0.980$ (a). The mode at $k\rho_s = 0.1$ is an interchange mode. Frequency averaged frequency $\langle\omega\rangle(k)$ (red dashed line), the mean $E \times B$ velocity $\omega = u_{E\times B}k$ (blue solid line), phase velocity from wavenumber average $\omega/\langle k\rangle$ (red dotted line), fitted mean of the Gaussian in dependence of wavenumber (black dashed line) and corresponding phase velocity by TDE (black dotted line) (b). Data is shown in the laboratory frame of reference. Figures taken from Ref. [12].

In ASDEX Upgrade usually a significant frequency broadening is present, however, it does not exceed the averaged frequency. In Fig. 9.1 the frequency broadening as estimated from Doppler reflectometry is $\Delta f_{meas}/\langle f_{meas}\rangle \approx 0.3$. Therefore typical L-mode plasmas at the plasma edge in ASDEX Upgrade are closer to a weak turbulence regime. Due to the turbulence the frequency is broadened by $\Delta\omega(k) = k\Delta u + u_{E\times B}\Delta k + \Delta k\Delta u$, where Δk is the nonlinear wavenumber broadening and Δu is the nonlinear broadening of the velocity spectrum. The measured frequency broadening is not only due to fluctuations at the probed wavenumber k_0 but also due to the finite spectral resolution Δk_0 [356, 357], resulting in a frequency broadening $2\pi\Delta f_{diag} = \Delta k_0 \cdot u$. Taking $\Delta k_0 = 2.2$ cm^{-1} we get $\Delta f_{diag}/\Delta f_{meas} \approx 0.5$. As Δf_{diag} basically gives the sensitivity of the diagnostics it is likely that Δf_{meas} provides the correct estimate of the frequency broadening by the turbulence. It does not exceed $\Delta\omega < 2\pi\Delta f_{meas}$. In a conservative approach the minimum frequency broadening by the turbulence would be $\Delta\omega > 2\pi(\Delta f_{meas} - \Delta f_{diag})$, therefore $\Delta\omega/\langle\omega\rangle \approx 0.15$–$0.3$.

In contrast to plasma core parameters, a weak turbulence regime in the plasma edge seems not to be easily accessible in GEMR. By fixing the background profiles to the initial conditions a reduction in the spectral broadening can be obtained. Except for very low frequencies the averaged frequency strongly exceeds the frequency broadening $\langle\omega\rangle(k) \gg \Delta\omega(k)$ (Fig. 9.4b) by $\langle\omega\rangle(k)/\Delta\omega(k) \approx 4$–$7$. This is of a similar order as in the experimental observation (Fig. 9.1) where the averaged frequency exceeds the frequency broadening by $\langle\omega\rangle(k)/\Delta\omega(k) \approx 1.5$–$3.5$ (taking into account broadening by diagnostic effects discussed above this factor maybe assumed to be$\langle\omega\rangle(k)/\Delta\omega(k) \approx 3$–$7$). At these low frequencies an interchange instability is present. As seen in

Fig. 9.5b $\langle\omega\rangle(k) \approx u_{E\times B}k$ and no significant wavenumber shift is observed. Approximating velocities with the center of gravity of the frequency [358] as done by Eq. (9.1) is not the usual evaluation method. Commonly a Gaussian is fitted to the logarithmic power spectrum $P(k_0, \omega)$. The center of the Gaussian is equated with the Doppler shift as the advecting velocity. Thus the background velocity is recovered. The averaged wavenumber $\langle k\rangle(\omega)$ strongly exceeds the wavenumber broadening $\Delta k(\omega)$ up to roughly $(a/c_s)\omega < 20$ (Fig. 9.4a). For low frequencies with low frequency broadening ($(a/c_s)\omega < 20$) the phase velocity follows the background velocity $\omega/\langle k\rangle \approx u_{E\times B}$ (Fig. 9.5b). At higher frequencies with significant broadening in wavenumber space (Fig. 9.4a) a propagation in electron diamagnetic direction is observed (Fig. 9.5b). Also a frequency dependent diagnostic will usually not resolve the wavenumber according to Eq. (9.2), but instead estimate the velocity by correlation. Indeed, the velocity estimated with TDE using a spatial separation of about 5 mm (black dotted line in Fig. 9.5b) recovers the background velocity (blue solid line in Fig. 9.5b) as shown by the overlap of the lines in Fig. 9.5b. In summary, this simulation does not show any significant phase velocity in the plasma frame nor dispersion.

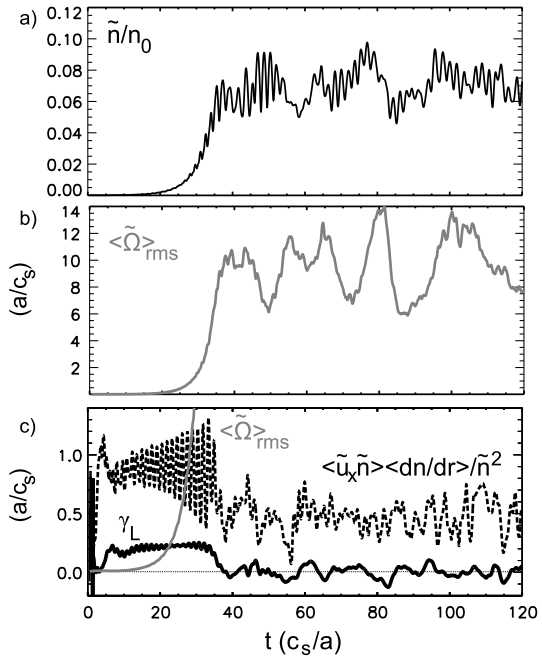

FIGURE 9.6: Marginal strong case: Density fluctuation level (a), vorticity fluctuation level (b), vorticity, growth rate γ_l, turbulence gradient drive rate (c) at the beginning of the simulation. Figures taken from Ref. [12].

How linear features can get lost in drift-wave turbulence can be found in Ref. [159], which is shortly summarized here. In the weak turbulence picture the linear growth rate balances the nonlinear broadening $\gamma_l \sim \Delta\omega$. This is not the case for fully developed drift-wave turbulence in the plasma edge; the

linear growth rate is much smaller than the rms vorticity $\gamma_l \ll \langle\tilde{\Omega}\rangle_{rms}$ [159]. As the nonlinear spectral transfer is mainly realized by the vorticity equation, the rms vorticity should be of the order of the frequency broadening $\langle\tilde{\Omega}\rangle_{rms} \sim \Delta\omega$. Regarding the aspect $\gamma \sim \Delta\omega$ fully developed drift-wave turbulence is not in the weak turbulence regime [159].

In the beginning of the simulation the transition to turbulence occurs and the growth phase can be studied. For $t < 30\ c_s/a$ the turbulence grows exponentially as seen by the amplitude in Fig. 9.6a. The growth rate is about $\gamma_l \approx 0.2\ c_s/a$ and are carried mainly by an interchange mode at $k\rho_s \approx 0.1$. As the density fluctuation level increases also the rms vorticity level increases. The rms vorticity equals to the inverse eddy-turn-over time. The vorticity is calculated by $\tilde{\Omega} = \nabla_\perp^2(\tilde{\phi}+\tilde{p}_i)$ and takes electrostatic potential and ion pressure fluctuations into account. At $t \approx 25\ c_s/a$ the rms vorticity exceeds the linear growth rate. Shortly after this at ($t \approx 35\ c_s/a$) the growth rate drops to zero. Also the turbulence gradient drive rate $\langle\tilde{u}_x\tilde{n}\rangle\langle dn/dr\rangle/\tilde{n}^2$ drops strongly. The turbulence level saturates. The turbulence has to generate its own vorticity through nonlinear self-sustainment [359, 217]. Similar to a background shear the nonlinear vorticity scatters small-structures apart before they can experience a linear instability. As a consequence linear features as the linear growth rate or propagation velocity can get lost. The growth rate $\gamma_l \approx 0.2\ c_s/a$ is far below $\langle\Omega\rangle_{rms} \approx$6–14 a/c_s, the vorticity rms level of the electrostatic potential fluctuations only is between 3–6 a/c_s. As the drift-wave phase velocity is much higher than the growth rate $\omega_l \gg \gamma_l$ it might survive. In Fig. 9.4b the black line shows the drift-wave dispersion relation $\omega_l = u_{e,dia}k_y/(1+\rho_s^2(k_x+k_y)^2)$ which is approximated by $u_{e,dia}k/(1+2\rho_s^2k^2)$ assuming isotropic structures $k_x = k_y$. The drift-wave eigenfrequency (black line in Fig. 9.4b) is in a similar order of magnitude as the spectral broadening $\omega_l \approx \Delta\omega$ (blue line in Fig. 9.4b). Note that one should not compare only the eigenfrequency $\omega_l(k_l)$ at a particular scale with its spectral broadening $\Delta\omega(k_l)$, since the drift wave $\omega_l(k_l)$ is also disturbed by different scales $k \neq k_l$. The total rms vorticity level $\tilde{\Omega}$ indicated by the gray shaded area in Fig. 9.4b) is at least similar to the linear eigenfrequency and mostly exceeds it (black line in Fig. 9.4b) which seems to be sufficient to mix and disturb the drift wave during its propagation and no typical drift-wave phase velocity is measured. The small-scale vorticity is generated at a rate similar to the diamagnetic drift frequency as previously observed in Ref. [217]. The structures are only advected by the background flow. The present regime shows features of strong turbulence $\gamma_l \ll \Delta\omega$, but as the eigenfrequency is close to the frequency broadening, $\omega_l \gg \Delta\omega$ is not fulfilled. Therefore, the presented regime is closer to strong than to weak turbulence.

9.4 Strong turbulence regime $\Delta\omega \gg \omega_l$

In the strong turbulence case the gradients evolve. The spectral broadening exceeds the averaged value for both the frequency and wavenumber (Fig. 9.7).

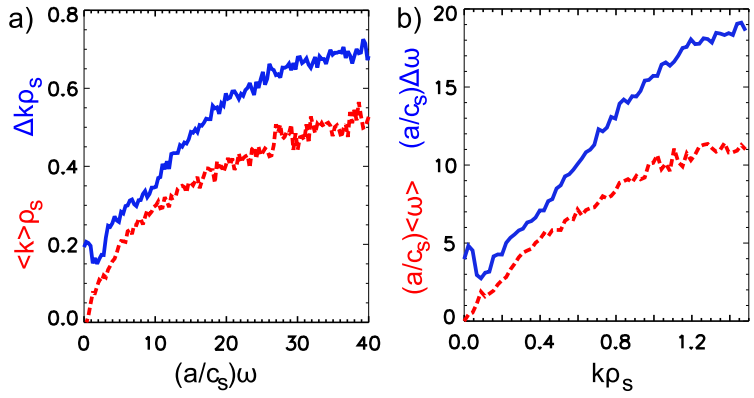

FIGURE 9.7: Strong turbulence case: Wavenumber (a) and frequency (b) broadening shown by blue solid lines compared to the average wavenumber and frequency shown by red dashed lines. The broadening exceeds the averaged values but is of the same order of magnitude. Data is shown in the laboratory frame of reference. Figures taken from Ref. [12].

As the broadening does not exceed the averaged values by orders of magnitude ($\Delta\omega/\langle\omega\rangle \approx \frac{3}{2}$, $\Delta k/\langle k\rangle \approx \frac{4}{3}$) the simulation also seems to marginally be in the strong turbulence regime. As we will see later, the simulations are in the strong turbulence regime.

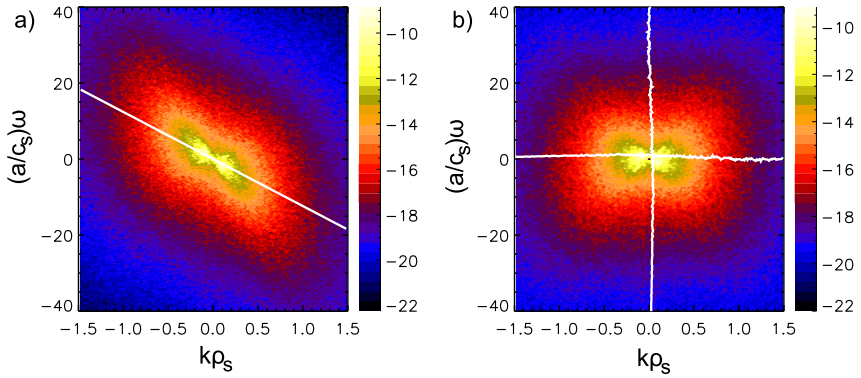

FIGURE 9.8: Strong turbulence case: Wavenumber-frequency power spectrum $P(k,\omega)$ of density fluctuations at $\rho = 0.995$. Data is shown in the laboratory frame of reference (a) and in the plasma frame of reference (b). Figures taken from Ref. [12].

The wavenumber-frequency spectrum of density fluctuations in the drift plane at the outboard midplane is shown in Fig. 9.8. The power distribution follows more or less the mean convective velocity $\omega = u_{E\times B}k$ as indicated by the white solid line. The mean convective velocity is in electron diamagnetic direction, which is defined negative here. In Fig. 9.8a it appears as if the turbulence amplitude is symmetrically spread around $\omega = u_{E\times B}k$. By integrating

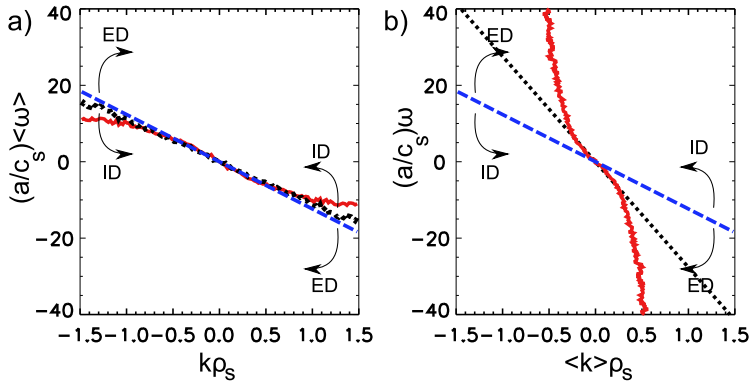

FIGURE 9.9: Strong turbulence case: Averaged frequency $\langle\omega\rangle$ in dependence of the wavenumber (a) and averaged wavenumber $\langle k\rangle$ in dependence of the frequency ω (b) (both red solid lines) in comparison with the mean convective velocity $\omega = u_{E\times B}k$ (blue dashed line) in electron diamagnetic direction. The phase velocities in the plasma frame are indicated by the arrows. The l.h.s. shows a phase velocity in ion diamagnetic, the r.h.s. in electron diamagnetic direction. The velocity as measured by a DR is included by the dotted black line in (a), the corresponding one by TDE technique is included as a black dotted line in (b). Data is shown in the laboratory frame of reference. Figures taken from Ref. [12].

in frequency space to estimate the mean frequency (Eq. (9.1)) a propagation in ion diamagnetic direction in the plasma frame is observed (see Fig. 9.9a). This is expected for ITG modes. However, if we integrate in wavenumber space to estimate the mean wavenumber (Eq. (9.2)) and compare it against frequency, modes at higher wavenumber propagate in electron diamagnetic direction in the plasma frame (Fig. 9.9b), which is characteristic of drift waves. Indeed estimating the velocity by TDE using a spatial displacement of 5 mm results in the phase velocity as shown by the black dotted line in Fig. 9.9b which is roughly two times the background $E \times B$ velocity. As the $E \times B$ velocity is roughly the ion diamagnetic velocity in electron diamagnetic direction the corresponding phase velocity as measured by TDE is the electron diamagnetic velocity as expected for electrostatic drift waves.

In summary, the structures propagate in ion diamagnetic direction at a given wavenumber and in electron diamagetic direction at a given frequency. In a linear framework this seems impossible. The reason of the discrepancy of different phase velocities $\langle\omega\rangle/k$ and $\omega/\langle k\rangle$ is the nonlinear broadening. In the case of drift-wave turbulence the power is transferred to low frequencies and low wavenumbers [111, 35, 10, 9] leading to the power spectrum being skewed to low wavenumbers and low frequencies. This is called the inverse energy cascade [89]. At a given wavenumber k the power is transferred to low frequencies responsible for a reduction of the effective frequency $\langle\omega\rangle$ and therefore also propagation velocity $\langle\omega\rangle/k$ compared to the background velocity. If the background velocity is in the electron diamagnetic direction, this leads

to a propagation in ion diamagnetic direction in the plasma frame.

At a given frequency ω the power is transferred to lower wavenumbers. This leads to a reduction of the effective wavenumber $\langle k \rangle$ at this frequency and therefore to an increase of the effective propagation velocity $\omega/\langle k \rangle$. If the background velocity is in the electron diamagnetic direction, the propagation velocity in the plasma frame is also in the electron diamagnetic direction.

By mapping the wavenumber-frequency power spectrum $P(k, \omega)$ to the plasma frame, $P(k, \omega - u_{E\times B}k)$, it has to be taken into account that in the present case the background velocity is time dependent $u_{E\times B}(t)$. Therefore, every sub time interval has to be mapped in the plasma frame and the ensemble average is done afterward. The wavenumber-frequency power spectrum $P(k, \omega)$ in the plasma frame is shown in Fig. 9.8b. It exhibits clear broadband characteristics. No signs of dispersion are observable. As in the present regime no eigenfrequency $\omega_l = \langle \omega \rangle - u_{E\times B}k$ is detectable, $\omega_l \ll \Delta\omega$. In Sec. 9.3 we have seen that also the growth rate is negligible $\gamma \ll \Delta\omega$. Therefore, the presented regime is not only marginal but clearly in the strong turbulence regime ($\omega_l, \gamma_l \ll \Delta\omega$).

A shift to low frequencies due to the nonlinear energy transfer as observed by the red line in Fig. 9.9a is not observed by the Doppler reflectometry [346, 345, 256] (Fig. 9.1b). By fitting a Gaussian the skewed part at particular low frequencies of the spectrum $P(k_0, \omega)$ which is the result of the cascade is basically ignored. In the average (Eq. (9.1)) the impact of this nonlinear shift is much stronger as the power is taken linearly and not logarithmically into account. The resulting Doppler shift is shown by the black dotted line in Fig. 9.9a. The Doppler shift is more or less dispersionless and very close to the mean $E \times B$ velocity, which is basically in agreement with Refs. [346, 345, 256].

9.5 Concluding remarks on strong L-mode turbulence

In this chapter the influence of strong fluctuation levels on the plasma turbulence just inside the last closed flux surface in the edge of magnetized confined plasmas is investigated by means of gyrofluid simulations. At typical fluctuation levels observed in this region, the rms vorticity level is high enough to suppress linear features of the turbulence. The physical reason is that the mixing rate of the turbulence exceeds the typical rates of the linear instability or wave (like growth rate or dispersion). The growth rate is certainly suppressed in any case, making linear instability analyses nonrelevant in this region. Instead of linear instabilities, the turbulence is driven by nonlinear self-sustainment. At sufficiently high fluctuation levels even the phase velocity can be suppressed. In the plasma core, where the fluctuation levels are much lower, a characterization of turbulence by linear stability analysis still makes sense. However, one should not transfer results, i.e. that most linear features of the turbulence transmit to the nonlinear regime, from the core to the edge.

At high-confinement regimes (I-mode and H-mode) in the plasma edge the fluctuation level is smaller than in L-mode. But certainly, the fluctuation levels are high enough to suppress the growth rate of any micro-instability (except for KBMs perhaps). Whether dispersion is relevant under this conditions has to be investigated in the future.

Chapter 10

Turbulence at the L-H transition

10.1 Zonal flow as trigger of the L-H transition

Theory predicts that the L-H transition can be explained by an intermediate, quasi-periodic transient stage, where turbulence, zonal flow, mean shear flow and the pressure gradient are coupled [360, 361]. The physical picture of this model is depicted in Fig. 10.1 and shows the variation of turbulence amplitude, zonal flow strength, and ion pressure gradient in dependence of the heating power. We will refer to this model as the Kim-Diamond model. Increasing the heating power does not lead to an enhancement of the pressure gradient in L-mode. Instead only the fluctuation level of the turbulence increases. In this sense, this fulfills the definition of profile stiffness, even though the ad-hoc model of transport stiffness as introduced in Sec. 4.4 might be not fulfilled. With increasing fluctuation level also the drive of the zonal flow increases (Secs. 3.6 and 5.2.3). At some point the drive overcomes the zonal flow damping rate. A finite zonal flow then begins to grow and extract kinetic energy from the turbulence and thereby acts to suppress the turbulence amplitude. This leads to saturation of the turbulence. However, as turbulence is suppressed the zonal flow drive also reduces. For input powers just below the transition threshold, self-regulation between turbulence and zonal flows occurs as an oscillatory behavior, characteristic for predator-prey systems (Sec. 3.6.3). These predator-prey oscillations have been observed in various devices [37, 362, 363, 364, 365]. This regime is called the *I-phase* [362]. **The I-phase must not be confused with the I-mode.** The I-mode is an improved energy confinement regime with H-mode-like energy confinement and L-mode-like particle confinement (see chapter 11). Back to the I-phase. Zonal flows can trigger the transition to high confinement by regulating the turbulence level and associated transport until the mean shear flow is high enough to suppress the remaining turbulence and associated transport, causing the pressure gradient to increase by radial force balance. As a result, the mean radial electric field shear increases to the point where it can maintain a

state of suppressed turbulence. Therefore, for sufficient high heating power (in H-mode) the pressure gradient increases with heating power and the profile is not stiff. For a faster heat power ramp, a classic L-H transition can occur, characterized by a single burst of zonal flow energy that extracts the most or all of the energy from the turbulence. This is followed by the collapse of the turbulence and onset of a strong radial electric field shear sustained by the ion pressure gradient [366].

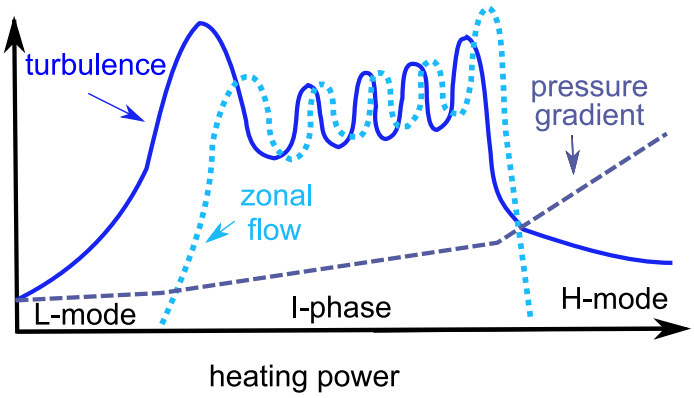

FIGURE 10.1: The picture of the L-H transition according to the Kim-Diamond model [360, 361].

All experimental investigations before 2012 have been dedicated to the temporal relationship between turbulence amplitudes, zonal flow amplitudes, and the evolution of the sheared background mean radial electric field; the results of these studies have been qualitatively consistent with the predator-prey model. However, an essential piece of the physics – namely the nonlinear exchange of energy between the turbulence (the prey) and the zonal flow (the first predator) in the presence of a background mean sheared $E \times B$ flow (second predator) has not been study during the L-H transition. In here presented work [13], the first study of this kind has been performed by inserting a suitably arranged Langmuir probe array inside the separatrix region of a discharge which undergoes an L-H transition. This provides the first quantitative measurement of the energetics of turbulence-zonal flow coupling during the L-H transition.

In order to motivate the data analysis strategy, it is useful to recapitulate a schematic set of coupled predator-prey equations for the zonal-flow – drift-wave system (Sec. 3.6.3). These are

$$\frac{\partial}{\partial t}\epsilon_T = \gamma_{eff}\epsilon_T - \langle \tilde{u}_r \tilde{u}_\theta \rangle \frac{\partial u_{ZF}}{\partial r}, \tag{10.1}$$

$$\frac{\partial}{\partial t}\epsilon_{ZF} = \langle \tilde{u}_r \tilde{u}_\theta \rangle \frac{\partial u_{ZF}}{\partial r} - \mu \epsilon_{ZF}. \tag{10.2}$$

Here $\epsilon_T = \langle \tilde{u}^2 \rangle$ and $\epsilon_{ZF} = \langle u_{ZF} \rangle^2$ are the turbulence and zonal flow energies, respectively, and γ_{eff} is a total, effective growth rate, including gradient drive,

mean shearing and nonlinear mixing. Thus $\gamma_{eff} = \gamma_{eff}(\nabla T, \nabla n, \langle \acute{u} \rangle, \epsilon_T, \ldots)$, which is addressed experimentally by studying fluctuation recovery rates γ_{eff} during the limit cycle regime occurring at the power threshold. The energy transfer given by the production term (Sec. 3.6.3)

$$\mathcal{P}_\perp = \langle \tilde{v}_r \tilde{v}_\theta \rangle \frac{\partial \langle v_{ZF} \rangle}{\partial r}, \tag{10.3}$$

is the Reynolds work of the fluctuations on the flow. $\langle \tilde{u}_r \tilde{v}_\theta \rangle \sim \pm \partial u_{ZF}/\partial r$ indicates negative (i.e. zonal flow growth) or positive (i.e. zonal flow damping) viscosity, respectively. This Reynolds work term is usually measured by bicoherence studies (Secs. 7.3.1 and 7.3.2) [142, 144, 301, 302, 317, 318, 367, 368]. However, bispectral analysis needs long stationary time series, which are generally not available in high-temperature fusion plasmas. Furthermore, the L-H transition is inherently non-stationary. Therefore, for estimating the energy transfer between the shear flow and the turbulence, we use an approach similar to that in Refs. [339, 11] in which the relevant quantities are computed in the time-domain using suitably filtered and averaged quantities. This approach is based on an K-ϵ model introduced in Sec. 3.6.2. Here μ is the total zonal flow damping rate, including collisional, charge exchange, and nonlinear damping. We do not present a direct measurement of μ here, but this might be approached by studying the decay rate of the zonal flow energy in the H-mode, when turbulence damping eliminates the Reynolds work source in the ϵ_{ZF} equation (10.2).

The obvious criterion for triggering of the L-H transition is $\partial \epsilon_T/\partial t < 0$, with a positive phase between $\langle \tilde{u}_r \tilde{u}_\theta \rangle$ and $\partial u_{ZF}/\partial r$ - i.e. negative viscosity which results in a net decay of the fluctuation energy. In this case, the zonal flow is sinking energy from the turbulence faster than the turbulence grows. This requires

$$\frac{\langle \tilde{u}_r \tilde{u}_\theta \rangle \frac{\partial \langle u_{ZF} \rangle}{\partial r}}{\gamma_{eff} \epsilon_T} > 1 \tag{10.4}$$

which emerges as a natural figure of merit for the collapse of the turbulence and the onset of transition. In terms of experimentally measurable quantities, Eq. (10.4) requires that the turbulence-to-zonal flow energy transfer $\mathcal{P}_\perp$ exceeds the change in turbulence intensity during a recovery period, i.e. $\mathcal{P}_\perp/\gamma_{eff}\langle \tilde{v}^2 \rangle > 1$. This condition then defines a criterion which the normalized energy transfer must satisfy. Thus a suitably arranged experiment can measure the appropriate quantities to test this model of the L-H transition.

Such an experiment has been carried out on the EAST tokamak [369]. The Reynolds stress has been measured with a Langmuir probe array consisting of three tips [368, 370, 364]. The probe array has been inserted $\sim$ 1.5 cm inside the separatrix as estimated by observing a break in the slope of the DC floating potential profile and also by estimating the separatrix position from reconstructions of the MHD equilibrium. Floating potential fluctuations are interpreted as plasma potential fluctuations. As discussed in Sec. 6.1 floating

potential measurements in high temperature experiments like EAST have to be taken with caution. Therefore, absolute numbers of the velocity might be corrupted by electron temperature fluctuations. Even the sign might change. However, also the structures in the electron temperature are tilted by the flow and therefore the Reynolds stress measurements by floating potential measurements should be proportional to the Reynolds stress and at least give the correct trend. One big advantage of Eq. (10.4) is that most systematic errors (even changes in sign) cancel each other due to the normalization.

The discharge shown in Fig. 10.2 in red has been reported in detail in Ref. [364]. For comparison also another discharge at similar plasma parameters is included in blue in the figures. Basic features of the discharge are shown in the original publications [13, 364]. At a second probe plunge the plasma is in the I-phase which exhibits multiple limit cycles. During this phase a zonal flow has been identified as a coherent mode at 2 kHz, which is driven by broadband turbulent fluctuations between 30 and 100 kHz [364]. The scale separation of the relevant quantities is necessary to extract their energy transfer by Eq. (10.3) which through the time-averaging operation requires the identification of the turbulent scales and (separately) the zonal flow scale. The effective growth rate γ_{eff} of the the first L-H transition is approximated by the turbulence recovery rate during the I-phase of the second plunge at similar parameters. The average turbulent energy recovery time has been estimated from 27 limit cycle oscillations in the dithering phase and found to be approximately 90 μs [13]. The net power input into the turbulence, which varies in proportion to the turbulent kinetic energy during the transition, is then given by $\gamma_{eff}\tilde{v}_{\perp}^2$.

Using the low-frequency intensity as an indicator for the zonal flow intensity is a common approach [367, 371, 368, 334]. Consistent with the observed frequencies for turbulent and flow scales, the Reynolds stress during the $L-H$ transition is calculated from high pass ($f > 15$ kHz) filtered floating potential fluctuations and the sheared flow from low pass ($f < 2$ kHz) filtered floating potential fluctuations which are then used to estimate the electric field and $E \times B$ drift motion. This scale separation is consistent with the previously identified regimes of turbulence and zonal flow in the EAST device [364]; however the results discussed below are not sensitive to the precise choice of these frequency bands and thus do not change the conclusions arising from the analysis. Measurements show that the poloidal velocity at the separatrix is small compared to the values at 1.5 cm inside. We thus take the poloidal velocity at the separatrix to be zero and calculate $\partial_r\langle u_\theta\rangle \approx -\langle u_\theta\rangle/\Delta r$, with $\Delta r = 1.5$ cm being the distance to the separatrix, allowing us to then estimate $\mathcal{P}_\perp \approx \langle\tilde{u}_r\tilde{u}_\theta\rangle\langle u_\theta\rangle/\Delta r$. It is unlikely that the probe is any deeper than 1.5 cm inside the LCFS (otherwise it would overheat and inject large quantities of impurities into the plasma). Therefore the estimated production values (shown in Fig. 10.2d) and e)) likely represent minima; actual production rates could be higher by as much as a factor of 2-3 determined mostly by uncertainties in the depth of probe penetration.

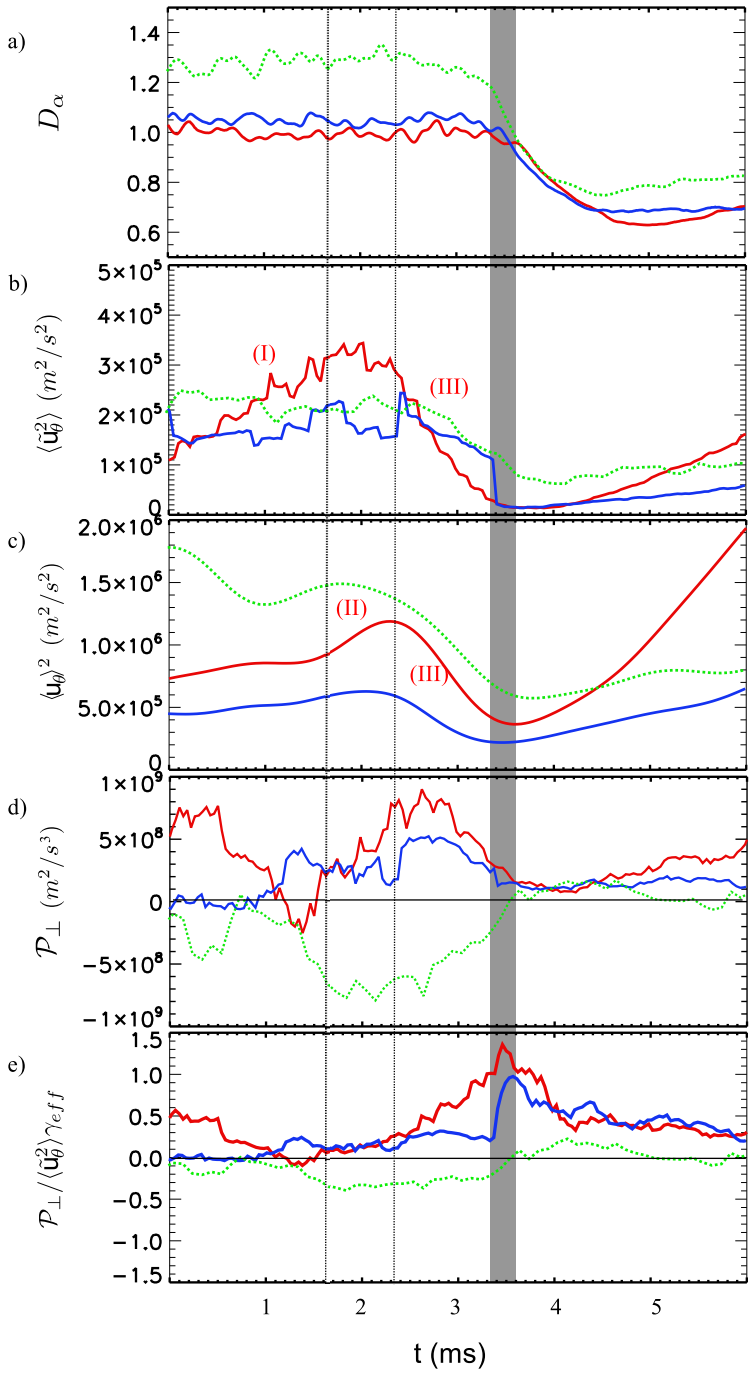

FIGURE 10.2: D_α (a), turbulent (b) and flow (c) fluctuation amplitude during L-H transition. Energy transfer between turbulence and shear flow (d) and normalized to turbulent fluctuation amplitude and energy recovery time (e). Data from 1.0-1.5 cm inside LCFS is denoted by blue and red curves. Data taken 1 cm outside of the LCFS in the SOL region denoted by green curve. Measurements have been carried out in EAST. Figure adapted from [13].

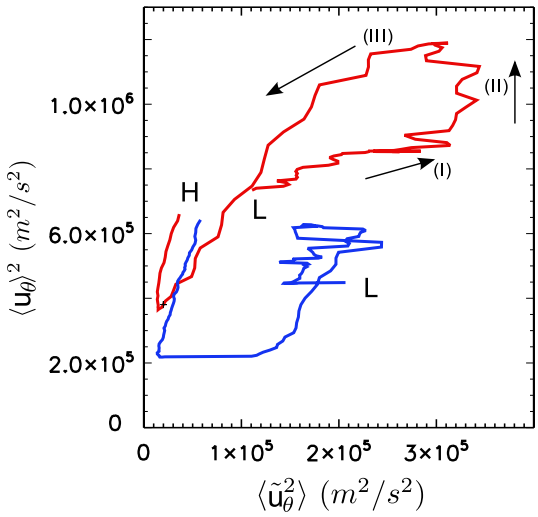

FIGURE 10.3: Hodograph of turbulent and flow energies during L-H transition. Measurements have been carried out on EAST. Figure adapted from [13].

Figure 10.2 shows the time traces of the D_α signal indicating an L-H transition. Here we have set $t = 0$ to correspond to the beginning of the drop in D_α for all of the discharges shown. To guide the eye the L-H transition is indicated by a gray box. The relation between the energy in the shear flow and the turbulence can also be represented by a hodograph as shown in Fig. 10.3 similar to that of Ref. [363]. In Figures 10.2 and 10.3 we define several key periods in the transition as phase (I), phase (II), and phase (III). The evolution of the kinetic energy in the turbulence and low frequency flow across this transition are shown in Figs. 10.2b and c. The results show that 3 ms before the L-H transition the turbulent fluctuation amplitude (Fig. 10.2b) increases defining phase (I) of the transition. At about 1 ms before the L-H transition the kinetic energy in the low frequency flow (Fig. 10.2c) builds up and the energy in the higher frequency fluctuations (Fig. 10.2b) drops, defining phase (II) of the transition. The growth of the flow appears on the fast, turbulent time scales (i.e. 100's of μs) providing a strong indication that the flow is turbulence generated, and therefore a zonal flow. We observe a small phase lag between flow and turbulent energy (Fig. 10.2b and c) consistent with the predator (zonal flow) following the prey (turbulence) in time. Once the shear flow grows to large enough amplitude, the turbulence induced flow shear then causes a reduction in the turbulent amplitude and the flow then begins to decay, defining phase (III) in the transition, consistent with observations in TJ-II [363]. The delay between the reduction in the turbulent amplitude and the drop of the D_α (Fig. 10.2a and b) most likely corresponds to a combination of the time needed for cross-field transport and parallel flow from the midplane region to the divertor region where the D_α emissions are observed. The kinetic energy transfer $\mathcal{P}_\perp$ from the turbulence into the shear flow continues to increase while the tur-

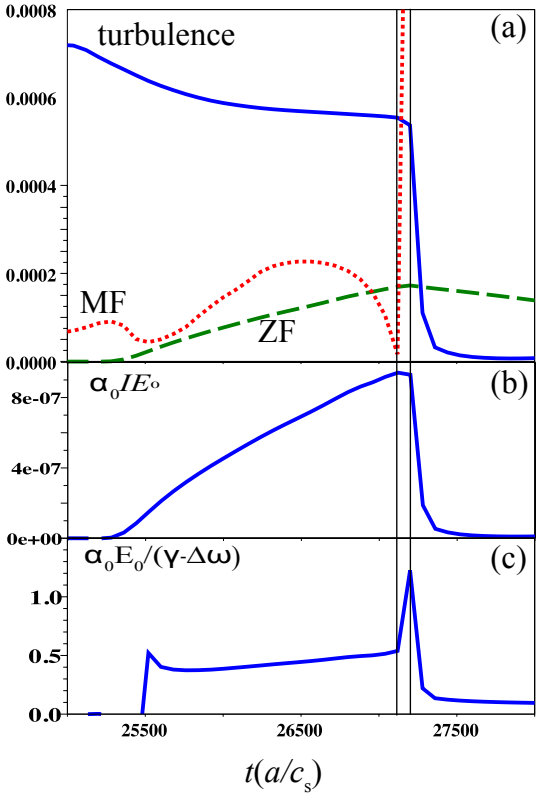

FIGURE 10.4: Predator-prey model with fast power ramp up. Evolution of the turbulent, zonal flow (ZF) and mean flow (MF) amplitudes (a), the zero frequency ZF shearing (b) and normalized energy transfer (c). Model is described in detail in [366], figure adapted from [13].

bulence amplitude is decreasing (Fig. 10.2d) during phase (III), while the L-H transition is approached as shown in Fig. 10.2d). This confirmed the earlier conjecture above the low frequency flow being actually driven by a transfer of energy from the turbulence. About 1 ms before the L-H transition occurs, the kinetic energy transfer $\mathcal{P}_\perp$ peaks. To evaluate whether this energy transfer is sufficient to reduce the turbulence level significantly the transfer rate must be compared to the energy input rate into the turbulence as discussed above. Using experimental data, we find the ratio of the production, $\mathcal{P}_\perp$, normalized by $\gamma_{eff}\langle\tilde{u}_\perp^2\rangle$ in Figure 10.2e. This ratio indicates the power transfer rate into the shear flow normalized by the power transfer into the turbulence from the combined effects of the free energy source and the background E_r shearing during periods of weak flow. As the D_α signal starts to drop (the traditional measure of the start of the L-H transition) the turbulence has already reached its minimum. Commensurate with the drop in D_α signal the flow production rate surpasses the turbulence recovery rate and the turbulence energy collapses to nearly zero. After the peak of the normalized production rate, the production $\mathcal{P}_\perp$ remains small. The low frequency flow begins to recover (Fig. 10.2c),

suggesting that after the transition the flow is sustained by non-turbulent processes. The growth of the radial electric field and associated flow shear after the drop in D_α light has already been shown to be associated with the growth of the ion pressure gradient [372]. No ion temperature profiles are available here, but the observation here is consistent with earlier result. Furthermore, in an analysis of similar data obtained just outside of the separatrix (shown in green in Fig. 10.2), no such transient behavior is observed. This indicates that these observations are isolated to the region inside the LCFS, and that on open field lines the turbulence amplitude simply collapses after the H-mode transition, as has been reported earlier [373].

The one-space, one-time multiple shearing predator-prey model [366] is used for comparison with the experimental results reported here from EAST. A fast ramp of the heating power is used to model the regular L-H transition. Under these conditions no limit-cycle oscillations are observed. Instead, a single burst of zonal flow energy and turbulence collapse is observed, followed by a classic L-H transition. A typical time trace around the L-H transition is shown in Fig. 10.4. Here Fig. 10.4a depicts the evolution of the amplitudes of the turbulence I, the zonal flow E_0^2 and the mean flow. The modest decrease of turbulence I in the early part of the model evolution is triggered by a rapid growth of the mean flow, or a decorrelation of turbulence drive by mean flow shearing. The coupling between the zonal flow and the turbulence is given by $\alpha_0 I E_0^2$, where α_0 is the coupling parameter between them. As seen in Fig. 10.4b the coupling increases toward the L-H transition. A small increase of zonal flow and a decrease of turbulence leads to a large peak in the production rate, normalized to the net energy input rate (Fig. 10.4c). This peak is a trigger of a rapid quench of turbulence, i.e. the L-H transition. Comparing the experimentally observed normalized energy production $\mathcal{P}_\perp/\gamma_{eff}\tilde{u}_\perp^2$ to the results in Fig. 10.4c, we observe a very similar peaking in the normalized energy production rate in both experiment and model.

Obtaining these types of probe data - which provide the key physics data needed to test the role of turbulence-zonal flow coupling in the L-H transition - is technically challenging and thus data from only a few discharges are available. Taken in isolation, such observations would not be sufficient to make a firm claim that the role of the zonal flow as a trigger mechanism for the L-H transition has been conclusively demonstrated. However, the results reported here cannot be viewed in isolation, but rather must be seen as building on the substantial body of evidence that turbulence-driven zonal flows or GAMs play an important role in triggering the L-H transition. For example, the observed transient shear flow just prior to the L-H transition certainly exhibits several features that are consistent with it being a zonal flow. In particular, it shows a strong bicoherence and Reynolds stress modulation indicating the nonlinear drive by the turbulence, features a toroidal mode number of zero and exhibits the characteristic predator-prey oscillations [364]. These features have been observed not only in EAST [364]. The limit-cycle behavior between the radial electric field and the turbulent amplitude just prior to the L-H transition has

also been shown in TJ-II [363]. Afterward, ASDEX-Upgrade [362] and DIII-D [365] have investigated these limit-cycles in detail documenting the existence of the I-phase. Both devices reported strong oscillations in the shearing rates in this regime showing the importance of time-varying shear flows during the limit-cycles. Where ASDEX Upgrade reported geodesic acoustic modes responsible for the limit-cycle behavior [362], the work on DIII-D points to low frequency zonal flows [365]. However, both emphasize the importance of turbulence generated shear flows. The new evidence reported here builds on these earlier results by investigating the physics of the trigger mechanism directly, by estimating the suppression strength due to the generation of these shear flows and by comparing the generation rate of the shear flows to the energy input rate from the free energy source. The present estimation (even though rough, but novel) shows that the zonal flow is strong enough to suppress the turbulence over a sufficient time so that a transition into the H-mode can occur. A comparison with the predator-prey model is able to reproduce these essential features. Taking together all these observations in different devices with different diagnostics and the good agreement with present modeling [366] provide evidence that the basic physical mechanism triggering the L-H transition is reasonably well captured by the Kim-Diamond model [361]. However, it is explicitly pointed out that other routes to the L-H transition may also exist, too.

In summary, the energies of as well as the energy transfer between low frequency shear flows and the ambient turbulence have been estimated during the L-H transition for the first time. In an L-H transition that does not exhibit an I-phase (as in [362, 365]), a transient increase in the zonal flow and turbulent stress are observed showing the important role of zonal flows in the L-H transition. When the rate of energy transfer from the turbulence into the zonal flow becomes comparable to the power input into the turbulent kinetic energy, then the turbulence amplitude collapses. The turbulent transport then drops, resulting in a decrease in the fueling of the open field line region. As a result the D_α signal in the divertor drops. Based on earlier results, it can be expected that the edge pressure gradients build up, resulting in the formation of a growing radial electric field just inside the LCFS which then sustains the turbulence suppression via the $E \times B$ shearing mechanism. As a result, the system is driven into the H-mode. The results reported here thus indicate that the strong turbulent suppression associated with this energy transfer from the turbulence into the zonal flow acts to trigger the L-H transition.

10.2 Ballooned transport induced Stringer-spin up

10.2.1 Magnetic signature around the L-H transition in ASDEX Upgrade

It has been observed that magnetic field fluctuations are strongly correlated with turbulent fluctuations in the I-phase of ASDEX Upgrade [62, 374]. Figure 10.5 shows different fluctuating time traces: the top row shows the Doppler shift (Fig. 10.5a) and the amplitude (Fig. 10.5b) measured by Doppler reflectometry (Sec. 6.2.2) proportional to velocity and density fluctuations, respectively. Figure 10.5c shows the fluctuations in the divertor current proportional to the transport. The bottom row shows the poloidal magnetic field fluctuations $\dot{B}_\theta$ measured at C09-23 (see Fig. 6.4). By comparing these four time series the magnetic field fluctuations are strongly correlated with the other signals and show the clearest signature. The predator-prey model [360, 361] (see Fig. 10.1) introduced in previous section (Sec. 10.1) does not include any electromagnetic effects. The question arises what is the reason of these fluctuations and what are their role within the I-phase?

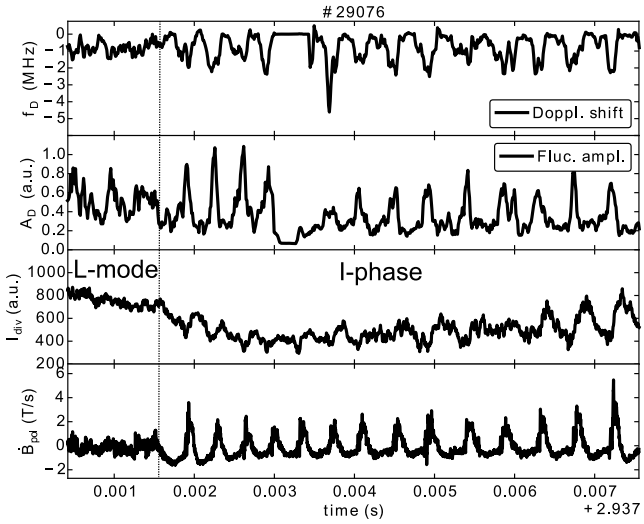

FIGURE 10.5: A transition from L-mode to I-phase in ASDEX Upgrade indicated by the vertical line. Fluctuations in the velocity are shown by the Doppler shift f_D (a), the amplitude of the fluctuations can be approximated by the amplitude A_D measured by the Doppler reflectometer (b), the divertor current I_{div} is proportional to the transport (c) and the time derivative of poloidal magnetic field fluctuations $\dot{B}_{pol}$ measured above the inner divertor C-09-23 (d).

To obtain a global picture of the poloidal mode structure the cross-correlation between different poloidally displaced Mirnov coils on a poloidal cross-section has been calculated. During the I-phase in ASDEX Upgrade the magnetic

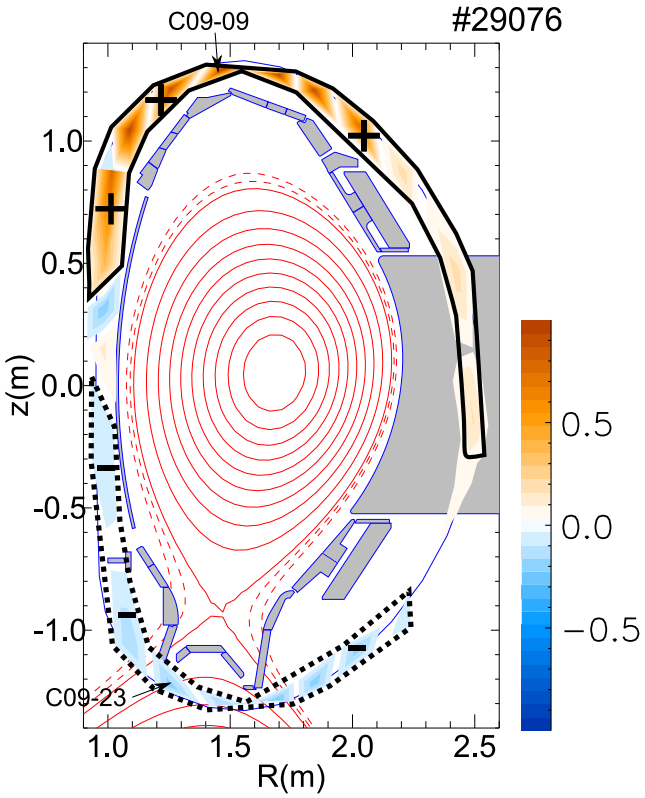

FIGURE 10.6: Poloidal mode structure from cross-correlation of poloidally displaced Mirnov coils (C09-09 is the reference coil) at the same toroidal position. Figure taken from Ref. [14]. Details of this particular discharge can be found in Ref. [375]. The shown feature, however, is universal for the I-phase in AUG.

fluctuations exhibit a pronounced up-down asymmetry as shown in Fig. 10.6. This corresponds to a poloidal mode number of $m = 1$. For the measurement of the toroidal mode structure an array of poloidal field pick-up coils, which is spread along the toroidal coordinate at fixed poloidal angle, was used (C09-17, C10-21, C04-17, C05-21, C07-17 in Fig. 6.4). The mode number is determined by the slope of a linear fit through the coil phases plotted over the coil positions [287]. The low-frequency oscillations exhibit a dominant $n = 0$ structure, where n is the toroidal mode number [14]. Therefore the magnetic structure is toroidally symmetric ($n = 0$) and up-down asymmetric ($m = 1$).

Similar magnetic oscillations have been recently observed in the I-phase of EAST [26] and HL-2A plasmas [376]. It has been proposed that these magnetic fluctuations are induced by the fluctuations of the equilibrium pressure gradient due to the equilibrium condition $\nabla p = \mathbf{J} \times \mathbf{B}$ [376, 26]. However, such fluctuations would exhibit an in-out asymmetry as they are carried by the Pfirsch-Schlüter current ($\langle \tilde{J}_\parallel \cos s \rangle$ with parallel current $\tilde{J}_\parallel$, ballooning angle s and zonal average $\langle \cdot \rangle$ as described below). This is explained in detail in Sec. 5.2.3. While the poloidal symmetry of the fluctuations has not been

studied in the tokamak HL-2A, the magnetic fluctuations in EAST show an up-down asymmetry instead of the expected in-out asymmetry of the Pfirsch-Schlüter current. The fluctuations are essentially the same as those in the M-mode (which seems to be the I-phase too) observed in JET with 'unknown origin' [377, 378] showing also an $m = 1$ mode with up-down asymmetry. Recently also the GLOBUS-M spherical tokamak found an up-down asymmetry of the poloidal magnetic field oscillations during I-phase [379].

Where additional Pfirsch-Schlüter current perturbations cannot be excluded, on AUG the up-down asymmetry $\langle \tilde{J}_\parallel \sin s \rangle$ is much more pronounced in amplitude than the in-out asymmetry [374]. Therefore, the focus of the present investigation is on the up-down asymmetric component. As shown in the following (Sec. 10.2.2) these fluctuations can result as a response to the transport events during the I-phase and are not related to the Pfirsch-Schlüter balance of the equilibrium.

Furthermore, as shown in Ref. [374] the limit cycle oscillations show magnetic precursors similar to those of type-III ELMs (Sec. 2.2.2). Also type-III ELMs can be modeled by reduced models [380, 381]. The limit cycles observed in reduced models of type-III ELMs result from the interaction of the gradient with the turbulence (as those limit cycles shown on the r.h.s. of Fig. 10.17), while limit cycle oscillations resulting from the interaction of zonal flows and turbulence should favor the limit-cycle behavior as shown on the left hand side of Fig. 10.17. These typ-III-ELM-like precursors are also observed in the I-phase of COMPASS [382]. A model describing these magnetic fluctuations based on the DALF model has been developed [383].

10.2.2 Stringer spin-up sideband balance

In the following an evolution equation for the up-down asymmetry in current and flows is deduced from the DALF model (see Sec. 5.2) similar to the derivation of the in-out asymmetric current and flow, which is the Pfirsch-Schlüter current or flow (see Sec. 5.2.3). Whereas the Pfirsch-Schlüter current is coupled to the zonal flow and geodesic acoustic mode (see Sec. 5.2.3) the up-down asymmetric current will be shown to be coupled to the ballooned transport and the Stringer spin-up.

The experimentally observed up-down asymmetry ($\sin s$) in the parallel current $\tilde{J}_\parallel$ as described in the second section can be written as $\langle \tilde{J}_\parallel \sin s \rangle$. The evolution can be obtained from Eq. (5.11) multiplied with $\sin s$ for the up-down asymmetry and zonally averaged afterward

$$\begin{aligned} \tfrac{\partial}{\partial t}\langle(\hat{\beta}\tilde{A}_\parallel + \hat{\mu}\tilde{J}_\parallel)\sin s\rangle = \; & -\frac{\partial}{\partial x}\langle \hat{\mu}\tilde{u}_{Ex}\tilde{J}_\parallel \sin s\rangle \\ & +\langle \tilde{b}_x \left(\frac{\partial \tilde{p}}{\partial x} - \frac{\partial \phi}{\partial x}\right)\sin s\rangle \\ & -\langle (p - \tilde{W})\cos s\rangle \\ & -C\langle \tilde{J}_\parallel \sin s\rangle. \end{aligned} \tag{10.5}$$

Here, $\langle \sin s \nabla_\parallel p \rangle = \langle \nabla_\parallel (p \sin s) \rangle - \langle p \nabla_\parallel \sin s \rangle = -\langle p \cos s \rangle$ is used since the zonal average of parallel derivatives vanishes. Up-down asymmetric current perturbations are coupled to the in-out asymmetric pressure and vorticity sidebands via $\langle (p - \tilde{W}) \cos s \rangle$ which will be investigated later. Due to $\langle \tilde{u}_\parallel \sin s \rangle = \langle \tilde{v}_\parallel \sin s \rangle + \langle \tilde{J}_\parallel \sin s \rangle$ up-down asymmetric current perturbations are coupled to up-down asymmetric flow perturbations which are investigated next. The up-down asymmetry in parallel momentum evolves according to $\langle$Eq. (5.12)$\cdot \sin s \rangle$

$$\begin{aligned} \hat{\epsilon} \tfrac{\partial}{\partial t} \langle \tilde{u}_\parallel \sin s \rangle = \; & -\frac{\partial}{\partial x} \langle \hat{\epsilon} \tilde{u}_{Ex} \tilde{u}_\parallel \sin s \rangle \\ & - \langle \tilde{b}_x \frac{\partial \tilde{p}}{\partial x} \sin s \rangle \\ & + \langle p \cos s \rangle - \mu_\parallel \langle \tilde{u}_\parallel \sin s \rangle. \end{aligned} \tag{10.6}$$

Up-down asymmetric flows are driven by the up-down asymmetric radial-parallel Reynolds stress $\langle \hat{\epsilon} \tilde{u}_{Ex} u_\parallel \sin s \rangle$ and saturated by the parallel ion viscosity $\mu_\parallel$. The up-down asymmetric radial-parallel Reynolds stress is the up-down asymmetric parallel momentum transport, which is large as the symmetry of the gyrokinetic distribution function $f(s, v_\parallel) = f(-s, -v_\parallel)$ gives an up-down asymmetric statistical moment of parallel momentum and due to ballooning of the potential the parallel momentum transport is up-down asymmetric [384]. This asymmetry is also the reason for the need of parallel symmetry breaking for intrinsic rotation, which is not needed to generate an up-down asymmetric flow. Additionally a coupling of the up-down symmetric flow $\langle \tilde{u}_\parallel \sin s \rangle$ with the in-out asymmetry in the pressure $\langle p \cos s \rangle$ is found, where the evolution of the latter is given by $\langle$Eq. (5.10) $\cdot \cos s \rangle$

$$\begin{aligned} \tfrac{\partial}{\partial t} \langle p_e \cos s \rangle = \; & -\frac{\partial}{\partial x} \langle \tilde{u}_{Ex} p_e \cos s \rangle \\ & - \frac{\partial}{\partial x} \langle \tilde{b}_x \tilde{v}_\parallel \cos s \rangle + \langle \tilde{J}_\parallel \sin s \rangle - \langle \tilde{u}_\parallel \sin s \rangle \\ & - \frac{\omega_B}{2} \langle (\frac{\partial p}{\partial x} - \tilde{u}_y) \sin 2s \rangle. \end{aligned} \tag{10.7}$$

The in-out asymmetry in the pressure can be understood as an in-out movement of the plasma column or by a local flattening of the pressure profile on the low field side. It can result from ballooned transport $\langle \tilde{u}_{Ex} p_e \cos s \rangle$. Another drive is an up-down asymmetric parallel electron flow $\langle \tilde{v}_\parallel \sin s \rangle$, which is connected to the parallel ion flow and current by $\langle \tilde{v}_\parallel \sin s \rangle = \langle \tilde{u}_\parallel \sin s \rangle - \langle \tilde{J}_\parallel \sin s \rangle$. In particular the ballooned transport $\langle \tilde{u}_{Ex} p_e \cos s \rangle$ can be expected to be quite large and could provide the most important turbulent drive for the here described sideband balance. Elongation of the magnetic equilibrium introduces $m = 2$ modes [385, 386], which appear to drive in-out asymmetric pressure disturbance by $\langle (\frac{\partial p}{\partial x} - \tilde{u}_y) \sin 2s \rangle$ which contains coupling to the pressure gradient $\partial p / \partial x$ as well as to the perpendicular flow $\tilde{u}_y = \partial \tilde{W} / \partial x$ with ion stream function $\tilde{W}$. The term arises from the curvature $\langle \cos s \mathcal{K} (\tilde{\phi} - p) \rangle = \langle \omega_B \frac{\partial}{\partial x} (\tilde{\phi} -$

$p)\cos s \sin s\rangle$ with the geodesic contribution to the curvature $\mathcal{K} = \omega_B \sin s \frac{\partial}{\partial x}$. Now $\cos s \sin s = \frac{1}{2}\sin 2s$ induces the coupling to the second harmonic. In general, a disturbance of the axis-symmetry of the magnetic equilibrium can drive in-out asymmetric pressure perturbations as well as in-out asymmetric flow perturbations.

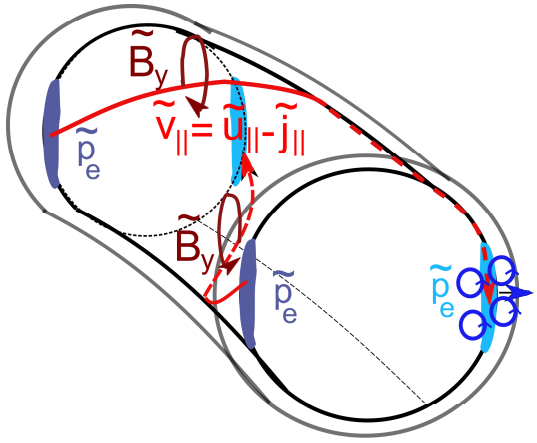

FIGURE 10.7: Schematic view of the Stringer spin-up sideband balance.

The evolution of this sideband system is closed by the in-out asymmetric vorticity $\langle\tilde{\Omega}\cos s\rangle = \langle\nabla_\perp^2 \tilde{W}\cos s\rangle$

$$\begin{aligned}\frac{\partial}{\partial t}\langle\tilde{\Omega}\cos s\rangle = \; & -\frac{\partial^2}{\partial x^2}\langle\tilde{u}_{Ex}\tilde{u}_y\cos s\rangle \\ & +\frac{\partial^2}{\partial x^2}\frac{1}{\hat{\beta}}\langle\tilde{b}_x\tilde{b}_y\cos s\rangle \\ & +\langle\tilde{J}_\parallel\sin s\rangle - \frac{\omega_B}{2}\langle\frac{\partial p}{\partial x}\sin 2s\rangle. \end{aligned} \tag{10.8}$$

Besides the disturbance of the axis-symmetry of the equilibrium, the in-out asymmetric vorticity is coupled to the ballooned perpendicular Reynolds stress and again the up-down asymmetry in the parallel current. Therefore also in an up-down symmetric equilibrium a ballooned perpendicular Reynolds stress leads to up-down asymmetric parallel current perturbations $\langle\tilde{J}_\parallel\sin s\rangle = \frac{\partial^2}{\partial x^2}\langle\tilde{v}_{Ex}\tilde{u}_y\cos s\rangle$. Due to the coupling of the in-out asymmetry in the pressure and flow, up-down asymmetric parallel current perturbations can be expected.

In conclusion, the observed up-down asymmetric magnetic fluctuations $\langle\tilde{J}_\parallel\sin s\rangle$ are coupled to up-down asymmetric flow perturbations $\langle\tilde{u}_\parallel\sin s\rangle$ via $\langle\tilde{u}_\parallel\sin s\rangle = \langle\tilde{v}_\parallel\sin s\rangle + \langle\tilde{J}_\parallel\sin s\rangle$ and in-out symmetric pressure $\langle p\cos s\rangle$ via Eqs. (10.5) and (10.7). Furthermore it is coupled to vorticity (as well as binormal shear flow) $\langle\tilde{\Omega}\sin s\rangle$ perturbations via Eqs. (10.5) and (10.8). Ballooned transport and Reynolds stress as well as the up-down asymmetric parallel-radial Reynolds stress are involved in the sideband balance. All these quantities cannot be expected to be small a priori. The induction of an up-down

asymmetric parallel flow $\langle \tilde{u}_\parallel \sin s \rangle$ by the ballooned transport $\langle \tilde{v}_{Ex} p_e \cos s \rangle$ is known for a long time. This is the *Stringer spin-up* [387, 388].

Based on the above derivation of the evolution equation of the up-down asymmetry in the current a simplified picture can be drawn as shown in Fig. 10.7. Strongly ballooned transport $\langle \tilde{u}_{Ex} p_e \cos s \rangle$ leads to an in-out asymmetry in the pressure $\langle p \cos s \rangle$, which directly induces an up-down asymmetry in flows and currents.

The presented set of equations (10.5)-(10.8) allows for multiple limit-cycle scenarios as shown in detail in the original reference [14].

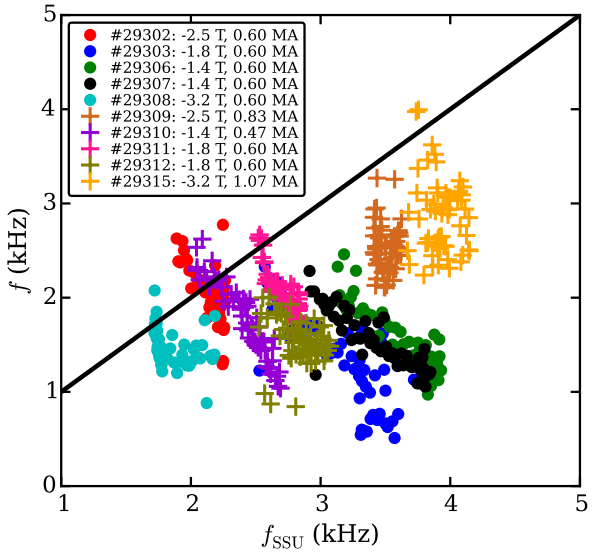

FIGURE 10.8: Stringer spin-up relaxation frequency $f_{SSU} = c_s/(2\pi qR)$ against limit-cycle frequencies of several AUG discharges.

As an example the ion relaxation of the ballooned transport is shown here. Replacing the parallel electron Eq. (10.5) by that of the ions (10.6) gives a coupling of the ballooned transport with the up-down asymmetric flow, which is the Stringer spin-up [387, 388]. Linearizing both equations gives $i\omega_{SSU}\langle \tilde{u}_\parallel \sin s \rangle = \frac{(1+\tau_i)}{\hat{\epsilon}} \langle p_e \cos s \rangle$ and $i\omega_{SSU}\langle p_e \cos s \rangle = -\langle \tilde{u}_\parallel \sin s \rangle$ corresponding to an eigenfrequency of $\omega_{SSU} = \sqrt{(1+\tau_i)/\hat{\epsilon}}$ (renormalization gives $f_{SSU} = c_{si}/(2\pi qR)$). Note that this scaling is by a factor $1/(\sqrt{2}q)$ smaller than the GAM frequency. This scales as $f_{SSU} \sim 1/q \sim I_p$ similar to the observation in the M-mode in JET [377] which scales with the poloidal Alfvén velocity [378]. It cannot explain the result of the multivariate linear regression for AUG limit cycles which gives $f_{I-phase} \sim 1/\beta_{t,ped} q_{95}^{3/2}$ with the toroidal plasma beta $\beta_{t,ped}$ measured in the pedestal [374]. Still, a comparison with the recent data base of I-phase discharges [374] shows an overall good qualitative agreement (Fig. 10.8). The experimental frequencies are below the frequency predicted by the Stringer spin-up relaxation frequencies. It seems that this relaxation gives

an upper boundary for the I-phase frequency. The inclusion of any kind of damping in the equation system would reduce f_{SSU}. However, considering the derivation of f_{SSU} is done for a simple large aspect ratio circular plasma. The corresponding GAM frequency of $f_{GAM} = \sqrt{2}c_{si}/2\pi R$ also predicts smaller frequencies as actually measured in the edge in AUG [389]. Taken divertor shaped equilibria may substantially improve the agreement between experiment and theory.

10.3 Magnetic shear induced Reynolds stress

Understanding the influence of a complex magnetic field structure on plasma turbulence opens up new perspectives for the optimization of transport and significant improvements of confinement in magnetically confined fusion plasmas. One important example where the magnetic configuration influences the confinement is the position of the X-point. In the unfavorable configuration, where the ion ∇B drift is directed away from the X-point, the power threshold of the L-H transition is higher than in the favorable configuration, where the ion ∇B drift is directed towards the X-point [390, 391, 392]. The underlying mechanism so far is still unknown.

Two of the main parameters determining confinement of magnetic fusion plasmas are magnetic and flow shear [393]. Flow shear, as well as magnetic shear, leads to a tilt of turbulent structures in the plane perpendicular to the magnetic field. The tilt of turbulent structures corresponds to a finite Reynolds stress. There are possible synergistic effects of magnetic and flow shear. Stronger magnetic shear leads to narrower layers of the zonal vorticity which is beneficial for confinement [394]. It is known that magnetic shear contributes to the $E \times B$ flow shearing rate [395, 396] and exhibits a contribution to the Reynolds stress [397]. This contribution can be due to a coupling to the radial-parallel Reynolds stress $\langle \tilde{u}_x \tilde{u}_\parallel \rangle$ by the sheared slab approximation as in Ref. [397], however the tilt due to the magnetic shear can also directly influence the Reynolds stress as explained in the following.

The Reynolds stress is subject to change due to geometric modifications of the boundary conditions [398]. In a single null configuration the X-point breaks the poloidal symmetry of the magnetic shear induced tilt of turbulent structures, transmitting a finite contribution of the Reynolds stress to the flux-surface average. This residual Reynolds stress works either to reinforce or weaken the background flow shear. The sign of the residual stress depends on the magnetic configuration. In one configuration the flow shear is stronger and favorable and in the other the flow shear is weaker, which is unfavorable. Indeed changes of the energy transfer rate from the turbulence into the low frequency zonal flow (proportional to the Reynolds stress) are observed with changing poloidal position of the X-point [272]. The poloidal position of the limiter could have similar effects in principle.

For comparison with the dynamics in physical space, zonal flow modeling

intrinsically requires flux surface averaged values of the Reynolds stress. However, not much is known about the spatial distribution of the Reynolds stress. In recent studies at the stellarator TJ-K [40], the Reynolds stress turned out to be strongly inhomogeneous on a flux surface. Thus, local measurements have to be interpreted with caution when comparing with theoretical predictions. This section reports on the natural poloidal structure of the Reynolds stress as a result of purely magnetic shear in tokamak experiments. In addition, the impact of the poloidal limiter position and the presence of an X-point on the flux-surface averaged Reynolds stress is investigated by means of turbulence simulations. The present section is based on Ref. [15].

In the following, the effect of magnetic shear on turbulent structures is compared to the effect of flow shear in the next Sec. 10.3.1. The development of residual Reynolds stress due to magnetic shear is also described in this section. The impact of divertor geometry on the poloidal pattern of the Reynolds stress is discussed and subsequently studied by means of flux-coordinate independent fluid simulations done with GRILLIX [399] in Sec. 10.3.2. At present, GRILLIX does not feature finite ion temperatures. Therefore, a self-consistent radial electric field is not present and the impact of the magnetic shear induced Reynolds stress on the radial electric cannot be studied with GRILLIX for the time being. Instead, we use the gyrofluid code GEMR [400, 190] to study this effect. GEMR includes a self-consistent equilibrium, but does not include X-point geometry. The impact of different limiter positions on the radial electric field and the Reynolds stress will be discussed and subsequently studied in the circular-limited configuration using Tore Supra parameters, by means of field-aligned gyrofluid simulations in Sec. 10.3.3.

10.3.1 Magnetic shear induced tilt of turbulent structures

In the presence of magnetic shear $\hat{s} = \frac{\rho}{q_s}\frac{dq_s}{d\rho}$ (with radial coordinate ρ and safety factor q_s) turbulent structures are progressively tilted as illustrated in Fig. 10.9. For positive magnetic shear $\hat{s} > 0$ the safety factor q_s is increasing with the radius. The field lines further outwards are less strongly twisted than further inwards. One can also understand this from the definition of the safety factor $q_s = N/M$, the ratio of toroidal N to poloidal revolutions M, corresponding to the ratio of the toroidal n to the poloidal mode number m. For $q_s = m/n$ increasing with radius ($\hat{s} > 0$), the poloidal mode number for a given toroidal mode number is increasing, hence the distance between the structures reduces with increasing radius. Whereas for the flux surfaces further inwards the poloidal mode is decreasing, hence the distance between the structures increases. In any case, magnetic shear leads to a poloidal tilt of magnetic flux tubes and associated turbulent structures. The tilt of the structures is equivalent to a finite Reynolds stress which is given by $\langle \tilde{u}_x \tilde{u}_y \rangle$. In a plasma with circular cross-section the structures above and below the midplane are tilted in opposite directions (Fig. 10.9). Thus, the tilt induced

by magnetic shear is up-down asymmetric. The geodesic curvature κ_g in a tokamak with circular cross-section changes sign at the midplane and has a sinusoidal form with minimum and maximum at bottom and top. In Ref. [40] it has been found that the poloidal distribution of the Reynolds stress roughly follows the geodesic curvature. At smaller radii the flow is low and above the midplane the outer flow would point downwards (negative shear) whereas below the midplane the outer flow would point upwards (positive shear). In a limited plasma with circular cross section the confined region is poloidally symmetric, and therefore the magnetic shear should not affect the zonally averaged Reynolds stress. Therefore, only if the poloidal symmetry is broken, can magnetic shear lead to a residual contribution to the zonal flow drive.

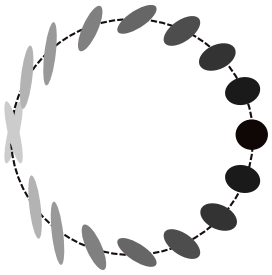

FIGURE 10.9: Illustration of the tilt of turbulent structures by magnetic shear. It is shown how turbulent structures are tilted by the magnetic shear. The tilt induced by magnetic shear is up-down asymmetric. Figure taken from Ref. [15].

Once a residual Reynolds stress is induced by the magnetic shear, it may act as a seed tilt, which can be self-amplified by the interaction of zonal flows and turbulence [398]. The Reynolds stress as the correlation between radial and perpendicular velocities $\langle \tilde{u}_x \tilde{u}_y \rangle \sim -k_x k_y |\tilde{\phi}^2|$ is proportional to the tilt which can be written in wavenumber space as $k_x k_y$. In an eikonal representation the radial wavenumber is subject to a change $k_x = -k_y \frac{\partial u_y}{\partial x} \tau_c$ if exposed to a sheared flow u_y over the correlation time τ_c. The magnetic shear $\hat{s}$ can lead to a tilt similar to the flow shear. Structures born at a particular position θ_0 (for example the outboard midplane $\theta_0 = 0$ for curvature-induced instabilities), which follow magnetic field lines are progressively tilted by the magnetic shear $k_x = k_y \theta \hat{s}$ [398, 401], where θ is the poloidal ballooning angle. The $\hat{s}$-induced Reynolds stress is given by [398, 401]

$$\Pi_{\hat{s}}(\theta) = -\hat{s}\theta \langle \tilde{u}_x^2(\theta) \rangle_t, \tag{10.9}$$

where $\langle \cdot \rangle_t$ denotes time average. The $\hat{s}$-residual Reynolds stress is given by the flux surface average $\langle \Pi_{\hat{s}}(\theta) \rangle_\theta$. In the case of a poloidally symmetric plasma, $\langle \Pi_{\hat{s}} \rangle_\theta$ vanishes. An imbalance between positive tilt and negative tilt can be provided by a poloidal truncation of the ballooning envelope, which can be provided by X-point resistivity [402] for diverted plasmas or the limiter position for limited plasmas [398, 401].

The derivation of Eq. (10.9) has been based on infinitesimal changes of the radial wavenumber by infinitesimal changes of the phase due to the effect of magnetic shear. For this reason Eq. (10.9) is valid only for an infinitesimal distance $\Delta\theta = \theta - \theta_0$ from the original poloidal angle θ_0, where the structure originates. This forces a linear dependence of Eq. (10.9) on the poloidal angle θ. However, the entire behavior of the tilt is important, because what matters in the end is the flux-surface average of this quantity and only taking into account a narrow or even infinitesimal region around the low-field side midplane might not be a good approximation. Since the turbulence level is high at the midplane on the low-field side, one might be tempted to argue that only this region matters, however, one must not forget that the $\hat{s}$-induced Reynolds stress is small due to the linear θ dependence. Also Eq. (10.9) allows only for a periodic solution, important for the confined region, if $\tilde{u}_x^2(\theta)$ vanishes at the opposite ballooning angle to the angle where the structures are generated $\tilde{u}_x^2(\theta_0 + \pi) = 0$. On the high-field side differently sheared structures coalesce coming from above and below the midplane. This leads to a cancellation of the $\hat{s}$-induced Reynolds stress. To take the coalescence into account, Eq. (10.9) can be modified according to

$$\Pi_{\hat{s}} = u_x^2(\theta_0) \left(e^{-\frac{(\theta-\theta_0)^2}{\Delta\theta^2}} \hat{s}(\theta - \theta_0) - e^{-\frac{(2\pi-\theta+\theta_0)^2}{\Delta\theta^2}} \hat{s}(2\pi - \theta + \theta_0) \right) \tag{10.10}$$

using $\tilde{u}_x^2(\theta) = \tilde{u}_x^2(\theta_0) e^{-\frac{(\theta-\theta_0)^2}{\Delta\theta^2}}$ as in Ref. [398]. This would provide a sinusoidal pattern of the Reynolds stress induced by tilt due to the magnetic shear as expected from basic considerations shown in Fig. 10.9.

It should also be noted that the flow shear V' used in Refs. [398, 401] is subject to variation along the poloidal angle. As the potential is a flux-function it should be constant on a flux-surface, but the $E \times B$ flow and therefore also the shear depends on the magnetic field strength. Additionally flux expansion effects have to be taken into account.

10.3.2 Impact of the X-point

In the presence of an X-point the X-point resistivity can act directly inside the confined region and therefore it can be expected that it has a much stronger effect on the Reynolds stress. The influence of the X-point on the tilt of turbulent structures by magnetic shear is illustrated in Fig. 10.10. Close to the outboard midplane the structures are expected to be tilted similarly to the case without X-point (Fig. 10.9). Approaching the X-point the structures become strongly elongated and thinned due to the strong magnetic shear close to the X-point. As very thin structures exhibit a high wavenumber these structures are strongly dissipated [402]. Therefore, the X-point directly truncates the ballooning envelope. This effect is not restricted to the scrape-off layer as in the limiter case described below. If the magnetic shear strongly varies with the ballooning angle, the magnetic shear $\hat{s}$ in Eq. (10.10) should be replaced by its local value $\frac{\rho}{q}\frac{\partial}{\partial\rho}\frac{B_\varphi(\theta)}{B_\theta(\theta)}$.

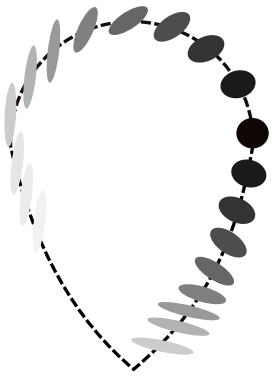

FIGURE 10.10: Impact of an X-point on the tilt of turbulent structures. Figure taken from Ref. [15], similar figures can be found in Refs. [398, 401].

Approaches based on field-aligned coordinates suffer from coordinate singularities due to the X-points. Flux-coordinate independent approaches offer the possibility to study these configurations. Such a flux-coordinate independent approach is done in the code GRILLIX [399]. An isothermal electrostatic drift-reduced Braginskii model [403] is simulated with different geometries. GRILLIX takes into account a realistic geometry. . Details on the simulation parameters can be found in Ref. [15].

As a first verification of our considerations we numerically investigate the effect of magnetic shear on individual structures. A typical field-aligned ballooning-like structure is considered in circular geometry without shear in Fig. 10.11a, with magnetic shear in Fig. 10.11c and in diverted geometry in Fig. 10.11e. The structures are all poloidally symmetric Gaussians at the outboard midplane and field aligned with a Gaussian ballooning envelope along the parallel direction. The structures are tilted and distorted according to the respective magnetic geometry. Several toroidal positions are shown overlaid in the left column of Fig. 10.11. Assuming plasma parameters of the turbulence simulations presented later on the corresponding Reynolds stresses $\Pi = \langle \mathbf{e}_\psi \cdot \nabla u \, (\mathbf{e}_\psi \times \mathbf{e}_\varphi) \cdot \nabla u \rangle_\varphi$ of the individual structure u are shown in the right column respectively (Figs. 10.11b,d,f). In the absence of magnetic shear the structure is not tilted (Fig. 10.11a) and is not associated with any Reynolds stress (Fig. 10.11b). Including magnetic shear, the structure is tilted (Fig. 10.11c) and the corresponding Reynolds stress shows the characteristic up-down asymmetry (Fig. 10.11d), which confirms the picture in Fig. 10.9. In divertor geometry, including X-points, the structure becomes strongly tilted and elongated at the upper high-field side and as well close to the lower X-point (Fig. 10.11e). Here we find the strongest contributions to the Reynolds stress from the individual structures (Fig. 10.11f). Keeping the structure and geometry fixed the Reynolds stress scales like $\Pi \propto \rho_s^{-2}$, i.e. for the same structures the absolute values of the Reynolds stress at half ρ_s would be four times larger. However, we want to note that instabilities and turbulence itself are

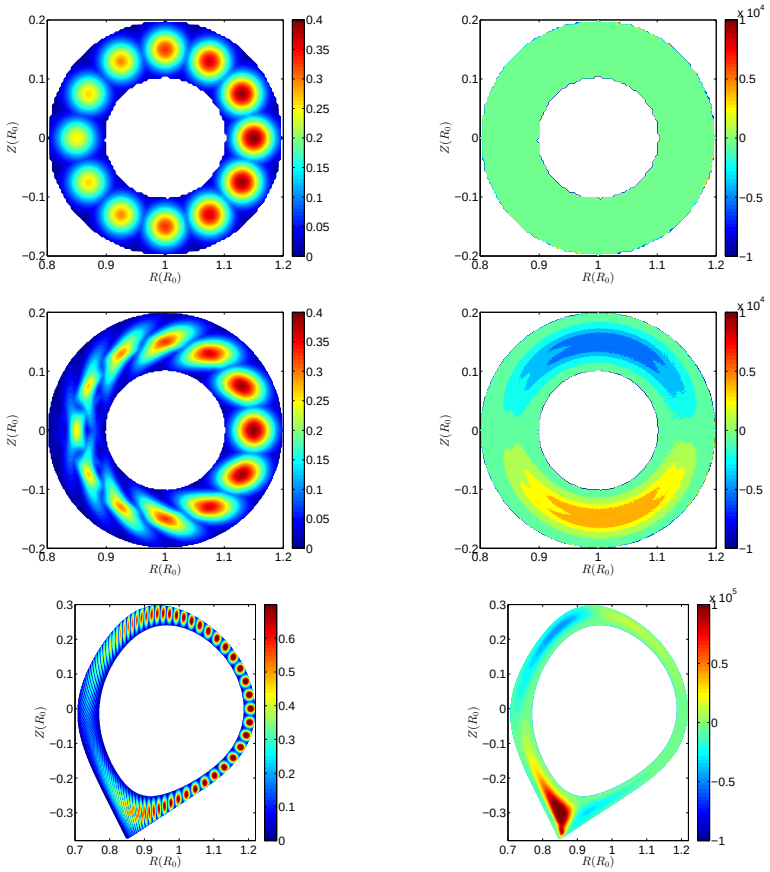

FIGURE 10.11: GRILLIX simulations: The left hand side shows poloidal cross-sections of an individual structure starting at the outboard midplane and summed over several toroidal positions (a,c,e). Assuming the same plasma parameters as in the turbulence simulations presented later on ($\rho_s/R_0 = 1 \cdot 10^{-3}$), and identifying the structure with normalized potential $e\phi/T_e$, the corresponding Reynolds stress is shown on the right hand side (b,d,f) in units of [m^2/s^2]. Both are shown in the case of a circular cross-section without magnetic shear (a,b), with magnetic shear (c,d) and in the case of a diverted plasma (e,f).Figure taken from Ref. [15].

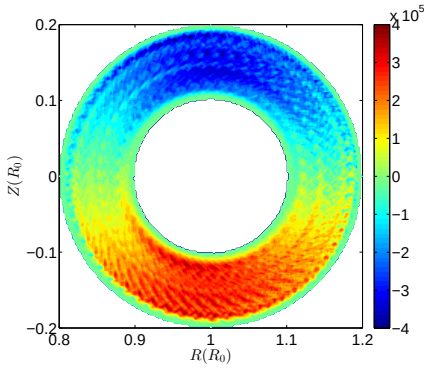

FIGURE 10.12: Reynolds stress $\langle \tilde{u}_r \tilde{u}_\theta \rangle_{\varphi,t}$ in $\mathrm{m}^2/\mathrm{s}^2$ in the poloidal plane in a circular cross-section simulated with GRILLIX including finite magnetic shear. Figure taken from Ref. [15].

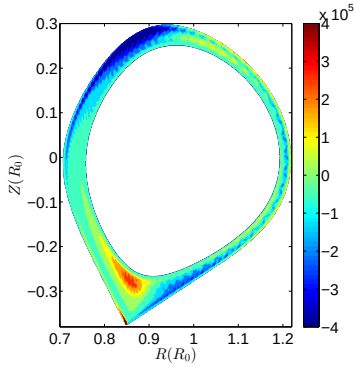

FIGURE 10.13: Reynolds stress $\langle \tilde{u}_r \tilde{u}_\theta \rangle_{\varphi,t}$ in $\mathrm{m}^2/\mathrm{s}^2$ in the poloidal plane in a diverted configuration with X-point simulated with GRILLIX. Figure taken from Ref. [15].

also sensitive to ρ_s.

For comparison with our basic considerations (Fig. 10.9) and for comparisons with the GEMR simulations shown later, simulations in a circular cross-section are performed with GRILLIX. Since our aim is a qualitative comparison, no detailed matching of the exact parameters is needed and we used previously performed simulations. The radial-poloidal Reynolds stress $\langle \tilde{u}_r \tilde{u}_\theta \rangle_{\varphi,t}$ has been computed and is shown in Fig. 10.12. Here $\langle \cdot \rangle_{\varphi,t}$ denotes an average over the toroidal (axissymmetric) angle and time. Qualitatively consistent with our preliminary considerations (Fig. 10.9), an up-down asymmetry in the Reynolds stress is observed here.

Figure 10.13 shows the radial-poloidal Reynolds stress $\langle \tilde{u}_r \tilde{u}_\theta \rangle_{\varphi,t}$ in divertor geometry. The up-down asymmetry is not as clear as in the circular cross-section. But on the high-field side some of this asymmetry appears to remain. Major contributions to the Reynolds stress can be found above the lower X-point and below the upper X-point. The enhanced magnetic shear in these

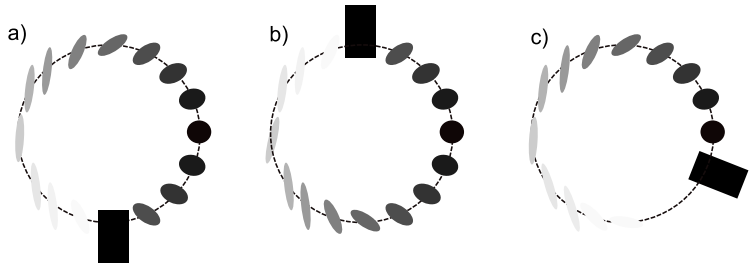

FIGURE 10.14: Impact of the limiter position on the tilt of turbulent structures. Figure taken from Ref. [15].

regions impacts the tilt of the structures and thus the Reynolds stress. Very close to the lower X-point the Reynolds stress vanishes as the magnetic shear is too strong, and due to the strong thinning of the structures they are dissipated. This is what is meant by the X-point resistivity. Close to the X-point this X-point resistivity acts to truncate the ballooning envelope. A bit further away the magnetic shear is not strong enough to dissipate the turbulent structures, but because the magnetic shear is very large the structures are very highly tilted leading to very strong contributions to the Reynolds stress. The basic structure of turbulence can in fact be traced back to the magnetic shear. The strongest contributions to the Reynolds stress in the case of turbulence (Fig. 10.13) can be found at the upper high-field side (positive Reynolds stress) and close to the lower X-point (negative Reynolds stress), which also show up for individual structures (Fig. 10.11f). Thus, to first order the poloidal variation of the Reynolds stress can be understood as the effect of magnetic shear on individual structures.

On the low-field side the Reynolds stress does not show a strong up-down asymmetry but instead is organized in bands with radially alternating signs. This is expected from a zonal flow staircase-like structure.

10.3.3 Impact of the limiter position

In the scrape-off layer (SOL) region the position of the limiter may induce a truncation of the ballooning envelope and can lead to a finite contribution to the zonally averaged Reynolds stress. Three examples are shown in Fig. 10.14. If the limiter is placed at the bottom (Fig. 10.14a) or the top (Fig. 10.14b) the fluctuation level directly behind the limiter is reduced, which leads to an up-down asymmetry. Besides the point directly at the low-field side (LFS) midplane where the asymmetry vanishes by definition, the asymmetry increases the closer the limiter is located to the LFS midplane (Fig. 10.14c). Direct impact of the limiter is restricted to the SOL region. However, a finite contribution to the zonally averaged Reynolds stress at the LCFS, at the boundary of the confined region, can impact the edge region, which may be nonlinearly self-amplified (Sec. 5.1.3). This can only be found out via simulations.

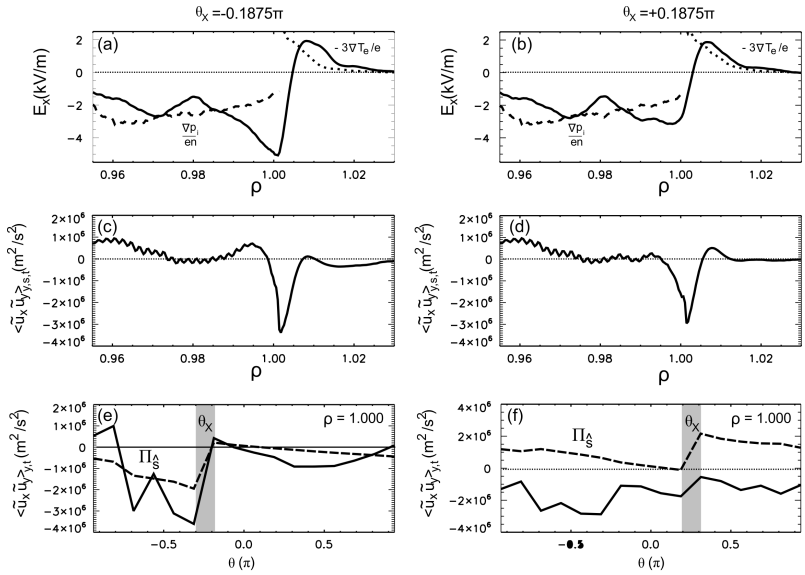

FIGURE 10.15: GEMR simulations of Tore Supra discharges. Radial electric field (a,b), radial profile of the zonally averaged Reynolds stress (solid line) (c,d), poloidally resolved contribution to the Reynolds stress (solid line) and the $\hat{s}$-residual Reynolds stress contribution (dashed line) at the separatrix $\rho = 1.00$ (e,f) for the lower $\theta_X = -33.75°$ (a,c,e) and upper limiter case $\theta_X = +33.75°$ (b,d,f). Figure taken from Ref. [15].

The influence of the limiter position has been investigated with the help of simulations carried out with GEMR (see Sec. 5.3). As GEMR is limited to circular plasma poloidal cross sections a comparison to experiments in such a geometry is desirable. In Ref. [401] the model of the $\hat{s}$-induced residual stress [398] has been compared to experiments in Tore Supra. The model parameters can be found in the original Ref. [15] or in Tab. C.1. A situation similar to the one described in Ref. [401] is intended to be studied where the limiter positions are $\theta_X = \pm 35°$, here we use $\theta_X = \pm 33.75°$.

In the lower limiter case, $\theta_X = -33.75°$, (Fig. 10.15a) the radial electric field is deeper at the separatrix than in the upper limiter case, $\theta_X = +33.75°$ (Fig. 10.15b). Therefore, in the GEMR simulations the lower limiter case shows better confinement properties for the favorable configuration. The radial electric fields are similar to the experimental values in Tore Supra [401]. The GEMR simulations found minima in the radial electric field at around 6 and 3 kV/m in the lower and upper limiter case, respectively. In the Tore Supra experiment the minima in the radial electric field for the lower and upper limiter case are at 7 and 4 kV/m [401]. Here, the ion diamagnetic velocity is defined negative for easier comparison with Refs. [398, 401]. Therefore, the shear across the LCFS is negative. Turbulence structures tilted in the direction of this shear exhibit a negative zonally averaged Reynolds stress as observed in Figs. 10.15c and d. When the zonally averaged Reynolds stress

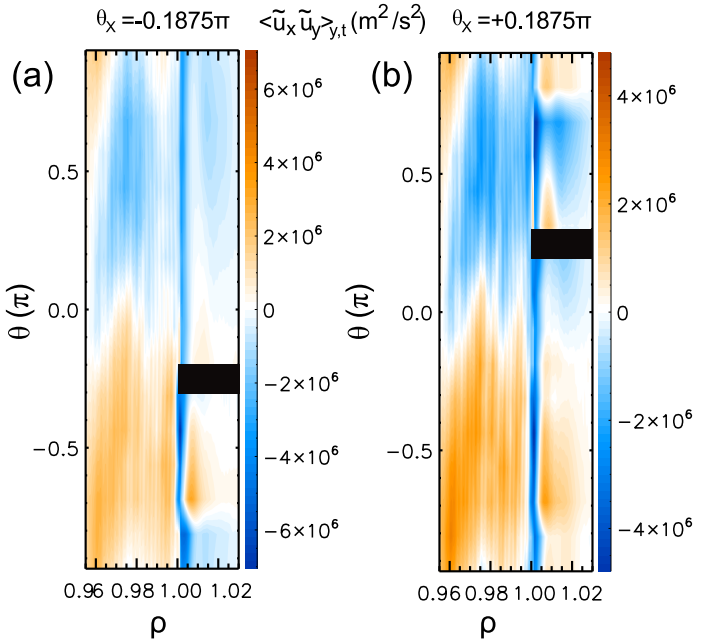

FIGURE 10.16: GEMR simulations of Tore Supra discharges. Poloidally and radially resolved Reynolds stress contribution $\langle \tilde{u}_x \tilde{u}_y \rangle_{y,t}$ for the upper limiter case $\theta_X = +33.75°$ (a) and the lower limiter case $\theta_X = -33.75°$ (b). Figure taken from Ref. [15].

drive $-\partial_x \langle \tilde{u}_x \tilde{u}_y \rangle_{y,s,t}$ is positive (Figs. 10.15c and d) this leads to an acceleration in electron diamagnetic direction (Figs. 10.15a and b). The zonally averaged Reynolds stress in the lower limiter case (Fig. 10.15c) is of similar order of magnitude to, but steeper than, than the upper limiter case (Fig. 10.15d). Therefore both the Reynolds stress drive $-\partial_x \langle \tilde{u}_x \tilde{u}_y \rangle_{y,s,t}$ as well as the turbulence suppression $\langle \tilde{u}_x \tilde{u}_y \rangle_{y,s,t} \partial_x \langle u_y \rangle_{y,s,t}$ are stronger in the former case. Here $\langle \cdot \rangle_a$ are the corresponding zonal (binormal and parallel) and time averages, with $a \in \{y, s, t\}$. Deeper into the confined region ($\rho < 0.99$) the Reynolds stress shows marginal impact on the limiter position (Figs. 10.15c and d and 10.16). The Reynolds stress is small at the outer midplane ($\theta = 0$), increases towards negative θ and decreases towards positive θ. Both contributions largely cancel out in the zonally averaged value (Fig. 10.15c and d). As expected by our preliminary consideration in the case of dominant impact of the magnetic shear (Fig. 10.9), the Reynolds stress mainly shows an up-down asymmetric $m = 1$ structure in the confined region, as shown in Fig. 10.16. This is not affected by the limiter position. Therefore, the impact of the magnetic shear on the structure tilt is stronger than the impact of the flow shear, and the limiters cannot influence the plasma far into the confined region.

10.4 Concluding remarks on the L-H transition

According to results presented in Sec. 10.1, which have been confirmed by several other experiments including DIII-D, TEXTOR and Alcator C-Mod [404, 258, 269, 270, 271] and reproduced by simulations [405, 406, 407] including the most sophisticated simulations possible for the time being (full-f gyrokinetic simulations including realistic geometry and SOL carried out by XGC1) [408, 409], the mystery of the L-H transition seemed to be resolved and to follow the predator-prey model by Kim and Diamond [360, 361]. Not all subsequent experiments have been in agreement with the Kim Diamond picture, though. Weak or insufficient zonal flow activity at the L-H transition have been found [410, 411, 412, 62, 413]. These experiments are discussed in more detail in the following.

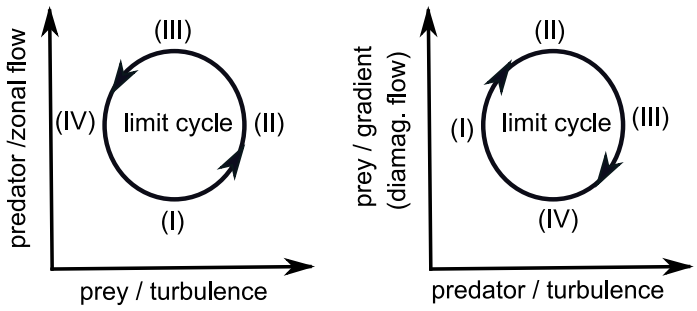

FIGURE 10.17: The figure of the right hand side (also shown in Fig. 3.8) shows the predator-prey limit cycle expected from the interaction between zonal flows and turbulence. On the left hand side is a limit cycle as expected from the interaction between the gradient and the turbulence.

In the HL-2A tokamak the limit cycles are first in the direction as expected for the interaction between zonal flows and turbulence (l.h.s. of Fig. 10.17), but before the actual transition to H-mode the limit cycles change direction [411]. This can be understood by the contribution of the gradient as depicted on the right hand-side in Fig. 10.17. If the turbulence level is low the gradient can increase (I), once the gradient increases it induces more turbulence and the gradient growth saturates (II), the enhanced turbulence level leads to a collapse of the gradient (III) and the drive of the turbulence reduces (IV). As the gradient contributes to the flow by its ion diamagnetic contribution (called neoclassical contribution in Ref. [62]) the flow can be a proxy for the gradient. This is in principle not in disagreement with the Kim-Diamond model as at some point the gradient has increased during the I-phase to give the dominant contribution to the total flow. In the JFT-2M tokamak the Reynolds stress has been found to be too weak to have impact on the flow [410], in NSTX the Reynolds stress has been found to even have the wrong sign [413]. In ASDEX

Upgrade the $E \times B$ flow has been compared to its neoclassical contribution and no signs of a zonal flow contribution have been found [62].

The results from ASDEX Upgrade [62] and DIII-D [365] show similarities, but partly also a very different behavior (most important the role of the neoclassical electric field). It might be that the L-H transition is not universal and the physics may depend on the collisionality for example (which in DIII-D is usually lower than in ASDEX-Upgrade). As the I-phase in DIII-D appears to be closer to the L-mode and the I-phase in ASDEX Upgrade appears closer to the H-mode, maybe zonal flow dominated predator-prey dynamics appears before the L-I transition in ASDEX Upgrade. Indeed, indications for limit cycles in agreement with the expectation of zonal flow-turbulence interaction have been found in the early phase of the I-phase in ASDEX Upgrade [414]. And there is the possibility that another mechanism is universally responsible for the L-H transition.

The observed up-down asymmetry in the poloidal magnetic field fluctuations in ASDEX Upgrade [14, 374] (Sec. 10.2.1) are related to strongly ballooned transport fluctuations [14] (Sec. 10.2.2). Therefore, the strongly pronounced up-down asymmetry points to a pressure-gradient-relaxation phenomenon (as depicted on the r.h.s. of Fig. 10.17) behind the observed limit-cycle oscillations in I-phase. Also the presence of type-III-ELM-like precursors [374] points to pressure gradient driven limit cycles. These are independent confirmations of the conclusion drawn in Ref. [62], that zonal flows play a minor role for the I-phase in ASDEX Upgrade.

Regarding the discrepancy in the Reynolds stress, the influence of the magnetic field topology on the poloidal Reynolds stress distribution (Sec.10.3), which has been motivated by a theoretical prediction [398] and a recent experimental finding [40]. The simulations carried out here reveal the strong poloidal asymmetry of the Reynolds stress. Hence, measurements at one poloidal positions should not be taken as representative of the zonal average. Therefore, it is not surprising that experiments on different devices with diagnostics at different positions find differences in sign and strength of the Reynolds stress: investigations of the impact of the Reynolds stress with respect to the L-H transition found that the Reynolds stress is strong enough [13, 404, 269, 258, 270, 271] to trigger the L-H transition or not [410, 413] (even with a different sign in Ref. [413]). To point this out explicitly, both is possible an overestimation or an underestimation of the flux-surface average Reynolds stress by taking a local measurement only. Even opposing Reynolds stress contributions have been found at two different poloidal locations [415].

Therefore, it seems unlikely that Reynolds stress measurements will reliable resolve the L-H transition, because Reynolds stress investigations demand measurements on the entire flux-surface, due to the non-homogeneous distribution described here, but also due to the nonlocality in wavenumber space [142], which demand resolution of the ion Larmor radius. Furthermore, as the zonal flow drive and damping are nonlocal in the radial domain (Sec. 8.3), several flux-surfaces have to be measured before evaluating a momentum or

energy balance.

Chapter 11

Turbulence in the I-mode

The I-mode is an improved energy confinement regime with H-mode-like energy confinement and L-mode-like particle confinement. A general introduction to the I-mode confinement regime can be found in Sec. 2.2.3. Up to now studies of turbulence in I-mode are restricted to Alcator C-Mod. Investigations in different experiments as the present one in ASDEX Upgrade are helpful to elaborate similarities and differences of turbulence in I-mode between Alcator C-Mod and ASDEX Upgrade and which phenomena are I-mode specific in general. **The I-phase must not be confused with the I-mode.** The I-phase is the regime at the transition from the low to high confinement regime. The interested reader is referred to Chapter 10.

Previous works at Alcator C-Mod showed that at the transition to the I-mode low frequency broadband fluctuations decrease while simultaneously a weakly coherent mode (WCM) in the density and magnetic fluctuations at high frequencies ($f \sim 100 - 300$ kHz) develops [77]. The WCM appears in the electron temperature T_e pedestal region ($0.95 < r/a < 1.0$ in Alcator C-Mod) [76] with a tail towards the pedestal top [79]. Fluctuation levels of the WCM in the density, magnetics and temperature are around $\tilde{n}/n \sim$ 10–16 %, $\tilde{B}/B \sim 0.01$–0.02 % and $\tilde{T}_e/T_e \sim$ 1–2 %, respectively [77, 79, 416]. The WCM is thought to be responsible for the regulation of the particle transport and therefore the cause of the L-mode like particle transport in the I-mode. While the WCM appears quite broadband in frequency space it is rather narrow in wavenumber space and has short wavelengths ($k_\theta = 1.3 \pm 0.5$ cm^{-1}) [79]. The WCM propagates in the electron diamagnetic direction in both the laboratory [76] and $E \times B$ frame [79]. In the $E \times B$ frame the propagation velocity is roughly a factor of three below the electron diamagnetic velocity [79]. The WCM can develop at low q_{95} and low collisionality and promptly disappears at the transition to the H-mode [76].

The nonlinear analysis in Ref. [79] showed a nonlinear coupling of the geodesic acoustic mode (GAM) and the WCM and also an energy transfer from the WCM into the GAM which constitutes a saturation mechanism for the WCM. Another effect is that the GAM scatters the energy of the central WCM peak by transferring energy below the WCM frequency from higher to

lower and above the WCM frequency from lower to higher frequencies. Thereby the GAM is responsible for the broadband feature of the WCM. Indeed, such a coupling to a rather low-wavenumber mode as the GAM is necessary to preserve the narrow width of the WCM in wavenumber. Therefore, the central frequency peak of WCM is acting as a source of the WCM. A basic conclusion from this is that there must by an underlying instability responsible for the WCM.

In the present chapter the turbulence in the I-mode regime of the ASDEX Upgrade will be characterized. The results presented in this chapter have been published in Refs. [16, 17]. Besides the WCM (see Sec. 11.1) and the GAM (see Sec. 11.2), also a mode at similar frequency as the WCM is present during the I-mode in ASDEX Upgrade. This can be identified as a global Alfvénic oscillation (see Sec. 11.3). Furthermore, strongly intermittent events of solitary waveform occur during the I-mode. These fluctuations are studied in more detail in Sec. 11.4. Some general introduction into different kinds of intermittency can be found in Chap. 3.5. Finally, a model to explain these intermittent events is proposed in Chap. 11.5.

11.1 Weakly coherent mode (WCM)

Typical density fluctuations at the transition from L- to I-mode are shown in Fig. 11.1 measured by normal incidence reflectometry (Sec. 6.2.1). Details on the reflectometry setup can be found in Ref. [16]. Density fluctuations in Figs. 11.1 were obtained for a cut-off density $n_e = 2.5 \cdot 10^{19}$ m^{-3} located at $\rho = 0.98 \pm 0.01$. In L-mode the turbulence is rather broadband (Fig. 11.1), In I-mode we observe two bands in frequency space, one at low frequencies ($f < 30$ kHz) and one at higher frequencies ($80 < f < 150$ kHz). Although the mode is not as pronounced in AUG, this behavior is very similar to the WCM observed in Alcator C-Mod [77, 79].

These fluctuations can also be observed at cut-off densities between $1.78 \cdot 10^{19}$ m^{-3} and $2.84 \cdot 10^{19}$ m^{-3}, but not so clearly pronounced. Therefore, this mode is located at $\rho = 0.97 - 0.99$ corresponding to the minimum E_r in I-modes at ASDEX Upgrade [60] and consistent with the recent observation on Alcator C-Mod [79]. The minimum of $(\nabla p_e)/ne$ is located at $\rho = 0.99$. The mode is also neither observed in the scrape-off layer region or at much higher densities. The electron density fluctuation level of the WCM estimated using the 1D C. Fanack model [417], was found to be between 6 and 13 %.

For better comparison, Fig. 11.2a shows the spectra of density fluctuations in L- and I-mode. In I-mode a rather broadband mode around 130 kHz is observed (the WCM). Turbulence is slightly reduced in the frequency range from 20 to 80 kHz and increased at higher frequencies. By means of charge exchange spectroscopy the mean poloidal velocity has been measured during beam blips which is used to translate the obtained frequency spectra into the plasma frame. This is shown in Fig. 11.2d. The wavenumber of the WCM

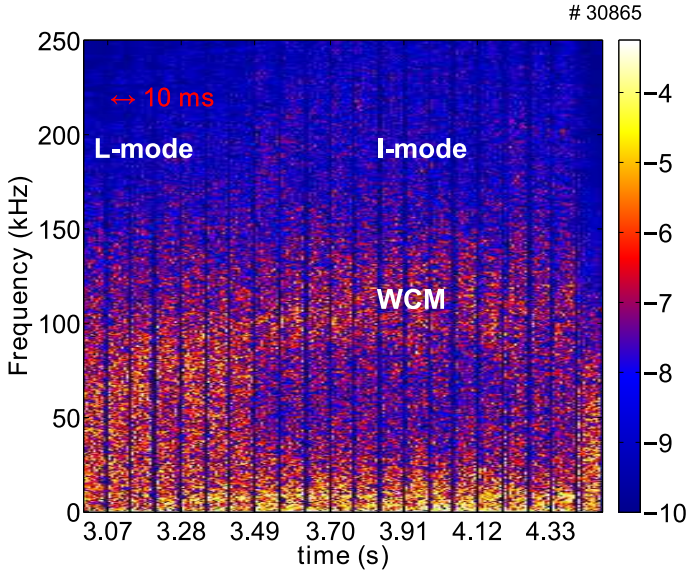

FIGURE 11.1: Spectrogram of density fluctuations from (hopping) reflectometry. Amplitudes are shown color-coded in logarithmic representation. Note that the plot is not continuous. Sub-windows of 10 ms length corresponding only to the cut-off layer density of $n_e = 2.5 \cdot 10^{19}$ m^{-3} are shown. The hopping reflectometry measures every 70 ms at this cut-off layer for 10 ms. Figure taken from Ref. [16].

found at $k_\theta = 2\pi f / v_\theta \approx 1.5$ cm^{-1} is similar to the Alcator C-Mod results [79]. In this representation we seen that the spectral power of the the WCM is actually not increased, but a result from the increased Doppler shift. The fluctuation amplitude decreases from L- to I-mode at all wavenumbers.

11.2 Geodesic acoustic mode (GAM)

It can be expected that the WCM is modulated by a geodesic acoustic mode (GAM) as in Alcator C-Mod [79]. GAMs can be directly observed in velocity fluctuations measured for example by Doppler reflectometry. Furthermore, GAMs show up in bispectra as they are nonlinearly driven and modulate the turbulence at the GAM frequency [303, 304]. The intrinsic modulation of all higher frequencies by the GAM can be used for the detection of GAMs (Sec. 7.2.1). The modulation shows up in the envelope of the fluctuations which will be used as a proxy for the GAM. The envelope of density fluctuations measured by hopping reflectometry has been estimated from fluctuations above 400 kHz. For better comparison with the density fluctuations the envelope in Fig. 11.2b is shown for a sub-window size of 1 ms corresponding to a frequency resolution of 1 kHz. A pronounced feature in the order of typical GAM frequencies is observed at around 8 kHz. The envelope at low frequencies around 8 kHz is about 2 orders of magnitude larger in I-mode pointing to

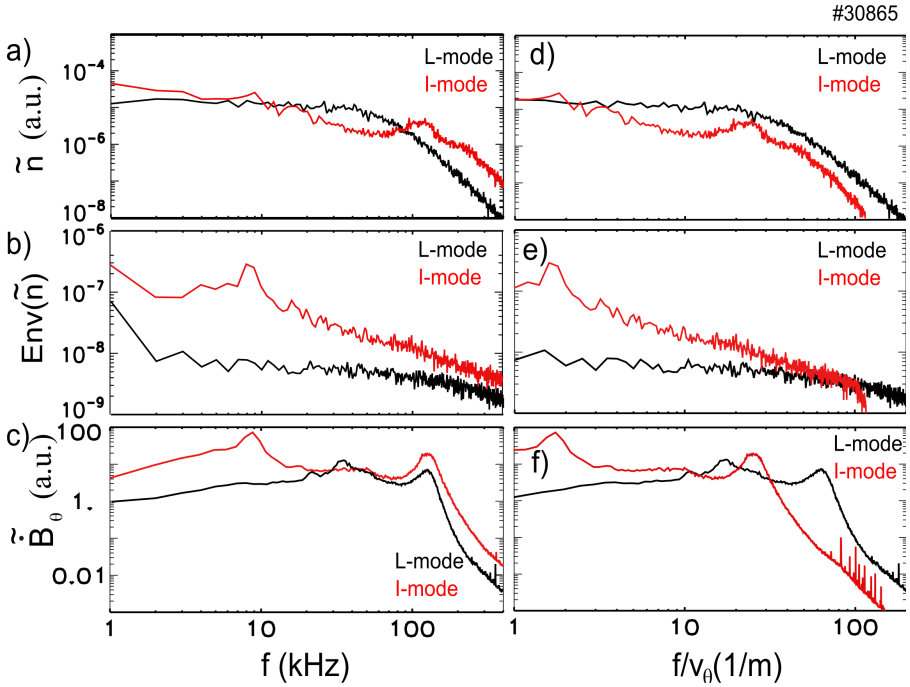

FIGURE 11.2: (a) Spectrum of density fluctuations from reflectometry, (b) its envelope deduced from density fluctuations and (c) magnetic fluctuations $\dot{B}_\theta$ below 400 kHz in L and I-mode. Spectra are also shown in the plasma frame (d-f) with $v_\theta \approx -2$ km/s in L-mode and $v_\theta \approx -5$ km/s in I-mode, respectively. Negative velocities are in the electron diamagnetic direction. Figure taken from Ref. [16].

a strong modulation of the turbulence at the GAM frequency. Compared to c_s/R_0 this frequency seems rather low. However, as we will see in the following section, it agrees well with the theoretical prediction of the GAM frequency.

In drift-wave turbulence, $E \times B$ nonlinearity in the density lead to an transfer of free energy from low to high wavenumbers (Sec. 5.1.2), corresponding to a transfer from low to high frequencies. As seen in Fig. 11.2d the turbulence level in the I-mode is reduced, and the increase in fluctuation level at high frequencies in Fig. 11.2a can be traced back rather to the Doppler shift though increased rotation in the I-mode than to an increase of free energy transfer from low to high frequencies by the GAM.

A study of the free energy transfer as done in Ref. [79] would require an estimate of the $E \times B$ nonlinearity $\mathrm{Re}(\tilde{n}^*(f)(\langle \hat{b} \times \nabla_\perp \tilde{\phi}(f_2) \cdot \nabla_\perp) \tilde{n}(f_1)\rangle)$ with magnetic field direction $\hat{b}$ and therefore the cross-bicoherence between density and potential fluctuations. Density fluctuations $\tilde{n}$ can be deduced from reflectometry. Potential fluctuation measurements are not available at ASDEX Upgrade. But with Doppler reflectometry poloidal velocities can be measured. Velocity fluctuations are approximated by the center of gravity of the Doppler shift given by $c_{gr} = \frac{\int df f S(f)}{\int df S(f)}$ with the power spectrum $S(f)$ of the Doppler reflectometer heterodyne signal. The center of gravity is calculated for sub-

windows of 1 μs length corresponding to 25 points (25 MHz acquisition). The amplitude of the Doppler reflectometer heterodyne signal is proportional to density fluctuations $\tilde{n}$. Also the amplitude of the reflectometer heterodyne signal is averaged over 1 μs. It should be pointed out that the center of gravity is measured in absolute units (Hz), which in general are not equal to the Doppler shift. Therefore, the the center of gravity does not allow for conclusions on the absolute value of the velocity fluctuations.

To investigate the nonlinear coupling between WCM and GAM, the cross-bicoherence can be estimated from the density fluctuations $\tilde{n}$ and the center of gravity $\tilde{c}_{gr}$ fluctuations

$$\hat{b}(f_1, f_2) = \sqrt{\frac{\|\langle \tilde{n}(f_1)\tilde{c}_{gr}(f_2)\tilde{n}^*(f_1+f_2)\rangle\|^2}{\langle\|\tilde{n}(f_1)\tilde{c}_{gr}(f_2)\|\rangle^2\langle\|\tilde{n}(f_1+f_2)\|\rangle^2}}. \tag{11.1}$$

Phase locking is a necessary condition for nonlinear coupling. A coupling of the GAM with the WCM as expected from recent Alcator C-Mod experiments [79] should be observable in the cross-bicoherence. The bispectral analysis is done for a sub-window size of 500 μs, resulting in 90 realizations and a frequency resolution of 2 kHz. The corresponding significance level is 0.011.

The bispectra for L-mode and I-mode are shown in Figs. 11.3a and 11.3b, respectively. In the L-mode no pronounced modes can be found. In I-mode a coupling of the center of gravity proportional to velocity fluctuations at low frequency ($\sim$ 10 kHz) with the broadband turbulence ($>$ 200 kHz) is observed. A pronounced coupling of these fluctuations at 10 kHz with the WCM (70 - 140 kHz) is found. The cross-bicoherence of 0.14 strongly exceeds the significance level. The WCM itself is also nonlinearly coupled to other frequencies. The velocity fluctuations of the WCM are coupled to low frequency density fluctuations ($f_1 < 20$ kHz) and to fluctuations near the WCM frequency. In addition, coupling of velocity fluctuations at the WCM frequencies with higher frequencies in the density fluctuations is observed ($f_1 > 200$ kHz for $f_2 = +f_{WCM}$ and $f_1 > 300$ kHz for $f_2 = -f_{WCM}$). This might indicate that the bursts in the density fluctuations observed with Doppler reflectometry [348] are nonlinearly generated by the WCM.

The nonlinear coupling of the GAM with the WCM is also observed in the bicoherence inferred from the envelope analysis of data from normal incidence reflectometry (results not shown here). Compared against each other the bispectra deduced from the Doppler reflectometry are more detailed. However, under the conditions of temporary strongly reduced fluctuation levels as present in I-mode or H-mode, Doppler reflectometry is very susceptible for misinterpretation.

11.3 Geodesic Alfvénic mode (GAlf)

Both density and magnetic field fluctuations show very similar features compare (Figs. 11.2a and 11.2c). Also the low-frequency fluctuations at 8 kHz seen

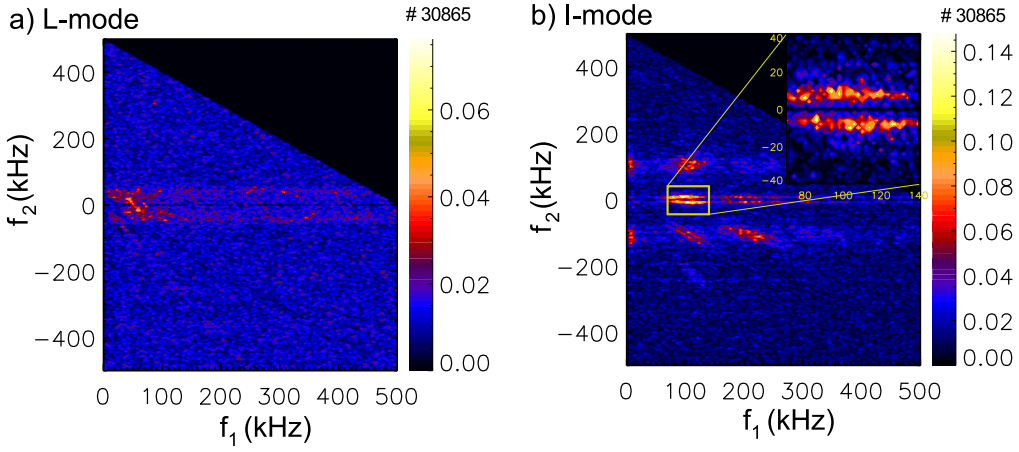

FIGURE 11.3: Bicoherence of density fluctuations from Doppler reflectometry in (a) L-mode and (b) I-mode. The frequency of density fluctuations f_1 couples with frequencies in velocity fluctuations f_2 to density fluctuations $f = f_1 + f_2$. Data is taken at upper X-mode at 80 GHz. Figure taken from Ref. [16].

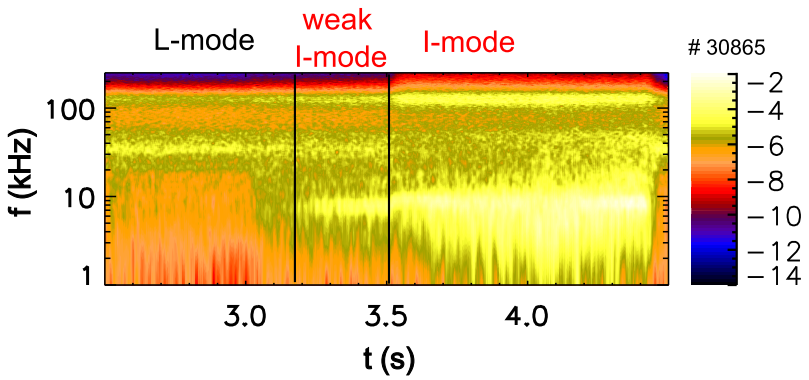

FIGURE 11.4: Spectogram of fluctuations in the time derivative of magnetic fluctuations $\dot{B}_\theta$ measured at the top of AUG (C09-09) in logarithmic amplitude representation.

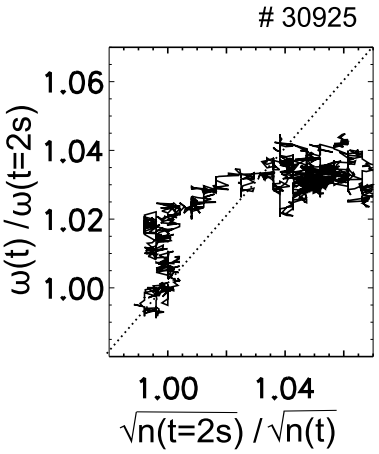

FIGURE 11.5: Frequency of maximum power in the magnetic fluctuations in the range between 100 and 200 kHz and inverse square root of the edge density normalized to their values at the beginning of the I-mode shown against each other. Figure taken from Ref. [16].

in the envelope of the density fluctuations are observed in the magnetic field fluctuations once the I-mode is accessed from $t = 3.2$ s on (Fig. 11.4). As a high-frequency zonal flow the GAM could potentially lead to the spontaneous confinement transition at $t = 3.2$ s and the drop in the diamagnetic contribution of the radial electric field $(\nabla p_i)/ne$. This has also been speculated in Ref. [79]. Note that magnetic fluctuations at the frequency of the WCM (130 kHz) can be detected well before the L-I transition. This is in contrast to the observations in Alcator C-Mod, where the frequency of the magnetic fluctuations follow the frequency of the WCM, which increases during the beginning of the I-mode [76]. Therefore, the magnetic fluctuations investigated in detail in the following are probably not related to the WCM even though appearing at a similar frequency.

The GAM is the oscillation between the zonal flow and its pressure sideband. These pressure sidebands are not only coupled to the turbulence but also to the global Alfvénic oscillation [223]. If the high-frequency magnetic oscillations at the WCM frequency are related to Alfvénic modes they should scale $\sim 1/\sqrt{n}$. This scaling can be investigated in a discharge with a steady I-mode phase where the density is varying smoothly over time. Figure 11.5 shows the frequency of the maximum power in the range between 100 and 200 kHz and therefore tracks the frequency changes of the high-frequency magnetic fluctuations, which appear also at around 140 kHz in this discharge and are proportional to $1/\sqrt{n}$ from the edge density measured with interferometry. To compare the time evolution both are normalized to their values at the beginning of the I-mode. This comparison is just a plausibility check as both signals are not matched in physical space. The long-time behavior (the time evolution is shown in detail in the original Ref. [16]) the high frequency oscillations

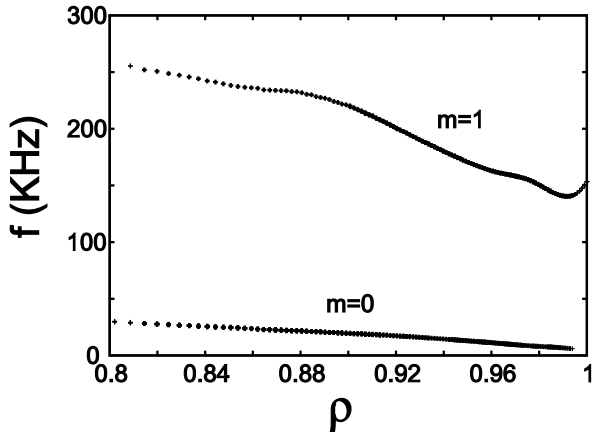

FIGURE 11.6: Spectrum of Alfvénic branch with $n = 0$ calculated with LIGKA. The $m = 0$ branch corresponds to the geodesic acoustic mode, the $m = 1$ branch to the geodesic Alfvénic mode. Figure taken from Ref. [16].

in the magnetic field follow the trend of $\sim 1/\sqrt{n}$ both increasing by about 5 %, which points to an Alfvénic mode. The two signals do not exhibit a clear correlation on shorter time scales, or in shorter I-mode phases.

The gyrokinetic eigenvalue solver LIGKA [418, 419] is used to determine the kinetic continuum branches for $(n = 0, m = 0)$ and $(n = 0, m = 1)$. The spectrum is shown in Fig. 11.6. At the position where the WCM ($f \sim 130$ kHz) and the GAM-like mode ($f \sim 8$ kHz) is observed in the density fluctuations ($\rho \sim 0.98$) the ($n = 0$, $m = 1$) branch is found at $f \sim 140$ kHz and the GAM branch ($n = 0$, $m = 0$) is found close to $f \sim 10$ kHz, respectively. Coherent modes are expected slightly below the minimum of the branches since the continuum damping is rather small there.

Motivated by the LIGKA results the mode characteristic has been investigated in detail by calculating the cross-power spectrum of toroidally and poloidally displaced Mirnov coils similar to Ref. [420]. The cross-phases divided by the toroidal and poloidal angular distances, respectively, give the corresponding mode numbers n and m. The cross-coherence and mode number are shown in Fig. 11.7. The WCM can be identified as an $n = 0$, $m = 1$ mode. For a coherent mode an increased coherency with respect to the surrounding frequencies can be expected. This is clearly visible for the toroidal correlation (Fig. 11.7a). The absence of increased coherency in poloidal direction (Fig. 11.7b) does not support a coherent mode at the WCM frequency in the magnetic fluctuations.

The toroidal mode number of the low-frequency mode is close to $n = 0$, the poloidal mode number is between $-1 \leq m \leq 1$. The estimation of the poloidal mode number as done here can be regarded as very rough as the local field line inclination is not taken into account. To obtain a global picture of the modes also the cross-correlation between different poloidally displaced Mirnov coils on a poloidal cross-section has been calculated. As shown in Fig. 11.7e,

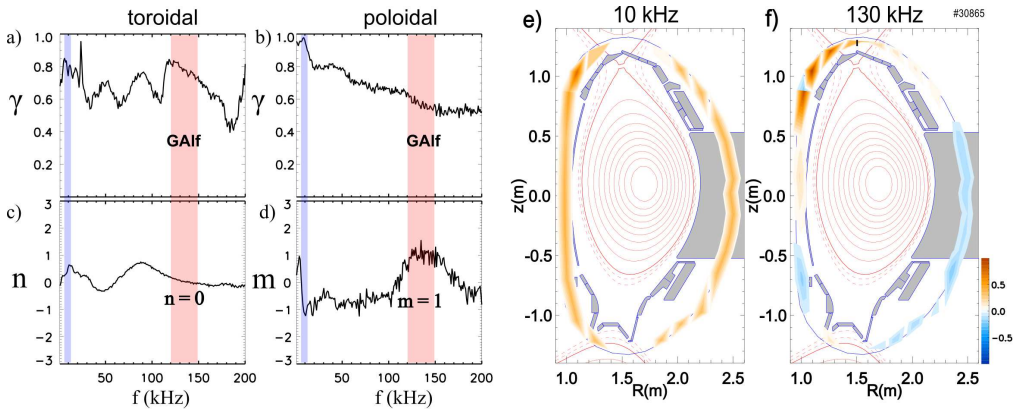

FIGURE 11.7: Cross-coherence (a,b) and toroidal (c) and poloidal mode numbers (d) during I-mode at 4 s of two mainly toroidally (C04-17 and C05-21) and poloidally (C09-09 and C09-08) displaced Mirnov coils. (e) Poloidal mode structures of the low (10 kHz) and (f) high (130 kHz) frequency oscillations during I-mode at 4 s shown by the cross-correlation without time lag ($\tau = 0$) of bandpass-filtered signals at the corresponding frequency (10 and 130 kHz, respectively) from one Mirnov coil as a reference (cross-correlation is 1) with poloidally displaced Mirnov coils at the same toroidal position. Figure taken from Ref. [16].

the 10 kHz mode exhibits a clear $m = 0$ mode structure and the mode close to the WCM-frequency corresponds to a $m = 1$ (Fig. 11.7f).

Whether the observed $m = 0$ mode characteristic of the low frequency mode at 10 kHz is compatible with a GAM is disputable. The GAM itself is electrostatic. It is theoretically expected that the GAM generates a halo of magnetic fluctuations with mode numbers of $m = \pm 2$ just outside the magnetic flux surface of the GAM [421]. This halo has been recently observed in TCV [422]. In this experiment (Fig. 11.7) the low-frequency mode exhibits such a halo, though the poloidal mode numbers are $m = \pm 1$. On the other hand, the observed ($n = 0$, $m = 0$) structure constitutes a zonal magnetic field, which has been predicted to be excited at the GAM frequency for finite β turbulence [423]. Here, further systematic studies of the magnetic signature of GAMs in ASDEX Upgrade are needed, also in the usual favorable configuration to evaluate if the here observed signature is related to the I-mode configuration in particular.

11.4 Strongly intermittent density fluctuations

The edge turbulence in L-mode is characterized by broadband fluctuations as measured by Doppler reflectometry (DR) in Fig. 11.8a. While the background density turbulence level is reduced in I-mode compared to the L-mode level, the I-mode in AUG exhibits strong intermittent density bursts (Fig. 11.8b) causing a heavy-tail probability distribution function [424, 83]. The bursts

exhibit a solitary waveform and last for about 2–10 μs [424, 83]. These bursts are not ELMs, the peeling-ballooning stability boundaries are far away from the experimental parameters in I-mode as calculated with the MISHKA code [83]. Furthermore, no pronounced magnetic signature as typical for type-I ELMs (in H-mode) [287] or type-III ELMs (in H-mode or I-phase) [374, 62] is observed. The bursts in I-mode show some similarities to inter-ELM fluctuations in H-mode as previously observed [425].

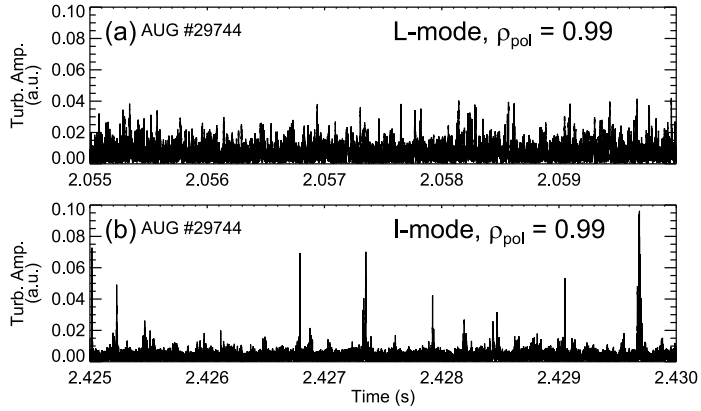

FIGURE 11.8: Comparison of turbulence amplitude behavior in (a) L- and (b) I-mode measured with Doppler reflectometry. Figure has been taken from Ref. [17].

Most importantly, the intermittent events show up in the divertor measured by absolute extended ultraviolet (AXUV) diode based bolometry [426] several tens of microseconds later than observed with the DR in the confined region at the minimum of the radial electric field [83]. The divertor impact in combination with the strong density perturbation in the confined region suggests that these bursts are playing an important role in hampering the density pedestal to develop. Although a proof by direct measurements of the particle transport is not possible as the bolometer detects rediation by a combination of density, temperature, and impurity concentration. The analysis of transient divertor heat loads shows that intermittent turbulent events, observed in the confinement region, are responsible for a significant part of divertor heat loads [427].

Previous results show a strong correlation between density bursts and the WCM. The bursts appear as wave trains with the frequency of the WCM [424]. Complementary to the previous analysis [424], a wavelet-based approach (Sec. 7.2.3) has been used in Ref. [17]. During the strongly intermittent bursts strong activity at the WCM and GAM frequency is found. An intermittent behavior of the GAM is not unusual and has been reported from most devices [358, 428, 429, 430, 431, 432, 433, 434, 435, 436, 437, 438, 439]. Strong activity of global modes (as the GAM or WCM) can lead to strongly localized turbulent activity. Intermittent transport emitted by the GAM has been studied theoretically near the critical gradient regime [440]. Also due to turbulence

localization the transport can become bursty [441].

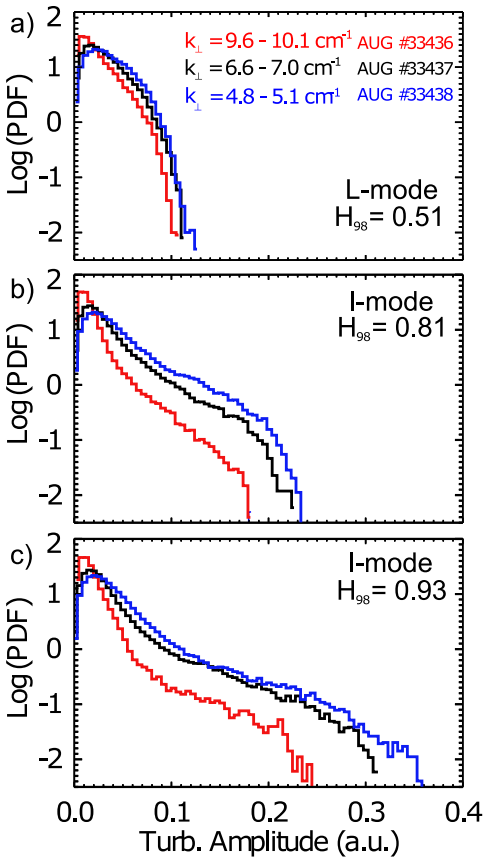

FIGURE 11.9: PDFs of density fluctuation amplitudes obtained at $\rho_{pol} = 0.99$ for different sizes, $k_\perp \approx 10$ cm^{-1}, $k_\perp \approx 7$ cm^{-1}, $k_\perp \approx 5$ cm^{-1} shown at the same level of confinement in L-mode at $H_{98} = 0.51$ (a) and I-mode at $H_{98} = 0.81$ (b) and at $H_{98} = 0.93$ (c). Heavy tails develop with improved confinement in I-mode. Larger structures show more pronounced tails. Figure has been taken from Ref. [17].

The perpendicular wavenumber measured with the Doppler reflectometer has been scanned between $k_\perp \approx$ 5–10 cm^{-1}. The deviation from Gaussian statistics increases with improving confinement [424, 83] as seen in Fig. 11.9 by the probability distribution function (PDF) of the density fluctuation amplitude. The density bursts are not only observed when small structures are probed, but also at rather large scales. At large scales the development of the heavy tail in the PDF is even more pronounced. Therefore, the intermittency in I-mode seems not to be related to small-scale intermittency in particular, but first of all to external intermittency (Sec. 3.5).

11.5 Generation of solitary-like structures

The density bursts exhibit a solitary waveform. Solitons are a result of a competition between self-steepening by a nonlinearity and dispersion as described for example in 1D by the Korteweg-de-Vries (KdV) equation. The non-linearity appearing in the KdV and Burgers equations are known to be responsible for intermittency in 1D systems [442]. Self-steepening results in the generation of higher harmonics. This is not possible for the standard nonlinearities in a magnetized plasma given by the $E \times B$ drifts. Those can be written as $\frac{T_e}{eB\rho_s^2}(\hat{\mathbf{z}} \times \nabla_\perp \tilde{\phi}) \cdot \nabla_\perp$ with electron temperature T_e, elementary charge e and $\rho_s = \sqrt{T_e m_i}/eB$. In wavenumber space $\nabla_\perp \to i\mathbf{k}$ this is proportional to $(\hat{\mathbf{z}} \times \mathbf{k}) \cdot \mathbf{k}' = \hat{\mathbf{z}}(\mathbf{k}' \times \mathbf{k})$. Therefore higher harmonics $\mathbf{k}' = c\mathbf{k}$ with constant scalar c cannot be generated directly. The observation of the generation of higher harmonics in the bispectrum is not as trivial as it seems.

Here, one possibility for the generation of such solitary-like structures is shown. Starting point is the advective part of the electron temperature of the Braginskii equation [403]

$$\frac{3}{2} n \frac{dT_e}{dt} = \frac{3}{2} \left(n \frac{\partial T_e}{\partial t} + n v_{E\times B} \nabla_\perp T_e \right). \tag{11.2}$$

In the next step, temperature and density are normalized by typical values, n_0 and T_{e0}, respectively. The normalized density and temperature are decomposed in background and fluctuating quantities $n = \bar{n} + \tilde{n}$ and $T_e = \bar{T}_e + \tilde{T}_e$. Making use of the Poisson bracket $u_{E\times B} \cdot \nabla_\perp = \left\{ \tilde{\phi}, \cdot \right\} = \partial_x \tilde{\phi} \partial_y - \partial_y \tilde{\phi} \partial_x$, with x the radial and y the binormal coordinate, the advective part can be written as

$$\frac{\partial \tilde{T}_e}{\partial t} = \bar{n} \left\{ \tilde{\phi}, \tilde{T}_e \right\} + \tilde{n} \left\{ \tilde{\phi}, \bar{T}_e \right\} + \tilde{n} \left\{ \tilde{\phi}, \tilde{T}_e \right\}. \tag{11.3}$$

In drift-wave ordering the gradients of the fluctuations are of the order of the gradients in the background values. Therefore, the first term is the highest in drift-wave ordering and the last two terms would be neglected. As a product of three fluctuating quantities the third term is negligibly small. However, the second term can be written as

$$\frac{\partial \tilde{T}_e}{\partial t} \sim \tilde{n} \frac{\partial \tilde{\phi}}{\partial y} \frac{\partial \bar{T}_e}{\partial x} \tag{11.4}$$

and in the case of these strong density bursts in I-mode, the density fluctuation level as well as the background temperature gradient are considered to be high. On the other hand the first term in competition is proportional to the temperature fluctuation level, which is considered to be low. This has been observed to be the case in Alcator C-Mod [416]. A confirmation in AUG is still pending. The transition of the dominant turbulence regime from drift-wave dominated to resistive ballooning dominated is expected to occur at $C\omega_B > 1$ [159], where the local normalized collisionality is given by

$C = 0.51(m_e/m_i)(qR/L_\perp)^2\nu_e(L_\perp/c_s)$ and $\omega_B = 2L_\perp/R$ with electron and ion masses m_e and m_i, respectively, safety factor q, collisionality ν_e and ion sound speed $c_s = \sqrt{T_e/m_i}$. For $n_e = 2.5 \cdot 10^{19}$ m^{-3}, $T_e = 250$ eV, $q = 5$ and $L_\perp = 2.5$ cm at $\rho = 0.98$ we get $C \approx 1$ and $\omega_B \approx 7.5 \cdot 10^{-3}$, hence $C\omega_B \ll 1$. It seems reasonable at these low collisionalities at high temperatures to assume adiabatic electrons with $\tilde{\phi} \approx \tilde{n}$. In this case the nonlinearity has the form $\sim \tilde{n}\partial_y\tilde{n}$ of a KdV-nonlinearity explicitly proportional to the radial temperature gradient. Therefore, drift-wave turbulence with intrinsically low transport can generate solitary-like temperature perturbations. How are those transmitted to the density? The adiabatic coupling including temperature perturbations is given by [403] $\tilde{\phi} - \tilde{n} - 1.71\tilde{T}_e \approx 0$. The temperature fluctuations can be approximated by $\tilde{T}_e \approx \frac{\tilde{\phi}-\tilde{n}}{1.71}$. For low temperature fluctuations $\tilde{\phi} \approx \tilde{n}$ is still valid. Therefore there is no contradiction with the argumentation above. Defining a small phase difference δ between potential and density fluctuations with $\tilde{\phi} = \tilde{n}(1 - i\delta)$, it follows $\tilde{T}_e \approx (\tilde{\phi} - \tilde{n})/1.71 = \tilde{n}(1 - 1 - i\delta)/1.71$. Density fluctuations can be induced by the temperature fluctuations as $\tilde{n} \approx i1.71\tilde{T}_e/\delta$. If the phase difference δ is small the bursts appear larger in the density than in the temperature. The temperature fluctuations also lead to particle transport $\Gamma = \tilde{u}_{E\times Bx}\tilde{n} = i(k_y/B)\tilde{\phi}\tilde{n}$. With the $i\delta$ response this can be written as $\Gamma = \tilde{v}_{E\times Bx}\tilde{n} = +(k_y 1.71^2 \tilde{T}_e^{\,2})/(\delta B)$. The associated heat transport is $q = \tilde{v}_{E\times Bx}\tilde{n}\tilde{T}_e = -\frac{1.71k_y^2\tilde{T}_e^3}{\delta B}$, which is small as $\tilde{T}_e$ is small and in the opposite direction as the particle transport.

One possible scenario for the generation of solitary-like density perturbations regulating the particle transport is the following: a close to adiabatic coupling between potential and density can induce a solitary-like perturbation in the electron temperature, if the density fluctuation level and the electron temperature gradient are high and the electron temperature fluctuation level is low. This temperature perturbation can be proportional to the phase shift between potential and density and an increase of the temperature fluctuation level can lead to an increase in particle transport accompanied by a soliton-like waveform in the density induced by the adiabatic coupling. By means of line ratio spectroscopy on helium [242] or correlation electron cyclotron emission [243] it may be possible in the near future in AUG to measure density and temperature fluctuations at the same point in space and time and hence their cross-phase allowing a quantitative examination of the presented scenario.

11.6 Concluding remarks of turbulence in the I-mode

The major mystery in I-mode is which mechanism is responsible for reducing only one of the transport channels. I-mode turbulence promises great insight to the interaction of energy and particle transport barriers in general. In this chapter it has been shown, that

i) The most prominent feature of turbulence in I-mode is the weakly-coherent mode (WCM) (Sec. 11.1), which is a result of the ambient turbulence being modulated by the geodesic acoustic mode (Sec. 11.2). Magnetic fluctuations appearing at the WCM frequency are due to a global Alfvénic mode.

ii) Strong intermittent bursts appear during the I-mode. These bursts are responsible for a significant part of divertor heat loads. A strong correlation between density bursts and the WCM is observed (Sec. 11.4).

iii) A possible generation mechanism of these bursts based on a Korteweg-de-Vries-like nonlinearity has been proposed in Sec. 11.5.

External intermittency is a basic process of the transition from a laminar to a turbulent flow. At the transition from laminar to turbulent flows, laminar and turbulent regions coexist in the same flow. The Kármán vortex street is a well known example for this. This is consistent with the kind of intermittency observed by Doppler reflectometry in I-mode. Most of the time the turbulence is strongly suppressed and the fluctuations are restricted to small periods in time. Interestingly, there is a further similarity with a specific transition scenario to a turbulent state. The transition to drift-wave turbulence is found to follow the Ruelle-Takens scenario which has been described in detail in Sec. 8.2. By increasing the control parameter the system passes through different regimes from periodic to quasi-periodic to mode locked to weakly turbulent regime. In the mode locked regime a quasi-coherent mode appears. In this regime a large-scale flow structure is generated by the inverse energy cascade process and coupled to small-scale density fluctuations (Sec. 8.2). Through this coupling the density perturbations are phase locked and synchronized to the large-scale flow and appear as a quasi-coherent mode. This appears to be very similar to the WCM, where the density fluctuations are phase locked by the GAM. From this point of view, the I-mode can be seen to be at the transition to turbulence. Also other high confinement regimes exhibit quasi-coherent modes and may be considered to be rather at the transition to turbulence than turbulent. For example in the usual H-mode also quasi-coherent fluctuations appear in the magnetics at high frequency [443, 286] and the turbulence level is small.

Recently, huge progress on I-mode operation in ASDEX Upgrade has been made. Usually during I-mode the confinement successively increases, leading to an I-H transition. Now I-modes can be operated stationarily in a reliable way via beta feedback control [427]. This will allow for more detailed studies of turbulence in the I-mode regime in the future.

Chapter 12

Scrape-off layer turbulence

The scrape-off layer (SOL) refers to the region outside the last closed flux surface (LCFS) in a limiter plasma or outside the separatrix in a divertor plasma. The SOL is characterized by open field lines ending on material surfaces. The SOL governs the heat load on the plasma facing components, determines the power and particle balance and regulates the impurity dynamics. Therefore, understanding the SOL is essential for future reactor design. Transport in the SOL is determined to a huge fraction by intermittently occurring structures of enhanced plasma pressure [444, 445, 446, 447]. In the poloidal cross-section or drift-plane they appear compact and localized and therefore are called *plasma blobs*. These structures are also field-aligned [448] and therefore also called *plasma filaments*. Blobs are driven by the interchange instability [449, 450] (see Sec. 4.2). Due to the field alignment the parallel wavenumber is $k_\parallel = 0$, which is also a main feature of the interchange instability. The interchange instability of a strong pressure perturbation induces a charge separation as indicated in Fig. 12.1. Potential perturbations shifted by a phase of $\pi/2$ with respect to the pressure perturbation compose a potential *dipole structure*. The potential perturbations exhibit different signs and the corresponding radial electric field results in an outwards propagation of the original pressure perturbation. The blob generates its own convective flow. Therefore, blobs intrinsically propagate radially outward, which leads to rather strong radial convective transport. The dipole configuration of the potential has another interesting aspect. As explained in Sec. 3.5.3 the generation position of intermittent structures corresponds to saddle points of the potential and the saddle point of the potential dipole structure is exactly at the center of the blob.

Whereas these considerations hold for low-temperature laboratory plasmas [451, 181], the tokamak SOL is more complicated. If finite ion temperatures are included a dipole potential structure is observed neither in fluid [452, 453] and global full-f gyrokinetic simulations [454] nor in experiments in ASDEX Upgrade [180]. Instead, the potential rather exhibits a monopole like structure. However, the monopole in the potential is shifted with respect to the density structure still resulting in radial propagation and a saddle point within the

blob structure even though not exactly at the center. The influence of finite ion temperatures on the different regimes of blob propagation will be investigated in Secs. 12.1.2 to 12.1.7. Sec. 12.1 is based to mainly on the publications [18, 19].

The strong radial transport is a major concern for the first wall. Recent estimates of the erosion on plasma facing components found dominant erosion by plasma blobs for pure deuterium plasmas. Taking an impurity concentration of only 1 % into account the background plasma parameters determine the total gross erosion [455]. Also a stronger convective SOL transport may be desirable to relieve the divertor. The scrape-off layer heat flux width $\lambda_q = -q/\nabla q$ is in current experiments just of a few millimeters [456], which compares well with a heuristic drift-based model [457] $\lambda_q \approx 2q_s\rho_s$. However, turbulence based models of λ_q over-predict this observation [458]. This let suggest that filamentary transport is not that important around the separatrix region. The generation of plasma blobs will be subject of Sec. 12.2, which is based on the publication [20].

12.1 Blob propagation regimes

12.1.1 Standard blob models

The standard blob model provides a simple mathematical description of plasma blobs. Starting with a monopole (single-peaked) density perturbation with a peak value higher than (usually 2.5 times) the surrounding rms level, the magnetic curvature induces a charge polarization. Two $E\times B$ flow vortices with different signs are created poloidally above and below the blob (see Fig. 12.1). The resulting $E \times B$ drift moves the density in the direction of lower magnetic field strength or to larger major radius R.

The main elements of the plasma blob physics (charge separation and connection to the wall) appear in the polarization equation [459]

$$\nabla \cdot \frac{d}{dt}\left(en\rho_s^2\frac{e}{T_e}\nabla_\perp\phi\right) + \frac{2c_s^2m_i}{RB}\frac{\partial n}{\partial y} = \frac{2ne^2c_s(\phi-\phi_{fl})}{L_\parallel T_e}, \qquad (12.1)$$

where ϕ is the plasma potential, c_s is the sound speed, $L_\parallel$ the parallel connection length, $\rho_s = \sqrt{T_e m_i}/eB$ with electron temperature T_e, ion mass m_i, magnetic field strength B and elementary charge e. The first term is the time evolution of the vorticity, the second term is the so-called interchange forcing (Sec. 5.2.1) responsible for the charge separation and the term on the right-hand side results from the sheath (see Sec. A.4), where the floating potential $\phi_{fl} \approx 3T_e/e$ is assumed to be constant in space and time. Under stationary conditions the parallel dynamics, i.e. the parallel current (right-hand side of Eq. (12.1)) is balanced with the interchange forcing (second term on the left hand side of Eq. (12.1)) to gain an expression of the potential dynamics

$$\phi = \frac{c_s\rho_s^2BL_\parallel}{R}\frac{1}{n}\frac{\partial n}{\partial y} + \phi_{fl}.$$

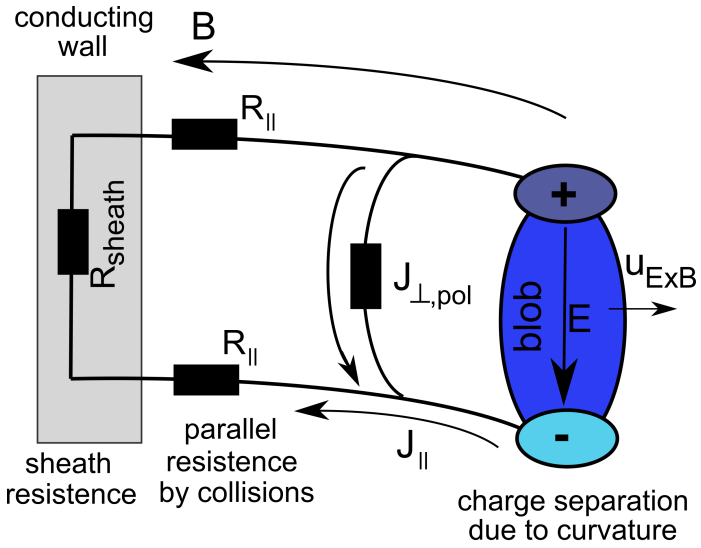

FIGURE 12.1: The blob equivalent electric circuit.

The time derivative of the vorticity (first term on the left hand side of Eq. (12.1)) is neglected, which leaves, as explained before, the polarization due to the magnetic field curvature as responsible for the blob propagation. It is assumed that the blob is radially advected with the $E \times B$ velocity associated with this potential. As the floating potential is constant it does has no impact on the radial velocity

$$v_b = -\frac{1}{B}\frac{\partial \phi}{\partial y} = -\frac{c_s \rho_s^2 L_\parallel}{R}\frac{\partial}{\partial y}\frac{1}{n}\frac{\partial n}{\partial y}. \tag{12.2}$$

By making the ansatz of an isolated blob parabolically shaped in y direction and propagating in radial (x) direction

$$n(x, y, t) = n(x)(x - v_b t)e^{-(y/\delta_b)^2}$$

with the size of the blob being δ_b. It follows that

$$\frac{\partial}{\partial y}\frac{1}{n}\frac{\partial n}{\partial y} = -(2/\delta_b^2).$$

Inserted into (12.2) the famous Krasheninnikov scaling arises [449, 460, 461]

$$v_b = 2c_s \left(\frac{\rho_s}{\delta_b}\right)^2 \frac{L_\parallel}{R}. \tag{12.3}$$

This is called the *sheath limited regime* of blob propagation. The application of this model to the radial propagation of ELM induced filaments has been done by Fundamenski [462].

As described by Garcia, there are several reasons why the conventional approximation of the sheath current may be insufficient [463]. It does not

comply with the observed ballooning and transport driven parallel flows and the assumption implies that it should be collisionless, while SOL plasmas often have significant collisionality. By neglecting the parallel current Garcia *et al.* obtain a blob propagation scaling independent of the parallel scale length and proportional to the square root of the blob size [463]

$$v_b = c_s \sqrt{\frac{2\delta_b}{R} \tilde{p}_e}, \tag{12.4}$$

where $\tilde{p}_e$ gives the blob pressure amplitude normalized to the background pressure. This scaling results from a balance between the first and the second term on the left-hand side of Eq. (12.1). In contrast to the Krasheninnikov model the sheath can be neglected. Recently this so-called *inertial regime* (Garcia scaling) and the sheath dissipation regime (Krasheninnikov scaling) have been unified by order of magnitude estimates [464] or by the inclusion of neutral collisions [465].

12.1.2 Blob model with warm ions

Most of the blob theories and simulations invoke cold ion models, which are realistic for most basic plasma physics experiments [465, 181, 466, 467, 182]. Here, theory and experiments of plasma blobs seem to converge [461]. The cold ion case is not realistic for the tokamak scrape-off layer, where typically the ion temperature T_i exceeds that of the electrons T_e [247, 289, 468, 469]. In the divertor it can be assumed that ion and electron temperature are thermally coupled resulting in $\tau_i = T_i/T_e \approx 1$ in agreement with the experiments at least in the near SOL [468]. Upstream the divertor in the case of a sheath connected plasma the parallel heat transport is dominated by conduction. Thus, the ion to electron temperature ratio can be roughly estimated by $\tau_i \sim (\kappa_e/\kappa_D)^{2/7} \sim 3$ [470] in agreement with the experiments [247, 289, 468]. Here $\kappa_{e,D}$ is the Spitzer heat conduction coefficient for electron and ion, respectively. Towards the wall, in the far SOL, the perpendicular transport by blobs becomes more important reducing the parallel transport by heat conduction and therefore modifying τ_i. In the far SOL $6 \leq \tau_i \leq 12$ is observed [469]. Therefore, the relevance of warm ions for the blob dynamics increases with the relevance of the blobs themselves. However, the SOL physics in the warm ion case relevant for fusion experiments have been only rarely investigated [452, 471, 472, 453] before subsequently presented work established a more detailed understanding of the role of warm ions in the SOL dynamics.

The following discussion is based on the DALF model (see Sec. 5.2) which includes finite ion effects. As seen above blobs are determined by the vorticity equation. The vorticity $\tilde{\Omega} = (1/B^2)\nabla_\perp^2 \tilde{W}$ is determined by the total ion flow stream function $\tilde{W} = \tilde{\phi} + \tau_i \tilde{p}_e$ which includes the ion pressure $\tilde{p}_i = \tau_i \tilde{p}_e$. The reason is that for finite ion temperatures also the ion diamagnetic velocity can change in time and has a contribution to the polarization drift. The first main difference to the standard blob models originates from the inclusion of

the ion diamagnetic contribution $\tilde{p}_i = \tau_i \tilde{p}_e$ to the polarization drift, which is neglected in the cold ion case. The negligence of $\nabla_\perp^2 \tilde{p}_i$ in the vorticity is equal to the negligence of the ion diamagnetic contribution to the polarization drift, which indirectly assumes MHD ordering [473]. If $\nabla_\perp^2 \tilde{p}_i$ is neglected, also $\nabla_\parallel \tilde{J}_\parallel$ should be neglected in a self-consistent treatment [473], which has been done self-consistently in the Garcia scaling (12.4).

An important difference to the cold ion case is that the dipolar vortex induced by the interchange drive is due to the ion pressure. This dipolar perturbation adds to the blob pressure inducing an asymmetry in poloidal direction, a feature also seen in simulations [452, 453]. Due to the asymmetry additional dipoles may form [453]. As the interchange drive will be stronger at the steeper flank this part of the blob will move faster resulting in a tilt of the blob. This effect is also called *blob spinning*. Additionally due to the tilt, the blob velocity is no longer just in the radial direction and a large fraction of the blob velocity v_b given by Eq. (12.15) may be in the poloidal direction. Also this has been seen in simulations [452, 453]. The poloidal fraction of the blob velocity will increase with the distance to the separatrix, effectively reducing the radial velocity of the blob.

The second term in Eq. (5.9) is the ion diamagnetic nonlinearity, which cascades energy from larger to smaller scales [474]. It can also be written as $\left\{\nabla_\perp \tilde{\phi}, \nabla_\perp \tilde{p}_i\right\}$ [473] consistent with the models in [452, 472]. Here $\{\cdot,\cdot\}$ denotes the Poisson bracket. The ion diamagnetic nonlinearity has been neglected in the derivation of the scaling laws.

To investigate the impact of the ion dynamics on the blob dynamics the parallel current equation (5.11) will be further simplified. First, no variation of the background pressure on a field line $\nabla_\parallel p_e = 0$ is assumed. Second, the normalized mass ratio $\hat{\mu}$ is neglected, which is justified as long as the effective growth rate of the blob stays below the ion-electron collision frequency. Both contributions to Eq. (5.11) possibly have an impact on the blob dynamics, but neither they result from the ion dynamics nor they are considered in the standard blob models. We leave these effects for future investigations.

The ion to electron temperature ratio τ_i has three main effects, all in the vorticity equation: It increases the interchange forcing and the drive of the blobs, it leads to polarisation currents which have a direct impact on the vorticity and it induces an additional nonlinearity which cascades energy to smaller scales, which can potentially break blobs apart.

Due to the simplifications explained above the scaling laws will be derived from the evolution of the polarization

$$\frac{d\nabla_\perp^2(\tilde{\phi} + \tau_i \tilde{p}_e)}{dt} = \nabla_\parallel \tilde{J}_\parallel - (1+\tau_i)\frac{2L_\perp}{R}\frac{\partial}{\partial y}\tilde{p}_e, \tag{12.5}$$

the electron pressure

$$\frac{d\tilde{p}_e}{dt} = \nabla_\parallel \tilde{J}_\parallel + \frac{2L_\perp}{R}\frac{\partial}{\partial y}(\tilde{\phi} - \tilde{p}_e), \tag{12.6}$$

and the parallel current

$$\beta \frac{\partial \tilde{A}_\parallel}{\partial t} = \nabla_\parallel (\tilde{p}_e - \tilde{\phi}) - C\tilde{J}_\parallel. \tag{12.7}$$

With the so-called *blob correspondence principle* [459, 461] (which is nothing else than a dimensional analysis by introducing typical scales, times and velocities as done in derivation of the cascades in Sec. 3.2), the linear instability of these fluid equations can be related to the radial blob velocity and scale size by

$$\omega_b \to \frac{v_b}{\delta_b}, \tag{12.8}$$

$$k_\perp \to \frac{1}{\delta_b}, \tag{12.9}$$

where ω_b is the characteristic blob frequency and $k_\perp$ is its perpendicular wavenumber. In the inertial regime of the standard blob models this characteristic blob frequency is the growth rate γ_b. In principle the blob correspondence principle also includes $L_\perp \to \delta_b$ and $k_\parallel \to 1/L_\parallel$, which is not applied here. The blob velocity is determined by the polarization (12.5), where in the inertial (or resistive) regime $\nabla_\parallel \tilde{J}_\parallel = 0$. If losses to the wall become important the sheath dissipation needs to be considered. Sheath dissipation $\sigma\phi/B$ [464] with sheath conductivity $\sigma = c_s/L_\parallel \rho_s^2$ can be included in the polarization equation (12.5). Due to its physical dimension it has to be normalized by $L_\perp \rho_s^2/c_s$ and it is included as $\sigma = L_\perp/L_\parallel$ resulting in

$$\nabla_\parallel \tilde{J}_\parallel = L_\perp/L_\parallel \tilde{\phi}. \tag{12.10}$$

12.1.3 Inertial regime

In the limit of a highly resistive plasma the parallel current is neglected. This regime corresponds to the hydrodynamic regime in the Hasegawa-Wakatani model (see Sec. 5.1). First as consistency check, the standard cold ion case ($\tau_i = 0$) (the case under MHD ordering) is derived. Then the warm ion case ($\tau_i \gg 1$) is studied and finally both regimes are unified.

In the cold ion case, both the polarization velocity and the vorticity are given by the potential $W = \tilde{\phi}$. The renormalized polarization equation (12.5) reads

$$\frac{L_\perp}{c_s}\frac{d}{dt}\rho_s^2 \nabla_\perp^2 \frac{L_\perp}{\rho_s}\tilde{\phi} = -\frac{2L_\perp}{R}\rho_s \frac{\partial}{\partial y}\frac{L_\perp}{\rho_s}\tilde{p_e}.$$

The blob velocity is the $E \times B$ velocity $\nabla\tilde{\phi} = -v_b/(\rho_s c_s)$

$$-\frac{L_\perp}{c_s^2}\frac{d}{dt}\rho_s \nabla_\perp \frac{L_\perp}{\rho_s} v_b = -\frac{2L_\perp}{R}\rho_s \frac{\partial}{\partial y}\frac{L_\perp}{\rho_s}\tilde{p_e}. \tag{12.11}$$

Applying dimensional analysis ($\partial/\partial x \to ik_x$, $\partial/\partial y \to ik_y$) to Eq. (12.11), assuming the blob is purely growing ($d/dt \to \gamma_b$) and the blob correspondence

principle ($\gamma_b = v_b/\delta_b$, $\delta_b = 1/k$) it is obtained that

$$\frac{L_\perp^2}{c_s^2}\frac{v_b^2}{\delta_b}\frac{1}{\delta_b} = \frac{2L_\perp}{R}\rho_s\frac{1}{\delta_b}\frac{L_\perp}{\rho_s}\tilde{p_e}. \tag{12.12}$$

and recover the scaling of Garcia (12.4). It should be noted that all derivations in this contribution are also valid for blobs being radially more strongly extended than poloidally $\delta_b = 1/k_y \gg 1/k_x$. Usually blobs exhibit this so-called streamer-like shape. In the presence of strong shear flows the blobs may be more strongly extended in the poloidal direction. In this case the poloidal size should still be taken as the blob size.

For moderate to high τ_i and/or strong pressure fluctuations which seem certainly justified for a blob, the ion flow stream function is determined by the ion pressure contribution $W = \phi + \tau_i p_e \approx \tau_i p_e$ and the polarization equation (12.5) reads

$$\frac{L_\perp}{c_s}\frac{d}{dt}\rho_s^2\nabla_\perp^2\frac{L_\perp}{\rho_s}\tau_i\tilde{p_e} = -(1+\tau_i)\frac{2L_\perp}{R}\rho_s\frac{\partial}{\partial y}\frac{L_\perp}{\rho_s}\tilde{p_e}. \tag{12.13}$$

Applying dimensional analysis ($d/dt \to i\omega_b = iv_b/\delta_b$) yields

$$-\frac{L_\perp}{c_s}\frac{v_b}{\delta_b}\rho_s^2\frac{1}{\delta_b^2}\frac{L_\perp}{\rho_s}\tau_i\tilde{p_e} = -(1+\tau_i)\frac{2L_\perp}{R}\rho_s\frac{1}{\delta_b}\frac{L_\perp}{\rho_s}\tilde{p_e}. \tag{12.14}$$

From the above given equation a scaling law for blob propagation can be derived

$$v_b = 2c_s\frac{(1+\tau_i)}{\tau_i}\left(\frac{\delta_b}{\rho_s}\right)^2\frac{\rho_s}{R} \tag{12.15}$$

revealing a square dependence on the blob size, in contrast to the standard models in Eqs. (12.3) and (12.4).

Before taking both contributions to the vorticity into account, the differences of the cold and warm ion cases are discussed in more detail. As the electrostatic potential ϕ has been neglected in the total ion stream function W, one could imagine that the electrostatic potential is not important for the blob dynamics and ask the question, what is the mechanism for blob propagation? The charge separation necessary for the blob propagation is hidden in the term $d/dt = \partial/\partial t + v_x\partial/\partial x$ with the advection v_x. Due to the gyroviscous cancellation upon advection the advective derivative $v_x\partial/\partial x$ is given by the $E\times B$ velocity only [475, 159]. As $i\omega_b = d/dt \approx v_x\partial/\partial x \approx iv_b/\delta_b$ the advective motion due to charge separation is contained in $v_b = \omega_b\delta_b$. Therefore, also in this case the propagation is given by the $E\times B$ velocity due to the charge separation resulting from the interchange drive. In the cold ion case the blob correspondence principle is used to relate the blob growth rate to the blob velocity and size by dimensional arguments $d/dt \approx \partial/\partial t = \gamma_b = v_b/\delta_b$. In the warm ion case it is an advection induced dispersion $d/dt \approx v_x\partial/\partial x \approx iv_b/\delta_b = i\omega_b$ balancing the effective gravity in stationary conditions, which can be also interpreted as wave propagation $v_b = \omega/k_x = \omega_b\delta_b$.

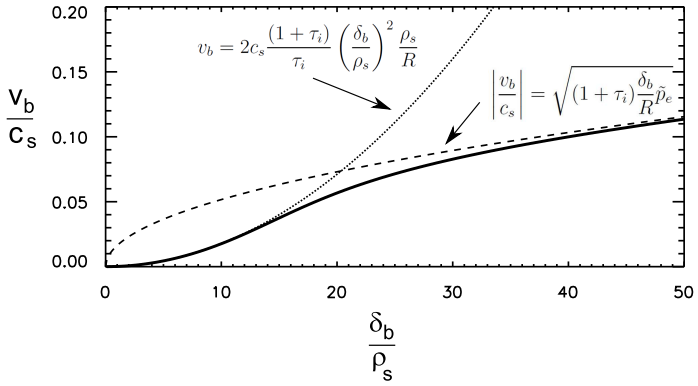

FIGURE 12.2: Blob velocity against blob size in the hot ion inertial regime. Plasma parameters used for this example are $\tau_i = 3$, $\tilde{p}_e = 1$, $\rho_s = 10^{-4}$ m, $R = 1.5$ m. Blobs with $\delta_b/\rho_s \ll \sqrt[3]{\tau_i^2 R/(8(1+\tau_i)\rho_s)} \approx 16$ are dominated by the ion contribution to the polarization, larger blobs are determined by the plasma potential. Figure adapted from Ref. [18].

Finally both contributions $\nabla_\perp^2 \tilde{\phi}$ and $\nabla_\perp^2 \tilde{p}_i$ to the vorticity are taken into account. The contributions from potential and pressure fluctuations are not in phase since we assume interchange characteristics

$$\left(\frac{v_b}{c_s}\right)^2 \frac{1}{\delta_b^2} - i\left(\frac{v_b}{c_s}\right)\frac{\tau_i \rho_s}{\delta_b^3}\tilde{p}_e = -i(1+\tau_i)\frac{2}{R\delta_b}\tilde{p}_e. \tag{12.16}$$

After completing the square

$$\left(\left(\frac{v_b}{c_s}\right) - i\left(\frac{\tau_i\rho_s}{2\delta_b}\tilde{p}_e\right)\right)^2 = -\underbrace{\left(\frac{\tau_i\rho_s}{2\delta_b}\tilde{p}_e\right)^2}_{f_i} - i\underbrace{(1+\tau_i)\frac{2\delta_b}{R}\tilde{p}_e}_{g}$$

and by matching real and imaginary parts, the blob velocity reads

$$\left|\frac{v_b}{c_s}\right| = \sqrt{\frac{\sqrt{f_i^2+g^2}-f_i}{2}}.$$

This result exhibits two limits illustrated by Fig. 12.2. For $|g| \gg |f_i|$, which holds for large blobs $(\delta_b/\rho_s)^3 \gg \tau_i^2 R\tilde{p}_e/(8(1+\tau_i)\rho_s)$, except a factor of $\sqrt{(1+\tau_i)/2}$, the τ_i-modified Garcia scaling is obtained

$$\left|\frac{v_b}{c_s}\right| = \sqrt{(1+\tau_i)\frac{\delta_b}{R}\tilde{p}_e}. \tag{12.17}$$

For smaller blobs $|g| \ll |f_i|$ and since $f_i > 0$

$$\begin{aligned}\left|\frac{v_b}{c_s}\right| &= \sqrt{\frac{f_i\sqrt{1+g^2/f_i^2}-f_i}{2}} \\ &\approx \sqrt{\frac{f_i(1+g^2/2f_i^2)-f_i}{2}} = \frac{1}{2}\sqrt{\frac{g^2}{f_i}},\end{aligned} \tag{12.18}$$

which recovers Eq. (12.15). Therefore, there are two inertial regimes, for smaller blobs the ion diamagnetic contribution to the polarisation current is responsible for their acceleration, where for larger blobs it is the $E \times B$ contribution. The first one is called the ion pressure dominated resistive ballooning regime (iRB) and the second the conventional resistive ballooning regime (RB). For typical SOL parameters ($\rho_s \sim 10^{-4}$ m, $R \sim 1$ m) the boundary between quadratic and square root blob size dependence is about $\delta_b/\rho_s \sim 10$.

In Ref. [18] it has been explicitly pointed out that the ion diamagnetic nonlinearity is dimensionally equal to the left-hand side of Eq. (12.13). Thus Eq. (12.15) gives also the maximum radial velocity at a given size in the linear approximation. Faster or non-isotropic structures will be strongly effected by the direct cascade of the ion diamagnetic nonlinearity and those structures will decay. Because potential and pressure perturbations do not have the same spatial structure and the impact of the ion diamagnetic nonlinearity is stronger on smaller structures compared to the ion diamagnetic contribution to the polarisation, just dimensional arguments could be misleading. A detailed numerical study has been necessary to investigate the canceling capabilities of the ion diamagnetic nonlinearity and its effects on the blob dynamics. In subsequent recent fluid and gyro-fluid simulations with seeded blobs the iRB regimes (blobs close to the ion Larmor radius scale) have been studied [476, 477]. In both studies the iRB scaling significantly underpredicts the blob velocity [476, 477].

12.1.4 Sheath dissipation regime

To model losses to the wall the divergence in the parallel current $\nabla_\parallel \tilde{J}_\parallel = L_\perp/L_\parallel \phi$ is taken into account. Just this term is included in the polarisation equation (12.5), everything else stays the same as in the full model Eq. (12.16). The sheath dissipation adds to the second term in Eq. (12.16) with $i(1/L_\parallel)(\delta_b^3/\rho_s^2)(v_b/c_s)$. The balance between the second term in Eq. (12.16) and $i(1/L_\parallel)(\delta_b^3/\rho_s^2)(v_b/c_s)$ gives the boundary

$$(\delta_b/\rho_s) = \sqrt[4]{\tau_i (L_\parallel/\rho_s)\tilde{p}_e} \tag{12.19}$$

between the inertial and the sheath effected regime. In the iRB inertial regime (12.15), blobs are smaller than $(\delta_b/\rho_s)^4 < \tau_i (L_\parallel/\rho_s)\tilde{p}_e$ (Fig. 12.3). If the sheath dissipation is stronger than the ion diamagnetic contribution to the polarisation, f_i can be substituted by $f_c = ((1/L_\parallel)(\delta_b^3/\rho_s^2))^2$. There are two sub-regimes of the sheath effected regime. The boundary is given by $|g| = |f_c|$ or

$$(\delta_b/\rho_s) \approx \sqrt[5]{8(1+\tau_i)\tilde{p}_e L_\parallel^2/(\rho_s R)}. \tag{12.20}$$

For blobs smaller than $(\delta_b/\rho_s)^5 \ll 8(1+\tau_i)\tilde{p}_e L_\parallel^2/\rho_s R$ the interchange forcing is most effective ($|g| \gg |f_c|$) and the inertial RB scaling (12.17) recovers. As seen in Fig. 12.3 the RB scaling gives an inaccurate reproduction of the curve

taking all terms into account. It is advised to take all terms into account in this regime. Further, it should be noted that the difference between the first and the second boundary is usually small, therefore the RB regime is very narrow and usually more difficult to see than in Fig. 12.3. Larger blobs will follow the Krasheninnikov scaling

$$\left|\frac{v_b}{c_s}\right| = (1+\tau_i)\left(\frac{L_\parallel}{R}\right)\left(\frac{\rho_s}{\delta_b}\right)^2 \tilde{p}_e, \tag{12.21}$$

except the additional drive by the factor of $(1+\tau_i)/2$. This regime will be called the sheath connected (SC) regime, here. Therefore under consideration of sheath dissipation we observe three regimes: the sheath non-effected iRB (12.15), the interchange dominated conventional RB regime (12.17) and the sheath connected regime (12.21).

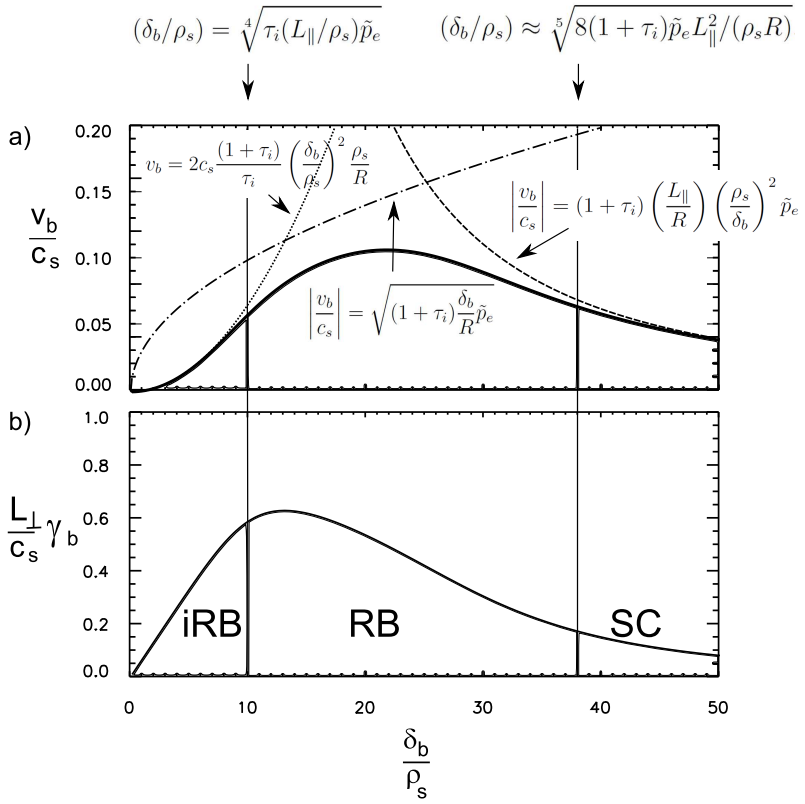

FIGURE 12.3: Blob velocity (a) and effective growth rate (b) against blob size in the sheath dissipation regime. Plasma parameters used for this example are $\tau_i = 3$, $\tilde{p}_e = 1$, $\rho_s = 10^{-4}$ m, $R = 0.4$ m, $L_\parallel = 10$ m. Blobs with $\delta_b/\rho_s \ll \sqrt[3]{\tau_i^2 R/(8(1+\tau_i)\rho_s)} \approx 10$ are dominated by the ion contribution to the polarization, larger blobs are determined by the plasma potential. Above $(\delta_b/\rho_s) \approx \sqrt[5]{8(1+\tau_i)\tilde{p}_e L_\parallel^2/(\rho_s R)} \approx 38$ the sheath dissipation dominates. Figure adapted from Ref. [18].

Obviously one might ask the question, in which of these regimes most of the blobs can be expected to occur. The blob correspondence principle states that the effective growth rate relates to the blob velocity by $\gamma_b = v_b/\delta_b$. Due to the additional factor of $1/\delta_b$, the maximum of the effective growth rate exhibits a maximum at the first boundary (12.19). For larger blobs the growth rate slightly decreases until the second boundary (12.20), where the growth rate strongly drops to $\sim \delta_b^{-3}$. As explained above the diamagnetic nonlinearity, which breaks the blob apart in smaller structures, as well as the tilt by the generation of additional dipoles in the vorticity will reduce the effective growth rate close to the first boundary and shift the scale, where most of the blobs will be detected closer to the second one. Except the factor of $\sqrt[5]{8(1+\tau_i)} \approx 2$ this expectation is in line with the standard blob theory [459]. As explained above the region of the RB regime is quite narrow which might explain, why in experimental investigations often only one blob size is detected [478].

12.1.5 Experimental and numerical comparisons

Next, these predictions are compared to experimental observations. Blob velocities and sizes have been measured in low-density L-mode discharges in ASDEX Upgrade using lithium beam emission spectroscopy (Li-BES) [263] (see Sec. 6.3) and, in L- and H-mode, gas-puff imaging (GPI) [274] (see Sec. 6.4).

The Li-BES measurements were done for a wide range of B in order to investigate the ρ_s dependence. The Li-BES signal is dominantly sensitive to the electron density. The GPI can measure the spatio-temporal behavior in more detail compared to the Li-BES with the penalty that the intensity depends on a combination of density and temperature. The results from the Li-BES analysis are presented from around $\rho_{pol} = 1.044$. The maximum intensity of the gas puff was located close to $\rho_{pol} = 1.065$. The experimental results are from the far SOL. The electron temperature was measured using Thomson scattering yielding for all discharges values in the range of $T_e = 12 \pm 8$ eV at the normalized poloidal flux coordinate position chosen as reference for the analysis of the Li-BES data [263]. Due to the lack of T_e profiles from probe measurements, T_e had to be assumed for the comparison of the GPI data with the analytical model. Here, in L-mode $T_e = 15 \pm 5$ eV and $T_e = 20 \pm 5$ eV in H-mode has been assumed [274].

To determine the blob size with Li-BES the radial half width at half maximum of the density perturbations is taken for the blob size. Due to the finite lifetime of the Li_{2p} state the blobs appear to be smeared out in the emission response [260]. For the detailed translation to the actual blob size we refer to Ref. [263]. We compare the cold ion case ($\tau_i = 0$) to the case with $\tau_i = 3$, which agrees with previous measurements in AUG [289] and simple theoretical considerations [470]. Assuming $\tau_i = 3$ the warm ion scaling predicts the blob size as measured by Li-BES (Fig. 12.4a) very well. From the GPI the blob size δ_b is determined by the poloidal semi axis of a fitted ellipse. Also the GPI measurements show a better accordance with the warm ion model ($\tau_i = 3$)

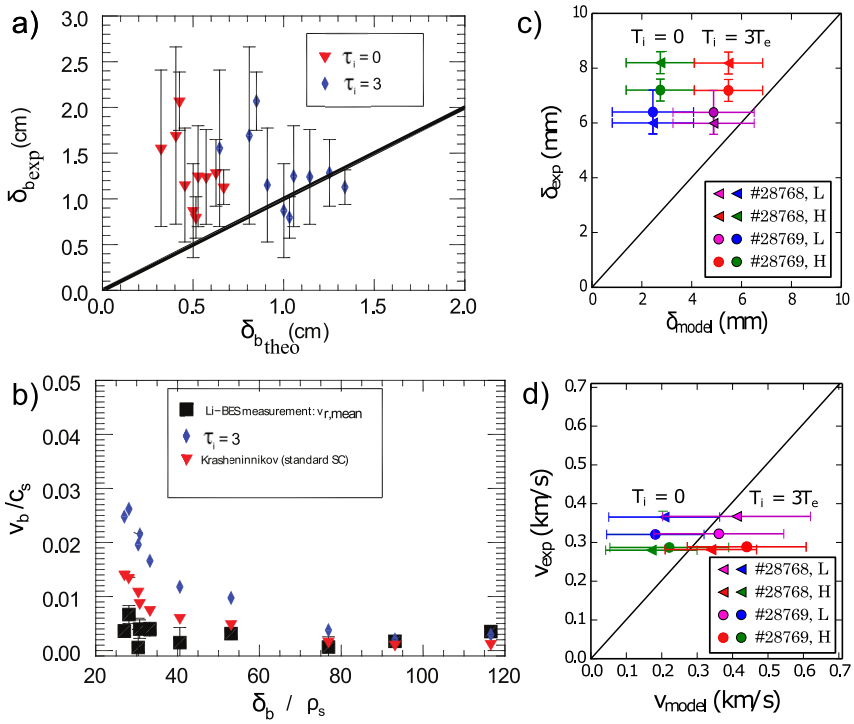

FIGURE 12.4: Characteristic blob size (a) and velocity (b) from LiBES compared with cold and warm-ion models (adapted from [19, 263]). Characteristic blob size (c) and velocity (d) from GPI compared with cold and warm-ion models (adapted from [19, 274]).

than with the cold-ion approximation (Fig. 12.4c). For the Li-BES data the radial velocity is calculated after conditionally averaging (Sec. 7.1.2), where the mean and maximum radial velocities are shown in Fig. 12.4b. The velocity decreases with increasing blob size indicating the sheath connected regime (Sec. 12.1.4). The absolute values from the scaling formula agree well with the measured mean velocities for larger blob sizes ($\delta_b/\rho_s > 50$). The measured maximum velocities generally exceed the cold ion sheath-connected scaling velocities especially for large blob sizes. For smallest blob sizes ($\delta_b/\rho_s \approx 30$), however, the scaling agrees well with the maximum velocities. Since the scaling formulas should be related to the maximum velocities rather than to the mean velocities as explained in [450], the better agreement of the warm ion case with the measurements points again to a possible influence of finite ion temperatures on the blob dynamics. Similar to the treatment of the simulated data an object recognition method has been used for the GPI data, where the blobs are tracked over several images and their radial velocity is estimated by their trajectories. In both, the Li-BES and GPI data the measured velocities are substantially smaller compared to the model predictions (Figs. 12.4b and 12.4d). Concerning the effect of uncertainties on the predictions by the model, the multiple dependence on the electron temperature (c_s, ρ_s, τ_i) is most

challenging.

Changing the toroidal magnetic field strength does not reveal any dependence on the blob size or velocity in the analysis of the Li-BES data, which is in contradiction to the explicit dependence in the model [263]. GEMR simulations carried out in comparison to measurements at Alcator C-Mod did also not show any magnetic field dependence in the simulation or the experiments [479]. Therefore, despite the overall good agreement in absolute numbers of blob sizes and velocities, it seems that still something is fundamentally wrong with these scaling laws.

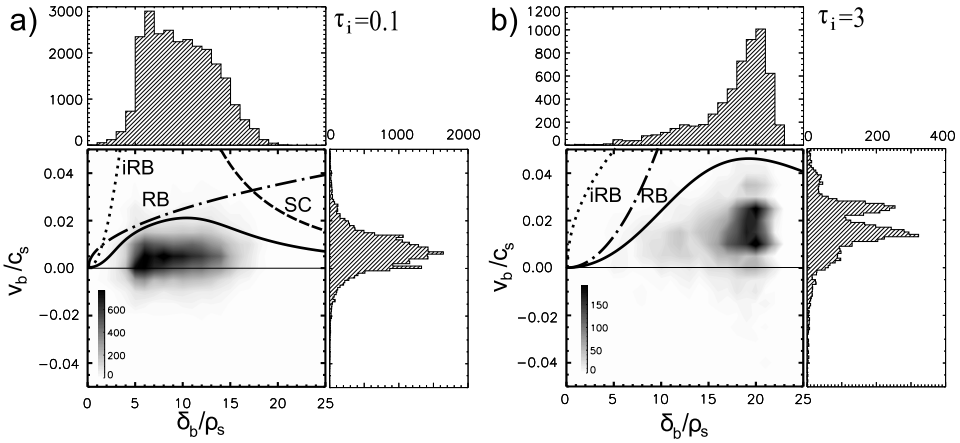

FIGURE 12.5: The center plot shows the distribution of blob sizes $\delta_b \rho_s$ and blob velocities v_b/c_s estimated from blob trajectories in a GEMR simulation with cold ions. The prediction (Eq. (12.16) solid line) as well as the limiting regimes (iRB dotted, RB dashed-dotted, SC dotted line) overlay the center plot. On the top the averaged blob size distribution and on the right-hand side the averaged blob velocity distribution is shown. Simulations results for cold ions ($\tau_i = 0.1$) are shown in (a) and for warm ions ($\tau_i = 3$) are shown in (b). Figure taken from Ref. [19].

Before the investigation presented here only a few studies of the effects of finite ion temperature on the blob dynamics had been carried out [452, 471, 453]. Mainly the dynamics of seeded blobs with predefined blob parameters (for example size, shape, amplitude) have been studied. We choose a different approach, where blobs are generated self-consistently and are not seeded. Such a simulation is provided by the three-dimensional gyrofluid electromagnetic turbulence model GEMR (see Sec. 5.3) used here. Within this framework, experimental and modeling results have already been compared with reasonably good agreement [479, 289, 180]. As GEMR is a 3D code no parallel closure is preassigned. Most of the effects, which are believed to play an important role for the plasma blob dynamics, are included in GEMR, namely, three-dimensional [480], electromagnetic [481], finite ion temperature [472, 18], finite Larmor radius [471] and shear flow (amongst others the zonal flow and the geodesic acoustic mode) effects [482, 483, 376]. Details on the simulation

parameters can be found in Tab. C.1 or in the original publication [19].

By an object recognition technique [285] (see Sec. 7.1.1) blob events are tracked over several images. The radial velocity of the trajectory is the blob velocity. The blob size is defined here by the diameter of a circle of the corresponding blob area, which is not circular in general. In this work, blob size and velocity of these trajectories are shown from the region from 1 cm to 2 cm outside the LCFS. The local plasma parameters are $\rho_s \approx 3.5 \cdot 10^{-4}$ m and $c_s \approx 43$ km/s, the connection length is about $L_\parallel \approx 15$ m. For better comparison with the experiment the blob-averaged fluctuation level of the density (of about $\tilde{n_e}/\langle n \rangle(\tau_i = 0.1) = 0.22$ and $\tilde{n_e}/\langle n \rangle = 0.48$) is taken as the blob amplitude. The normalization is done with the local background density $\langle n \rangle(r)$ as typically done in the experiments, and not with one density n_0 for all radial positions as typically done in the simulations. Taking n_0 as the LCFS value, local large fluctuations can be still small in the simulation $\tilde{n_e}/n_0 < \tilde{n_e}/\langle n \rangle$ as $n_0 > \langle n \rangle(r)$. The blob amplitudes strongly exceed the total fluctuation level of about $\tilde{n_e}/\langle n \rangle = 0.022$. For both the cold ion (Fig. 12.5a) and warm ion (Fig. 12.5b) case, the simulated blob size-velocity distribution is within the limits, shown by the dotted (iRB), dashed-dotted (RB) and dotted (SC) lines. For cold ions the predicted blob size-velocity dependence agrees very well with the simulated distribution. As the ion to electron ratio increases the density gradient in the SOL becomes flatter. We observe less but larger and faster blobs (Fig. 12.5b). As finite ion temperature effects become important the blob size distribution changes from positively skewed to negatively skewed and a bimodal velocity distribution develops. In the simulation the mean blob size changes from $\delta_b/\rho_s(\tau_i = 0.1) \approx 10$ to $\delta_b/\rho_s(\tau_i = 3) \approx 18$, where the cold ion model [459] predicts $\delta_b/\rho_s = \sqrt[5]{\tilde{p}_e L_\parallel^2/(\rho_s R)} \approx 18$ for $\tau_i = 0.1$ and $\delta_b/\rho_s \approx 21$ for $\tau_i = 3$. The changes are mainly due to changes in the blob amplitudes. The warm ion model predicts blobs appearing in the RB inertial regime [18]. This is between the maximum growth rate given by $\gamma_b = v_b/\delta_b$ [18] (which is $\delta_b/\rho_s(\tau_i = 0.1) \approx 4$ and $\delta_b/\rho_s(\tau_i = 3) \approx 14$) and the boundary to the SC regime given by Eq. (12.20) (which is $\delta_b/\rho_s(\tau_i = 0.1) \approx 27$ and $\delta_b/\rho_s(\tau_i = 3) \approx 41$, respectively). The present simulations are in the inertial RB regime. For finite ion temperatures the blob size distribution is limited to a very narrow region of only a few ρ_s. This feature is often observed in the experiments [478] and is a further indication that finite ion temperature effects play a significant role in the blob dynamics of high-temperature fusion plasmas.

12.1.6 Transition from sheath limited to inertial regime at high density

For magnetic confinement fusion devices such as ITER the power load on the foreseen divertor target material, tungsten, must be kept below $P \approx 10$ MWm^{-2}, which can only be achieved under detached or partially detached conditions [484]. Detachment is achieved at high SOL plasma densities. Fur-

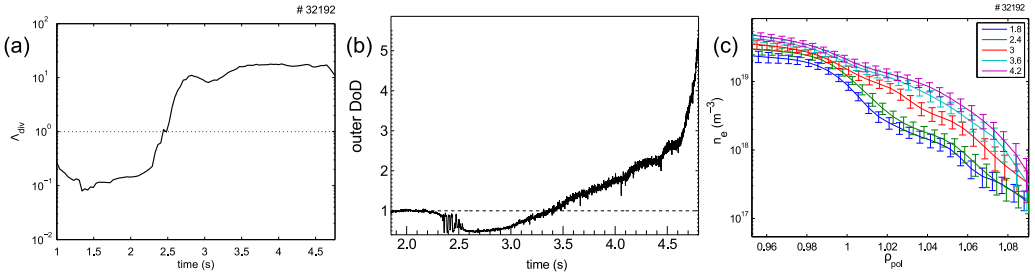

FIGURE 12.6: Shoulder formation in the SOL at high densities, (a) divertor collisionality measured by Langmuir probes, (b) degree of detachment DOD and (c) evolution of the density profile measured by Li-BES.

thermore, also the fusion performance depends on the density and therefore a reactor should run at high densities. The extrapolation of SOL transport based on experimental observations conducted in present tokamaks with attached divertors and low collisionalities may be seriously underestimating the future particle and heat fluxes onto the main chamber wall. With increasing background density a transition in SOL transport can occur, manifesting itself in the development of a shoulder in the radial density profile [485, 486, 487]. As proposed by Myra et al. [488] recent experiments in ASDEX Upgrade show that this transition occurs when a critical collisionality $\Lambda = (\nu_{ei} L_{\parallel})/(\omega_{ce}\rho_s)$ threshold is exceeded [489]. Here, ω_{ce} is the electron cyclotron frequency and ν_{ei} is the electron-ion collisionality. It has been found that the divertor parameters matter and for $\Lambda_{div} > 1$ larger, faster but fewer blobs have been observed [489]. The increase of filamentary transport leads to the shoulder formation [489]. The formation of the density shoulder and the divertor collisionality Λ_{div} is shown in Fig. 12.6. The critical divertor collisionality is exceeded at $t \approx 2.5$s. The detachment is classified by the notation of the *degree of detachment* (DOD), which is defined as the ratio between the calculated and the measured ion flux to the target. Details on the estimation procedure are given in Ref. [490]. The degree of detachment is shown in Fig. 12.6b. The flux to the outer divertor falls below the two-point model estimate at $t = 2.3$ s. The outer divertor detaches at $t = 3.5$ s. The density profiles show that the shoulder formation occur before $t = 3.0$ s, thus before the outer divertor detaches. This transition occurs in both in L-mode and in H-mode [491, 492]. The physical reason is that the plasma filaments are disconnected from the wall, the parallel current cannot be dissipated by the sheath and the curvature drive is balanced by the polarization current. A transition from the sheath limited regime (Sec. 12.1.4) of blob propagation to the inertial regime (Sec. 12.1.3) of blob propagation occurs [493]. The experimental data of the blob velocity-size dependence is in excellent agreement, once the influence of the amplitude is assumed to be $\tilde{n}/(\bar{n} + \tilde{n})$ instead of $\tilde{n}/\bar{n}$. This modification is motivated by full-f simulations [494]. Furthermore, the experimental results indicated that the ions have to be around $T_i \approx 3T_e$ in the sheath limited regime and cold in

the inertial regime after the transition [493]. Subsequent studies could show that the ion temperature indeed cools down after the transition [491].

Enhanced filamentary transport may be also important during the detachment process. Due to $E \times B$ drift induced by the sheath potential the power load to both divertors is not equally distributed [495], but the outer divertor receives much more power. Therefore, the inner divertor detaches first with increasing density. Different states are observed during the detachment process as described in Ref. [490]. Once the plasma blob propagation transitions to the inertial regime, they can overcome a much larger radial distance and can be seen in the far-SOL on the high-field side midplane [496]. These filaments allow for enhanced neutral flux into the region upstream of the X-point [497], which facilitates an upstream movement of ionization and recombination regions in the inner divertor and correspondingly allows for neutral flux through the private flux region to the outer divertor. This facilitates the detachment of the outer divertor.

12.1.7 Electromagnetic regime

It is known that ELM filaments carry a substantial current [498]. Due to Ampére's law the parallel current induces a magnetic field $\tilde{J}_\parallel = -\nabla_\perp^2 A_\parallel$, which translates within our scaling to $\tilde{A}_\parallel = (\delta_b/\rho_s)^2 \tilde{J}_\parallel$. For large blobs this will give a large contribution even at rather small $\hat{\beta}$. If the electromagnetic contribution dominates over the collisionality, Eq. (12.7) is given by

$$\hat{\beta}\frac{L_\perp}{c_s}\frac{v_b}{\delta_b}\left(\frac{\delta_b}{\rho_s}\right)^2 \tilde{J}_\parallel = -\frac{L_\perp}{\rho_s}\frac{L_\parallel}{\delta_\parallel}(\tilde{\phi} - \tilde{p}_e) \tag{12.22}$$

which is solved for $(\tilde{\phi} - \tilde{p}_e)$ and inserted into (12.6). From that a response of the parallel current can be deduced

$$\nabla_\parallel \tilde{J}_\parallel = \frac{\frac{L_\perp^2}{\rho_s \delta_b}\frac{v_b}{c_s}\tilde{p}_e}{1 - \frac{2L_\perp^2 \hat{\beta}}{R\rho_s}(\frac{\delta_\parallel}{L_\parallel})^2 \frac{v_b}{c_s}}. \tag{12.23}$$

For $1 \gg \frac{2L_\perp^2 \hat{\beta}}{R\rho_s}(\frac{\delta_\parallel}{L_\parallel})^2 \frac{v_b}{c_s}$ the adiabatic limit ($\nabla_\parallel \tilde{J} = d/dt(\tilde{p}_e) \rightarrow \tilde{\phi} = \tilde{p}_e$) is taken. Electromagnetic effects dominate the divergence of the parallel current for

$$1 \ll \frac{2L_\perp^2 \hat{\beta}}{R\rho_s}(\frac{\delta_\parallel}{L_\parallel})^2 \frac{v_b}{c_s}. \tag{12.24}$$

Note that here $\hat{\beta}$ is additionally normalized with $(L_\parallel/L_\perp)^2$. For example, an experimentally observed $\beta = nT/(B^2/2\hat{\mu}_0)$ in the order of 0.01 translates with $(L_\parallel/L_\perp) \sim 10^2$ to a $\hat{\beta}$ in the order of 10^2. Of course, for typical SOL conditions a β of only 10^{-5} to 10^{-4} can be expected, which rules out electromagnetic effects for modifying the dynamics. However, at least during pellet ablation,

the formation of high $\beta \sim 0.05$ drifting plasmoids has been observed [499] and it can be expected that the local β of ELM filaments is much higher than 10^{-4}. Then Eq. (12.23) reads

$$\nabla_\parallel \tilde{J}_\parallel = -\frac{R}{2\delta_b \hat{\beta}} \left(\frac{L_\parallel}{\delta_\parallel}\right)^2 \tilde{p}_e. \tag{12.25}$$

This gives the closure for the parallel current in (12.5). This term adds to the effective gravity. With the Alfvén velocity $u_A = B/\sqrt{4\pi n_0 m_i}$, $\hat{\beta} = (c_s/u_A)^2(L_\parallel/L_\perp)^2$ and a normalized Alfvén frequency $\omega_A = (u_A/\delta_\parallel)(L_\perp/c_s)$ the effective gravity can be written as

$$g = \omega_B \frac{\rho_s}{L_\perp} \left(1 + \tau_i + \left(\frac{\omega_A}{\omega_B}\right)^2\right).$$

Usually $g \gg f_i$ and the radial velocity is given by

$$\left|\frac{v_b}{c_s}\right| = \sqrt{\frac{\omega_B}{2}\frac{\rho_s}{L_\perp}\left(1 + \tau_i + \frac{\omega_A^2}{\omega_B^2}\right)\left(\frac{\delta_b}{\rho_s}\right)} \tag{12.26}$$

which gives a square root dependence on the filament size as suggested in experiments [469]. As the contribution of the electromagnetic part $\omega_A \sim 1/\delta_\parallel$ depends on the parallel extent of the structure, different parallel extents will result in a branch-like distribution in the v_b-δ_b scatter plot as experimentally observed [469].

Finally the requirements for the electromagnetic regime are summarized. For blobs larger $\delta_b/\rho_s > 2\Lambda L_\parallel/R = C\omega_B$, also $(\omega_A^2/\omega_B)(\delta_b/\rho_s) > C/\hat{\beta}$ holds. Together with relation (12.24), which is equal to $(L_\perp/\rho_s)(v_b/c_s) \gg (\omega_A^2/\omega_B)$, $(v_b/c_s)(\delta_b/\rho_s)(L_\perp/\rho_s) > (C/\hat{\beta})$ is fulfilled. Therefore, the electromagnetic regime is valid in finite beta turbulence ($\beta > m_e/m_i$), for blobs exceeding the velocity of $(v_b/c_s) > (R\rho_s)/(2\beta L_\parallel^2)$ with a size above $(\delta_b/\rho_s) > 2\Lambda L_\parallel/R$.

12.2 Blob birth

As described above a lot of progress has been made in understanding the propagation of blobs and the relation between blob size δ_b and velocity v_b [449, 450, 18, 464, 263, 274, 500, 476]. However, it is still unknown or there is no general agreement on how, where and at which rate blobs are generated [501]. Two generation mechanisms of plasma blobs are introduced in the following. The top row of Fig. 12.7 shows the common picture of blob generation [461]. A streamer is generated in the confined region and propagates into the shear layer at the separatrix. The shear tears apart the streamer into two smaller more isotropic structures. The structure penetrating into the SOL constitutes a blob and radially propagates due to interchange forcing. The row at the bottom of Fig. 12.7 shows the process due to turbulence spreading [502]. Structures in

the confined region and the SOL move along the background flow. This leads to enhanced collisions for these structures. The structures merge, particles and energy get mixed by the superposition of their $E \times B$ flow. Due to the shear the structure is torn apart again. Due to the process structures in the near SOL enhance their density and temperature, which leads to enhanced interchange forcing and the blob propagates outward. The spreading picture of blob generation is investigated in detail in the Sec. 12.2.3.

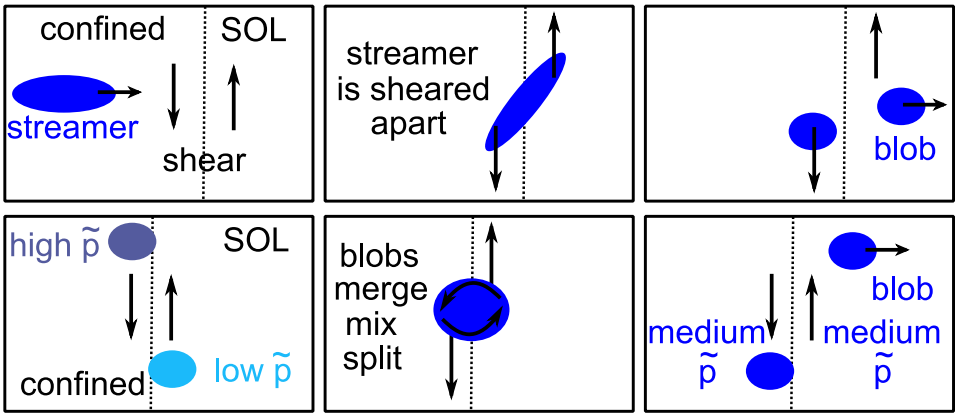

FIGURE 12.7: Schematic view of the blob generation process as explained in the main text.

Blob generation in linear devices due to elliptic instability
Elliptic instabilities are introduced in Sec. 3.3.5. Also vortices in a plasma should be subject to these kinds of instabilities [503]. In the following, an example relevant for linear plasma devices is briefly discussed. In linear devices the blob-ejection process is preceded by an acceleration of an $m = 1$ mode [504, 505, 506, 466]. Due to the $E \times B$ drift every perturbation in the potential is equivalent to a vortex. An $m = 1$ mode in the potential consists of a negative and positive perturbation, these are two vortices rotating in opposite directions and therefore an $m = 1$ mode is a counter-rotating vortex pair. Also the dipolar potential structure associated with plasma blobs is a counter-rotating vortex pair. It could be shown that the flow preceding the blob ejection in a linear device exhibits signs of the cooperative elliptical instability [275].

12.2.1 Skewness and blob trajectories

Intermittency is associated with non-Gaussian statistics, hence finite skewness and kurtosis (Sec. 3.5.1). As blobs correspond to large events in the amplitude distribution function, blob activity corresponds to large skewness values. Therefore, also the region where blobs occur exhibit a positive skewness, where the region where no blobs occur the skewness is zero. Blob birth is commonly associated with the skewness of density fluctuations crossing zero [507, 508, 461, 509]. By means of gyrofluid simulations carried out with the

GEMR code (Sec. 5.3) the generation of plasma blobs has been investigated. Details on the simulation parameter can be found in Tab. C.1 or in the original publication [20]. The results presented here occur for a wide range of simulation parameters [501].

The skewness and kurtosis profiles of the simulation are shown in Figs. 12.8d and e. Both are small inside the confined region pointing to a non-intermittent character of the fluctuations. Across the separatrix both increase indicating a more intermittent behavior outside. The skewness takes very small values 1 to 2 cm inside the confined region. This region coincides with the maximum in $-\nabla n/n$ (Fig. 12.8a). Assuming that the position of zero skewness is the position of the plasma blob generation, blobs would be generated about 2 cm inside the confined region. From that, blobs are expected to be generated inside the confined region and propagate across the LCFS into the SOL. As we will see in the following this interpretation is misleading.

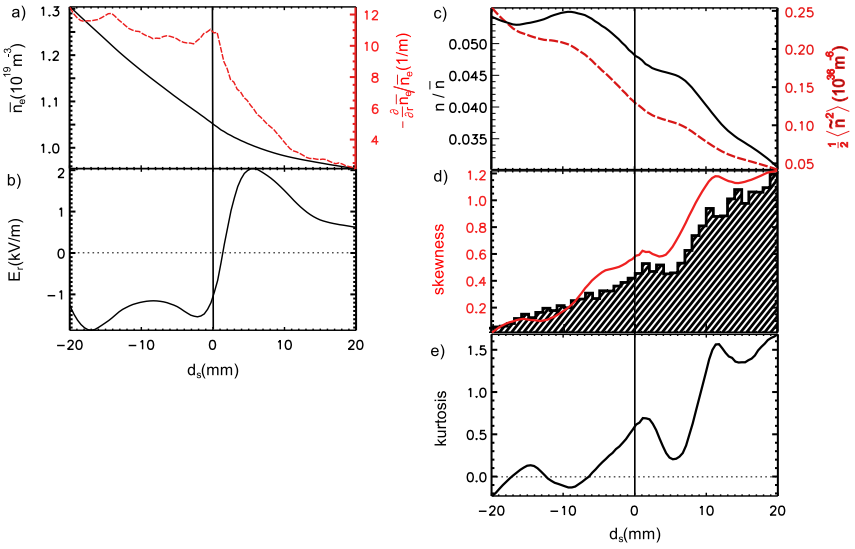

FIGURE 12.8: (a) Background density and inverse background density gradient length, (b) background radial electric field around the LCFS, radial profiles of the (c) density fluctuation amplitude, (d) skewness of density fluctuations and radial distribution of blob trajectories, (e) excess kurtosis of density fluctuations. Figures taken from Ref. [20].

The simulation provides the possibility to observe the blob generation directly. A snapshot of the density fluctuations is shown in Fig. 12.9a. Turbulent structures have a higher fluctuation amplitude inside the confined region as also shown by Fig. 12.8c. The reason is the stronger gradient. Outside the LCFS more positive than negative turbulent structures are observed, which can also be seen in the skewness (Fig. 12.8d). Positive density perturbations, which appear coherent and isolated, are blobs. Blobs are detected more frequently in the SOL. To investigate, where blobs originate from, they have to be defined first. Blob identification is done by three conditions. For every time step we

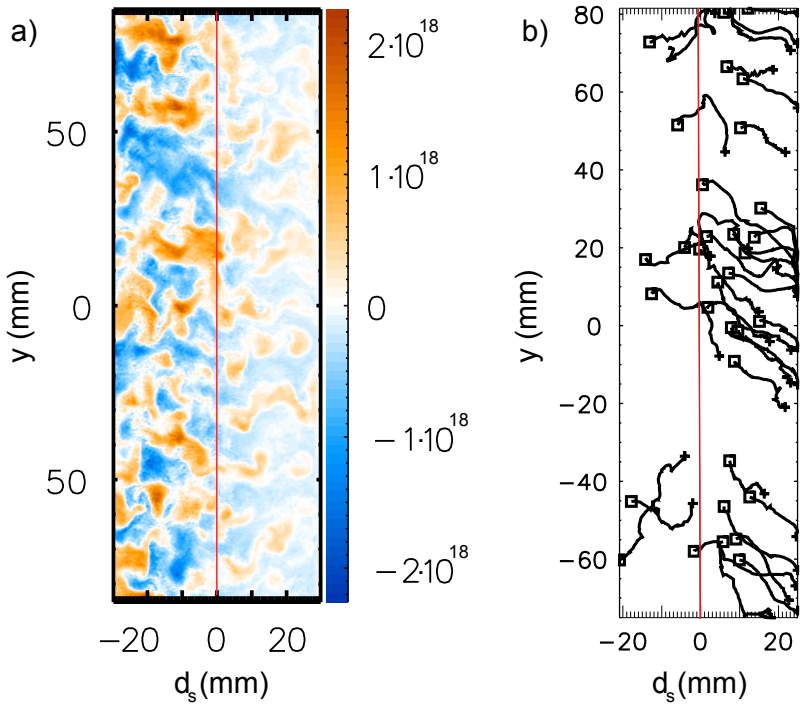

FIGURE 12.9: (a) Snapshot of the fluctuating density. (b) Examples of blob trajectories. Figures taken from Ref. [20].

identify blobs by two conditions. First we define blobs as positive density fluctuations, which exceed the standard deviation by a factor of 2.5. The radially local value of the standard deviation is used here, since it is usually used in experimental investigations. Second the blob has to fulfill this condition over a spatial extent of at least 11 points of the simulation grid ($\approx 8\rho_s \approx 5$ mm). After possible blobs have been identified for every time step these are tracked using the algorithm of Ref. [285]. Only structures which can be tracked for at least 50 time steps (≈ 25 μs) are considered as blobs. That is the third condition. The radial distribution of blob trajectories is inserted in Fig. 12.8d, showing a good agreement of the occurrence of the detected blobs with the skewness. The radial position of the first occurrence of a structure satisfying these conditions is the plasma blob birth location. The last occurrence will be defined as the blob death.

Examples for blob trajectories are shown in Fig. 12.9b. Blobs are generated over the entire domain. This observation is also shown in the blob birth statistics in Fig. 12.10a. Also the blob occurrence shows a pronounced poloidal asymmetry. Most of the blobs are detected above the midplane pointing to the fact that the magnetic configuration impacts the local dynamics similar to Ref. [41]. Some blobs form inside the confined region, where the background gradients are high, and propagate outwards (Fig. 12.10c). Most of them cross the separatrix (Fig. 12.10d). These are usually generated close to the LCFS (Fig. 12.10e). By propagating across the LCFS they change the poloidal prop-

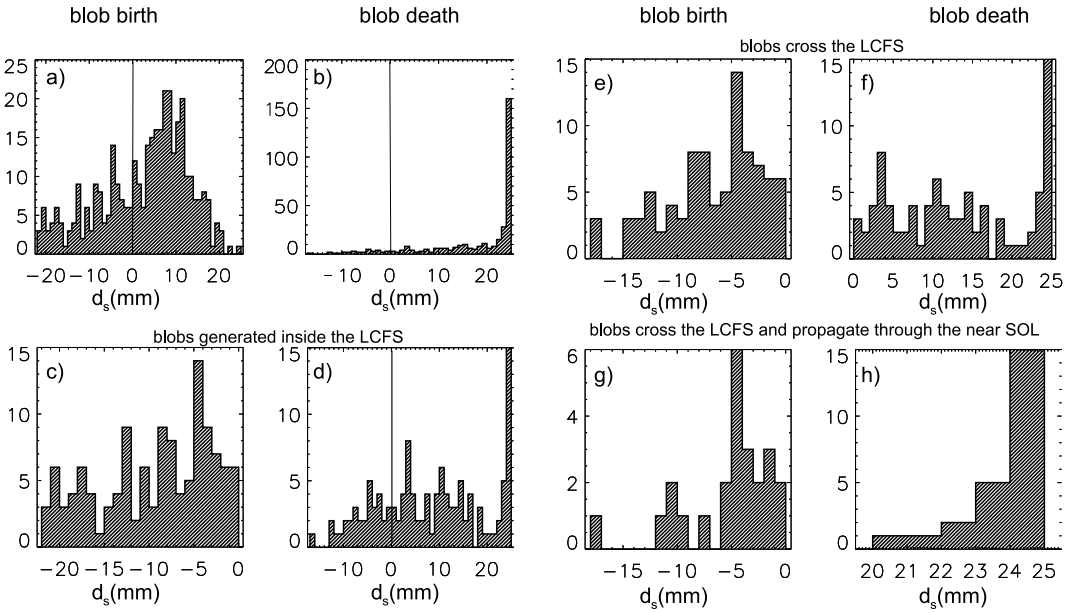

FIGURE 12.10: Statistics of the (a,c,e,g) birth and (b,d,f,h) death location of the detected blobs also under selective conditions: only blob which are generated inside the LCFS (c,d), which cross the separatrix (e,f) and which are generated inside the LCFS and propagate into the far SOL (g,h) are considered. Figures taken from Ref. [20].

agation direction (Fig. 12.9b). In the confined region blobs propagate in the electron diamagnetic direction, in the SOL in the ion diamagnetic direction. A remarkable fraction of blobs vanishes at the shear layer by either being torn apart or strained out [142], but most blobs reach the boundary of the simulation.

12.2.2 Blob occurrence rate

The prediction of the the blob occurrence rate [510], blob detection rate f_d [511] or simply blob frequency [455], as part of the blob duty cycle $f_d\tau_b$ or blob packing fraction is of great use for practical considerations about the blob transport, the SOL width [510, 512] and plasma-wall interaction [455, 512], since especially the large amplitude events carry the most energy and particles. For practical purposes the blob occurrence rate has to be estimated by experience from devices currently in operation [455, 510, 512]. It is basically assumed that the occurrence rate is same as in present devices. A predictive formula for the blob occurrence rate has not been available. A recently developed model enables the quantitative prediction of the blob detection rate in a fusion plasma [511]. The basic idea is shortly presented in the following: A dominant instability generates seed fluctuations, where only those at a particular size are allowed to become blobs. The most stable blob size δ_b

[513, 514] defines a selection rule on which scale the seed fluctuations can develop to blobs. Seed fluctuations at this particular size are generated by the rate $f_g = (u_{E\times B} + u_{ph})/\delta_b$, where $u_{E\times B}$ and u_{ph} are the $E \times B$ background and phase velocity (of the driving instability), respectively. If the amplitude distribution function is known, one can calculate how many events per time exceeding the standard deviation by the desired level are generated. This is the blob occurrence rate. This prediction has been compared with GEMR simulations with varying collisionality and shear layer strength. The prediction shows a robust agreement within a factor of two despite varying generation positions and driving instabilities [501].

12.2.3 Turbulence spreading in(to) the SOL

Finally the energetics is investigated. A simple K-ϵ model (see Sec. 3.6.2) is derived to investigate turbulence spreading (Sec. 3.8). Let us consider the radial convective part of the continuity equation only

$$\frac{\partial n}{\partial t} = -u_r \frac{\partial}{\partial r} n \tag{12.27}$$

neglecting damping and cross-field coupling. Fluctuations are defined by taking the difference to the zonal and time average $\langle\cdot\rangle = \int dydsdt$ as the mean quantity $\tilde{n} = n - \langle n\rangle$. For simplicity the radial background flow is neglected $\langle\tilde{u}_r\rangle = 0$ and the plasma turbulence is incompressible in the perpendicular plane, therefore $\partial_r v_r$ cancels out with its binormal counterpart. The evolution of the mean density neglecting sources, sinks and dissipation of simplicity is given by

$$\frac{\partial\langle n\rangle}{\partial t} = -\langle\tilde{u}_r \frac{\partial}{\partial r}\tilde{n}\rangle = -\frac{\partial}{\partial r}\langle\tilde{u}_r\tilde{n}\rangle. \tag{12.28}$$

We see that the background density is affected by the divergence of the turbulent transport $\Gamma = \langle\tilde{u}_r\tilde{n}\rangle$. As a divergence it conserves particles within the boundaries. The evolution of the background free energy is

$$\frac{1}{2}\frac{\partial\langle n\rangle^2}{\partial t} = -\langle n\rangle\frac{\partial}{\partial r}\langle\tilde{u}_r\tilde{n}\rangle = -\frac{\partial}{\partial r}(\langle n\rangle\langle\tilde{u}_r\tilde{n}\rangle) + \langle\frac{\partial n}{\partial r}\rangle\langle\tilde{u}_r\tilde{n}\rangle. \tag{12.29}$$

The total free energy $(1/2)(\langle n\rangle + \tilde{n})^2$ evolution is given by

$$\begin{aligned}\tfrac{1}{2}\tfrac{\partial\left\langle(\langle n\rangle+\tilde{n})^2\right\rangle}{\partial t} &= -\left\langle(\langle n\rangle + \tilde{n})\tilde{u}_r\frac{\partial}{\partial r}(\langle n\rangle + \tilde{n})\right\rangle \\ &= -\langle n\rangle\frac{\partial}{\partial r}\langle\tilde{u}_r\tilde{n}\rangle - \langle\frac{\partial n}{\partial r}\rangle\langle\tilde{u}_r\tilde{n}\rangle - \langle\tilde{n}\tilde{u}_r\frac{\partial\tilde{n}}{\partial r}\rangle.\end{aligned} \tag{12.30}$$

Subtracting the mean evolution gives the evolution of the turbulent free energy

$$\frac{1}{2}\frac{\partial\langle\tilde{n}^2\rangle}{\partial t} = -\langle\frac{\partial n}{\partial r}\rangle\langle\tilde{u}_r\tilde{n}\rangle - \langle\tilde{n}\tilde{u}_r\frac{\partial\tilde{n}}{\partial r}\rangle. \tag{12.31}$$

Using $\partial_r\langle\tilde{u}_r\tilde{n}\tilde{n}\rangle = 2\langle\tilde{u}_r\tilde{n}\partial_r\tilde{n}\rangle$ results in

$$\frac{1}{2}\frac{\partial\langle\tilde{n}^2\rangle}{\partial t} = -\langle\frac{\partial n}{\partial r}\rangle\langle\tilde{u}_r\tilde{n}\rangle - \frac{1}{2}\frac{\partial}{\partial r}\langle\tilde{u}_r\tilde{n}^2\rangle. \tag{12.32}$$

The first term of this equation appears with a different sign in the evolution of the background free energy (last term in Eq. (12.29)) and therefore constitutes a transfer term, which transfers the free energy from the background to the turbulent field. Where transport is responsible for the main loss of particles, it is the main drive of turbulence. We define the local drive of the turbulence by

$$\mathcal{D} = -\langle\frac{\partial n}{\partial r}\rangle\langle\tilde{u}_r\tilde{n}\rangle. \tag{12.33}$$

The second term is a divergence and preferentially transports the fluctuation amplitude from unstable to stable regions. This is the turbulence spreading term

$$\mathcal{S} = -\frac{1}{2}\frac{\partial}{\partial r}\langle\tilde{u}_r\tilde{n}^2\rangle. \tag{12.34}$$

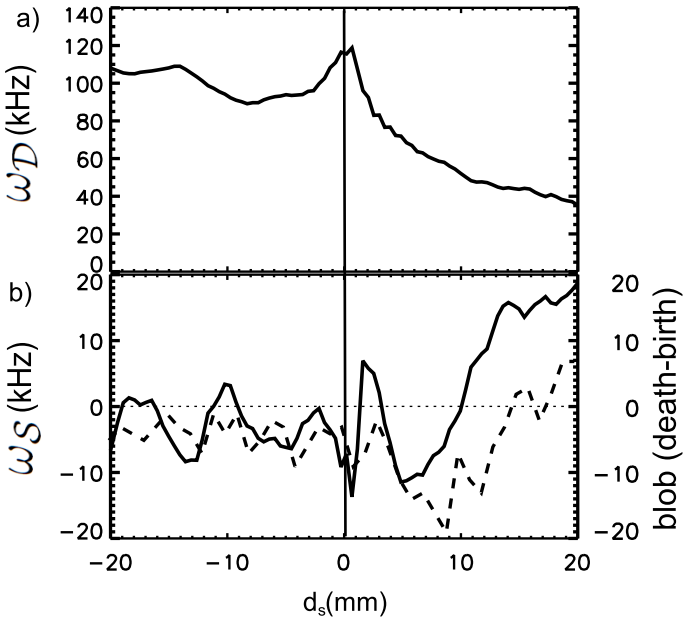

FIGURE 12.11: (a) Energetic drive by the background gradient and (b) turbulence spreading of density fluctuations (solid line). The dashed line in (b) shows the number of blobs that died reduced by the number of blobs born. Figure taken from Ref. [20].

Next, we use GEMR simulations already analyzed before (Sec. 12.2.1) to estimate the quantities discussed above. The present analysis is restricted to the same 2D plane at the low-field side midplane already analyzed in Figs. 12.8, 12.9 and 12.10 where blobs are prominent. The region considered here is

similar to those of a 2D simulation or experimental data from gas-puff imaging at the outboard midplane. It can easily be applied by using the average of $\langle\cdot\rangle = \int dydt$. For 1D probe measurements as by a reciprocating Langmuir probe $\langle\cdot\rangle = \int dt$ may be used. Figure 12.11 compares the rates of turbulent drive by the background gradient

$$\omega_{\mathcal{D}} = \frac{-\langle\frac{\partial n}{\partial r}\rangle\langle\tilde{u}_r\tilde{n}\rangle}{\frac{1}{2}\langle\tilde{n}^2\rangle} \tag{12.35}$$

with the rate of turbulence spreading

$$\omega_{\mathcal{S}} = \frac{-\frac{1}{2}\frac{\partial}{\partial r}\langle\tilde{u}_r\tilde{n}^2\rangle}{\frac{1}{2}\langle\tilde{n}^2\rangle}, \tag{12.36}$$

both normalized to the local fluctuation amplitude. The normalized turbulent drive as shown in Fig. 12.11a is interpreted as the local linear effective growth rate and the normalized turbulence spreading as shown in Fig. 12.11b as the nonlocal nonlinear growth rate. The local linear effective growth rate is higher in the confined region and peaks at the LCFS. The turbulent drive is very similar to the inverse background gradient (Fig. 12.8a). However, most of the blobs are generated in some distance to this position (Fig. 12.10).

The shear layer has been associated with blob formation [461, 482, 483, 376, 502]. Here it is located close to the LCFS (Fig. 12.8b). At the LCFS a transfer of free energy by turbulence spreading from the confined region into the SOL is observed. Compared to the linear growth rate this energy transfer is small (10%). This corresponds to the cascade-like picture of turbulence spreading [343] recently investigated at the shear layer close to the LCFS in simulations and experiments [502].

In the SOL, turbulence spreading transports the free energy from the region 7 mm outside the LCFS into the far SOL. The generation location of the turbulent intensity transport corresponds to the position, where the radial electric field exhibits its maximum (Fig. 12.8a) and the blobs are generated. The blob source is given by the number of blobs born reduced by the their deaths. The negative of the blob source (dashed line in Fig. 12.11b) roughly follows the turbulence spreading (solid line in Fig. 12.11b). Turbulence spreading connects blob sources and sinks. The analysis of turbulence spreading indicates a blob birth location of 7 mm outside the LCFS which is pretty close to the actual birth position at 9 mm, whereas the condition of crossing zero skewness (Fig. 12.8d) would predict the blob birth region at 20 mm inside the LCFS. Turbulence spreading provides a more suitable diagnostic for the blob birth location than the skewness alone. Spreading becomes stronger further out and reaches half of the local drive 2 cm outside the LCFS (comparing the solid lines in Fig. 12.11a and b). Therefore, it can be expected that turbulence spreading is the main drive in the far SOL. Turbulence spreading in the main SOL is mainly carried by the blobs and not by the cascade-like interaction which is more relevant around the separatrix. The results presented in this section have been recently experimentally confirmed in the COMPASS tokamak [515].

12.3 Concluding remarks on SOL turbulence

The main results of this chapter can be summarized as follows:

i) The basic plasma blob propagation model relies on the assumption of cold ions, which does not hold in high-temperature fusion experiments. The impact of finite ion temperatures on plasma blob propagation has been included into this model (Secs. 12.1.3 and 12.1.4), which lead to increased agreement of experiments and simulations (Sec. 12.1.5).

ii) Under reactor relevant conditions at high densities, the SOL density profile flattens and filamentary transport is increased (Sec. 12.1.6).

iii) It has still been unknown or there is no general agreement on how, where, and at which rate blobs are generated. The results in Sec. 12.2 show that blobs do not have to be generated in the confined plasma and may be a SOL-only phenomenon. First attempts on predicting the blob occurrence rate are presented.

iv) Turbulence in the far-SOL cannot be driven by the gradients as turbulence in the confinement region. Therefore, transport in the far-SOL is essentially coupled to the confined region or the near-SOL. Such nonlocal coupling can be described by turbulence spreading. In Sec 12.2.3 a turbulence spreading model of the SOL is presented.

Chapter 13

Conclusions

Turbulence is a very complex phenomenon. Compared to neutral fluids, turbulence in magnetically confined fusion plasmas involves even more fields (velocity, densities, temperatures, heat fluxes, electrostatic and magnetic potentials for at least two species). Key issues are to predict and to understand transport of particles, heat and momentum, which determine the confinement of the magnetically confined fusion plasma and hence its technical and economic feasibility. At lower turbulence levels higher energy confinement times could be achieved, which could allow operation of a future fusion reactor at smaller macroscopic scales. Key questions are:

i) What are the driving instabilities of plasma turbulence and what is their dependence on plasma parameters and magnetic geometry?

ii) How can plasma turbulence be suppressed, reduced or maybe even avoided?

The traditional way of understanding plasma turbulence is still strongly based on quasi-linear theory: Plasma turbulence is thought to develop due to the linear growth of infinitesimal perturbations, which nonlinearly saturate to the turbulent state. The driving linear instability sets the typical scale (called injection range), the cross-phases between the different fields (densities, temperatures, electrostatic and magnetic potentials), and by their combination also the particle and heat transport. In this sense, plasma turbulence is not universal and may be classified by its driving instability (for example ITG, ETG, MTM, drift-wave or resistive ballooning turbulence). Understanding the dependence of the growth rates of the different instabilities on plasma parameters or magnetic geometry may provide means to reduce the resulting turbulent transport. A possibility to suppress the turbulence is provided by shear flows. It is widely accepted that shear flows tear apart small-scale turbulent structures. As a result the typical length scale of the turbulence and hence the turbulent transport is reduced.

In case of large fluctuation amplitudes, it seems questionable if quasi-linear theory still provides a sufficient framework. In the plasma edge the fluctuation amplitudes are observed to reach from the order of 10 % in the confined

region to order of unity in the scrape-off layer. At these high fluctuation levels nonlinear effects become more important and even new physical mechanisms arise due to the dynamics of the amplitudes of the turbulent fluctuations themselves. Examples for purely nonlinear effects are the cascades (investigated in detail in Sec. 8.1) and *turbulence generated shear flows*, so-called zonal flows. Examples for such new mechanisms are *turbulence self-sustainment*, where the turbulence can nonlinearly drive transport and thereby sustain itself even though the growth rates can be negative, and *turbulence spreading*, where the turbulence can radially spread into regions, which are otherwise stable. Both can lead to turbulence in linear stable situations, which is called subcritical turbulence. The three mechanisms turbulence self-sustainment, turbulence spreading and turbulence-shear flow interaction correspond to the mechanisms of generation, transport and possibly suppression of the turbulence amplitudes. Specific questions arising and discussed in the here presented work include

i) Once finite perturbations are present, they drive transport and the turbulence can sustain itself without any need of linear instabilities. If linear instabilities are not necessary, what is the process for the transition from the 'laminar' to the turbulent state in drift-wave turbulence (Sec. 8.2)? How does turbulence self-sustainment effect linear properties as dispersion (Chap. 9)? Due to improved confinement at some point the amplitude may be that low that the system is not in the turbulent state anymore (Chap. 11). Does 'turbulence' in this state show similarities to the transition from the 'laminar' to the turbulent state (Sec. 8.2)?

ii) How does turbulence spreading effect zonal flow formation (Sec. 8.3)? How can turbulence spreading be quantified or measured (Sec. 12.2.3)?

iii) What is the radial structure of the generation mechanism of zonal flows (Sec. 8.3)? What is the poloidal structure of their generation mechanism (Sec. 10.3)? How does the magnetic geometry effect zonal flow formation (Sec. 10.3)? And, finally, can these turbulence generated shear flows be strong enough to trigger a transition to improved confinement (Sec. 10)?

In the following the results obtained within this work will be summarized to gain deeper insight into these three topics: turbulence self-sustainment, turbulence spreading and turbulence-shear flow interaction.

Subcriticality and self-sustainment have been investigated during the transition to drift-wave turbulence in a linear low temperature plasma experiment (Sec. 8.2). Self-sustainment is achieved due to the interplay between the inverse and direct cascades of kinetic and free energy, respectively (Fig. 5.1). Kinetic energy is transferred towards larger scales ($k\rho_s < 1$). Due to adiabatic coupling the energy is transferred to the free energy, which is transferred to smaller scales ($k\rho_s \approx 1$). The excited fluctuations lead to transport, which in presence of a gradient, lead to additional turbulent drive. Due to adiabatic coupling free energy at $k\rho_s \approx 1$ is transferred to kinetic energy, which

is transferred to larger scales. Prior to the transition to the weak turbulent regime, a quasi-coherent mode appears. This quasi-coherent mode is a result of phase-locking the subcritically excited density fluctuations (generated by the direct cascade) via a large-scale flow, generated by the inverse cascade (Sec. 8.2). Subcriticality and self-sustainment have also been investigated in simulations of L-mode plasmas (Chap. 9). The turbulence is fully developed and the spectra are broadband. Here, the small-scale vorticity generated by the self-sustainment process can suppress wave-like linear features (even the phase velocity). In particular the growth rate becomes irrelevant. At lower fluctuation levels, experiments in ASDEX Upgrade show that the turbulence in the improved confinement regime (I-mode) is not broadband, but instead dominated by the so-called weakly coherent mode (Chap. 11). The weakly coherent mode is a quasi-coherent feature, where the driving region is phase-locked by a turbulence generated flow (the geodesic acoustic mode). In this sense the I-mode turbulence is very similar to the phase-locked regime appearing before the transition to the turbulence state (Sec. 8.2). Interestingly, turbulence in I-mode becomes very intermittent. The intermittency during I-mode is of the type of external intermittency, which is a signature of a flow being at the transition from the laminar to the turbulent state. Quasi-coherent modes also appear in H-mode [443, 286] and in regimes of reduced turbulence induced by plasma biasing [139].

Turbulence spreading has been investigated with respect to zonal flow generation in a linear experiment (Sec. 8.3). Zonal flow generation is a spatially nonlocal process. Turbulence driven by a pressure gradient spreads into the region of strong shear, where energy is transferred from the fluctuations to the mean flow. The mean kinetic energy is radially transported via the Reynolds stress towards the region of strong mean flow. Therefore, the excitation and dissipation regions of the zonal flow are radially disjunct. Furthermore, turbulence spreading should be relevant for the scrape-off layer (SOL) (Chap. 12) and in particular dominant for the far-SOL. The turbulence drive is given as the product of the transport and the gradient. In the far-SOL the gradients get very shallow and at some point the locally driven transport cannot account for the reduction of the gradient anymore. However, due to the transport of the fluctuation amplitude, turbulence in the far-SOL can be excited. A turbulence spreading model for the SOL is presented in Sec. 12.2.3.

The role of turbulence generated zonal flows in transport barrier formation at the transition from low confinement (L-mode) to high confinement (H-mode) is one of the most controversially discussed topics in magnetically confined fusion plasmas. It is discussed in detail in Chap. 10. The regime between L- and H-mode (the I-phase) is dominated by limit-cycle oscillations (LCOs). These LCOs have been predicted by a predator-prey model [360, 361], where turbulence generated flow and equilibrium flow shear are two competing predators interacting with drift-wave turbulence (prey). The example from the pipe flow, where by initially increasing turbulence intensities a complete collapse of turbulence can be accomplished [4], is somehow similar to the idea behind the L-H

transition by Kim and Diamond. By increasing the pressure gradient, the turbulence intensity is strongly increased, leading to the development of a strong flow shear completely suppressing the turbulence. This theory is supported by various experiments [362, 365, 364, 13, 404, 410, 376, 26, 258] which found that turbulence suppression by flow generation appears strong enough to trigger a transition into the H-mode [13, 404, 258, 271]. On the other hand other experiments show only weak or insufficient zonal flow activity at the L-H transition [410, 376, 412, 62]. At first glance this seems to be in contradiction. To resolve this contradiction from an experimental point of view is a demanding task as zonal flow generation is nonlocal in physical space (Sec. 8.3) and the Reynolds stress is not homogenous on a flux-surface in diverted geometry (Sec. 10.3), hence plasma potential and ion pressure fluctuations of the complete poloidal cross-section in the entire pedestal region have to be measured with a resolution of ρ_s. However, this possible contradiction can be easily resolved by the following consideration. The energy transfer from the turbulence to the shear flow is the Reynolds stress multiplied by the flow shear. Therefore, both the equilibrium flow shear and the zonal flow shear contribute to the energy transfer. Assuming the energy transfer from the turbulence to the shear flow to be strong enough to suppress the turbulence completely, the energy gain of the mean flow is just in the order of the fluctuation level of the turbulence (10 %). Defining the zonal flows as the turbulence driven difference to the equilibrium flow, the kinetic energy of the zonal flow would be at best in the order of this energy gain. The zonal flow would be dissipated via geodesic and adiabatic transfer to the global Alfvén oscillation, which is resistively dissipated (Sec. 5.2.3). It seems therefore impossible for the zonal flow to have major impact on the total flow, although the energy transfer process (mainly due to the equilibrium flow shear) can still have substantial impact on the turbulence level, successively reducing transport, increasing gradients and therefore the equilibrium flow. This energy transfer process is part of the zonal flow physics picture and does not appear in a framework considering the equilibrium flow only. Therefore, the energy transfer process should be important to understand shear flow suppression, because the paradigmatic shear decorrelation and the associated quenching rule (Sec. 3.7) do not apply to high-amplitude L-mode conditions in the plasma edge (Chap. 9). Shear decorrelation and the quenching rule might rather be applicable, once the fluctuation level is reduced as in high confinement regimes.

Seen in the general context, the here introduced methodology offers a somewhat different perspective on plasma edge turbulence compared to the well-established quasi-linear point of view. Optimizing the linear growth rates of driving instabilities seems rather meaningless for the plasma edge. To understand plasma edge turbulence it is indispensable to investigate the flow of the generalized turbulence energies and the energy exchange terms between the different fields and scales. These exchange terms determine the nature of turbulence as for example the individual gradient drive of the fluctuation amplitudes, the relative strength of electrostatic and magnetic transport and

shear flow suppression by energy exchange. The relative strength of the exchange terms determines the cross-phases, which set the relative strength of the different transport channels. These determine the gradient scale lengths of the different fields. Understanding the complex interplay between the different exchange terms and their dependence on plasma parameters and magnetic geometry seems to be the key to design appropriate plasma edge turbulence. Viewed from this angle studying the impact of magnetic fluctuations, high density operation and different ratios of the gradient scale lengths in particular on the self-sustainment mechanism seem to be reasonable next steps to gain deeper insight into still not well enough understood phenomena as for example the transition to different confinement regimes (L-H and L-I transitions).

Appendix A

Introduction to plasma dynamics

The two main important quantities describing a fluid are the particle density n and the velocity u, with the particle density given in units of m^{-3}. In a plasma we have to consider at least two different species of charged particles: electrons and ions. Each species follows its own fluid equation, therefore two fluid equations are needed to describe the plasma. These species will be distinguished by the index j with $j = e$ for the electrons and $j = i$ for the ions. For neutral fluids we will skip the index. In plasmas electrons and ions are distinguished by their mass m_j and charge q_j. We will consider the mass density

$$\rho_{mj} = m_j n_j \tag{A.1}$$

and the charge density

$$\rho_j = q_j n_j. \tag{A.2}$$

The flow velocity $u_j = \langle v_j \rangle$ is the average $\langle \cdot \rangle$ of the statistically distributed particle velocity v_j. Also the temperature T_j is related to the particle velocity via

$$\frac{3}{2} T_j = \frac{1}{2} m_j \langle v_j^2 \rangle. \tag{A.3}$$

Related quantities are the kinetic pressure

$$p_j = n_j T_j \tag{A.4}$$

and the electric current density

$$\mathbf{J} = \sum_j q_j n_j \mathbf{u}_j. \tag{A.5}$$

A.1 Magnetized plasmas

This work mainly considers magnetized plasmas, to which a short introduction is given. In a magnetic field of strength B the particles (ions and electrons) are

subject to the Lorentz force, which leads to gyration of the particles around the magnetic field lines. This gyromotion exhibits a characteristic frequency called gyration or cyclotron frequency

$$\omega_c = \frac{qB}{m}. \tag{A.6}$$

The radius of the gyration is called the *Larmor radius*

$$\rho_L = \frac{\sqrt{2mT}}{qB} \tag{A.7}$$

which has an additional dependence on the temperature T. Both particle species follow their own equation of motion

$$\rho_m \frac{d}{dt}\mathbf{u} = -\nabla p + \rho(\mathbf{E} + \mathbf{u} \times \mathbf{B}) \pm \mathbf{R}_{ei} \tag{A.8}$$

which is similar to the Navier-Stokes Eq. (3.4). Because the particles are charged electromagnetic forces (Coulomb force $\rho\mathbf{E}$ and the Lorentz force $\rho(\mathbf{u} \times \mathbf{B})$) appear. Viscosity can be neglected because the thin gases we consider do not exhibit strong viscous effects. Instead, a friction force between ions and electrons appears. Due to the action-reaction principle both forces are equal and opposite. The friction forces can be written as

$$\mathbf{R}_{ei} = -\mathbf{R}_{ie} = (en)^2(\mathbf{u}_e - \mathbf{u}_i)/\sigma \tag{A.9}$$

where σ is the electric conductivity (and $1/\sigma$ the electric resistivity). The friction can also be written as being proportional to the ion-electron collision frequency ν_{ei}

$$\mathbf{R}_{ei} = -\mathbf{R}_{ie} = nm_e\nu_{ei}(\mathbf{u}_e - \mathbf{u}_i). \tag{A.10}$$

Finally, from the conservation of energy the *equation of state*

$$\frac{p}{\rho_m^\gamma} = \text{const} \tag{A.11}$$

follows, which is also known from thermodynamics. The adiabaticity coefficient γ depends on the degrees of freedom f of the system for adiabatic processes: $\gamma = (f+2)/f$. For isothermal processes $\gamma = 1$.

A.2 Drifts in magnetized plasmas

Turbulence in a magnetized plasma occurs mainly perpendicular to the magnetic field. As velocity perturbations are the heart of turbulence the velocity perpendicular to the magnetic field is of major importance. To obtain the perpendicular motion we have to take the cross product of Eq. (A.8) and $\mathbf{B}$. The term corresponding to the Lorentz force using the vector identities

$(\mathbf{A}\times\mathbf{B})\times\mathbf{C} = -\mathbf{C}\times(\mathbf{A}\times\mathbf{B}) = -((\mathbf{C}\cdot\mathbf{B})\mathbf{A} - (\mathbf{C}\cdot\mathbf{A})\mathbf{B})$ gives the perpendicular velocity $(\mathbf{u}\times\mathbf{B})\times\mathbf{B} = -\mathbf{u}_\perp B^2$. Solving Eq. (A.8)$\times\mathbf{B}$ for $\mathbf{u}_\perp$ yields

$$\mathbf{u}_\perp = \frac{\mathbf{E}\times\mathbf{B}}{B^2} - \frac{\nabla p\times\mathbf{B}}{\rho B^2} - \frac{\rho_m}{\rho}\frac{\frac{d\mathbf{u}}{dt}\times\mathbf{B}}{B^2}. \tag{A.12}$$

The first term is the $E\times B$ drift which is usually the strongest one. As a strong pressure gradient will often be present the second term, the so-called diamagnetic drift, will also be important. The last term is the polarisation drift. Diamagnetic and polarisation drifts can lead to currents

$$\mathbf{J} = en(\mathbf{u}_i - \mathbf{u}_e). \tag{A.13}$$

As the $E\times B$ drift has no charge or mass dependency it is equal for ions and electrons and does not lead to currents, in contrast to the other two terms. The diamagnetic current is given by

$$\mathbf{J}_{dia} = -\frac{\nabla p\times\mathbf{B}}{B^2} \tag{A.14}$$

with total pressure $p = p_e + p_i$. The polarisation drift

$$\mathbf{u}_{\perp,pol} = -\frac{m}{qB^2}\left(\frac{\partial\mathbf{u}}{\partial t}\times\mathbf{B} + ((\mathbf{u}\cdot\nabla)\mathbf{u})\times\mathbf{B}\right) \tag{A.15}$$

can be further evaluated by some approximations. First, we neglect the second term $(\mathbf{u}\cdot\nabla)\mathbf{u}$, which is responsible for all nonlinear interactions (Secs. 3.6.1 and 5.1). Assuming the polarization drift to be of lower order than the $E\times B$ and the diamagnetic drift, the polarization drift can be iteratively solved

$$\mathbf{u}_{\perp,pol} = -\frac{m}{qB^2}\left(\frac{(\dot{\mathbf{E}}\times\mathbf{B})\times\mathbf{B}}{B^2} - \frac{(\nabla_\perp\dot{p}\times\mathbf{B})\times\mathbf{B}}{\rho B^2}\right), \tag{A.16}$$

with $\mathbf{E} = -\nabla_\perp\phi$. This can be written as

$$\mathbf{u}_{\perp,pol} = \frac{m}{qB^2}\dot{\mathbf{E}} - \frac{m}{q^2nB^2}\nabla_\perp\dot{p}. \tag{A.17}$$

In textbooks of basics plasma physics, the second term is usually omitted for simplicity. Both terms depend on the mass and are therefore governed by the ions. The polarization drift induces a polarization current. The second term induces a polarization drift by a temporal change of the diamagnetic velocity. This term becomes important for hot ions due to the temperature dependence of the pressure gradient (Chap.12).

A.3 Flows parallel to the magnetic field

Even if the perpendicular motion is more important for the turbulence investigated in this work, some basic knowledge about the motion parallel to the

magnetic field line is required, too. We are going to study how electrons and ions react to density perturbations parallel to the magnetic field (here in z-direction). This induces a pressure perturbation, a parallel pressure gradient and, therefore, a parallel force, too. As the electrons are lighter they will respond first. The parallel equation of motion (A.8) for the electrons can be written as

$$\rho_m \frac{\partial u_z}{\partial t} = -\frac{\partial p}{\partial z}. \tag{A.18}$$

Assuming a constant temperature T_e and isothermal electrons $\gamma = 1$ leads to

$$n m_e \frac{\partial u_z}{\partial t} = -T_e \frac{\partial n}{\partial z}. \tag{A.19}$$

In linearized form the left hand side can in principle be split up in $\tilde{n} m_e \frac{\partial u_{z0}}{\partial t}$ (which vanishes if we assume a constant background flow $u_{z0} = \text{const}$) and $n_0 m_e \frac{\partial \tilde{u}_z}{\partial t}$. After making the wave ansatz

$$n = n_0 + \tilde{n} e^{i(kz - \omega t)}, \tag{A.20}$$

with $\partial_t \to -i\omega$ and $\nabla \to ik$, Eq. (A.19) yields

$$-n_0 m_e i\omega \tilde{u}_z = -T_e ik\tilde{n}. \tag{A.21}$$

To relate both fluctuating quantities $\tilde{u}_z$ and $\tilde{n}$ we make use of the linearized continuity equation

$$\frac{\partial}{\partial t}\tilde{n} + \nabla(n_0 \tilde{u}_z) = 0. \tag{A.22}$$

Making again the wave ansatz

$$i\omega\tilde{n} = ikn_0\tilde{u}_z \tag{A.23}$$

we obtain

$$\frac{\omega}{k}\frac{\tilde{n}}{n_0} = \tilde{u}_z. \tag{A.24}$$

Substituting this in (A.21) yields

$$-n_0 m_e i\omega \frac{\omega}{k}\frac{\tilde{n}}{n_0} = -T_e ik\tilde{n}. \tag{A.25}$$

A dispersion relation showing a wave character results in

$$\left(\frac{\omega}{k}\right)^2 = \frac{T_e}{m_e}. \tag{A.26}$$

Equation (A.26) describes the so-called *electron sound wave*. Its phase velocity is the electron sound velocity

$$c_{se} = \sqrt{\frac{T_e}{m_e}}. \tag{A.27}$$

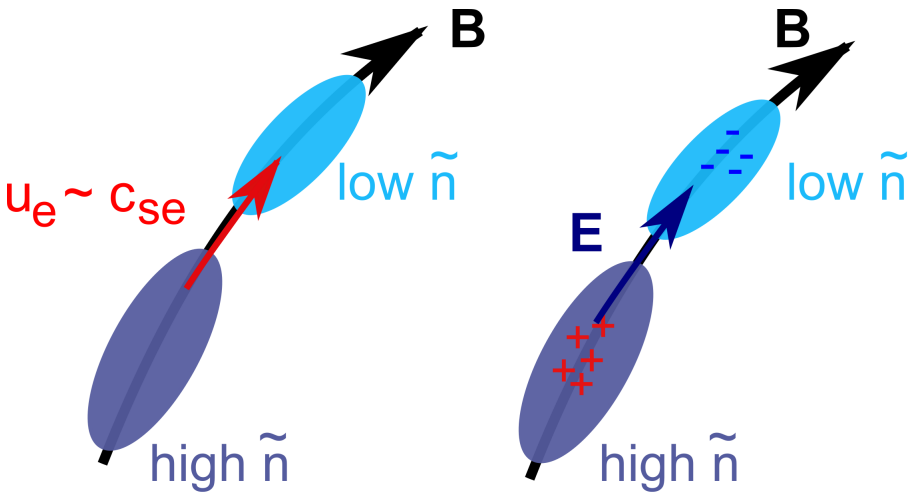

FIGURE A.1: Ion sound wave dynamics.

Electrons respond with this velocity to a density or pressure perturbation as shown on the right hand side of Fig. A.1.

The electron motion from the high density to the low density region will induce an electric field E_z, which counteracts the electron motion. This is shown on the left hand side of Fig. A.1. The electric potential $E_z = -\partial_z \tilde{\phi}$ can be estimated in equilibrium ($\partial_t \tilde{u}_z = 0$) from the equation of motion (A.8) for the electrons

$$-en_0 ik\tilde{\phi} + ikT_e\tilde{n} = 0 \tag{A.28}$$

or

$$\frac{e\tilde{\phi}}{T_e} = \frac{\tilde{n}}{n_0}. \tag{A.29}$$

This is the *Boltzmann relation* or *Boltzmann response*. Is it fulfilled the electrons are called *adiabatic electrons*. With regard to the Boltzmann relation, potential fluctuations are typically normalized by e/T_e and the density fluctuations by a typical background value n_0.

For a real equilibrium, the electric field accelerates the ions. Starting again with the equation of motion (A.8), but this time for the ions, including the electric field generated by the electrons yields

$$\rho_m \frac{\partial u_z}{\partial t} = \rho E_z - \frac{\partial p}{\partial z}. \tag{A.30}$$

Now we assume a constant ion temperature T_i but leave γ as a variable. After making use of the wave ansatz and the Boltzmann relation (A.29) for the electric field $E_z = -ik\tilde{\phi}$ we get

$$nm_i i\omega\tilde{u}_z = en_0 ik\frac{T_e}{e}\frac{\tilde{n}}{n_0} + T_i\gamma ik\tilde{n}. \tag{A.31}$$

The velocity and density fluctuations are related by the continuity equation (A.21). Also for the ions a wave equation

$$\frac{\omega}{k} = \sqrt{\frac{T_e + \gamma T_i}{m_i}} \tag{A.32}$$

is found with the ion sound velocity

$$c_{si} = \sqrt{\frac{T_e + \gamma T_i}{m_i}}. \tag{A.33}$$

This is called the *ion sound wave* or *ion acoustic wave*. Also for cold ions the acceleration by the electrons will lead to the ion sound velocity. We will call this the *ion sound velocity* or *ion acoustic velocity*

$$c_s = \sqrt{\frac{T_e}{m_i}}. \tag{A.34}$$

Both velocities are related by the ion to electron temperature ratio $\tau_i = \frac{T_i}{T_e}$

$$c_{si} = \sqrt{1 + \tau_i} c_s. \tag{A.35}$$

The ion sound velocity for cold ions c_s (and not the ion sound velocity including finite ion temperatures c_{si}) gives a good typical velocity for plasma turbulence modeling for the following reasons: The heart of turbulence is the nonlinearity $\mathbf{u} \cdot \nabla \mathbf{u}$ (3.4), which appears in the polarisation drift (A.15). The neglected nonlinearity can even induce a polarisation current. As the polarization drift is mass dependent the ions matter most. Therefore, a typical timescale or velocity should be related to the ions, too. Furthermore, the ion sound speed does not vanish for cold ions, which is an often used approximation. A vanishing typical velocity for normalization would be not appropriate. Furthermore, if magnetic effects are important these can be included straightforward by a second control parameter. The plasma β gives the square root of the ratio between the Alfvén velocity (characteristic for magnetic effects) and the ion acoustic velocity. The typical time is given by the ion cyclotron frequency (A.6). The resulting typical length is c_s/ω_{ci}

$$\rho_s = \frac{\sqrt{T_e m_i}}{eB}, \tag{A.36}$$

the *hybrid Larmor radius* of ions and electrons. Again, the advantage is that for cold ions it takes finite values. Therefore, ρ_s, ω_{ci} and c_s provide a consistent description of the typical length, time and velocity even for a cold magnetized plasma and ion temperature and magnetic effects can be controlled by τ_i and β, respectively.

A.4 Plasma at a wall

If the plasma is in contact to a solid material (wall), the lighter and more mobile electrons will migrate to the wall and charge it negatively with respect to the plasma potential ϕ. Due to the negative potential barrier, slower electrons are prevented from reaching the wall until electron and ion fluxes balance and the net flux ceases. The resulting potential is called the *floating potential* ϕ_{fl}. The electron current is given by

$$I_e = I_{e,sat} \exp\left(-\frac{e(\phi - \phi_{fl})}{T_e}\right), \tag{A.37}$$

where the electron saturation current $I_{e,sat} = -enA\sqrt{T_e/(2\pi m_e)}$ is obtained by integrating over a Maxwellian electron velocity distribution. Here, A is the effective area of the wall element or probe. The floating potential leads to an electric field accelerating ions towards the wall. The regions close to the wall will be occupied by more ions which in turn screen this electric field to the main part of the plasma. The region, where the potential has dropped is called the *sheath*. However, ions will be accelerated towards the wall and are drained from the plasma. In steady state these ions have to be supplied by the plasma. The ions at the sheath can react with their ion sound speed c_{si} on the potential. The kinetic energy of the ions is supplied by the potential drop across the pre-sheath

$$e(\phi - \phi_s) = \frac{1}{2} m_i c_{si}^2 \tag{A.38}$$

with the sheath potential ϕ_s. For cold ions $e(\phi - \phi_s) = \frac{1}{2}T_e$. This is called the *Bohm criterion*, which states that the ion velocity at the sheath entrance has to exceed the ion sound speed. The plasma density at the sheath is given by

$$n_s = n \exp\left(-\frac{e(\phi - \phi_s)}{T_e}\right). \tag{A.39}$$

For cold ions the plasma density at the sheath is $n_s = n\exp(-0.5) \approx 0.61n$. The corresponding parallel ion current flux is $\Gamma_i \approx 0.61 n c_{si}$. The ion current is given by the ion saturation current

$$I_{i,sat} = +eA\Gamma_i = 0.61 enA\sqrt{\frac{T_e + \gamma_i T_i}{m_i}}. \tag{A.40}$$

From ambipolarity follows that the ion and electron current (A.37) balance each other and the floating potential can be deduced

$$\phi_{fl} = \phi - \frac{T_e}{e} \ln\left(\frac{1}{0.61}\sqrt{\frac{T_e}{T_e + \gamma_i T_i}}\sqrt{\frac{m_i}{2\pi m_e}}\right). \tag{A.41}$$

Floating potential and ion saturation current are important for Langmuir probe measurements (see Sec. 6.1) and for the scrape-off layer dynamics (Chapter 12).

The derivation here is a bit simplified, additional secondary electron emission has to be taken into account [516], which can be quite strong in the scrape-off layer [517]. If the total gross erosion of the wall material is determined by the impurities [455], a larger ion to electron temperature ratio τ_i, as discussed in detail in Chap. 12, is beneficial, since the reduced floating potential leads to less acceleration of the heavier impurities and less sputtering (main process of material removal of the wall).

A.5 Magnetohydrodynamic (MHD) waves

Up to now only electrostatic plasmas have been addressed. In magnetized plasma electromagnetic effects can become important and they become particularly important at high pressure gradients (hence high plasma beta) occurring in improved confinement regimes. In this section the parallel dynamics including electromagnetic effects is introduced.

Ideal MHD is based on the following equations: the continuity equation

$$\frac{\partial \rho}{\partial t} + \nabla \cdot (\rho \mathbf{u}) = 0, \tag{A.42}$$

the force balance or equation of motion

$$\rho \frac{\partial \mathbf{u}}{\partial t} + \rho \mathbf{u} \cdot \nabla \mathbf{u} = \mathbf{J} \times \mathbf{B} - \nabla p, \tag{A.43}$$

the equation of state written in the isothermal limit

$$\nabla p = c_s^2 \nabla \rho, \tag{A.44}$$

Ampere's law

$$\nabla \times \mathbf{B} = \mu_0 \mathbf{J}, \tag{A.45}$$

Faraday's law

$$\nabla \times \mathbf{E} = -\frac{\partial \mathbf{B}}{\partial t}, \tag{A.46}$$

and Ohm's law

$$\mathbf{E} + \mathbf{u} \times \mathbf{B} = 0. \tag{A.47}$$

By combining Eqs. (A.43, A.44, A.45) we get

$$\rho \frac{\partial \mathbf{u}}{\partial t} + \rho \mathbf{u} \cdot \nabla \mathbf{u} = -c_s^2 \nabla \rho + \frac{1}{\mu_0} (\nabla \times \mathbf{B}) \times \mathbf{B} \tag{A.48}$$

and by combining Eq. (A.46) and (A.47)

$$\frac{\partial \mathbf{B}}{\partial t} = \nabla \times (\mathbf{u} \times \mathbf{B}). \tag{A.49}$$

We decompose the quantities into background values and perturbations $\rho = \rho_0 + \tilde{\rho}$, $\mathbf{B} = \mathbf{B}_0 + \tilde{\mathbf{B}}$ and assume the fluid is at rest $\mathbf{u} = \tilde{\mathbf{u}}$. Eqs. (A.42), (A.48) and (A.49) are linearized

$$\frac{\partial \tilde{\rho}}{\partial t} + \rho_0 \nabla \cdot \tilde{\mathbf{u}} = 0, \tag{A.50}$$

$$\rho_0 \frac{\partial \tilde{\mathbf{u}}}{\partial t} + c_s^2 \nabla \tilde{\rho} + \frac{1}{\mu_0} \mathbf{B}_0 \times (\nabla \times \tilde{\mathbf{B}}) = 0, \tag{A.51}$$

$$\frac{\partial \tilde{\mathbf{B}}}{\partial t} - \nabla \times (\tilde{\mathbf{u}} \times \mathbf{B}_0) = 0. \tag{A.52}$$

By differentiating (A.51) with respect to time a wave equation for $\tilde{\mathbf{u}}$ can be obtained

$$\rho_0 \frac{\partial^2 \tilde{\mathbf{u}}}{\partial t^2} + c_s^2 \nabla \frac{\partial \tilde{\rho}}{\partial t} + \frac{1}{\mu_0} \mathbf{B}_0 \times \left(\nabla \times \frac{\partial \tilde{\mathbf{B}}}{\partial t} \right) = 0.$$

Subsequently substituting (A.50) and (A.52) yields

$$\rho_0 \frac{\partial^2 \tilde{\mathbf{u}}}{\partial t^2} + c_s^2 \nabla (\nabla \cdot \tilde{\mathbf{u}}) + \mathbf{u}_A \times (\nabla \times (\nabla \times (\tilde{\mathbf{u}} \times \mathbf{u}_A))) = 0, \tag{A.53}$$

where

$$\mathbf{u}_A = \frac{\mathbf{B}_0}{\sqrt{\mu_0 \rho_0}} \tag{A.54}$$

is the *Alfvén velocity*. We make the ansatz of harmonic oscillations $\tilde{\mathbf{u}}(\mathbf{x}, t) = \tilde{\mathbf{u}} \exp(i\mathbf{k}\mathbf{x} - i\omega t)$ to replace $\nabla \to i\mathbf{k}$ and $\partial_t \to -i\omega$ and obtain a dispersion relation

$$-\omega^2 \tilde{\mathbf{u}} + c_s^2 (\mathbf{k} \cdot \tilde{\mathbf{u}}) \mathbf{k} - \mathbf{u}_A \times (\mathbf{k} \times (\mathbf{k} \times (\tilde{\mathbf{u}} \times \mathbf{u}_A))) = 0.$$

Using the vector identity $\mathbf{A} \times (\mathbf{B} \times \mathbf{C}) = \mathbf{B}(\mathbf{A} \cdot \mathbf{C}) - \mathbf{C}(\mathbf{A} \cdot \mathbf{B})$ the dispersion relation can also be written as

$$-\omega^2 \tilde{\mathbf{u}} + (c_s^2 + u_A^2)(\mathbf{k} \cdot \tilde{\mathbf{u}}) \mathbf{k} + (\mathbf{k} \cdot \mathbf{u}_A)((\mathbf{k} \cdot \mathbf{u}_A) \tilde{\mathbf{u}} - (\mathbf{u}_A \cdot \tilde{\mathbf{u}}) \mathbf{k} - (\mathbf{k} \cdot \tilde{\mathbf{u}}) \mathbf{u}_A) = 0. \tag{A.55}$$

A.5.1 Shear Alfvén wave

Considering a propagation along the magnetic field ($\mathbf{k} \| \mathbf{B}_0$) it follows that $\mathbf{k} \cdot \mathbf{u}_A = k u_A$. The dispersion relation (A.55) reduces to

$$(k^2 u_A^2 - \omega^2) \tilde{\mathbf{u}} + \left(\frac{c_s^2}{u_A^2} - 1 \right) k^2 (\mathbf{u}_A \cdot \tilde{\mathbf{u}}) \mathbf{u}_A = 0 \tag{A.56}$$

which allows for two idealized propagation directions. First, we consider $\tilde{\mathbf{u}} \| \mathbf{B}_0$. For this case the dispersion relation is given by $u_{ph} = \omega / k = c_s$, which is the ion acoustic wave (A.34). The other possibility is a transverse wave $\tilde{\mathbf{u}} \perp \mathbf{B}_0$ and $\tilde{\mathbf{u}} \cdot \mathbf{k} = 0$. For this case the dispersion relation is given by

$$u_{ph} = \frac{\omega}{k} = u_A, \tag{A.57}$$

which is the *tranversal Alfvén wave*. The associated magnetic field perturbation can be calculated from (A.52)

$$-\omega\tilde{\mathbf{B}} - \mathbf{k} \times (\tilde{\mathbf{u}} \times \mathbf{B}_0) = 0$$

to be $\tilde{\mathbf{B}} = -(B_0/(\omega/k))\mathbf{u}$ (with ω/k from (A.57)) which is antiparallel to the fluid perturbation and perpendicular to $\mathbf{B}_0$. As the magnetic perpendicular perturbation leads to a deformation of the original magnetic field it gets sheared. Therefore this wave is also called *torsional or shear Alfvén wave*.

A.5.2 Magnetoacoustic wave

Considering a propagation just perpendicular to $\mathbf{B}_0$ ($\mathbf{k} \perp \mathbf{B}_0$) it follows that $\mathbf{k} \cdot \mathbf{u}_A = 0$ and the dispersion relation (A.55) reduces to

$$-\omega^2\tilde{\mathbf{u}} + (c_s^2 + u_A^2)(\mathbf{k} \cdot \tilde{\mathbf{u}})\mathbf{k} = 0.$$

A finite frequency requires $(\mathbf{k}\cdot\tilde{\mathbf{u}})\|\mathbf{k}$ ($\rightarrow (\mathbf{k}\cdot\tilde{\mathbf{u}}) = k\tilde{u}$). The wave is longitudinal and the dispersion relation becomes

$$u_{ph} = \frac{\omega}{k} = \sqrt{c_s^2 + u_A^2}. \tag{A.58}$$

Since the phase velocity u_{ph} depends on the sound velocity it is called *magnetoacoustic wave*. The enhanced propagation velocity compared to the shear Alfvén wave is due to the contribution of compressional effects in parallel direction. The wave is also called *longitudinal Alfvén wave* since it is propagating longitudinal or *fast Alfvén wave* due to the faster propagation velocity compared to the shear Alfvén wave.

A.5.3 Global Alfvén modes

Alfvén modes in toroidal geometry are characterized by (ω, n, m) with frequency ω and toroidal and poloidal mode numbers n and m, respectively. These are global modes and between these modes frequency gaps are observed. Global Alfvén modes can be excited by resonant interaction between fast particles with these modes. In current experiments these fast particles originate mainly from the heating (NBI or ICRH). In an actual reactor additional α particles will be subject to a strong interaction with global Alfvén modes.

The following explanation is adopted from Ref. [16]. Alfvénic eigenmodes with $n \neq 0$ are called *beta induced Alfvénic eigenmodes*, those with $n = 0$ are called *global Alfvénic eigenmodes*. The branch with $(n = 0, m = 0)$ corresponds to the geodesic acoustic mode. The global branch with $(n = 0, m = 1)$ is here referred to as *geodesic Alfvénic mode*. The gyrokinetic eigenvalue solver (we will use LIGKA in Sec. 11.3) can be used to determine the kinetic continuum branches. The equations solved (by LIGKA) are the quasi-neutrality equation (QN) and the gyrokinetic moment equation (GKM) that together with the

gyrokinetic equation for the particle distribution functions form a consistent model for electromagnetic perturbations in tokamak geometry [418, 419]. It can be shown [518] that the implemented equations have the following general dispersion relation as analytical limit [519, 520, 521]:

$$\frac{\omega^2}{\omega_A^2}\quad\left(1-\frac{\omega_p^*}{\omega}\right)-\bar{k}_{\|m}^2R_0^2=\sum_{a=i,e}2\frac{v_{th,a}^2}{\omega_A^2R_0^2}\Bigg(-\Big[H(x_{a,m-1})+H(x_{a,m+1})\Big]+$$
$$\tau_a\Big[\frac{N^m(x_{a,m-1})N^{m-1}(x_{a,m-1})}{D(x_{a,m-1})}+\frac{N^m(x_{a,m+1})N^{m+1}(x_{a,m+1})}{D(x_{a,m+1})}\Big]\Bigg)\quad\text{(A.59)}$$

where $\omega_A = u_A/R_0 = \sqrt{B^2/\mu_0 m_i n_i}$ is the Alfvén frequency and $\bar{k}_{\|m}^2$ stands for the parallel wave vector including the toroidal coupling up to first order in ϵ, e.g. $\bar{k}_{\|m}^2 = \Big(k_{\|m}^2 + k_{\|m+1}^2 \pm \sqrt{(k_{\|m}^2 - k_{\|m+1}^2)^2 + 4\hat{\epsilon}^2 r^2 k_{\|m}^2 k_{\|m+1}^2}\Big)/\Big(2(1-\hat{\epsilon}^2 r^2)\Big)$ where $\hat{\epsilon} = 5r/2R_0$. Further,

$$x_{a,m} = \frac{\omega}{|k_{\|,m}|v_{th,a}};\qquad v_{th,a} = \sqrt{\frac{2T_a}{m_a}};\qquad \omega_p^* = \sum_i \frac{k_\theta}{eBn_i}\frac{\partial p_i}{\partial r}\frac{m_i n_i}{m_{eff}n_e};\qquad \tau = T_e/T_a.$$

The definitions for the polynomials H, N, D including the complex plasma dispersion function can be found e.g. in Refs. [519, 518]. The upper index m in $N^m(x_{m-1})$ refers to the poloidal mode number m to be used in $\omega_m^* = \frac{T_i}{eB}k_{m,\theta}\frac{\nabla n}{n}$. For the geodesic acoustic mode, taking into account the $m = \pm 1$ sidebands, the following dispersion relation can be derived from the one above for large safety factor q [522, 523]:

$$\omega_G^2/\omega_{t,i}^2 = \hat{\omega}_G^2 = q^2\Big[\frac{7}{4}+\tau\Big]\Big[1+\frac{2(23+16\tau+4\tau^2)}{q^2(7+4\tau)^2}\Big]\qquad\text{(A.60)}$$

with $\omega_{t,i} = v_{th,i}/qR_0$. For the $m = 1$ branch, the main contribution comes from the $k_\| = -1/qR$ term on the left hand side of equation (A.59).
The coefficients for the dispersion relation are calculated numerically, based on realistic particle orbits. A Nyquist contour solver is employed to find local solutions in the complex plane. The results presented in Sec. 11.3 are calculated with the HAGIS code [524], where realistic geometry and experimental profiles are used.

Appendix B

Mathematical description of plasma instabilities

B.1 Interchange

The interchange instability can be mathematically described as follows. Let the magnetic field be in z-direction with its gradient in the negative radial (x-)direction. The plasma pressure also exhibits a gradient in the negative x-direction. The plasma potential is perturbed in y-direction (perpendicular to the magnetic field and the radial direction)

$$\tilde{\phi} = \phi \exp(ik_y y).$$

The density will be perturbed also in y-direction. As seen in Fig. 4.1 this density will be in phase with the radial $E \times B$ velocity $\tilde{u}_{E\times B}$, thus

$$\tilde{n} = n \exp(ik_y y - i\pi/2).$$

Both are related by the continuity equation

$$\frac{\partial \tilde{n}}{\partial t} = -\tilde{u}_{E\times Bx} \frac{\partial}{\partial x} n_0 = \frac{\partial n_0}{\partial x} \frac{ik_y \tilde{\phi}}{B}$$

where $\tilde{u}_{E\times Bx} = -ik_y \tilde{\phi}/B$ was used. Its integral with respect to time reads

$$\tilde{n} = \int dt \frac{\partial n_0}{\partial x} \frac{ik_y \tilde{\phi}}{B}.$$

A density perturbation leads to a perturbation of the diamagnetic current via $\tilde{J} \times B = \nabla \tilde{p} = T \nabla \tilde{n}$

$$\tilde{J}_{dia,x} = -\frac{(T_e + T_i) ik \tilde{n}}{B}.$$

We calculate the radial derivative of this. As the magnetic field is inhomogeneous, a divergence of the diamagnetic current remains

$$\frac{\partial \tilde{J}_{dia,x}}{\partial x} = \frac{k_y^2}{B} (\frac{\partial}{\partial x} \frac{1}{B}) (T_e + T_i) \frac{\partial n_0}{\partial x} \int dt \tilde{\phi}.$$

By introducing a gradient scale length for the pressure $L_n^{-1} = -\nabla n_0/n_0$ and the magnetic field $L_B^{-1} = -\nabla B/B$ this expression can be simplified to

$$\frac{\partial \tilde{J}_{dia,x}}{\partial x} = -\frac{k_y^2 n_0}{B^2}\frac{(T_e + T_i)}{L_n L_B}\int dt\tilde{\phi}.$$

As a result of quasineutrality $\nabla \cdot \tilde{J}_{dia} + \nabla \cdot \tilde{J}_{pol} = 0$, the divergence of the diamagnetic current is balanced by the divergence of the ion polarization current $(m_i n/B^2)\nabla\cdot\dot{\mathbf{E}}$. We neglect the additional contribution due to the divergence of the magnetic field in the polarization current. As the electric field perturbation is in y-direction

$$\frac{m_i n_0}{B^2}\frac{\partial}{\partial t} ik_y(-ik_y)\tilde{\phi} = -\frac{\partial \tilde{J}_{dia,x}}{\partial x}$$

which gives

$$-\frac{m_i n_0 k_y^2}{B^2}\frac{\partial^2}{\partial t^2}\tilde{\phi} = \frac{k_y^2 n_0 (T_e + T_i)}{B^2}\frac{1}{L_n L_B}\tilde{\phi}$$

with $c_s = \sqrt{T_e/m_i}$ and $\tau_i = T_i/T_e$

$$\frac{\partial^2}{\partial t^2}\tilde{\phi} = -\frac{(1+\tau_i)c_s^2}{L_n L_B}\tilde{\phi}.$$

The growth rate is

$$\gamma = \sqrt{\frac{(1+\tau_i)}{L_n L_B}}c_s \tag{B.1}$$

which is positive and exponentially growing for $L_n L_B > 0$. Hence, the magnetic field gradient and the density gradient are in the same direction, which is the case on the low field side. The instability is a purely growing mode, no eigenfrequency or phase velocity is associated with it. In the good curvature region on the high field side the interchange instability is stable. Turbulence dominated by the interchange instability is called resistive ballooning mode (RBM) turbulence.

B.2 Drift waves

B.2.1 Drift Ordering

Only low-frequency ω plasma oscillations with

$$\frac{\omega}{\omega_{ci}} \sim \epsilon \ll 1, \tag{B.2}$$

will be investigated where ω_{ci} is the ion gyration frequency. Only small perturbations

$$\frac{e\tilde{\phi}}{T_0} \sim \frac{\tilde{n}}{n_0} \sim \frac{\rho_s}{L_n} \sim \frac{\omega}{\omega_{ci}} \sim \epsilon \ll 1 \tag{B.3}$$

will be considered. For typical perpendicular and parallel wave numbers

$$k_\perp \rho_s \sim 1 \Rightarrow k_\parallel / k_\perp \sim \epsilon \tag{B.4}$$

should hold. The perpendicular gradients of perturbations should be of the same order as those of the background

$$\frac{\nabla \tilde{n}}{\nabla n_0} \sim \frac{\nabla e\tilde{\phi}}{\nabla T_0} \sim 1. \tag{B.5}$$

B.2.2 Dispersion relation of stable drift wave

Let the density gradient point into negative x-direction, the magnetic field direction in z-direction. We neglect any effects of the curvature, therefore no contributions from $n\nabla \cdot (\mathbf{u}_{E\times B} + \mathbf{u}_{dia})$ are considered. The density gradient gives rise to a diamagnetic drift of the electrons

$$u_{e,dia} = \frac{T_e}{L_n e B_0}, \tag{B.6}$$

where $L_n^{-1} = -(1/n_0)(dn_0/dx)$. We assume harmonic perturbations along the y-direction. The electrons follow the background magnetic field in the direction parallel to the magnetic field

$$\frac{\partial u_{e\parallel}}{\partial t} + (\mathbf{u}_e \cdot \nabla) u_{e\parallel} = \frac{e}{m_e}\frac{\partial \phi}{\partial z} - \frac{1}{m_e n_e}\frac{\partial p_e}{\partial z}. \tag{B.7}$$

The electron motion is adiabatic and the inertia of the electron can be neglected. The left hand side of the equation vanishes. Furthermore, for isothermal electrons

$$e\frac{\partial \phi}{\partial z} - \frac{T_e}{n_e}\frac{\partial n_e}{\partial z} = 0 \tag{B.8}$$

holds. Its integral reads

$$\frac{n_e}{n_0} = e^{e\phi/T_e}. \tag{B.9}$$

For a density perturbation $\tilde{n}_e$ with $n_e = n_{e0} + \tilde{n}_e$ we find (A.29)

$$\frac{\tilde{n}_e}{n_0} = \frac{e\tilde{\phi}}{T_e}. \tag{B.10}$$

The ions fulfill the continuity equation

$$\frac{\partial \tilde{n}_i}{\partial t} + \tilde{u}_{E\times Bx}\frac{dn_0}{dx} = 0 \tag{B.11}$$

with

$$\tilde{u}_{E\times Bx} = -\frac{1}{B_0}\frac{\partial \tilde{\phi}}{\partial y}. \tag{B.12}$$

The equation of motion of the ions (A.30) reads

$$\frac{\partial \tilde{u}_{i\parallel}}{\partial t} = -\frac{e}{m_i}\frac{\partial \tilde{\phi}}{\partial z} \tag{B.13}$$

or

$$\tilde{u}_{i,\parallel} = \frac{k_\parallel}{\omega}\frac{e\tilde{\phi}}{m_i}. \tag{B.14}$$

The polarization drift is given by

$$\tilde{u}_{i,pol} = \frac{m_i}{qB_0^2}\dot{\tilde{E}} = \frac{m_i}{qB_0^2}(-i\omega)(-ik_y\tilde{\phi}). \tag{B.15}$$

Substituting the ion gyration frequency $\omega_{ci} = eB_0/m_i$, it follows that

$$\tilde{u}_{i,p} = -\frac{T_e}{\omega_{ci}m_i}\frac{m_i}{B_0 e}\omega k_y\frac{e\tilde{\phi}}{T_e} = -\frac{T_e}{m_i\omega_{ci}^2}\omega k_y\frac{e\tilde{\phi}}{T_e}. \tag{B.16}$$

Continuity demands

$$\frac{\partial \tilde{n}_i}{\partial t} + \tilde{u}_{E\times Bx}\frac{\partial n_0}{\partial x} + n_0\frac{\partial}{\partial y}\tilde{u}_{i,p} + n_0\frac{\partial \tilde{u}_{i,\parallel}}{\partial z} = 0 \tag{B.17}$$

to hold. Taking into account Eqs. (B.12) and (B.16) yields

$$\frac{\partial \tilde{n}_i}{\partial t} - \frac{1}{B_0}\frac{\partial \tilde{\phi}}{\partial y}\frac{\partial n_0}{\partial x} - n_0\frac{T_e}{m_i\omega_{ci}^2}\omega k_y\frac{\partial}{\partial y}\frac{e\tilde{\phi}}{T_e} + n_0\frac{\partial \tilde{u}_{i,\parallel}}{\partial z} = 0 \tag{B.18}$$

$$\frac{1}{n_0}\frac{\partial \tilde{n}_i}{\partial t} + \frac{T_e\kappa_n}{eB_0}\frac{e\partial\tilde{\phi}}{T_e\partial y} - \frac{T_e}{m_i\omega_{ci}^2}\omega i k_y^2\frac{e\tilde{\phi}}{T_e} + \frac{\partial \tilde{u}_{i,\parallel}}{\partial z} = 0. \tag{B.19}$$

In Fourier space under the assumption of a harmonic perturbation and using Eq. (B.6) this can be written as

$$-i\omega\frac{\tilde{n}_i}{n_0} + u_{e,dia}ik_y\frac{e\tilde{\phi}}{T_e} - \frac{T_e}{m_i\omega_{ci}^2}\omega i k_y^2\frac{e\tilde{\phi}}{T_e} + \frac{ik_\parallel^2}{\omega}\frac{e\tilde{\phi}}{m_i} = 0. \tag{B.20}$$

Hence,

$$\frac{\tilde{n}_i}{n_0}\omega = \frac{e\tilde{\phi}}{T_e}\left(u_{e,dia}k_y - \frac{T_e}{m_i}\frac{1}{\omega_{ci}^2}\omega k_y^2 + \frac{k_\parallel^2}{\omega}\frac{T_e}{m_i}\right). \tag{B.21}$$

It follows in comparison with Eq. (B.9) (quasi-neutrality) that the dispersion relation of stable drift wave is

$$\omega^2(1 + k_y^2\rho_s^2) - \omega\omega_{e,dia} - k_\parallel^2 c_s^2 = 0 \tag{B.22}$$

with $\rho_s = c_s/\omega_{ci}$ and $c_s = (T_e/m_i)^{1/2}$. Usually the parallel wavenumber is comparatively small and the finite ion inertia can be neglected. In this case the drift-wave dispersion relation reads

$$\omega = \frac{u_{e,dia}k_y}{1 + k_\perp^2\rho_s^2}. \tag{B.23}$$

The drift wave propagate in the electron diamagnetic direction in the binormal direction with the electron diamagnetic velocity as its phase velocity

$$\omega = \omega_{e,dia} = k_y u_{e,dia}. \tag{B.24}$$

It should be noted that no advection by the electron diamagnetic velocity has been assumed in the beginning and this phase velocity is a result of the radial advection. The dispersion relation of the drift wave is shown in Fig. B.1. Due to the polarization drift the drift wave exhibit backward wave characteristics at around $k_y \rho_s \approx 1$. This can lead to interesting effects as discussed in Sec. 8.3. The relevance of this linear phase velocity for typical L-mode plasmas will be discussed in detail in Chap. 9.

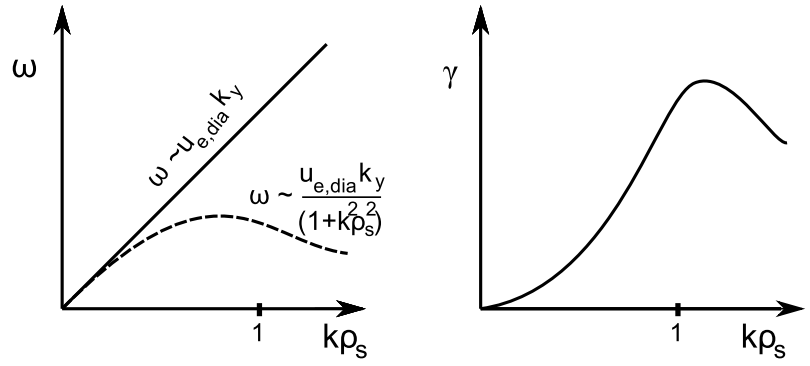

FIGURE B.1: Dispersion relation and growth rate of resistive drift wave.

B.2.3 Instability of the drift wave

As long the electrons are moving freely along the magnetic field lines the Boltzmann relation (B.10) holds and the drift wave is stable. There are different possibilities to limit this free movement of the electrons, as collisionality between electrons and ions, Landau damping, electron inertia or induction. This results in a modification of the Boltzmann relation and density and potential fluctuations are not any longer in phase:

$$\frac{\tilde{n}_e}{n_0} = \frac{e\tilde{\phi}}{T_e}\left(1 - i\delta\right). \tag{B.25}$$

Substituted in Eq. (B.10) of this Eq. in the derivative of Eq. in (B.24) yields

$$\omega = \frac{k_y u_{e,dia}}{1 - i\delta} \approx k_y u_{e,dia}(1 + i\delta). \tag{B.26}$$

Considering the electron-ion collisionality ν_{ei} the parallel electron motion (see Eq. (A.10)) is hampered

$$e n_e i k_\parallel \tilde{\phi} - T_e i k_\parallel \tilde{n}_e - n_e m_e \nu_{ei} \tilde{u}_{e,\parallel} = 0.$$

It is possible to get an estimate of the parallel electron motion:

$$\tilde{u}_{e,\parallel} = \frac{ik_\parallel T_e}{m_e \nu_{ei}} \left(\frac{e\tilde{\phi}}{T_e} - \frac{\tilde{n}}{n_0} \right).$$

Substitution in the electron continuity

$$\frac{\partial \tilde{n}}{\partial t} + \tilde{u}_{E\times Bx} \frac{\partial n_0}{\partial x} + n_0 \frac{\partial \tilde{u}_{e,\parallel}}{\partial z} = 0$$

yields

$$-\omega \frac{\tilde{n}}{n_0} + ik_y \frac{\kappa T_e}{B_0 e} \frac{e\tilde{\phi}}{T_e} - \frac{k_\parallel^2 T_e}{m_e \nu_{ei}} \left(\frac{e\tilde{\phi}}{T_e} - \frac{\tilde{n}}{n_0} \right) = 0$$

for harmonic perturbations. This can be rewritten as

$$\frac{\tilde{n}}{n_0} \left(\omega + ik_\parallel^2 \frac{T_e}{m_e \nu_{ei}} \right) = \frac{e\tilde{\phi}}{T_e} \left(u_{e,dia} k_y + ik_\parallel^2 \frac{T_e}{m_e \nu_{ei}} \right),$$

hence

$$\frac{\tilde{n}}{n_0} = \frac{e\tilde{\phi}}{T_e} \left(\frac{\omega_{e,dia} + ik_\parallel^2 D_\parallel}{\omega + ik_\parallel^2 D_\parallel} \right)$$

with $D_\parallel = \frac{T_e}{m_e \nu_{ei}}$. With further simplifications and the assumption of $k_\parallel^2 D_\parallel \gg \omega$ we obtain with

$$\frac{\omega_{e,dia} + ik_\parallel^2 D_\parallel}{\omega + ik_\parallel^2 D_\parallel} \frac{\omega + ik_\parallel^2 D_\parallel}{\omega - ik_\parallel^2 D_\parallel} \approx \frac{\omega_{e,dia}\omega + (k_\parallel^2 D_\parallel)^2 + ik_\parallel^2 D_\parallel (\omega - \omega_{e,dia})}{(k_\parallel^2 D_\parallel)^2}$$

$$\frac{\tilde{n}}{n_0} = \frac{e\tilde{\phi}}{T_e} \left(1 - i \frac{1}{k_\parallel^2 D_\parallel} (\omega_{e,dia} - \omega) \right).$$

This result is compared with that of the ions (B.21), where the parallel ion motion is neglected as it is much smaller than that of the electrons

$$\frac{\omega_{e,dia}}{\omega} - \rho_s^2 k_y^2 = 1 - i \frac{1}{k_\parallel^2 D_\parallel} (\omega_{e,dia} - \omega).$$

This yields the dispersion relation

$$\omega(1 + \rho_s^2 k_y^2) - i\omega \frac{1}{k_\parallel^2 D_\parallel} (\omega_{e,dia} - \omega) - \omega_{e,dia} = 0 \tag{B.27}$$

with real frequency (c.f. (B.23))

$$\omega = \frac{\omega_{e,dia}}{(1 + \rho_s^2 k_y^2)}$$

and growth rate

$$\gamma = \frac{\nu_{ei} m_e}{k_\parallel^2 T_e} \omega_{e,dia}^2 \rho_s^2 k_y^2. \tag{B.28}$$

The growth rate by collisions is illustrated in Fig. B.1. The growth rate peaks around $k\rho_s \approx 1$, which is the typical scale of electrostatic drift-waves. How the magnetic field topology influences the growth rate is studied in detail in theory and experiments in Refs. [525, 41], respectively.

B.2.4 Alfvénic coupling

In the electrostatic limit the drift wave is coupled to the ion sound wave (last term of (B.22). If additional electromagnetic effects are taken into account the drift wave has also the possibility to couple to the Alfvén wave (see Sec. A.5). The ratio between both phase velocities is an important control parameter, the plasma beta (2.2)

$$\frac{\beta}{\mu_{ei}} = \frac{c_s^2}{u_A^2} \tag{B.29}$$

with electron to ion mass ratio $\mu_{ei} = m_e/m_i$ and Alfvén speed u_A (see Eq. (A.54)).

To study electromagnetic effects magnetic fluctuations

$$\tilde{\mathbf{B}} = \nabla \times \tilde{\mathbf{A}} \tag{B.30}$$

need to be included. These are defined by the vector potential $\tilde{\mathbf{A}}_\parallel = \tilde{A}_\parallel \hat{\mathbf{z}}$ only in the direction parallel to the magnetic field. This leads to magnetic fluctuations only perpendicular to the magnetic field

$$\tilde{\mathbf{B}}_\perp = \nabla_\parallel \tilde{A}_\parallel \times \hat{\mathbf{z}}. \tag{B.31}$$

The vector potential also modifies the parallel electric field

$$E_\parallel = -\nabla_\parallel \tilde{\phi} - \frac{1}{c}\frac{\partial \tilde{A}_\parallel}{\partial t}. \tag{B.32}$$

The main modification of the perpendicular magnetic field fluctuations is that they lead to a perpendicular displacement following the field lines (the parallel dynamics). Thereby parallel derivations are modified according to

$$\nabla_\parallel = \frac{\partial}{\partial z} + \frac{\tilde{\mathbf{B}}_\perp}{B_0} \cdot \nabla. \tag{B.33}$$

The effect is called *magnetic flutter* and can lead to perpendicular transport. It is in particular important for electromagnetic instabilities like the micro-tearing mode (Sec. 4.7) and kinetic ballooning mode (Sec. 4.8).

Including these modifications to the derivation of the drift-wave dispersion described above we get the following dispersion relation [162]

$$\begin{aligned}&(\beta + \mu_{ei} k_\perp^2)\omega - \beta k_y v_{e,dia} \\ &-\mu_{ei} k_\parallel^2 c_s^2 \left(\frac{1 + k_\perp^2 \rho_s^2}{\omega} - \frac{k_y v_{e,dia}}{\omega^2} \right) \\ &= -\mu_{ei}\nu_{ei} k_\perp^2 \rho_s^2.\end{aligned} \tag{B.34}$$

For simplicity we assume $\mu_{ei} \approx \beta \ll 1$, $\nu_{ei} \approx 0$. The dispersion relation splits up in two limit cases: One for low, one for high frequencies. For low frequencies $\omega \sim k_\perp u_{e,dia}$ we recover the electrostatic dispersion relation including the ion polarization effect (c.f. (B.23))

$$\omega = \frac{k_\perp u_{e,dia}}{1 + k_\perp \rho_s^2}.$$

For higher frequencies $\omega \gg k_\perp u_{e,dia}$

$$\omega^2 = k_\parallel^2 u_A^2 \frac{1 + k_\perp^2 \rho_s^2}{1 + k_\perp^2 \delta_{es}^2} \tag{B.35}$$

holds, which recovers the Alfvénic dispersion $\omega_A = k_\parallel u_A$ (c.f. (A.54)) for $\mu_{ei} \approx \beta$. Here $\delta_{se} = \rho_s \sqrt{\frac{\mu_{ei}}{\beta}}$ is the collisionless electron skin depth.

Appendix C

Plasma turbulence models

C.1 Derivation of Hasegawa-Wakatani equations

As in the case of the basic drift-wave instability we assume a constant gradient in the background density $n_0 = n_0(x)$. The gradient is normalized to

$$\kappa_n = -\frac{1}{n_0}\frac{\partial n_0}{\partial x}.$$

Quasi-neutrality is equivalent to

$$\nabla \cdot \mathbf{J} = 0. \tag{C.1}$$

The current density $\mathbf{J}$ is decomposed into its components perpendicular and parallel to the background magnetic field

$$\nabla \cdot \mathbf{J}_\perp + \nabla \cdot \mathbf{J}_\parallel = 0.$$

The drifts determine the perpendicular current. Since the $\mathbf{E} \times \mathbf{B}$ -drift is independent of the charge it does not lead to any current. The diamagnetic and the polarization drifts result in the following current densities

$$\mathbf{J_{dia}} = -\frac{\nabla p \times \mathbf{B}}{B^2} \qquad \text{and} \qquad \mathbf{J_{pol}} = (m_e + m_i)\frac{n}{B^2}\dot{\mathbf{E}},$$

respectively.

First we consider the diamagnetic contribution. The divergence of the diamagnetic current is

$$-\nabla \cdot \left(\frac{\nabla p \times \mathbf{B}}{B^2}\right) = -\frac{1}{B^2}\left(\mathbf{B} \cdot (\nabla \times \nabla p) - \nabla p \cdot (\nabla \times \mathbf{B})\right).$$

As the rotation of gradient fields is zero, the first term vanishes and since the magnetic field is homogenous the second term vanishes, too. Therefore, $\nabla \cdot \mathbf{J}_{dia} = 0$. Note that, in a curved magnetic field the diamagnetic contribution

remains. Hence, only the polarization current contributes to $\nabla \cdot \mathbf{J}_\perp$, where we fairly assume $m_e + m_i \approx m_i$. The term $\nabla n \cdot \nabla_\perp \phi$ can be neglected by drift ordering. From quasi-neutrality (C.1) the vorticity equation

$$\nabla_\parallel \cdot \mathbf{J}_\parallel = -\nabla_\perp \cdot \mathbf{J}_\perp = \frac{m_i n}{B^2} \nabla_\perp^2 \dot{\phi} \tag{C.2}$$

follows. Here, $\Omega = \nabla_\perp^2 \phi$ is the (scalar) vorticity as deduced by the $E \times B$ velocity. The changes in vorticity are balanced by the parallel current which is carried by the lighter electrons. We consider the electron continuity equation. Due to their lower mass the polarization drift can be neglected:

$$\frac{d}{dt} n = -\nabla \cdot (n \mathbf{u}_{\parallel \mathbf{e}}) = \frac{1}{e} \nabla \cdot \mathbf{J}_\parallel. \tag{C.3}$$

Finally the parallel component of the equation of motion (A.8) is used

$$m_e n \frac{d}{dt} \mathbf{u}_{\parallel \mathbf{e}} = \nabla_\parallel p_e + en(\mathbf{E}_\parallel + (\mathbf{u_e} \times \mathbf{B})_\parallel) - \mathbf{R}_{\parallel \mathbf{ei}}. \tag{C.4}$$

The Lorentz force has no contribution in direction of the magnetic field. Thus, the third term on the right-hand side is zero. The change of momentum of the fluid parallel to $\mathbf{B}$ can be realized by a change in the pressure, the Coulomb force or due to the friction force $\mathbf{R_{ei}} = ne \left(\frac{\mathbf{J}_\parallel}{\sigma_\parallel} + \frac{\mathbf{J}_\perp}{\sigma_\perp} \right)$. Here σ is the electric conductivity $\sigma_\parallel = 1.96 \sigma_\perp = 1.96 \frac{ne^2}{m_e \nu_e}$. In general the electric field is given by $\mathbf{E} = -\nabla \phi - \partial_t \mathbf{A}$, with vector potential $\mathbf{A}$. From the electron equation of motion we get a *generalized Ohm's law*

$$\frac{m_e}{e} \frac{d}{dt} \mathbf{J}_\parallel = \nabla_\parallel p + en(-\nabla_\parallel \phi - \partial_t \mathbf{A}) - \frac{en}{\sigma_\parallel} \mathbf{J}_\parallel. \tag{C.5}$$

Our minimum turbulence model now contains three equations. The continuity equation for the electrons (C.3) is coupled via the parallel current to the vorticity equation (C.2). Finally we have an equation of the parallel electron motion (C.5). Note that it is the parallel current (hence the electron flux) which couples potential and density dynamics. As seen and used before quasi-neutrality reads

$$\nabla \cdot J_{\perp,i} \simeq \nabla_\parallel \cdot J_{\parallel,e}.$$

In the electrostatic limit Ohm's law (C.5) yields

$$\frac{m_e \nu_e}{1.96 e} \mathbf{J}_\parallel = \nabla_\parallel p - en \nabla_\parallel \phi. \tag{C.6}$$

By neglecting the electron inertia, the parallel current $J_\parallel$ in Eq. (C.2) can be inserted in Eq. (C.3). Due to the separation of perpendicular and parallel dynamics $\nabla \cdot \nabla_\perp = \nabla_\perp^2$ and $\nabla \cdot \nabla_\parallel = \nabla_\parallel \cdot \nabla_\parallel$. Two coupled equations result

$$\frac{m_i n}{B^2} d_t \nabla_\perp^2 \phi = \frac{1.96 e}{m_e \nu_e} \nabla_\parallel \cdot (\nabla_\parallel p - en \nabla_\parallel \phi)$$

$$d_t n = \frac{1.96}{m_e \nu_e} \nabla_\parallel \cdot (\nabla_\parallel p - en \nabla_\parallel \phi). \tag{C.7}$$

We will utilize normalized units

$$\begin{aligned} \tfrac{e\phi}{T} &\to \phi & \frac{\tilde{n}}{n_0} &\to n \\ \rho_s \nabla &\to \nabla & \frac{1}{c_s}\mathbf{u} &\to \mathbf{v} \\ \tfrac{c_s}{\rho_s} t &\to t & L_\parallel \nabla_\parallel &\to \nabla_\parallel. \end{aligned}$$

to express Eqs. (C.2) and (C.7) in a more convenient way. We start with the continuity equation (C.7). The operator containing the advective derivative deserves our particular attention

$$\begin{aligned} d_t = &\ \partial_t + \mathbf{u}_{\mathbf{E}\times\mathbf{B}} \cdot \nabla_\perp \\ = &\ \partial_t + \frac{\mathbf{B} \times \nabla_\perp \phi}{B^2} \cdot \nabla_\perp \\ \to &\ \frac{c_s}{\rho_s}\partial_t + \frac{T_e}{B_0 \rho_s^2 e}(\hat{\mathbf{z}} \times \nabla_\perp \phi) \cdot \nabla_\perp \\ = &\ \frac{c_s}{\rho_s}\partial_t + \frac{T_e}{m_i}\frac{m_i}{eB_0}\frac{1}{\rho_s^2}(\hat{\mathbf{z}} \times \nabla_\perp \phi) \cdot \nabla_\perp \qquad \text{(C.8)} \\ = &\ \frac{c_s}{\rho_s}(\partial_t + \{\phi, \cdot\}). \qquad \text{(C.9)} \end{aligned}$$

In the last step the ion cyclotron frequency $\omega_{ci} = eB_0/m_i$, the ion sound speed $c_s = \sqrt{T_e/m_i}$ and $\rho_s = c_s/\omega_{ci}$ have been used. $\{a, b\} = \partial_x a \partial_y b - \partial_y a \partial_x b$ is the Poisson bracket known from (quantum) mechanics. The Poisson bracket represents the nonlinearity and can be considered to be the heart of this model. Even though the nonlinearity depends on the power of two on the fluctuating quantities, it is not small. Due to drift ordering (Sec.B.2.1) $\partial_t \sim \mathbf{u} \cdot \nabla$. The density evolution is given by

$$d_t n \to \frac{c_s n_0}{\rho_s}(\partial_t \frac{\tilde{n}}{n_0} + \{\phi, \frac{\tilde{n}}{n_0}\} - \frac{\partial_x n_0(x)}{n_0}\partial_y \phi).$$

Let us consider the right-hand side of Eq. (C.7)

$$\nabla_\parallel \cdot (\nabla_\parallel p - en \nabla_\parallel \phi) \to \frac{1}{L_\parallel}\nabla_\parallel \cdot \left(\nabla_\parallel (n_0 T_e + n_0 n T_e) - e(n_0 + n_0 n)\nabla_\parallel \frac{T_e \phi}{e} \right). \tag{C.10}$$

Within the first bracket the background density does not change along a field line $\nabla_\parallel n_0 = 0$, therefore only fluctuations have to be taken into account. Furtermore, $n_0 \nabla_\parallel n \cdot \nabla_\parallel \phi \ll n_0 \cdot \nabla_\parallel^2 \phi$. The right-hand side of the continuity equation (C.7) reads

$$\frac{1.96}{m_e \nu_e}\nabla_\parallel \cdot (\nabla_\parallel p - en \nabla_\parallel \phi) \to \frac{c_s n_0}{\rho_s}\frac{1}{\nu}\nabla_\parallel^2 (n - \phi)$$

with the parallel collisionality $\nu = \nu_e/(1.96\omega_{ce})$, $\nabla_\parallel$ is normalized by $L_\parallel \sim \rho_s$. In the same way we proceed with the vorticity equation and get the *Hasegawa-Wakatani equations in 3D*

$$\partial_t n + \{\phi, n\} + \kappa_n \partial_y \phi = \frac{1}{\nu}\nabla_\parallel^2 (n - \phi) \tag{C.11}$$

$$\partial_t \Omega + \{\phi, \Omega\} = \frac{1}{\nu}\nabla_\parallel^2 (n - \phi). \tag{C.12}$$

The *Hasegawa-Wakatani equations in 2D* are given by

$$\partial_t n + \{\phi, n\} + \kappa_n \partial_y \phi = C(\phi - n) \tag{C.13}$$

$$\partial_t \Omega + \{\phi, \Omega\} = C(\phi - n). \tag{C.14}$$

The parallel dynamics have been approximated by a characteristic coupling parameter $C = 1/(L_\parallel^2 \nu)$ with a typical parallel wavelength $\nabla_\parallel^2 \approx -(1/L_\parallel)^2$.

In the following the linear features of Hasegawa-Wakatani turbulence are examined for consistency. Starting with the potential response on a density fluctuation, by recasting (5.4) for the potential it is obtained that

$$\phi = n + \frac{1}{C}(\partial_t n + \{\phi, n\} + \kappa_n \partial_y \phi).$$

For an adiabatic electron response ($C \Rightarrow \infty$) it is observed that $\phi = n$. The Boltzmann relation is consistently recovered. Next, the dispersion relation of the Hasegawa-Wakatani system is derived. All nonlinear terms in Eqs. (5.4) and (5.5) are neglected. Equation (5.5) is recast for the density within the coupling term and the result is substituted in Eq. (5.4). After Fourier transform we gain

$$k^2\omega^2 - iC(1 + k^2)\omega + iCk_y\kappa_n = 0. \tag{C.15}$$

For $C \to \infty$ (adiabatic limit) we get

$$\omega = \frac{\kappa_n k_y}{1 + k^2},$$

the dispersion relation for drift waves (B.23). In first approximation we substitute this dispersion relation into the quadratic (first) term of (C.15). This expression is solved for ω in the second term to get the imaginary part

$$\gamma = \mathrm{Im}(\omega) = \frac{1}{C}\frac{k^2 k_y^2 \kappa_n^2}{(1 + k^2)^3}.$$

This corresponds to the growth rate consistent with the previous considerations (Eq. (B.28)). Electrons experience a finite resistance during their parallel motion. For this reason the drift wave can get unstable.

C.2 The gyrofluid code GEMR

C.2.1 Gyroaveraging

Kinetic theory describes the evolution of a distribution function $f(\mathbf{x}, \mathbf{v}, t)$ where $\mathbf{x}$ is the spatial coordinate vector, $\mathbf{v}$ the velocity vector and t the time. The main equation is called the Vlasov equation

$$\frac{\partial}{\partial t} f + \mathbf{v} \cdot \nabla f + \frac{q}{m}(\mathbf{E} + \mathbf{v} \times \mathbf{B}) \cdot \nabla_v f = 0. \tag{C.16}$$

To get rid of the fast gyromotion guiding center variables can be introduced

$$\mathbf{X} = \mathbf{x} - \frac{mc}{eB(\mathbf{x})} \mathbf{b}(\mathbf{x}) \times \mathbf{v} \tag{C.17}$$

$$\mu = \frac{m v_\perp^2}{2B(\mathbf{x})} \tag{C.18}$$

$$v_\parallel = \mathbf{v} \cdot \mathbf{b}(\mathbf{x}), \tag{C.19}$$

$$\frac{\partial}{\partial t} f + \dot{\mathbf{X}} \cdot \nabla f + \dot{v}_\parallel \frac{\partial f}{\partial v_\parallel} + \dot{\mu} \frac{\partial f}{\partial \mu} = 0, \tag{C.20}$$

$$\dot{\mathbf{X}} = v_\parallel \mathbf{b} + \mathbf{v}_E + \mathbf{v}_d \tag{C.21}$$

where the $E \times B$ drift is given by

$$\mathbf{v}_E = \frac{c}{B_0} \mathbf{b} \times \nabla J_0 \phi \tag{C.22}$$

and the diamagnetic drift by

$$\mathbf{v}_d = \frac{v_\parallel^2}{\Omega} \mathbf{b} \times (\mathbf{b} \cdot \nabla \mathbf{b}) + \frac{\mu}{\Omega} \mathbf{b} \times \nabla B, \tag{C.23}$$

where the first term is the curvature drift, the second the ∇B drift.

$$\dot{v}_\parallel = -\frac{e}{m} \mathbf{b} \cdot \nabla J_0 \phi - \mu \mathbf{b} \cdot \nabla B + v_\parallel (\mathbf{b} \cdot \nabla \mathbf{b}) \mathbf{v}_E \tag{C.24}$$

These terms describe FLR effects, mirror effects and toroidal momentum balance. Averaging over the gyro-angle θ is done with the gyro-averaging operator

$$\langle \cdot \rangle_{gy} = \frac{1}{2\pi} \int_0^{2\pi} d\theta \tag{C.25}$$

The Fourier representation of the gyro-averaged potential is given by

$$\langle \phi \rangle_{gy} = \frac{1}{2\pi} \int_0^{2\pi} d\theta \phi(\mathbf{r}) = \int \mathbf{dk} \frac{1}{2\pi} \int_0^{2\pi} d\theta e^{i\mathbf{kx}} \phi(\mathbf{k}) \tag{C.26}$$

with

$$\mathbf{x} = \mathbf{X} + \rho \begin{pmatrix} \cos\theta \\ -\sin\theta \\ 0 \end{pmatrix}. \tag{C.27}$$

It has to be known that

$$\begin{aligned} \mathbf{k}\cdot\mathbf{x} &= \rho(k_1\cos\theta - k_2\sin\theta) \\ &= \rho(k_1\cos(\theta'-\theta_0) - k_2\sin(\theta'-\theta_0)) \\ &= \rho k_1(\cos\theta'\cos(-\theta_0) - \sin\theta'\sin(-\theta_0)) \\ &-\rho k_2(\cos\theta'\sin(-\theta_0) + \sin\theta'\cos(-\theta_0)) \\ &= \rho(k_1\cos\theta_0 + k_2\sin\theta_0)\cos\theta' + \rho(k_1\sin\theta_0 - k_2\cos\theta_0)\sin\theta' \end{aligned}$$

which has to be inserted into Eq. (C.26). This expression can be simplified, since one is free to choose

$$k_1\cos\theta_0 + k_2\sin\theta_0 = k_\perp$$

and

$$k_1\sin\theta_0 - k_2\cos\theta_0 = 0$$

which yields

$$\cos\theta_0 = \frac{k_1}{k_\perp}$$

and

$$\sin\theta_0 = \frac{k_2}{k_\perp}. \tag{C.28}$$

This results in a more handy expression for $\mathbf{k}\cdot\mathbf{x}$ given by

$$\mathbf{k}\cdot\mathbf{x} = \rho k_\perp\cos\theta' \tag{C.29}$$

with $\rho = v_\perp/\omega_c$. Therefore, the gyro-averaged potential (C.26) can be given by

$$\langle\phi\rangle_{gy} = \int \mathbf{dk} e^{i\mathbf{k}\cdot\mathbf{X}} \frac{1}{2\pi}\int_0^{2\pi} d\theta e^{i\frac{k_\perp v_\perp}{\omega_c}(\cos\theta)}\phi(\mathbf{k}). \tag{C.30}$$

By identifying the Bessel function

$$J_0(b) = \frac{1}{\pi}\int_0^{\pi} d\theta e^{ib\cos\theta} \tag{C.31}$$

in the gyro-averaged potential, Eq. (C.30) can also be written as

$$\langle\phi\rangle_{gy} = \int \mathbf{dk} e^{i\mathbf{k}\mathbf{X}}\phi(\mathbf{k}) J_0(\frac{k_\perp v_\perp}{\Omega}). \tag{C.32}$$

This operator introduces FLR effects

$$J_0(\frac{k_\perp v_\perp}{\Omega}) = \sum_n \frac{1}{(n!)^2}(i\frac{k_\perp v_\perp}{2\Omega})^{2n} \approx \sum_n \frac{1}{(n!)^2}(i\frac{\rho_L}{2})^{2n}\nabla_\perp^{2n} \approx (1 - (\frac{\rho_L}{2})^2\nabla_\perp^2). \tag{C.33}$$

C.2.2 Gyrofluid

Fluid-dynamical equations are derived from kinetic theory by taking appropriate moments of the velocity-average kinetic equations. The moment of zero order is the density

$$n = \int f d^3v. \tag{C.34}$$

The first order (mean) gives the particle flux density. In principle this is related to the momentum and a finite mean will give a flow. The parallel flow velocity $u_\parallel$ is determined by

$$nu_\parallel = \int f v_\parallel d^3. \tag{C.35}$$

The perpendicular velocity will be determined by the potential later. The flow is the particle movement in a preferential direction. The irregular movement of the particles give rise to the temperature. The irregular movement can be described by the variance. The second order moment (variance) describing the flow of momentum, is called the stress tensor. This gives the pressure. Here we have to distinguish the perpendicular

$$p_\perp = (m/2) \int f v_\perp^2 d^3v \tag{C.36}$$

and the parallel pressure

$$p_\parallel = m \int f (v_\parallel - u_\parallel)^2 d^3v \tag{C.37}$$

as the magnetic field will allow for different velocity distributions along and perpendicular to the magnetic field. For the parallel pressure a mean parallel velocity has to be accounted for, a mean perpendicular velocity is expected to be zero. Note that the perpendicular direction has two degrees of freedom. The pressure defines the temperatures by

$$p_{\perp,\parallel} = nT_{\perp,\parallel}. \tag{C.38}$$

The difference between $T_\parallel$ and $T_\perp$ is the temperature anisotropy. This can lead to micro-instabilities as the mirror or the firehose instability. For example the solar wind is known to exhibit a temperature anisotropy. In a tokamak plasma heating or magnetic field line expansion can lead to temperature anisotropies.

The third order moment (corresponding to the skewness) is the energy flux density, which gives the parallel heat flux. The skewness is a measure of the asymmetry of the probability distribution. A positive skew indicates that the tail on the right side of the probability density function is longer or fatter than the left side. The particles in the tail carry the heat flux [470]. The perpendicular heat flux will be a result of the transport and therefore from the potentials. However, the parallel heat transport also slits up into two

contributions due to the different distributions parallel and perpendicular to the magnetic field. The perpendicular(-parallel) heat flux is given by

$$q_{\parallel,\perp} \equiv q_\perp = (m/2) \int f v_\perp^2 (v_\parallel - u_\parallel) d^3v \tag{C.39}$$

and the parallel(-parallel) heat flux

$$q_{\parallel,\parallel} \equiv q_\parallel = m \int f (v_\parallel - u_\parallel)^3 d^3v. \tag{C.40}$$

C.2.3 Time dependent magnetic equilibrium in GEMR

In the following the magnetic equilibrium of GEMR is introduced. Here it is important to note that GEMR describes plasma turbulence in field aligned geometry and as the magnetic field is curved in a tokamak it uses curvilinear coordinates. A point in three dimensions $\mathbf{r}$ can be described by three curvilinear coordinates $\mathbf{r}(u^1, u^2, u^3)$. For example in cylinder geometry the curvilinear coordinates are a radius, an angle and one coordinate describing the height above the polar plane or in spherical coordinates it is a radius and two (polar and azimuthal) angles. The basis vectors can be defined locally by either the tangents $\mathbf{e}_i = \partial\mathbf{r}/\partial u^i$ or by the normals $\mathbf{e}^i = \partial u^i/\partial\mathbf{r} = \nabla u^i$. The tangents $\mathbf{e}_i$ are called *covariant* vectors and are in general not necessarily perpendicular to each other and neither normalized. Also the normals $\mathbf{e}^i$ (called *contravariant*) are in general not necessarily perpendicular and normalized. However, co- and contravariant vectors are reciprocal to each other $\mathbf{e}^i\mathbf{e}_j = \delta_{ij}$. The geometry can be described by the metric coefficients $g_{ij} = \mathbf{e}_i \cdot \mathbf{e}_j$ or $g^{ij} = \mathbf{e}^i \cdot \mathbf{e}^j$. Regular used magnetic field aligned coordinates are Clebsch, Boozer [526] and Hamada [527] coordinates. GEMR uses Hamada coordinates, which are orthogonal straight magnetic field line coordinates where also the current is straight [527].

Due to the twist of the magnetic field lines the Pfirsch-Schlüter current sets in (see Sec. 5.2.3). This current induces a vertical magnetic field which in superposition with the external magnetic field and the magnetic field induced by the plasma current leads to a radial outwards shift of the magnetic axis. This shift is called the *Grad-Shafranov shift* and the equation describing the equilibrium is called the *Grad-Shafranov equation* (Eq. (C.44)). The MHD equilibrium is given by the balance of current $\mathbf{J}$ and pressure gradient ∇p

$$\mathbf{J} \times \mathbf{B} = c\nabla p. \tag{C.41}$$

Here still CGS units are used. The current is determined by Ampere's law

$$\mathbf{J} = \frac{c}{4\pi} \nabla \times \mathbf{B}. \tag{C.42}$$

The magnetic field in a cylindrical coordinate system (R,z,ϕ) can be described by

$$\mathbf{B} = I\nabla\phi + \nabla\psi \times \nabla\phi, \tag{C.43}$$

where I and ψ are scalar functions depending only on R and z. The magnetic field in a tokamak is axisymmetric. The poloidal plane (Rz-plane) is perpendicular to the symmetry direction $\nabla\phi$. From Eq. (C.43) follows $\mathbf{B}\cdot\nabla\psi = 0$ which means that magnetic field lines lie on flux-surfaces of constant ψ and the flux surfaces can be labeled accordingly. The function $\psi(R,z)$ can be identified with the poloidal flux ψ_p by the relation $\psi_p = -2\pi\psi$. The function $I(R,z)$ can be identified with the poloidal current I_p through a disk of radius R lying in the horizontal plane (spanned by ∇R and $\nabla\phi$ at $z=0$), given by the relation $I_p = \frac{c}{2}I$ [528]. $I(R,z)$ is a flux function and can be found in the *Grad-Shafranov equation*

$$4\pi R^2\frac{\partial p}{\partial\psi} + I\frac{\partial I}{\partial\psi} + R^2\nabla\cdot\frac{\nabla\psi}{R^2} = 0. \tag{C.44}$$

The magnetic equilibrium field in GEMR is described in straight-field-line Hamada coordinates (V,θ,ζ), where $V = V(\psi)$ is the volume surrounded by the flux surface labeled with the poloidal flux ψ, θ and ζ are poloidal and toroidal Hamada angles. In GEMR cylindrical Hamada coordinates (R,z,ϕ) are used given by [529]

$$V = \oint_\psi 2\pi R dR dz \tag{C.45}$$

where the integral is evaluated for the area enclosed by a curve of constant poloidal flux ψ in the poloidal plane. The poloidal Hamada angle

$$\theta = \left(\oint\frac{1}{\mathbf{B}\cdot\nabla\eta}d\eta\right)^{-1}\int_{\eta_0}^{\eta}\frac{1}{\mathbf{B}\cdot\nabla\eta'}d\eta' \tag{C.46}$$

is evaluated from a cyclic coordinate η satisfying the relations $\nabla\cdot\nabla\phi = 0$ and $\mathbf{B}\cdot\nabla\eta \neq 0$, assuming $\theta = \theta(V,\eta)$. The toroidal Hamada coordinate

$$\zeta = \frac{\phi}{2\pi} + \frac{I(V)}{2\pi}\int_{\eta_0}^{\eta}\frac{1}{\mathbf{B}\cdot\nabla\eta'}\left(\left\langle\frac{1}{R^2}\right\rangle - \frac{1}{R^2}\right)d\eta' \tag{C.47}$$

is based on the relation $\mathbf{B}\cdot\nabla\zeta = \frac{\partial\psi(V)}{\partial V}$. The brackets denote flux-surface average $\langle\cdot\rangle = \oint d\theta$. $I(V)$ is a scalar function (see Eqs. (C.43) and (C.44)). The field-aligned coordinates in GEMR are a radial coordinate based on (C.45)

$$x = V = 2\pi^2 R_0 r^2, \tag{C.48}$$

a parallel coordinate similar to an extended ballooning angle (the poloidal Hamada angle (C.46))

$$s = \theta, \tag{C.49}$$

and a binormal coordinate based on a combination of Eqs. (C.46) and (C.47)

$$y_k = q\theta - \zeta - \alpha_k. \tag{C.50}$$

Here R_0 is the major radius. The radial coordinate r is normalized to the minor radius a. Magnetic shear deformation is taken into account by shifting

the y-coordinate by $\alpha_k = q\theta_k + \Delta\alpha_k$ where α_k is chosen in such a way that ∇x and ∇y_k are locally orthogonal at $\theta = \theta_k$ [529].

The evolution of the profiles in GEMR is self-consistently coupled to the magnetic Shafranov equilibrium for circular flux surfaces. The preset safety factor profiles determines the initial magnetic equilibrium. In each time step the change of the safety factor profile is computed by [400]

$$\Delta\frac{1}{q} = -\frac{\delta_0\beta_{e0}R_0}{r}\frac{\partial}{\partial r}\langle A_\parallel\rangle_{y_k,s}. \tag{C.51}$$

The time dependent Shafranov shift modifies the metric elements according to a $s-\alpha$ model in lowest order in r/R_0 by

$$g^{xx} = \nabla x\cdot\nabla x = \left(\frac{\partial V}{\partial x}\right)^2 = (2\pi)^4(R_0 r)^2 \tag{C.52}$$

$$g_k^{yy} = \nabla y_k\cdot\nabla y_k = \frac{q^2}{(2\pi r)^2} \tag{C.53}$$

$$g_k^{xy} = \nabla x\cdot\nabla y_k = \frac{\partial q}{\partial x}(\theta-\theta_k) - \frac{\partial d_s}{\partial x}\sin(2\pi s) - \Delta\frac{\partial\alpha_k}{\partial x} \equiv 0 \tag{C.54}$$

where the last equation is at $\theta = \theta_k$. The local magnetic shear by the Pfirsch-Schlüter current is given by $\frac{\partial d_s}{\partial x}\sin(2\pi s)$. In order to force g_k^{xy} to vanish locally at $\theta = \theta_k$ the shift in the y-coordinate is set to $\alpha_k = q\theta_k - d_s\sin\theta_k$ and

$$d_s = -\frac{\delta_0\beta_{e0}q^2R_0}{\pi r}\frac{\partial}{\partial r}\langle A_\parallel\cos(2\pi s)\rangle_{y_k,s}. \tag{C.55}$$

When the magnetic flutter is evaluated the axisymmetric part of $A_\parallel$ is subtracted to avoid that is considered twice.

Transport by the gradient-driven turbulence leads to a degradation of the gradients. Profile maintenance can only be achieved by sources which is done in GEMR by source/sink zones at the radial boundaries. The zonal components (profile perturbations with respect to the initial profile) are feedback dissipated towards the initially specified profile. More details can be found in Ref. [530].

One particular strength of GEMR is that the simulation does not end at the last closed flux surface, but the SOL is included. The open field lines corresponding to the SOL are implemented by the boundary conditions via a perturbed Debye sheath current [531]. The actual boundary conditions used in the simulation, which include the temperature dynamics, can be found in Ref. [530].

C.2.4 Main limitations of GEMR

The strength of GEMR is the completeness of the physics model. Most kinds of instabilities relevant for the plasma edge can be excited. All relevant nonlinear phenomena as for example subcritical turbulence, different cascades, zonal

flows or geodesic acoustic modes are included. Compared to any other fluid based model the completeness of the model is unsurpassed for the time being. As GEMR is a gyrofluid model it is much faster compared to a gyrokinetic model.

Although GEMR is a global model including a time-dependent equilibrium (see above), GEMR is based on local model equations. Given local reference values in density n_0 and temperature T_{e0} define δ, β and ν. These three parameters (δ, β, ν) determine the characteristic dynamics. GEMR is a δ-f model, which means that the fluctuation levels have to be small $\tilde{n}/n_0 \sim \tilde{T}_e/T_{e0} \ll 1$. The SOL on the contrary is characterized by high local fluctuation levels approaching unity and above. However, as the reference surface used for normalization (with density n_0 and electron temperature T_{e0}) is usually at the separatrix or mid-pedestal and not in the SOL the fluctuation level has to be small only compared to this reference surface and not to the local value.

With increasing distance to the reference surface the parameters (δ, β, ν) differ from the value calculated from the local values due to the profile evolution. This induces an inconsistency usually referred to as *stratification issue* [237]. As the reference surface is usually taken to be the separatrix or mid-pedestal in particular the SOL exhibit an overestimated plasma β and an underestimated collisionality ν.

As GEMR is a global model which by the time-dependent self-consistent equilibrium, it allows for arbitrary evolving zonal profiles of the dependent variables (potential, temperatures, densities). These zonal perturbations are the differences to the initial profile, which can lead to strong modifications. However, for large differences to the initial profile the present input parameter (δ, β, ν) are not consistent with the profiles anymore. Therefore, the difference of the converged profiles has to be small compared to the initial input parameters. Therefore, in practice the input parameter (δ, β, ν) cannot be chosen arbitrary, but have to be guessed in such a way that they lead to stable converged profiles. This can only be done with experience.

Another assumption of the local model is that the gradient scale lengths are comparable in length and those length are small compared to the simulation size domain $L_n \sim L_{T_e} \sim L_{Ti} \ll \Delta r$, where Δr is the simulation size domain. In GEMR the simulation size domain sets the characteristic gradient scale length. Therefore, simulations with steeper gradients lead to smaller simulation size domains. Another limitation is the intrinsic circular cross-section. Most discharges in ASDEX Upgrade exhibit highly shaped equilibria including an X-point. Effects of elongation and triangularity cannot be taken into account. Also effects of the X-point geometry cannot be studied. For the SOL atom physics is important. Ionization and recombination processes determine the SOL to a large degree which are not included in the model equations.

C.2.5 GEMR simulation parameters

Simulations have been carried out at ASDEX Upgrade parameters $R = 1.65$ m, $a = 0.5$ m, except for the results in Sec. 10.3.3, which are at Tore supra parameters ($R = 2.4$ m, $a = 0.70$ m, $B = 3.5$ T). The following table C.1 shows the input parameters of the GEMR simulations presented in this work.

Sec.	n_e 10^{19} m^{-3}	T_e eV	τ_i	δ 10^{-3}	β 10^{-5}	ν	$L_{Te}(cm)$ cm	$L_n(cm)$ cm
9.2	4.5	2k	1	5.38	315	0.03	20	6.7
9.3	2	120	1	1.32	8.39	4.08	5	2.5
9.4	2	100	1	1.20	6.99	5.88	5	2.5
10.3.3	0.4	40	1	0.43	0.28	9.26	3.5	3.5
12.1.5	1.2	60	0.1, 3	0.86	2.14	19.6	4.5	9
12.2.1	1.2	60	1	0.86	2.14	19.6	4.5	9
12.2.3	1.2	60	1	0.86	2.14	19.6	4.5	9

TABLE C.1: Simulation parameters of the GEMR simulations shown in this work.

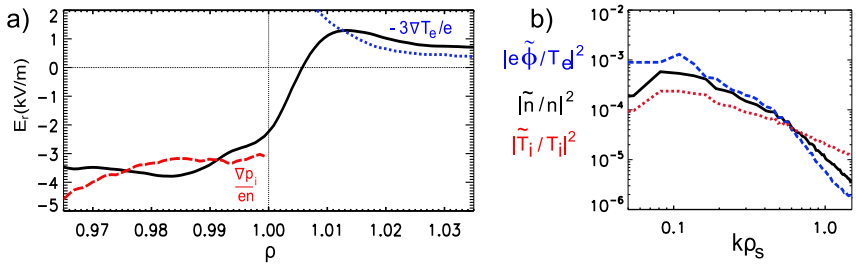

FIGURE C.1: Strong turbulence case (Sec. 9.4): a) Radial electric field (black solid line), ion pressure contribution (red dashed line) and sheath potential contribution (blue dotted line) to the radial electric field. Wavenumber spectra of normalized potential (blue), density (black) and ion temperature (red) fluctuations. At low wavenumbers potential perturbations are strongest, corresponding to ballooning modes, at higher wavenumbers density and potential fluctuations are similar and the ion temperature fluctuations are strongest, pointing to ITG-drift-wave turbulence.

As an example a typical case will be presented here. The radial electric field is shown in Fig. C.1a; It is dominated by its ion pressure contribution in the confined region and by the sheath potential in the scrape-off layer. Depending on the wavenumber the turbulence shows different features. At low wavenumbers ($k\rho_s < 0.2$) the strong potential perturbations corresponds to

resistive ballooning modes (see Fig. C.1b). At higher wavenumbers ($k\rho_s > 0.2$) density and potential fluctuation amplitudes are similar which is characteristic for drift-wave turbulence. At even higher wavenumbers ($k\rho_s > 0.6$) the ion temperature fluctuations are strongest pointing to ITG-drift-wave turbulence.

Appendix D

Nonlinear Instability

D.1 Parametric oscillator

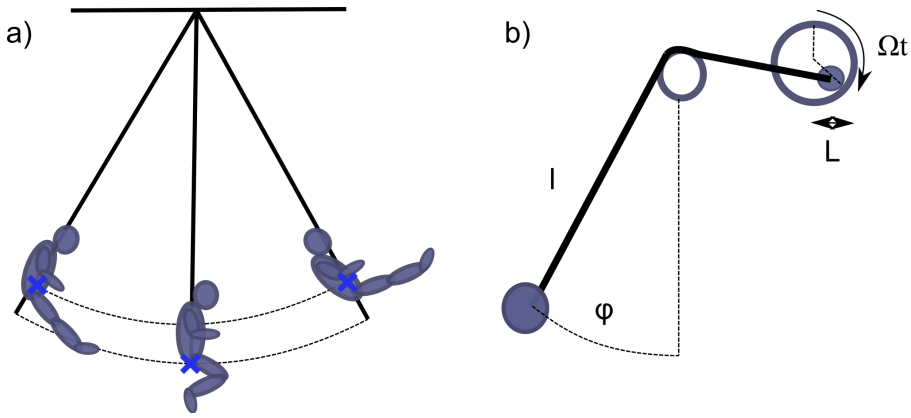

FIGURE D.1: Person on a swing (a), pendulum with modulated length (b).

For the common harmonic oscillator describing a displacement x with a restoring force $-Dx$ given by

$$m\frac{\partial^2 x}{\partial t^2} + Dx = 0 \tag{D.1}$$

the mass m and the constant D can in principle depend on time

$$m(t)\frac{\partial^2 x}{\partial t^2} + D(t)x = 0. \tag{D.2}$$

Therefore, the frequency can generally be time dependent $\omega^2(t) = D(t)/m(t)$.

One example is a person on a swing as shown in Fig. D.1a. By changing its center of mass the person is able to amplify the oscillation up to twice the frequency. Likewise a modulation of the length of a common pendulum can have a similar effect (Fig. D.1b). The length of the pendulum is modulated

externally by an excentric rotating at a frequency Ω. Similarly if the excentric is rotating with double the frequency of the eigenfrequency of the pendulum it can amply the oscillation. This will pump energy into the system. The case of the pendulum with the modulated length can be described by

$$\frac{\partial^2 \varphi}{\partial t^2} = \omega^2(t)\varphi \tag{D.3}$$

with

$$\omega^2(t) = \frac{g}{l + L\cos(\Omega t + \Phi)} \approx \omega_0^2(1 - \frac{L}{l}\cos(\Omega t + \Phi)). \tag{D.4}$$

The parametric oscillator is linked to fluctuations in general. An oscillation is described by a relation between space x and time t

$$\frac{\partial^2 x}{\partial^2 t} + \mathcal{F}(x) = 0 \tag{D.5}$$

with $\mathcal{F}$ being any complicated nonlinear function leading to a stationary solution $\bar{x}$. Fluctuations ξ are small deviations from the solution $x = \bar{x} + \xi$. The force operator can be expanded as

$$\mathcal{F}(x) \approx \mathcal{F}(\bar{x}) + \frac{\partial \mathcal{F}}{\partial x}\Big|_{x=\bar{x}}\xi = \frac{\partial \mathcal{F}}{\partial x}\Big|_{x=\bar{x}}\xi. \tag{D.6}$$

As the stationary solution does not exhibit any time derivative, an equation for the fluctuations can be obtained

$$\frac{\partial^2 \xi}{\partial t^2} + \frac{\partial \mathcal{F}}{\partial x}\Big|_{x=\bar{x}}\xi \tag{D.7}$$

As a specific example we come back to the pendulum with modulated rope length. Without damping, this pendulum is described by *Mathieu's differential equation*

$$\frac{\partial^2}{\partial t^2}x(t) + \omega_0^2(1 - 2\epsilon\cos(\Omega t))x(t) = 0 \tag{D.8}$$

The eigenfrequency at constant rope length l is $\omega_0 = \sqrt{g/l}$, the phase Φ has been set to zero and for the ratio between the modulation amplitude L and the rope length we define a small parameter $2\epsilon = L/l$. The rotation frequency of the excentric is given by Ω. It drives the system and is called the modulation frequency. Using a Fourier ansatz

$$x(t) = \frac{1}{2\pi}\int x(\omega)e^{-i\omega t}d\omega \tag{D.9}$$

and

$$\cos(\Omega t) = \frac{1}{2}\left(e^{i\Omega t} + e^{-i\Omega t}\right). \tag{D.10}$$

This is inserted this into Eq. (D.8), multiply by $e^{-i\omega' t}$ and subsequently integrated over time, resulting in

$$\int d\omega(\omega^2 - \omega_0^2)x(\omega)\delta(\omega - \omega') = -\epsilon\omega_0^2\int d\omega x(\omega)(\delta(\omega - \Omega - \omega') + \delta(\omega + \Omega - \omega')). \tag{D.11}$$

After integration over ω we obtain the *mode-coupling equation*

$$(\omega^2 - \omega_0^2)x(\omega) = -\epsilon\omega_0^2(x(\omega + \Omega) + x(\omega - \Omega)) \tag{D.12}$$

the amplitude of the mode at the response frequency of the system ω depends on the amplitudes of two other modes at frequencies $\Omega+\omega$ and $\Omega-\omega$. Those two modes are side bands of the driver frequency Ω. In the following we will study two concrete cases leading to a nonlinear instability. The decay instability at $\omega \approx \omega_0$ and the modulational instability at $\omega \ll \omega_0$.

How these two kinds of parametric instabilities can be distinguished with a bispectral analysis will be shown later in chapter 7.3.1 (see Fig. 7.5).

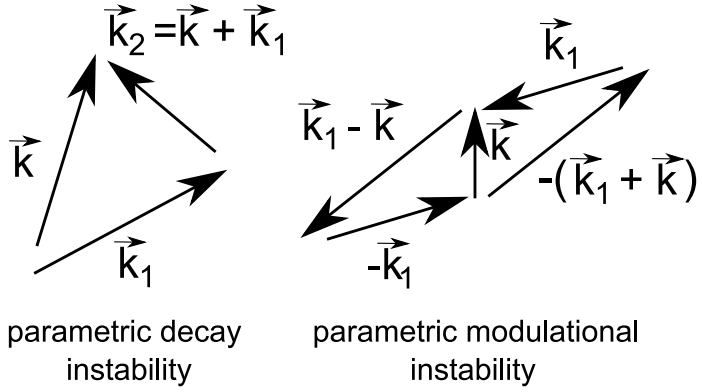

FIGURE D.2: For the parametric decay instability a mode $\mathbf{k}$ decays in $\mathbf{k}_1$ and $\mathbf{k}_2 = \mathbf{k}_1 - \mathbf{k}$. For the the parametric modulational instability a mode $\mathbf{k}_1$ can drive a mode $\mathbf{k}$ by interaction with two virtual sideband modes $\mathbf{k}_1 - \mathbf{k}$ and $\mathbf{k}_1 + \mathbf{k}$.

D.2 Parametric decay instability

A solution in the vicinity of the natural frequency ω_0 will provide the parametric decay instability. The driver is assumed to be at approximately twice the natural frequency of the oscillator $\Omega \approx 2\omega_0$ with a small frequency miss-match of $\Delta = \Omega - 2\omega_0$. This can be motivated by experience (the person on the swing described above for example). According to Eq. (D.12) three modes have to be included. These are

$$\omega \approx \omega_0 \tag{D.13}$$

$$\omega + \Omega \approx \omega_0 + 2\omega_0 \approx 3\omega_0 \tag{D.14}$$

$$\omega - \Omega \approx \omega_0 - 2\omega_0 \approx -\omega_0 \tag{D.15}$$

which would entrain further modes. In order to close the set of mode-coupling equations to be involved, it is assumed that the amplitude of the $3\omega_0$ mode is small. This is reasonable as it is far away from the eigenfrequency or resonance

ω_0. Thus the problem can be reduced to the two coupled equations, both obtained from Eq. (D.12)

$$(\omega^2 - \omega_0^2)x(\omega) = -\epsilon\omega_0^2 x(\omega - \Omega) \tag{D.16}$$

and

$$((\omega - \Omega)^2 - \omega_0^2)x(\omega - \Omega) = -\epsilon\omega_0^2(x(\omega) + x(\omega - 2\Omega)) \approx -\epsilon\omega_0^2 x(\omega), \tag{D.17}$$

where $x(\omega - 2\Omega) = x(-3\omega_0)$ is again assumed to be small as it is far from the eigenfrequency. The l.h.s. of (D.16) can be further simplified

$$(\omega^2 - \omega_0^2) = (\omega + \omega_0)(\omega - \omega_0) \approx 2\omega_0(\omega - \omega_0) \tag{D.18}$$

where we used $(\omega + \omega_0) \approx 2\omega_0$. Similarly the l.h.s. of (D.17) can be simplified by

$$\begin{aligned}(\omega - \Omega)^2 - \omega_0^2 = \;& \omega^2 - 2\omega\Omega + \Omega^2 - \omega_0^2 \\ & = (\omega^2 - \omega_0^2) + \Omega^2 - 2\omega\Omega \\ & \approx 2\omega_0(\omega - \omega_0) + \Omega(\Omega - 2\omega) \\ & \approx 2\omega_0(\omega - \omega_0 + \Delta + 2\omega_0 - 2\omega) \\ & \approx -2\omega_0(\omega - \omega_0 - \Delta).\end{aligned}$$

By multiplying both equations (D.16) and (D.17) and taking into account the simplifications discussed above yields

$$-4\omega_0^2(\omega - \omega_0)(\omega - \omega_0 - \Delta) = \epsilon^2\omega_0^4, \tag{D.19}$$

which has two solutions for the response frequency

$$\omega_{1,2} = \omega_0 + \frac{\Delta}{2} \pm \frac{1}{2}\sqrt{\Delta^2 - \epsilon^2\omega_0^2}. \tag{D.20}$$

Imaginary square roots are associated with instability, which is the case for

$$\epsilon^2 > \frac{\Delta^2}{\omega_0^2}. \tag{D.21}$$

The modes at ω_0 gain energy at the expense of the mode at $\Omega \approx 2\omega_0$. This can be interpreted as the mode at Ω decays into two modes at ω_0. The interaction as in this example is often local in frequency or wavenumber space in the sense that the frequencies or wavenumbers involved in the process do not differ by much more than a factor of two. Therefore, such a process can describe the eddy mitosis behind the Richardson cascade (see Sec. 3.2).

D.3 Parametric modulational instability

By setting the driving or pump frequency close to the eigenfrequency $\Omega \approx \omega_0$ another nonlinear instability can be obtained with a response at low frequencies $\omega \ll \Omega$. This is called the *modulational instability*. The frequency miss match is also assumed to be small and given by $\Delta = \Omega - \omega_0$. From the mode coupling equation (D.12) follows

$$(\omega^2 - \omega_0^2)x(\omega) \approx -\omega_0^2 x(\omega) = -\epsilon\omega_0^2(x(\omega+\Omega) + x(\omega-\Omega)). \tag{D.22}$$

The mode at ω couples to two modes $\omega \pm \Omega$, these are called *sidebands*. Therefore two additional equations for the sidebands are needed. These are

$$((\omega+\Omega)^2 - \omega_0^2)x(\omega+\Omega) = -\epsilon\omega_0^2(x(\omega+2\Omega) + x(\omega)) \approx -\epsilon\omega_0^2 x(\omega) \tag{D.23}$$

and

$$((\omega-\Omega)^2 - \omega_0^2)x(\omega-\Omega) = -\epsilon\omega_0^2(x(\omega) + x(\omega-2\Omega)) \approx -\epsilon\omega_0^2 x(\omega). \tag{D.24}$$

In the last step it has been assumed that the modes far away from the resonance are small $x(\omega \pm 2\Omega) \approx x(\pm 2\Omega) \ll x(\Omega) \approx x(\omega)$. Using

$$(\omega \pm \Omega)^2 - \omega_0^2 = \omega^2 \pm \omega\Omega + \Omega^2 - \omega_0^2 \approx (\Omega + \omega_0)(\Omega - \omega_0) \pm 2\omega\Omega \approx 2\omega_0(\Delta \pm \omega)$$

after the division of Eq. (D.23) by Eq. (D.24) a dispersion relation of the *modulational instability* is obtained

$$1 = -\frac{1}{2}\epsilon^2\left(\frac{1}{\omega-\Delta} - \frac{1}{\omega+\Delta}\right) \tag{D.25}$$

with the solutions

$$\omega_{1,2} = \pm\sqrt{\Delta(\epsilon^2\omega_0 + \Delta)}. \tag{D.26}$$

The modulational instability gets unstable for a driving frequency below the eigenfrequency, $\Omega < \omega_0$, $\Delta < 0$ and $|\Delta| \geq \epsilon^2\omega_0$. The frequency response at ω is not in resonance with the harmonic oscillator. Therefore this coupling is also called *non-resonant coupling*.

Bibliography

[1] OECD/IEA, *Energy to 2050, Scenarios for a sustainable future* (OECD/IEA, Paris Cedex 16, France, 2003).

[2] Shell scenarios, *Sky, meeting the goals of the Paris Agreements* (Shell, www.shell.com/skyscenario, 2018).

[3] P. H. Diamond, S. I. Itoh, and K. Itoh, *Modern Plasma Physics* (Cambridge University Press, 2010, New York).

[4] J. Kühnen *et al.*, Nature Physics **14**, 386 (2018).

[5] O. Reynolds, Phil. Trans. R. Soc. A **175**, 935 (1883).

[6] A. Tsinober, *An informal introduction to turbulence* (Kluwer Academic Publishers, 2001, Dortrecht).

[7] F. M. T. Nieuwstadt, B. J. Boersma, and J. Westerweel, *Turbulence* (Springer, Swisterland, 2016).

[8] N. Howard *et al.*, Nuclear Fusion **56**, 014004 (2016).

[9] P. Manz, G. Birkenmeier, M. Ramisch, and U. Stroth, Phys. Plasmas **19**, 082318 (2012).

[10] P. Manz, M. Xu, S. C. Thakur, and G. R. Tynan, Plasma Phys. Controll. Fusion **53**, 095001 (2011).

[11] P. Manz *et al.*, Phys. Plasmas **19**, 012309 (2012).

[12] P. Manz *et al.*, Plasma Phys. Controll. Fusion **60**, 085002 (2018).

[13] P. Manz *et al.*, Phys. Plasmas **19**, 072311 (2012).

[14] P. Manz *et al.*, Phys. Plasmas **23**, 052302 (2016).

[15] P. Manz *et al.*, Phys. Plasmas **25**, 072508 (2018).

[16] P. Manz *et al.*, Nucl. Fusion **55**, 083004 (2015).

[17] P. Manz *et al.*, Nucl. Fusion **57**, 086002 (2017).

[18] P. Manz *et al.*, Phys. Plasmas **20**, 102307 (2013).

[19] P. Manz *et al.*, Plasma Phys. Controll. Fusion **57**, 014012 (2015).

[20] P. Manz *et al.*, Phys. Plasmas **22**, 022308 (2015).

[21] U. Stroth, P. Manz, and M. Ramisch, Plasma Phys. Controll. Fusion **53**, 024006 (2011).

[22] J. Wesson, *Tokamaks* (Clarendon, Oxford, 1987).

[23] P. C. Stangeby, *The Plasma Boundary of Magnetic Fusion Devices* (Institute of Physics, Bristol, Philadelphia, 2000).

[24] N. Fedorczak *et al.*, Phys. Plasmas **19**, 122302 (2012).

[25] G. S. Xu *et al.*, Nuclear Fusion **54**, 013007 (2014).

[26] G. S. Xu *et al.*, Nuclear Fusion **54**, 103002 (2014).

[27] L. M. Shao *et al.*, Plasma Phys. Controll. Fusion **60**, 035012 (2018).

[28] T. Sunn Pedersen *et al.*, Nature Comm. **7**, 13493 (2016).

[29] N. Krause *et al.*, Rev. Sci. Instrum. **73**, 3474 (2002).

[30] U. Stroth *et al.*, Phys. Plasmas **11**, 2558 (2004).

[31] M. Ramisch *et al.*, Phys. Plasmas **12**, 032504 (2005).

[32] N. Mahdizadeh *et al.*, Plasma Phys. Controll. Fusion **49**, 1005 (2007).

[33] K. Rahbarnia *et al.*, Plasma Phys. Controll. Fusion **50**, 085008 (2008).

[34] P. Manz *et al.*, Plasma Phys. Controll. Fusion **50**, 035008 (2008).

[35] P. Manz, M. Ramisch, and U. Stroth, Plasma Phys. Controll. Fusion **51**, 035008 (2009).

[36] P. Manz, M. Ramisch, and U. Stroth, Phys. Plasmas **16**, 042309 (2009).

[37] P. Manz, M. Ramisch, and U. Stroth, Phys. Rev. E **82**, 056403 (2010).

[38] G. Birkenmeier, M. Ramisch, B. Schmid, and U. Stroth, Phys. Rev. Lett. **110**, 145004 (2013).

[39] B. Schmid, P. Manz, M. Ramsich, and U. Stroth, Phys. Rev. Lett. **118**, 055001 (2017).

[40] B. Schmid, P. Manz, M. Ramsich, and U. Stroth, New. J. Physics **19**, 055003 (2017).

[41] G. Birkenmeier *et al.*, Phys. Rev. Lett. **107**, 025001 (2011).

[42] W. Gekelman, S. Vincena, D. Leneman, and J. Maggs, J. Geophys. Res. **102**, 7225 (1997).

[43] W. Gekelman *et al.*, Phys. Plasmas **18**, 055501 (2011).

[44] C. Charles and R. Boswell, Appl. Phys. Lett. **82**, 1356 (2003).

[45] S. A. Cohen *et al.*, Phys. Plasmas **10**, 2593 (2003).

[46] X. Sun *et al.*, Phys. Rev. Lett. **95**, 025004 (2005).

[47] B. W. Longmier *et al.*, Plasma Sources Sci. Technol. **20**, 015007 (2011).

[48] A. von Stechow, O. Grulke, and T. Klinger, Plasma Phys. Controll. Fusion **58**, 014016 (2016).

[49] M. J. Baldwin and R. P. Doerner, Nucl. Fusion **48**, 035001 (2008).

[50] B. Unterberg *et al.*, Fusion Eng. Design **86**, 1797 (2011).

[51] N. Ohno, Plasma Phys. Controll. Fusion **59**, 034007 (2017).

[52] S. Chakraborty Thakur *et al.*, Phys. Plasmas **20**, 012304 (2013).

[53] Z. Yan *et al.*, Phys. Plasmas **15**, 092309 (2008).

[54] M. Xu *et al.*, Phys. Plasmas **16**, 042312 (2009).

[55] M. Xu *et al.*, Phys. Plasmas **17**, 032311 (2010).

[56] F. Wagner *et al.*, Phys. Rev. Lett. **49**, 1408 (1982).

[57] H. Biglari, P. H. Diamond, and P. W. Terry, Phys. Fluids, B **2**, 1 (1990).

[58] J. W. Connor and H. R. Wilson, Plasma Phys. Controll. Fusion **42**, R1 (2000).

[59] J. Kim *et al.*, Phys. Rev. Lett. **72**, 2199 (1994).

[60] E. Viezzer *et al.*, Nucl. Fusion **53**, 053005 (2013).

[61] F. L. Hinton and R. D. Hazeltine, Rev. Mod. Phys. **48**, 239 (1976).

[62] M. Cavedon *et al.*, Nucl. Fusion **57**, 014002 (2017).

[63] H. Zohm, Plasma Phys. Controll. Fusion **38**, 105 (1996).

[64] A. Herrmann *et al.*, Journal of Nuclear Materials **313**, 759 (2003).

[65] A. Loarte *et al.*, Physics of Plasmas **11**, 2668 (2004).

[66] Y. Liang, Fusion Science and Technology **59**, 586 (2011).

[67] H. R. Wilson, S. C. Cowley, A. Kirk, and P. B. Snyder, Plasma Phys. Controll. Fusion **48**, A71 (2006).

[68] P. B. Snyder *et al.*, Phys. Plasmas **9**, 2037 (2002).

[69] P. B. Snyder *et al.*, Nucl. Fusion **49**, 085035 (2009).

[70] P. B. Snyder *et al.*, Nucl. Fusion **44**, 320 (2004).

[71] H. R. Wilson and S. C. Cowley, Phys. Rev. Lett. **92**, 175006 (2004).

[72] N. Oyama *et al.*, Plasma Phys. Controll. Fusion **48**, A171 (2006).

[73] J. Stober *et al.*, Nucl. Fusion **45**, 1213 (2005).

[74] E. Viezzer, Nucl. Fusion **58**, 115002 (2018).

[75] F. Ryter *et al.*, Plasma Phys. Controll. Fusion **40**, 725 (1998).

[76] D.-G. Whyte *et al.*, Nucl. Fusion **50**, 105005 (2010).

[77] A. E. Hubbard *et al.*, Phys. Plasmas **18**, 331 (2011).

[78] R. M. McDermott *et al.*, Phys. Plasmas **16**, 056103 (2009).

[79] I. Cziegler *et al.*, Phys. Plasmas **20**, 055904 (2013).

[80] A. E. Hubbard *et al.*, Nucl. Fusion **56**, 086003 (2016).

[81] A. Hubbard *et al.*, Proc. of the 26^{th} IAEA Fusion Energy Conf., Kyoto, Japan EX3 (2016).

[82] F. Ryter *et al.*, Nucl. Fusion **57**, 016004 (2017).

[83] T. Happel *et al.*, Plasma Phys. Controll. Fusion **59**, 014004 (2017).

[84] Y. R. Martin, T. Takizuka, and the ITPA CDBM H-mode Threshold Database Working Group, J. Phys.: Conf. Ser. **123**, 012033 (2008).

[85] L. F. Richardson, Proc. Roy. Soc. London A **110**, 709 (1926).

[86] A. N. Kolmogorov, C. R. acad. Sci. U.S.S.R. **30**, 301 (1941).

[87] G. Boffetta and R. E. Ecke, Annu. Rev. Fluid. Mech. **44**, 427 (2011).

[88] R. Fjørtoft, Tellus **5**, 225 (1953).

[89] R. H. Kraichnan, Phys. Fluids **10**, 1417 (1967).

[90] C. E. Leith, Phys. Fluids **11**, 671 (1968).

[91] G. K. Bathchelor, Phys. Fluids **12**, 233 (1969).

[92] R. H. Kraichnan and D. Montgomery, Rep. Prog. Phys. **43**, 547 (1980).

[93] J. Paret and P. Tabeling, Phys. Fluids **10**, 3126 (1998).

[94] S. Chen *et al.*, Phys. Rev. Lett. **96**, 084502 (2006).

[95] *Atmospheric Motion and Ocean Fluid Dynamics*, edited by G. K. Vallis (Cambridge University Press, 2006, Cambridge).

[96] C. Cerretelli and C. H. K. Williamson, J. Fluid. Mech. **475**, 41 (2003).

[97] L. K. Brandt and K. K. Nomura, Phys. Fluids **18**, 051701 (2006).

[98] R. R. Trieling, O. U. Velasco Fuentes, and G. J. F. van Heijst, Phys. Fluids **17**, 087103 (2005).

[99] S. Kida, J. Phys. Soc. Jpn. **50**, 3517 (1981).

[100] G. L. Eyink, Physica D **207**, 91 (2005).

[101] L. N. Howard and R. Krishnamurti, J. Fluid Mech. **170**, 385 (1986).

[102] D. G. Dritschel and D. W. Waugh, Phys. Fluids A **4**, 1737 (1992).

[103] P. S. Marcus, T. Kundu, and C. Lee, Phys. Plasmas **7**, 1630 (2000).

[104] A. Mariotti, B. Legras, and D. G. Dritschel, Phys. Fluids **6**, 3954 (1994).

[105] P. S. Marcus, Annu. Rev. Astron. Astrophys. **31**, 523 (1993).

[106] M. R. Schoeberl, L. R. Lait, P. A. Newman, and J. E. Rosenfield, Journal of Geophysical Research: Atmospheres **97**, 7859 .

[107] T. Leweke and C. Willamson, J. Fluid Mech. **360**, 85 (1998).

[108] S. Le Dizes and F. Laporte, J. Fluid. Mech. **471**, 169 (2002).

[109] R. H. Kraichnan, J. Fluid Mech. **5**, 497 (1959).

[110] A. J. Domaradzki, Phys. Fluids **31**, 2747 (1988).

[111] S. J. Camargo, D. Biskamp, and B. D. Scott, Phys. Plasmas **2**, 48 (1995).

[112] B. D. Scott, in *Plasma Physics: Confinement, Transport and Collective Effects (Lect. Notes Phys. 670)*, edited by A. Dinklage, T. Klinger, G. Marx, and L. Schweikhard (Springer, Berlin Heidelberg, 2005), p. 173.

[113] C. Letellier, Comptes Rendus Mecanqique **345**, 642 (2017).

[114] P. A. Davidson, *Turbulence* (Oxford University Press, Oxford, UK, 2015).

[115] K. Nam, T. M. Antonsen, P. N. Guzdar, and E. Ott, Phys. Rev. Lett. **83**, 3426 (1999).

[116] D. Bernard, Europhys. Lett **50**, 333 (2000).

[117] G. Boffetta, A. Celani, S. Muscacchio, and Vergassola, Phys. Rev. E **66**, 026304 (2002).

[118] A. Okubo, Deep-Sea Res. **17**, 445 (1970).

[119] D. Weiss, Physica D **48**, 273 (1991).

[120] W. B. Daniel and M. A. Rutgers, Phys. Rev. Lett. **89**, 134502 (2002).

[121] P. H. Diamond, S.-I. Itoh, K. Itoh, and T. S. Hahm, Plasma Phys. Controll. Fusion **47**, R35 (2005).

[122] F. H. Busse, Chaos **4**, 123 (1994).

[123] P. S. Marcus and C. Lee, Chaos **4**, 269 (1994).

[124] M. Heimpel, J. Aurnou, and J. Wicht, Nature **438**, 193 (2005).

[125] A. Hasegawa, C. G. Maclennan, and Y. Kodama, Phys. Fluids **22**, 11 (1979).

[126] A. Fujisawa *et al.*, Phys. Rev. Lett. **93**, 165002 (2004).

[127] J. C. Hillesheim *et al.*, Phys. Rev. Lett. **116**, 065002 (2016).

[128] P. H. Diamond and Y. P. Kim, Phys. Fluids, B **3**, 1626 (1991).

[129] A. I. Smolyakov, P. H. Diamond, and M. Malkov, Phys. Rev. Lett. **84**, 491 (2000).

[130] A. I. Smolyakov, P. H. Diamond, and V. I. Shevchenko, Phys. Plasmas **7**, 1349 (2000).

[131] P. H. Diamond *et al.*, Nucl. Fusion **41**, 1067 (2001).

[132] M. A. Malkov and P. H. Diamond, Phys. Plasmas **8**, 3996 (2001).

[133] O. Reynolds, Phil. Trans. R. Soc. A **186**, 123 (1895).

[134] B. Pope, *Turbulent Flows* (Cambridge University, Cambridge, UK, 2000).

[135] K. Avila *et al.*, Science **333**, 192 (2011).

[136] T. S. Hahm and P. H. Diamond, J. Korean Phys. Soc. **73**, 747 (2018).

[137] V. Volterra, Nature **118**, 558 (1926).

[138] I. Shesterikov *et al.*, Nucl. Fusion **52**, 042004 (2012).

[139] M. Ramisch *et al.*, Plasma Phys. Controll. Fusion **49**, 777 (2007).

[140] T. Windisch, O. Grulke, and T. Klinger, J. Nuc. Mat. **390-391**, 395 (2009).

[141] K. W. Gentle, K. Liao, K. Lee, and W. L. Rowan, Plasma Science and Technology **12**, 391 (2010).

[142] P. Manz, M. Ramisch, and U. Stroth, Phys. Rev. Lett. **103**, 165004 (2009).

[143] M. Ramisch *et al.*, Plasma Phys. Controll. Fusion **52**, 124015 (2010).

[144] M. Xu *et al.*, Phys. Rev. Lett. **107**, 055003 (2011).

[145] T. Happel *et al.*, Phys. Plasmas **18**, 102302 (2011).

[146] A. Kendl, Plasma Phys. Controll. Fusion **60**, 025017 (2018).

[147] V. Naulin, A. H. Nielsen, and J. J. Rasmussen, Phys. Plasmas **12**, 122306 (2005).

[148] X. Garbet *et al.*, Physics of Plasmas **14**, 122305 (2007).

[149] K. Ida *et al.*, Nuclear Fusion **55**, 013022 (2015).

[150] F. Hariri *et al.*, Physics of Plasmas **23**, 052512 (2016).

[151] P. Migliano *et al.*, Nuclear Fusion **56**, 014002 (2016).

[152] H. Oertel, *Prandtl's Essentials of Fluid Mechanics* (Springer, New York, Berlin, Heidelberg, 2004), p. 676.

[153] J. Z. Wu, H.-Y. Ma, and M.-D. Zhou, *Vorticity and Vortex Dynamics* (Springer, Berlin, Heidelberg, New York, 2006).

[154] Frisch, *Turbulence* (Cambridge University, Cambridge, 1995).

[155] Z. Yan *et al.*, Phys. Plasmas **18**, 056117 (2011).

[156] B. D. Scott, J. F. Drake, and A. B. Hassam, Phys. Rev. Lett. **54**, 1027 (1985).

[157] W. Guttenfelder *et al.*, Phys. Plasmas **19**, 056119 (2012).

[158] D. Told *et al.*, Phys. Plasmas **16**, 055901 (2008).

[159] B. D. Scott, Phys. Plasmas **12**, 062314 (2005).

[160] T. Görler and F. Jenko, Phys. Rev. Lett. **100**, 185002 (2008).

[161] P. Manz *et al.*, Plasma Phys. Controll. Fusion **56**, 035010 (2014).

[162] U. Stroth, *Plasmaphysik - Phänomene, Grundlagen, Anwendungen* (Vieweg, Teuber, Wiesbaden, 2011).

[163] A. M. Dimits *et al.*, Phys. Plasmas **7**, 969 (2000).

[164] K. Miyamoto, *Fundamentals of Plasma Physics and Controlled Fusion* (NIFS-PROC-48, NIFS, Toki, Japan, 2000).

[165] K. Itoh, S.-I. Itoh, and A. Fukuyama, *Transport and Structural Formation in Plasmas* (IOP, London, England, 1999), chapter 12.

[166] B. D. Scott, New J. Physics **4**, 52 (2002).

[167] S. Maeyama *et al.*, Phys. Rev. Lett. **114**, 255002 (2015).

[168] M. J. Pueschel and F. Jenko, Phys. Plasmas **17**, 062307 (2010).

[169] G. G. Whelan, M. J. Pueschel, and P. W. Terry, Phys. Rev. Lett. **120**, 175002 (2018).

[170] J. Citrin *et al.*, Phys. Rev. Lett. **111**, 155001 (2013).

[171] A. D. Siena *et al.*, Nuclear Fusion **58**, 054002 (2018).

[172] F. Ryter *et al.*, Phys. Rev. Lett. **86**, 5498 (2001).

[173] F. Ryter *et al.*, Phys. Rev. Lett. **85**, 085001 (2005).

[174] J. E. Rice *et al.*, Phys. Rev. Lett. **107**, 265001 (2011).

[175] C. Angioni *et al.*, Nucl. Fusion **52**, 114003 (2012).

[176] W. L. Zhong *et al.*, Phys. Rev. Lett. **111**, 265001 (2013).

[177] A. Casati, C. Bourdelle, X. Garbet, and F. Imbeaux, Phys. Plasmas **15**, 042310 (2008).

[178] H. L. Berk *et al.*, Nucl. Fusion **33**, 263 (1993).

[179] Y. Sarazin *et al.*, J. Nucl. Mater. **313-316**, 796 (2003).

[180] B. Nold *et al.*, New. J. Phys. **14**, 063022 (2012).

[181] T. Happel *et al.*, Phys. Rev. Lett. **102**, 255001 (2009).

[182] G. Fuchert *et al.*, Plasma Phys. Controll. Fusion **55**, 125002 (2013).

[183] S.-I. Itoh, K. Itoh, and M. Yagi, Phys. Rev. Lett. **91**, 045003 (2003).

[184] A. Ishizawa and N. Nakajuma, Phys. Plasmas **17**, 072308 (2010).

[185] M. Muraglia *et al.*, Phys. Rev. Lett. **107**, 095003 (2011).

[186] X. Z. McDevitt, C. J. Tang and Z. Guo, Phys. Rev. Lett. **111**, 205002 (2013).

[187] W. A. Hornsby, Plasma Phys. Controll. Fusion **57**, 054018 (2015).

[188] O. Agullo, Phys. Plasmas **24**, 042308 (2017).

[189] O. Agullo, Phys. Plasmas **24**, 042309 (2017).

[190] A. Kendl, B. D. Scott, and T. T. Ribeiro, Phys. Plasmas **17**, 072302 (2010).

[191] D. Dickinson *et al.*, Plasma Phys. Controll. Fusion **53**, 115010 (2011).

[192] D. Dickinson *et al.*, Phys. Rev. Lett. **108**, 135002 (2012).

[193] D. Hatch *et al.*, Nucl. Fusion **55**, 063028 (2015).

[194] D. Hatch *et al.*, Nucl. Fusion **56**, 104003 (2016).

[195] N. T. Gladd, J. F. Drake, C. L. Chang, and C. S. Liu, Phys. Fluids **23**, 1182 (1980).

[196] A. Diallo *et al.*, Phys. Plasmas **20**, 012505 (2013).

[197] H. Doerk, *Gyrokinetic Simulation of Microtearing Turbulence* (Ph.D thesis, Universität Ulm, 2012).

[198] H. Doerk *et al.*, Phys. Plasmas **19**, 055907 (2012).

[199] S. Maeyama, T.-H. Watanabe, and A. Ishizawa, Phys. Rev. Lett. **119**, 195002 (2017).

[200] M. S. Chu *et al.*, Phys. Rev. Lett. **41**, 247 (1978).

[201] C. Z. Cheng, Phys. Fluids **25**, 1020 (1982).

[202] J. Dong, L. Chen, and F. Zonca, Nucl. Fusion **39**, 1041 (1999).

[203] G. Zhao and L. Chen, Phys. Plasmas **9**, 861 (2002).

[204] G. L. Falchetto, J. Vaclavick, and L. Villard, Phys. Plasmas **10**, 1424 (2003).

[205] P. B. Snyder *et al.*, Nucl. Fusion **51**, 103016 (2011).

[206] P. B. Snyder *et al.*, Phys. Plasmas **19**, 056115 (2012).

[207] B. D. Scott, Plasma Phys. Controll. Fusion **45**, A385 (2003).

[208] P. B. Snyder and G. W. Hammett, Phys. Plasmas **8**, 744 (2001).

[209] W. Horton, D.-I. Choi, and B.-G. Hong, Phys. Fluids **26**, 1461 (1983).

[210] K. Aleynikova and A. Zocco, Phys. Plasmas **24**, 092106 (2017).

[211] W. Horton, Rev. Mod. Physics **71**, 735 (1999).

[212] G. R. Tynan, A. Fujisawa, and G. M. McKee, Plasma Phys. Controll. Fusion **51**, 113001 (2009).

[213] A. Hasegawa and M. Wakatani, Phys. Rev. Lett. **50**, 682 (1983).

[214] A. Hasegawa and H. Mima, Phys. Rev. Lett. **39**, 205 (1977).

[215] J. G. Charney, Geofys. Publ. **17**, 3 (1948).

[216] F. Y. Gang, B. D. Scott, and P. H. Diamond, Phys. Fluids, B **1**, 1331 (1989).

[217] B. D. Scott, Phys. Fluids, B **4**, 2468 (1992).

[218] B. D. Scott, Plasma Phys. Controll. Fusion **34**, 1977 (1992).

[219] B. Kadoch, W. J. Bos, and K. Schneider, Phys. Rev. Lett. **105**, 145001 (2010).

[220] S. Garland, K. Reuther, M. Ramisch, and P. Manz, Phys. Plasmas **24**, 112307 (2017).

[221] B. D. Scott, Contrib. Plas. Phys. **38**, 171 (1998).

[222] B. Scott, Plasma Phys. Controll. Fusion **40**, 823 (1998).

[223] B. D. Scott, New J. Phys. **7**, 92 (2005).

[224] W. Fundamenski and O. E. Garcia, Comparsion of Coulomb collsion rates in the Plasma Physics and Magnetically Confined Fusion Literature, EFDA-JET report R(07)01 (2007).

[225] A. Zeiler, D. Biskamp, J. F. Drake, and P. N. Guzdar, Phys. Plasmas **3**, 2951 (1996).

[226] B. N. Rogers, J. F. Drake, and A. Zeiler, Phys. Rev. Lett. **81**, 4396 (1998).

[227] B. LaBombard *et al.*, Nucl. Fusion **45**, 1658 (2005).

[228] P. N. Guzdar, R. G. Kleva, A. Das, and R. K. Kaw, Phys. Rev. Lett. **87**, 015001 (2001).

[229] M. Z. Tokar, Phys. Rev. Lett. **91**, 095001 (2003).

[230] V. Naulin *et al.*, Phys. Plasmas **12**, 052515 (2005).

[231] A. Kendl and B. D. Scott, Phys. Plasmas **12**, 064506 (2005).

[232] W. Dorland and G. W. Hammett, Phys. Fluids, B **5**, 812 (1993).

[233] M. A. Beer and G. W. Hammett, Phys. Plasmas **3**, 4046 (1996).

[234] B. D. Scott, Phys. Plasmas **7**, 1845 (2000).

[235] D. Strintzi and B. D. Scott, Phys. Plasmas **11**, 5452 (2004).

[236] D. Strintzi, B. D. Scott, and A. J. Brizard, Phys. Plasmas **12**, 052517 (2005).

[237] B. D. Scott, Phys. Plasmas **17**, 102306 (2010).

[238] S. I. Braginskii, *Reviews of Plasma Physics, edited by M. A. Leontovich* (Consultants Bureau, New York, 1965).

[239] W. Suttrop and A. G. Peeters, IPP report 1/306 (1997).

[240] S. K. Rathgeber *et al.*, Plasma Phys. Controll. Fusion **55**, 025004 (2013).

[241] I. G. J. Classen *et al.*, Rev. Sci. Instrum. **81**, 10D929 (2010).

[242] M. Griener *et al.*, Review of Scientific Instruments **88**, 033509 (2017).

[243] S. J. Freethy *et al.*, Review of Scientific Instruments **87**, 11E102 (2016).

[244] T. Pütterich *et al.*, Phys. Rev. Lett. **102**, 025001 (2009).

[245] E. Viezzer, T. Pütterich, R. Dux, and R. M. McDermott, Rev. Sci. Instrum. **83**, 103501 (2012).

[246] M. Cavedon *et al.*, Rev. Sci. Instrum. **88**, 043103 (2017).

[247] M. Kočan and J. P. Gunn, Plasma Phys. Controll. Fusion **52**, 045010 (2010).

[248] S. Enge *et al.*, Phys. Rev. Lett. **105**, 175004 (2010).

[249] S. Chakraborty Thakur *et al.*, Rev. Sci. Instrum. **83**, 10D708 (2012).

[250] N. Mahdizadeh *et al.*, Plasma Phys. Controll. Fusion **47**, 569 (2005).

[251] J. Horacek *et al.*, Nucl. Fusion **50**, 105001 (2010).

[252] F. Gennrich and A. Kendl, Plasma Phys. Controll. Fusion **54**, 015012 (2012).

[253] O. Grover *et al.*, Rev. Sci. Instrum. **88**, 063501 (2017).

[254] J. Adamek *et al.*, Contr. Plasma Phys. **50**, 854 (2010).

[255] J. Adamek *et al.*, Rev. Sci. Instrum. **87**, 043510 (2016).

[256] D. Prisiazhniuk *et al.*, Plasma Phys. Controll. Fusion **59**, 025013 (2016).

[257] T. Happel *et al.*, Plasma Phys. Controll. Fusion **59**, 054009 (2017).

[258] Z. Yan *et al.*, Phys. Rev. Lett. **112**, 125002 (2014).

[259] E. Wolfrum *et al.*, Rev. Sci. Instrum. **64**, 2285 (1993).

[260] M. Willensdorfer *et al.*, Plasma Phys. Controll. Fusion **56**, 025008 (2014).

[261] J. Schweinzer *et al.*, Plasma Phys. Controll. Fusion **34**, 1173 (1992).

[262] R. Fischer, E. Wolfrum, J. Schweinzer, and the ASDEX Upgrade Team, Plasma Phys. Controll. Fusion **50**, 085009 (2008).

[263] G. Birkenmeier *et al.*, Plasma Phys. Controll. Fusion **56**, 075019 (2014).

[264] I. Cziegler, J. L. Terry, J. W. Hughes, and B. LaBombard, Phys. Plasmas **17**, 056120 (2010).

[265] Y. Sechrest *et al.*, Phys. Plasmas **18**, 022306 (2011).

[266] Y. Sechrest, T. Munsat, D. J. Battaglia, and S. J. Zweben, Nucl. Fusion **52**, 123009 (2012).

[267] S. C. Liu *et al.*, Rev. Sci. Instrum. **83**, 123506 (2012).

[268] I. Shesterikov *et al.*, Rev. Sci. Instrum. **84**, 053501 (2013).

[269] I. Shesterikov *et al.*, Phys. Rev. Lett. **111**, 055006 (2013).

[270] I. Cziegler *et al.*, Plasma Phys. Controll. Fusion **56**, 075013 (2014).

[271] I. Cziegler *et al.*, Nucl. Fusion **55**, 083007 (2015).

[272] I. Cziegler *et al.*, Phys. Rev. Lett. **118**, 105003 (2017).

[273] S. J. Zweben, J. L. Terry, D. P. Stotler, and R. J. Maqueda, Rev. Sci. Instrum. **88**, 041101 (2017).

[274] G. Fuchert *et al.*, Plasma Phys. Controll. Fusion **56**, 125001 (2014).

[275] P. Manz *et al.*, Phys. Rev. Lett. **107**, 195004 (2011).

[276] E. J. Strait, E. D. Fredrickson, J.-M. Moret, and M. Takechi, Fusion Sci. Technol. **53**, 304 (2008).

[277] I. H. Hutchinson, *Principles of Plasma Diagnostics* (Cambridge University Press, Cambridge, 2005).

[278] L. M. Shao *et al.*, Plasma Phys. Controll. Fusion **55**, 105006 (2013).

[279] T. Kobayashi *et al.*, Rev. Sci. Instrum. **85**, 083507 (2014).

[280] G. Zhao and L. Chen, Phys. Rev. E **79**, 046316 (2009).

[281] D. Prisiazhniuk *et al.*, Plasma Phys. Controll. Fusion **60**, 075003 (2018).

[282] R. Balescu, *Aspects of Anormalous Transport in Plasmas* (IoP, 2005, Bristol, Philadelphia).

[283] T. Munsat and S. J. Zweben, Rev. Sci. Instrum. **77**, 103501 (2006).

[284] J. R. Myra *et al.*, Nucl. Fusion **53**, 073013 (2013).

[285] J. C. Crocker and D. G. Grier, J. Colloidal Interface Sci. **179**, 298 (1996).

[286] F. M. Laggner *et al.*, Plasma Phys. Controll. Fusion **58**, 065005 (2016).

[287] F. Mink *et al.*, Plasma Phys. Controll. Fusion **58**, 125013 (2016).

[288] A. Mink *et al.*, Nucl. Fusion **58**, 026011 (2018).

[289] M. Kočan *et al.*, Plasma Phys. Controll. Fusion **54**, 085009 (2012).

[290] M. Kočan *et al.*, Nucl. Fusion **52**, 023016 (2012).

[291] D. M. Jenkins and D. G. watts, *Spectral analysis and its applications* (Holden-Day, San Francisco, 1968).

[292] H. L. Pecseli, *Fluctuations in Physical Systems* (Cambridge University Press, Cambridge, 2000).

[293] H. J. Harker and Ilić, Rev. Sci. Instrum. **45**, 1315 (1974).

[294] Y. Nagashima *et al.*, Plasma Phys. Controll. Fusion **49**, 1611 (2007).

[295] J. M. Beall, Y. C. Kim, and E. J. Powers, J. Appl. Phys. **53**, 3933 (1982).

[296] N. Mahdizadeh *et al.*, Phys. Plasmas **11**, 3932 (2004).

[297] Y. K. Kim and E. J. Powers, Phys. Fluids **21**, 1452 (1978).

[298] Y. K. Kim and E. J. Powers, IEEE Transactions on Plasma Science **PS-7**, 120 (1979).

[299] M. Ramisch, *Bispektralanalyse turbulenter Fluktuationen am Experiment TEDDI* (Diplomarbeit, Christian-Albrechts-Universität Kiel, 2001).

[300] H. L. Pecseli and J. Trulsen, Plasma Phys. Controll. Fusion **35**, 1701 (1993).

[301] R. A. Moyer, G. R. Tynan, C. Holland, and M. J. Burin, Phys. Rev. Lett. **87**, 135001 (2001).

[302] G. S. Xu, B. N. Wan, M. Song, and J. Li, Phys. Rev. Lett. **91**, 125001 (2003).

[303] Y. Nagashima *et al.*, Phys. Rev. Lett. **95**, 095002 (2005).

[304] K. J. Zhao *et al.*, Phys. Rev. Lett. **96**, 255004 (2006).

[305] A. Fujisawa *et al.*, Plasma Phys. Controll. Fusion **49**, 211 (2007).

[306] H. Xia and M. G. Shats, Phys. Rev. Lett. **91**, 155001 (2003).

[307] T. Yamada, Plasma Phys. Controll. Fusion **17**, 052313 (2010).

[308] M. Xu *et al.*, Phys. Rev. Lett. **108**, 245001 (2012).

[309] C. P. Ritz *et al.*, Phys. Rev. Lett. **62**, 1844 (1989).

[310] C. P. Ritz, E. J. Powers, and R. D. Bengston, Phys. Fluids, B **1**, 153 (1989).

[311] J. S. Kim *et al.*, Phys. Plasmas **3**, 3998 (1996).

[312] D. A. Baver and P. W. Terry, Phys. Plasmas **12**, 042303 (2005).

[313] D. A. Baver, P. W. Terry, and C. Holland, Phys. Plasmas **16**, 032309 (2009).

[314] D. Biskamp, *Magnetohydrodynamic Turbulence* (Cambridge University, Cambridge, 2003).

[315] D. C. Leslie, *Developments in the theory of turbulence* (Clarendon Press, Oxford, 1973).

[316] M. D. Millionshchikov, C. R. Acad. Sci. U.S.S.R. **32**, 615 (1941).

[317] H. Xia and M. G. Shats, Phys. Plasmas **11**, 561 (2004).

[318] C. Holland *et al.*, Phys. Plasmas **14**, 056112 (2007).

[319] Y. Nagashima *et al.*, Phys. Plasmas **16**, 020706 (2009).

[320] C.-Y. An, B. Min, and C.-B. Kim, Plasma Phys. Controll. Fusion **59**, 115006 (2017).

[321] C.-B. Kim, C.-Y. An, and B. Min, Scientific Reports **8**, 8622 (2018).

[322] V. Naulin and K. H. Spatschek, Phys. Rev. E **55**, 5883 (1997).

[323] M. Wakatani and A. Hasegawa, Phys. Fluids **27**, 611 (1984).

[324] C. H. Bruneau, P. Fischer, and H. Kellay, EPL **78**, 34002 (2007).

[325] T. Klinger *et al.*, Plasma Phys. Controll. Fusion **39**, B145 (1997).

[326] M. J. Burin *et al.*, Phys. Plasmas **12**, 052320 (2006).

[327] F. Brochard, E. Gravier, and G. Bonhomme, Phys. Rev. E **73**, 036403 (2006).

[328] F. M. Poli, M. Posesta, and A. Fasoli, Phys. Plasmas **14**, 052311 (2006).

[329] U. Krauschke and H. Schluter, Plasma Phys. Controll. Fusion **32**, 1149 (1990).

[330] D. L. Jasby, Phys. Fluids **15**, 1590 (1972).

[331] F. M. Poli, M. Podesta, and A. Fosoli, Phys. Plasmas **14**, 052311 (2007).

[332] B. A. Grierson, M. W. Worsek, and M. E. Mauel, Phys. Plasmas **16**, 055902 (2009).

[333] G. R. Tynan *et al.*, Plasma Phys. Controll. Fusion **48**, S51 (2006).

[334] Z. Yan *et al.*, Phys. Plasmas **17**, 032302 (2010).

[335] V. Naulin, New J. Phys. **4**, 28 (2002).

[336] I. M. Held, WHOI proceedings (2000).

[337] P. H. Diamond *et al.*, Plasma Phys. Controll. Fusion **50**, 124018 (2008).

[338] E. Sánchez *et al.*, J. Nucl. Mat. **337**, 296 (2005).

[339] B. Gonçalves *et al.*, Phys. Rev. Lett. **96**, 145001 (2006).

[340] A. Fujisawa *et al.*, Nucl. Fusion **47**, S718 (2007).

[341] S. Oldenbürger, F. Brochard, and G. Bonhomme, Phys. Plasmas **18**, 032307 (2011).

[342] T. Kobayashi *et al.*, Plasma Fusion Res. **6**, 2401082 (2011).

[343] Ö. D. Gürcan, P. H. Diamond, T. S. Hahm, and Z. Lin, Phys. Plasmas **12**, 032303 (2005).

[344] T. Estrada, C. Hidalgo, and T. Happel, Nucl. Fusion **51**, 032001 (2011).

[345] G. D. Conway *et al.*, Plasma Phys. Controll. Fusion **46**, 951 (2004).

[346] M. Hirsch *et al.*, Plasma Phys. Controll. Fusion **43**, 1641 (2001).

[347] G. D. Conway *et al.*, Nucl. Fusion **46**, S799 (2006).

[348] T. Happel *et al.*, Physics of Plasmas **22**, 032503 (2015).

[349] L. Vermare *et al.*, Physics of Plasmas **18**, 012306 (2011).

[350] A. B. Navarro *et al.*, Phys. Plasmas **22**, 042513 (2015).

[351] G. I. Taylor, Proc. R. Soc. London Ser. **A164**, 476 (1938).

[352] C. C. Lin, Q. Appl. Maths. **10**, 295 (1953).

[353] B. B. Kadomtsev, *Plasma Turbulence* (Academic, New York, 1965), p. chapter 3.

[354] J. A. Krommes, Phys. Rep. **360**, 1 (2002).

[355] S. Nazarenko, *Wave turbulence* (Springer, Heidelberg Dordrecht London New York, 2011).

[356] V. V. Bulanin and M. V. Yafanov, Plasma Phys. Rep. **32**, 47 (2006).

[357] T. Happel, E. Blanco, and T. Estrada, Rev. Sci. Instrum. **81**, 10D901 (2010).

[358] G. D. Conway *et al.*, Plasma Phys. Controll. Fusion **47**, 1165 (2005).

[359] B. D. Scott, Phys. Rev. Lett. **65**, 3289 (1990).

[360] P. H. Diamond, Y. M. Liang, B. A. Carreras, and P. W. Terry, Phys. Rev. Lett. **72**, 2565 (1994).

[361] E. Kim and P. H. Diamond, Phys. Rev. Lett. **90**, 185006 (2003).

[362] G. D. Conway *et al.*, Phys. Rev. Lett. **106**, 065001 (2011).

[363] T. Estrada *et al.*, Europhys. Lett. **92**, 35001 (2010).

[364] G. S. Xu *et al.*, Phys. Rev. Lett. **107**, 125001 (2011).

[365] L. Schmitz *et al.*, Phys. Rev. Lett. **108**, 155002 (2012).

[366] K. Miki *et al.*, Phys. Plasmas **19**, 092306 (2012).

[367] A. Fujisawa *et al.*, Plasma Phys. Controll. Fusion **48**, A365 (2006).

[368] A. D. Liu *et al.*, Phys. Rev. Lett. **103**, 095002 (2009).

[369] G. S. Xu *et al.*, Nuclear Fusion **51**, 072001 (2011).

[370] W. Zhang *et al.*, Rev. Sci. Instrum. **81**, 113501 (2010).

[371] C. Hidalgo *et al.*, Europhys. Lett. **87**, 55002 (2009).

[372] K. H. Burrell *et al.*, Plasma Phys. Controll. Fusion **38**, 1313 (1996).

[373] R. A. Moyer *et al.*, Phys. Plasmas **2**, 2397 (1995).

[374] G. Birkenmeier *et al.*, Nucl. Fusion **56**, 086009 (2016).

[375] S. H. Müller *et al.*, Phys. Plasmas **21**, 042301 (2014).

[376] J. Cheng *et al.*, Nucl. Fusion **53**, 093008 (2013).

[377] E. R. Solano *et al.*, Proc. of the 40^{th} Europ. Conf. on Plasma Physics, Espoo, Finland P4.111 (2013).

[378] E. R. Solano *et al.*, Nucl. Fusion **57**, 022021 (2017).

[379] A. Y. Yashin *et al.*, Nucl. Fusion **58**, 112009 (2018).

[380] Y. Igitkhanov, O. Pogutse, G. Janeschitz, and J. Cordy, Contrib. Plasma Phys. **40**, 368 (2000).

[381] D. Constantintinescu *et al.*, Phys. Plasmas **18**, 062307 (2011).

[382] O. Grover *et al.*, Nucl. Fusion **58**, 112010 (2018).

[383] F. Pesamosca, *A model for dynamical oscillations in magnetically confined fusion plasmas at the transition to high confinement* (Master thesis, Politecnico di Milano, Milan, Italy, 2015).

[384] Y. Camenen *et al.*, Phys. Plasmas **16**, 062501 (2009).

[385] J. Ball *et al.*, Plasma Phys. Controll. Fusion **56**, 095014 (2014).

[386] T. Watari *et al.*, Phys. Plasmas **12**, 062304 (2005).

[387] T. E. Stringer, Phys. Rev. Lett. **22**, 770 (1969).

[388] A. B. Hassam and J. F. Drake, Phys. Fluids, B **5**, 4022 (1993).

[389] G. D. Conway *et al.*, Plasma Phys. Controll. Fusion **50**, 055009 (2008).

[390] ASDEX team, Nucl. Fusion **29**, 1959 (1989).

[391] J. Sniper *et al.*, Nucl. Fusion **36**, 1217 (1996).

[392] A. E. Hubbard *et al.*, Plasma Phys. Controll. Fusion **40**, 689 (1998).

[393] K. H. Burrell, Phys. Plasmas **4**, 1499 (1997).

[394] A. Kendl and B. D. Scott, Phys. Rev. Lett. **90**, 035006 (2003).

[395] T. S. Hahm and K. H. Burrell, Phys. Plasmas **2**, 1648 (1995).

[396] T. S. Hahm *et al.*, Nucl. Fusion **53**, 093005 (2013).

[397] H. Sugama and W. Horton, Phys. Plasmas **1**, 345 (1994).

[398] N. Fedorczak, P. H. Diamond, G. R. Tynan, and P. Manz, Nucl. Fusion **52**, 103013 (2012).

[399] A. Stegmeir *et al.*, Plasma Phys. Controll. Fusion **60**, 035005 (2018).

[400] B. D. Scott, Contrib. Plasma Phys. **46**, 714 (2006).

[401] N. Fedorczak *et al.*, Plasma Phys. Controll. Fusion **55**, 124024 (2013).

[402] D. Farina, R. Pozzoli, and D. D. Ryutov, Nucl. Fusion **9**, 1315 (1993).

[403] A. Zeiler, J. F. Drake, and B. Rogers, Phys. Plasmas **4**, 2134 (1997).

[404] G. R. Tynan *et al.*, Nucl. Fusion **53**, 073053 (2013).

[405] K. Miki *et al.*, Phys. Rev. Lett. **110**, 195002 (2013).

[406] G. Y. Park *et al.*, Phys. Plasmas **22**, 032505 (2015).

[407] B. Li *et al.*, Physics of Plasmas **24**, 055905 (2017).

[408] C. S. Chang *et al.*, Phys. Rev. Lett. **118**, 175001 (2017).

[409] S. Ku *et al.*, Phys. Plasmas **25**, 056107 (2018).

[410] T. Kobayashi *et al.*, Phys. Rev. Lett. **111**, 035002 (2013).

[411] J. Cheng *et al.*, Phys. Rev. Lett. **110**, 265002 (2013).

[412] K. Itoh *et al.*, Plasma Phys. Controll. Fusion **57**, 092001 (2015).

[413] A. Diallo, S. Banerjee, S. J. Zweben, and T. Stoltzfus-Dueck, Nucl. Fusion **57**, 066050 (2017).

[414] A. Medvedeva *et al.*, Plasma Phys. Controll. Fusion **59**, 125014 (2017).

[415] R. Wilcox *et al.*, Nucl. Fusion **56**, 036002 (2016).

[416] A. E. White *et al.*, Nucl. Fusion **51**, 113005 (2011).

[417] C. Fanack *et al.*, Plasma Phys. Controll. Fusion **38**, 1915 (1996).

[418] H. Qin, W. M. Tang, and G. Rewoldt, Physics of Plasmas **6**, 2544 (1999).

[419] P. Lauber, S. Günter, A. Könies, and S. D. Pinches, Journal Of Computational Physics **226**, 447 (2007).

[420] J. Cheng *et al.*, Nuclear Fusion **54**, 114004 (2014).

[421] C. Wahlberg, Plasma Phys. Controll. Fusion **51**, 085006 (2009).

[422] C. A. de Meijere *et al.*, Plasma Phys. Controll. Fusion **56**, 072001 (2014).

[423] N. Chakrabarti *et al.*, Phys. Plasmas **15**, 112310 (2008).

[424] T. Happel *et al.*, Nucl. Fusion **56**, 064004 (2016).

[425] V. V. Bulanin *et al.*, Technical Physics Letters **37**, 340 (2011).

[426] M. Bernert *et al.*, Rev. Sci. Instrum. **85**, 033503 (2014).

[427] T. Happel *et al.*, Nuclear Fusion and Energy submitted (2018).

[428] A. Fujisawa *et al.*, Plasma Phys. Controll. Fusion **48**, S31 (2006).

[429] T. Ido *et al.*, Nucl. Fusion **46**, 512 (2006).

[430] A. V. Melnikov *et al.*, Plasma Phys. Controll. Fusion **48**, S87 (2006).

[431] Y. Hamada *et al.*, Plasma Phys. Controll. Fusion **48**, S177 (2006).

[432] J. Cheng *et al.*, Nucl. Fusion **49**, 085030 (2009).

[433] J. R. Robinson *et al.*, Plasma Phys. Controll. Fusion **54**, 105007 (2012).

[434] J. C. Hillesheim *et al.*, Phys. Plasmas **19**, 022301 (2012).

[435] A. Storelli *et al.*, Physics of Plasmas **22**, 062508 (2015).

[436] C. Silva *et al.*, Nucl. Fusion **56**, 106026 (2016).

[437] V. Bulanin *et al.*, Nuclear Fusion **56**, 016017 (2016).

[438] A. D. Gurchenko *et al.*, Plasma Phys. Controll. Fusion **58**, 044002 (2016).

[439] V. V. Bulanin *et al.*, Plasma Phys. Controll. Fusion **58**, 045006 (2016).

[440] K. Miki, Y. Y. Kishimoto, N. Miyato, and J. Q. Li, Phys. Rev. Lett. **99**, 145003 (2007).

[441] T. Kobayashi *et al.*, Phys. Plasmas **22**, 112301 (2015).

[442] E. Balkovsky, G. Falkovich, I. Kolokolov, and L. V., Phys. Rev. Lett. **78**, 1452 (1997).

[443] A. Diallo *et al.*, Phys. Rev. Lett. **112**, 115001 (2014).

[444] J. Boedo *et al.*, Phys. Plasmas **8**, 4826 (2001).

[445] G. Y. Antar, G. Counsell, Y. Yang, and P. Devynck, Phys. Plasmas **10**, 419 (2003).

[446] Y. H. Xu, S. Jachmich, and R. R. Weynats, Plasma Phys. Controll. Fusion **47**, 1841 (2005).

[447] J. Cheng *et al.*, Plasma Phys. Controll. Fusion **52**, 055003 (2010).

[448] O. Grulke, J. L. Terry, B. LaBombard, and S. J. Zweben, Phys. Plasmas **13**, 012306 (2006).

[449] S. Krasheninnikov, Phys. Lett. A **283**, 368 (2001).

[450] O. E. Garcia *et al.*, Plasma Physics and Controlled Fusion **48**, L1 (2006).

[451] S. H. Müller *et al.*, Phys. Plasmas **14**, 110704 (2007).

[452] D. Jovanovic, P. K. Shukla, and F. Pegorano, Phys. Plasmas **15**, 112305 (2008).

[453] N. Bisai and P. K. Kaw, Phys. Plasmas **20**, 042509 (2013).

[454] R. M. Churchill, C. S. Chang, S. Ku, and J. Dominski, Plasma Phys. Controll. Fusion **59**, 105014 (2017).

[455] G. Birkenmeier *et al.*, Nucl. Fusion **55**, 033018 (2015).

[456] T. Eich *et al.*, Phys. Rev. Lett. **107**, 215001 (2011).

[457] R. J. Goldston, Nucl. Fusion **52**, 013009 (2012).

[458] J. R. Myra, D. A. D'Ippolito, and D. A. Russell, Phys. Plasmas **22**, 042516 (2015).

[459] S. Krasheninnikov and A. Smolyakov, Phys. Plasmas **15**, 055909 (2008).

[460] S. I. Krasheninnikov, D. A. D'Ippolito, and J. R. Myra, J. Plasma Phys. **74**, 679 (2008).

[461] D. A. D'Ippolito, J. R. Myra, and S. J. Zweben, Phys. Plasmas **18**, 060501 (2011).

[462] W. Fundamenski, W. Sailer, and JET EFDA contributors, Plasma Phys. Controll. Fusion **46**, 233 (2004).

[463] O. E. Garcia, N. H. Bian, and W. Fundamenski, Phys. Plasmas **13**, 082309 (2006).

[464] R. Kube and O. E. Garcia, Phys. Plasmas **18**, 102314 (2011).

[465] C. Theiler *et al.*, Phys. Rev. Lett. **103**, 065001 (2009).

[466] S. H. Müller *et al.*, Plasma Phys. Controll. Fusion **51**, 055020 (2009).

[467] I. Furno *et al.*, Phys. Rev. Lett. **106**, 245001 (2011).

[468] S. Elmore *et al.*, Plasma Phys. Controll. Fusion **54**, 065001 (2012).

[469] A. Schmid, A. Herrmann, H. W. Müller, and the ASDEX Upgrade Team, Plasma Phys. Controll. Fusion **50**, 045007 (2008).

[470] P. C. Stangeby and A. W. Leonard, Nucl. Fusion **51**, 063001 (2011).

[471] J. Madsen *et al.*, Phys. Plasmas **18**, 112504 (2011).

[472] N. Bisai, R. Singh, and P. K. Kaw, Phys. Plasmas **19**, 052509 (2012).

[473] B. D. Scott, Phys. Plasmas **14**, 102318 (2007).

[474] A. Pakyari and V. P. Pavlenko, Phys. Plasmas **3**, 3628 (1996).

[475] A. I. Smolyakov, J. Can. Phys. **76**, 1998 (1998).

[476] J. Olsen *et al.*, Plasma Phys. Controll. Fusion **58**, 044011 (2016).

[477] M. Held, M. Wiesenberger, J. Madsen, and A. Kendl, Plasma Phys. Controll. Fusion **56**, 126005 (2016).

[478] R. Kube *et al.*, J. Nucl. Mater. **438**, S505 (2013).

[479] S. J. Zweben *et al.*, Phys. Plasmas **16**, 082505 (2009).

[480] J. R. Angus, M. V. Umansky, and S. I. Krasheninnikov, Phys. Rev. Lett. **108**, 215002 (2012).

[481] G. S. Xu *et al.*, Phys. Plasmas **17**, 022501 (2010).

[482] I. Furno *et al.*, Phys. Rev. Lett. **100**, 055004 (2008).

[483] G. S. Xu *et al.*, Nuclear Fusion **49**, 092002 (2009).

[484] R. A. Pitts *et al.*, J. Nucl. Mater. **438**, 48 (2013).

[485] B. LaBombard *et al.*, Phys. Plasmas **8**, 2107 (2001).

[486] D. Rudakov *et al.*, Nuclear Fusion **45**, 1589 (2005).

[487] O. E. Garcia *et al.*, Journal of Nuclear Materials **363-365**, 575 (2007).

[488] J. R. Myra, D. A. Russell, and D. A. D'Ippolito, Physics of Plasmas **13**, 112502 (2006).

[489] D. Carralero *et al.*, Nucl. Fusion **54**, 123005 (2014).

[490] S. Potzel *et al.*, Nucl. Fusion **54**, 013001 (2014).

[491] D. Carralero *et al.*, Nucl. Fusion **57**, 056044 (2017).

[492] D. Carralero *et al.*, Nucl. Mat. and Energy **12**, 1189 (2017).

[493] D. Carralero *et al.*, Phys. Rev. Lett. **115**, 215002 (2015).

[494] M. Wiesenberger, J. Madsen, and A. Kendl, Phys. Plasmas **21**, 092301 (2014).

[495] L. Aho-Mantila *et al.*, Plasma Phys. Controll. Fusion **59**, 035003 (2017).

[496] V. Nikolaeva *et al.*, Plasma Phys. Controll. Fusion **60**, 055009 (2018).

[497] P. Manz *et al.*, Nucl. Mater. Energy **12**, 1152 (2017).

[498] N. Vianello *et al.*, Phys. Rev. Lett. **106**, 125002 (2011).

[499] H. W. Müller *et al.*, Nucl. Fusion **42**, 301 (2002).

[500] N. R. Walkden *et al.*, Nucl. Fusion **55**, 113022 (2015).

[501] R. Häcker, G. Fuchert, D. Carralero, and P. Manz, Phys. Plasmas **25**, 012315 (2018).

[502] B. Nold *et al.*, Phys. Plasmas **21**, 102304 (2014).

[503] S. Rath and S. Sridhar, Phys. Fluids B **4**, 1367 (1992).

[504] T. Windisch, O. Grulke, and T. Klinger, Phys. Plasmas **13**, 122303 (2006).

[505] G. Y. Antar, J. H. Yu, and G. R. Tynan, Phys. Plasmas **14**, 022301 (2007).

[506] D. C. Pace *et al.*, Phys. Plasmas **15**, 122304 (2008).

[507] J. A. Boedo *et al.*, Physics of Plasmas **10**, 1670 (2003).

[508] B. Nold *et al.*, Plasma Phys. Controll. Fusion **52**, 065005 (2010).

[509] N. Yan *et al.*, Plasma Phys. Controll. Fusion **55**, 115007 (2013).

[510] N. Fedorczak *et al.*, Nucl. Mat. and Energy **12**, 838 (2017).

[511] G. Fuchert *et al.*, Plasma Phys. Controll. Fusion **58**, 054006 (2016).

[512] R. Wenninger *et al.*, Nucl. Fusion **57**, 046002 (2017).

[513] D. A. D'Ippolito and J. R. Myra, Phys. Plasmas **10**, 4029 (2003).

[514] A. Y. Aydemir, Phys. Plasmas **12**, 062503 (2005).

[515] J. Seidl *et al.*, Proceedings of the 45th EPS Conference on Plasma Physics, Prague P1.1103 (2018).

[516] R. Schrittwieser *et al.*, Plasma Phys. Controll. Fusion **44**, 567 (2002).

[517] J. Gunn, Plasma Phys. Controll. Fusion **54**, 085007 (2012).

[518] P. Lauber, Physics Reports **533**, 33 (2013).

[519] F. Zonca, L. Chen, and R. Santoro, Plasma Physics and Controlled Fusion **38**, 2011 (1996).

[520] F. Zonca *et al.*, Nuclear Fusion **49**, 085009 (2009).

[521] P. Lauber *et al.*, Plasma Physics and Controlled Fusion **51**, 124009 (2009).

[522] H. Sugama and T.-H. Watanabe, Journal of Plasma Physics **72**, 825 (2006).

[523] H. Sugama and T.-H. Watanabe, Journal of Plasma Physics **74**, 139 (2008).

[524] S. D. Pinches *et al.*, Computer Physics Communications **111**, 133 (1998).

[525] M. H. Nasim, T. Rafiq, and M. Persson, Plasma Phys. Controll. Fusion **46**, 193 (2004).

[526] A. H. Boozer, Phys. Plasmas **24**, 1999 (1981).

[527] S. Hamada, Nucl. Fusion **2**, 23 (1962).

[528] J. Peer, *Magnetic Field structure and non-axisymmetric resonant magnetic perturbations in gyrofluid simulations of tokamak edge plasmas* (PhD thesis, University Innsbruck, Innsbruck, Austria, 2013).

[529] B. D. Scott, Phys. Plasmas **8**, 447 (2001).

[530] T. T. Ribeiro and B. Scott, Plasma Phys. Controll. Fusion **50**, 055007 (2008).

[531] T. T. Ribeiro and B. Scott, Plasma Phys. Controll. Fusion **47**, 1657 (2005).

Index

Acknowledgements

For enabling the possibility to write my 'Habilitation' I thank my 'Fachmentorat' Ulrich Stroth, Andreas Bausch and Eric Sonnendrücker. I am profoundly grateful to Ulrich Stroth, who already supervised my PhD thesis in Stuttgart, and with whom I had the honor and the pleasure to work with also in the recent years. He has become a constant role model as a scientist, teacher and leader. Furthermore, he has always been a valuable adviser in any regard. I thank Bruce Scott, who developed not only the physical basis of this work (DALF and GEM model) but also the GEMR code, which he made available to me. The here presented work is mainly build upon the spirit of his work.

I own very much to my colleagues, many of them friends now, without their support and direct or indirect contribution this work would not have been possible. I am honored to have and had the possibility to collaborate with these gifted researchers from whom I was able to learn and improve my research skills. But I am also honored by their friendship. In particular in this regard I thank my former fellow students Alf Köhn and Tim Happel. We have not always worked at the same place, but that we are still in the plasma community together gives me a kind of family feeling. Next I want to thank Gregor Birkenmeier for his friendship and continuous support, I know him also from my PhD time in Stuttgart and we have been colleagues since I arrived in Garching.

I thank George Tynan for incorporating me into his group in UCSD. He guided me openly and friendly. He found the right mix between project oriented work and the freedom to just try something out. Due to the small working group, we post-docs tied together and have done huge progress. I want to thank Saikat Chakraborty Thakur for keeping the machine running, helping me with carrying out experiments, the probe construction and for the enjoyable coffee brakes, Nicolas Fedorczak for our endless inspiring discussions and analytic modeling, Min Xu for his organization talent and helpful support whenever needed regarding scientific and non-scientific problems. I thank Istvan Cziegler for insights on I-mode physics, Christian Brandt and my best man Timo Dittmar for their friendship. I thank Guosheng Xu for providing the data from EAST and Achim von Keudell for providing data from fluorocarbon thin-film deposition experiments. Finally, I am honored that the virtuosic scientist Patrick Diamond has been my co-supervisor. Thanks again to George Tynan for this exciting and inspiring experience.

Here in Garching, I started to work in the group of Elisabeth Wolfrum. She guided the group in a very competent and cordial way. Her positive attitude and enthusiasm have been always motivating. First, I worked on scrape-off layer physics, where I teamed up with Daniel Carralero and we could

enhance the visibility of scape-off layer related work in ASDEX Upgrade. He has been my main collaborator at ASDEX Upgrade for several years and it was a pleasure to work with him. Regarding the scrape-off layer work I also want to thank Golo Fuchert and Gregor Birkenmeier. Subsequently I could explore different topics. I thank Julian Boom, Ivo Classen for introducing me to the ECE data. For our work on the I-phase I acknowledge in particular Gregor Birkenmeier and Marco Cavedon, for our work on the I-mode Tim Happel and for our work on divertor phenomena Steffen Potzel and Marco Wischmeier. It is clear that experimental work is always a broader team effort. I thank the plasma edge physics group, in particular Florian Laggner, Felician Mink, Michael Griener, Georg Harrer and Branka Vanovac, the turbulence group, in particular Tim Happel, Garrard Conway, Dmitrii Prisiazhniuk, Valentina Nikolaeva, Anna Medvedeva, Pascale Hennequin, the IST reflectometry team around Carlos Silva and of course the ASDEX Upgrade team. For help from the theory side I thank in particular Tiago Ribeiro, Philipp Lauber, Alexander Kendl, Alessandro Biancalani, Klaus Hallatschek and Andreas Stegmeir. For our recent work on the density limit and power exhaust related physics I want to thank Thomas Eich. The collaboration with him is quite fun and has been very motivating for me in the last year. Regarding my recent work I also want to thank Ulrich Stroth again, allowing me to built a water turbulence experiment at IPP. I thank Simon Sebold for deciding doing the related Master thesis and Rodrigo Arredondo Parra for helping us within this project.

Sometimes low temperature plasma experiments are more suitable to study phenomena in plasma turbulence. I have been very lucky that I could keep a constant collaboration with my former supervisor Mirko Ramisch form the university in Stuttgart. He and his team, particularly Bernhard Schmid, Stephen Garland and Til Ullmann carried out such experiments.

Teaching is an important part of the habilitation process. For help regarding the associated exercises I thank in particular Merlin Mitschek, Maximilian Jokel, Martin Uphoff and Ivan Erofeev. I thank Philipp Lauber for doing the plasma physics seminar with me year by year. I thank all students coming to my lectures, seminars and exercises every week. I thank the Bachelor and Master students who conducted their thesis with me, in particular I want to thank Federico Pesamosca and Paul Heinrich. I did a two-year pedagogical training at TUM, which helped me improving my educational skills. I would like to thank our trainers around Annette Spiekermann and all participants of the ProLehreIntensiv course, in particular my task force Anna Cattani-Scholz, Mirza Cokoja and Sabine Schneider. Since several years I am study supervisor of the Garching division of the PhD Helmholtz graduate school for plasma physics. This work gave me a deeper insight into all the different research directions within IPP. I would like to thank all PhD students of IPP and Birger Buttenschön and Peter Kurz for their collaboration.

Special gratitude is owed to Mirko Ramisch and Kirsi Manz for their huge effort proof reading this thesis. I also acknowledge proof reading of selected chapters or larger parts of this thesis by Gregor Birkenmeier, Klara Höfler and

Nils Leuthold.

Finally I want to express my thankfulness to those who have been on my side year by year or day by day: my friends and my family for warmth and protection. Please forgive that I did not spent the time all of you had deserved. I like to thank my friends Thorsten Plambeck and Chris Buthmann, that we could anyway stay in contact over the years and distance. In particular I am thankful to my parents Peter and Heidrun, my brother Marvin, my great love Kirsi, my stepson Antti and our son Colin for their endless continuous support.